

21 DEC 1999

*Gas Turbine Laboratory
Department of Aeronautics and Astronautics
Massachusetts Institute of Technology
Cambridge, MA 02139*

FINAL REPORT
for AFOSR GRANT #F49620-96-1-0407

**ACTIVE CONTROL OF AEROELASTICITY AND
INTERNAL FLOWS IN TURBOMACHINERY**

submitted to

Air Force Office of Scientific Research/NA
801 N. Randolph Street
Arlington, VA 22203-1977

ATTN: Dr. Tom Beutner

PRINCIPAL
INVESTIGATOR:

James D. Paduano
Gas Turbine Laboratory, MIT

CO-INVESTIGATORS:

Alan H. Epstein
Gas Turbine Laboratory, MIT

Edward M. Greitzer
Gas Turbine Laboratory, MIT

DTIC QUALITY INSPECTED 44

PERIOD REPORTED:

January 1, 1996 - September 30, 1999

November 1999

20000111 128

REPORT DOCUMENTATION PAGE

AFRL-SR-BL-TR-00

399

Public reporting burden for this collection of information is estimated to average 1 hour per response, including the gathering and maintaining the data needed, and completing and reviewing the collection of information. Send comments regarding this burden estimate or any other aspect of this collection of information, including suggestions for reducing this burden, to Washington Headquarters Services, Directorate for Information Operations and Reports, 1215 Jefferson Davis Highway, Suite 1204, Arlington, VA 22202-4302, and to the Office of Management and Budget, Paperwork Reduction Project (0704-0188), Washington, DC 20503.

0003

1. AGENCY USE ONLY (Leave Blank)		2. REPORT DATE 12/6/99		3. REPORT TYPE AND DATES COVERED Final Technical Report: 1/1/96-9/30/99	
4. TITLE AND SUBTITLE Active Control of Aeroelasticity and Internal Flows in Turbomachinery				5. FUNDING NUMBERS Grant F49620-96-1-0407	
6. AUTHORS J. D. Paduano, A. H. Epstein, E.M. Greitzer, C. E. S. Cesnik					
7. PERFORMING ORGANIZATION NAME(S) AND ADDRESS(ES) Dept. of Aeronautics and Astronautics Massachusetts Institute of Technology 77 Massachusetts Ave., 31-264 Cambridge, MA 02139				8. PERFORMING ORGANIZATION REPORT NUMBER	
9. SPONSORING / MONITORING AGENCY NAME(S) AND ADDRESS(ES) Air Force Office of Scientific Research/NA 801 N. Randolph St. Arlington, VA 22203-1977				10. SPONSORING / MONITORING AGENCY REPORT NUMBER	
11. SUPPLEMENTARY NOTES The views, opinions and/or findings contained in this report are those of the author(s) and should not be construed as an official Department of the Army position, policy, or decision, unless so designated by other documentation.					
12a. DISTRIBUTION / AVAILABILITY STATEMENT Approved for public release; distribution unlimited.				12b. DISTRIBUTION CODE	
13. ABSTRACT (Maximum 200 words) This report describes work carried out at the Gas Turbine Laboratory at MIT during the period 1/1/96 - 9/30/99, in the area of active control of turbomachinery. Within the overall project, three main research areas were pursued. These are, in brief: I. Active control of rotating stall with inlet distortion; II. Injectors as actuators for rotating stall control; III. Active stabilization of surge in an aeroengine; and IV. Development of an active rotor for aeroelasticity diagnostics, system identification, and control.					
14. SUBJECT TERMS Active Control of Fluid Systems, Compressor Aeromechanics, Surge, Rotating Stall, Flutter and Forced Response, Inlet Distortion.				15. NUMBER OF PAGES 108	
				16. PRICE CODE	
17. SECURITY CLASSIFICATION OF REPORT UNCLASSIFIED	18. SECURITY CLASSIFICATION OF THIS PAGE UNCLASSIFIED	19. SECURITY CLASSIFICATION OF ABSTRACT UNCLASSIFIED	20. LIMITATION OF ABSTRACT U		

NSN 7540-01-280-5500

Standard Form 298 (Rev. 2-89)
Prescribed by ANSI Std. Z39-1298-102

ACTIVE CONTROL OF AEROELASTICITY AND INTERNAL FLOWS IN TURBOMACHINERY

James D. Paduano Alan H. Epstein Edward M. Greitzer
Carlos Cesnik Marthinus van Schoor

Executive Summary

Herein we report on a diverse program in active control of turbomachinery, whose results fall into two classes. The first set of results constitute follow-on work in the area of active control of compressor rotating stall and surge in aeroengines, and the second set represent a new research area in modeling and control of aeroelasticity in turbomachinery. Major steps forward in the state of the art were made in both of these areas. Rotating stall and surge control methods were advanced and demonstrated on full-scale devices. Following this, the infrastructure for, and first applications of, active control of aeroelasticity were developed. The most outstanding of our contributions are listed in this summary; an objective-by-objective review of the program results follows. Accomplishments and new findings are then summarized, followed by relevant references, some of which are attached as appendices to the report.

Active control of rotating stall in the face of inlet distortion was taken on during the first part of this program, as a priority for maximizing the utility of active control in Air Force applications. Several experimental studies were conducted, culminating in demonstration, in a cooperative program with NASA Glenn, of rotating stall control in a transonic compressor with both circumferential and radial inlet distortion in July 1997 [1]. Modeling, identification, and robust nonlinear control procedures developed in this program and demonstrated in the MIT 3-stage compressor have proven themselves in various industrial scale and Air Force applications (including a recent full-scale test at Wright Patterson [2]).

Active stabilization of an aeroengine was demonstrated in March 1998. The surge dynamics of an Allied Signal 700 hp-class helicopter engine were identified, robust controllers were designed, and the dynamics were stabilized, extending the stable operating range of the compressor [3]. This result marked the first demonstration of *stabilization* of an aeroengine as a dynamical system, and subsequent operation at previously unreachable conditions.

Finally, significant progress was made toward modeling and control of aeroelasticity in turbomachinery. This new area of endeavor has benefited greatly from the smart engines expertise generated at MIT. At this time, a comprehensive set of modeling techniques are in place, demonstrations of passive control (mistuning methods) have been carried out on models of industrial devices, and a piezo-actuated active rotor blade for identification, diagnostics, and control of aeroelasticity has been built. In May of 1999, optimal mistuning of the GE "Fan C" rotor was analytically demonstrated in collaboration with Caltech (PRET program) [4], using models developed under an AASERT grant [5-8]. This demonstration of a unique passive control technique is targeted for experimental demonstration on the active rotor. In September 1999, under this grant and a DURIP grant, a 20,000 RPM spin test facility for testing the active rotor was completed.

Design and development of rotor blades for the active rotor has been a major recent research activity under the grant reported on herein. Prototypes of an active rotor blade design are currently being tested in the spin test facility. These blades achieve an industrial

transonic blade shape using graphite-epoxy spars and a high strength Rohacell core. Active control is achieved through piezo actuation and strain gauge sensing. The active rotor concept culminates the research activities in aeroelasticity, providing a vehicle for demonstration of the new results on modeling, passive control, and active control of aeroelastic phenomena in turbomachinery. Significant additional testing and development of this concept are still required, but major design challenges have been identified and addressed. These results, as well as results of work completed in previous years, is outlined in greater detail in the next section.

Objectives

In this section, a task-by-task description of the objectives of the program is given, followed by a brief statement of the results associated with that task. Where applicable, publications relating to the task are given. Significant new findings and Accomplishments are discussed in more detail in the next section.

Task 1.1: Complete analytical studies of active surge stabilization in small gas turbine engines with the aim of (1) elucidating the unsteady engine behavior important to engine stability, and (2) demonstrating that it is indeed possible to do closed loop stabilization of aircraft engines and realize a practical benefit.

Results: Figure 1 shows the main results from this task [3]. It shows that the unsteady

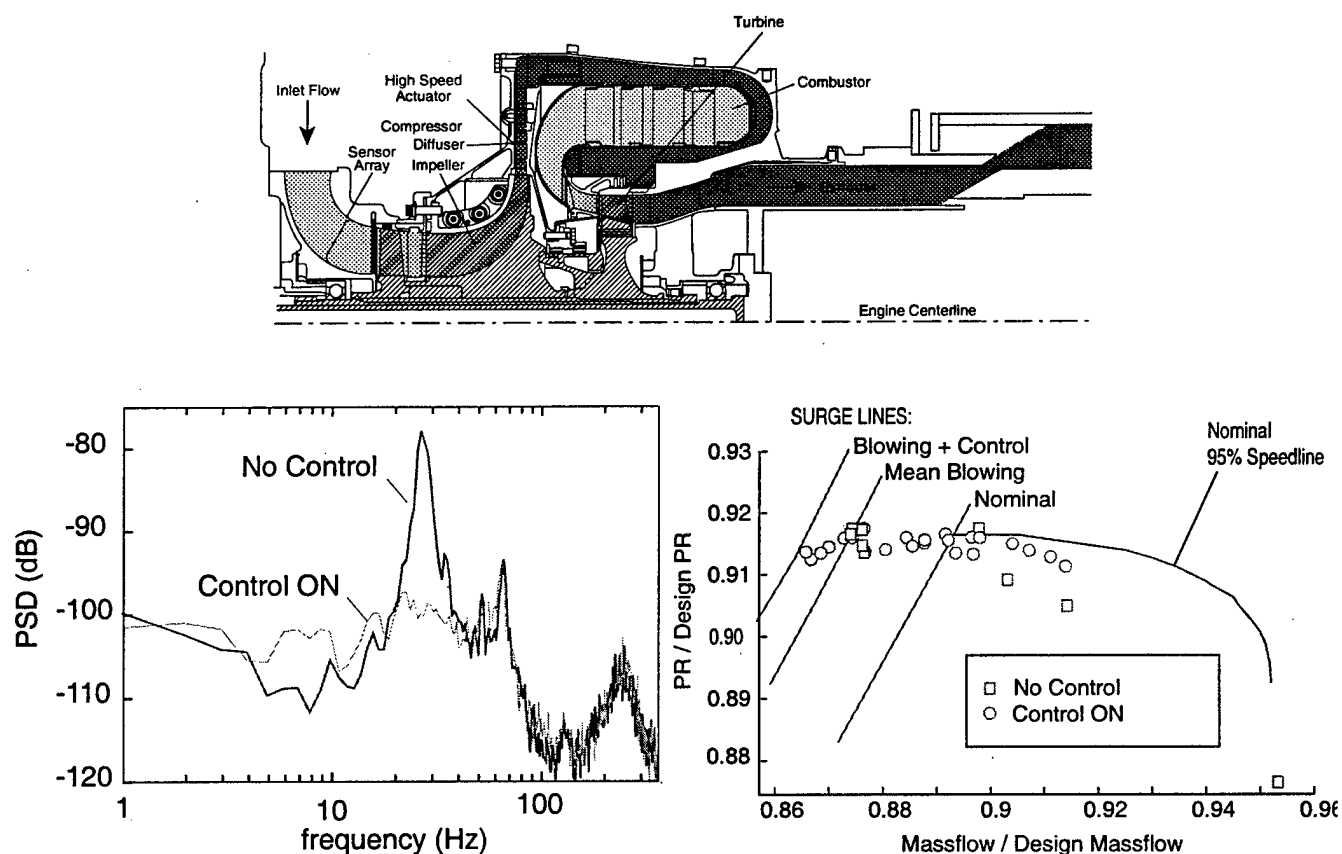


Figure 1: Active control of the LTS-101 engine. Spectrum (left) shows pre-surge behavior with and without control, compressor map (right) shows range extension

engine behavior prior to surge is dominated by two eigenmodes, both of which can be predicted by surge modeling techniques developed at MIT. The larger, 27 Hz peak corresponds to the Greitzer surge model instability, and the second, 70 Hz peak corresponds to an acoustic resonance which interacts with surge control actuators and sensors. Figure 1 also shows that by understanding, identifying, and stabilizing these eigenmodes, the compressor operating range can be extended. This is the first full-scale validation that closed-loop stabilization is possible and beneficial.

Task 1.2: Complete experimental research on the use of jet actuation to improve the performance of actively stabilized compressors and to improve theoretical models of such machines.

Results: Theoretical models of jet actuation were finalized and compared to experiment in [9]. Figure 2 shows the conceptual model used to generate a fluid-mechanical model of the injection process in a two-dimensional setting. Results in the 3-stage compressor at MIT and concurrent tests at NASA Lewis led to the conclusion that 3-dimensional effects (tip clearance flow modification) must be exploited to fully realize the performance benefits of jet injection. The NASA Lewis injectors, in contrast to those in the MIT 3-stage compressor, directed flow into the tip region. By so doing, it was shown that significant steady-state and unsteady gains in compressor range could be obtained with jet injection actuation.

Task 1.3: Continue the theoretical and experimental research on active compressor stabilization with inlet distortion, completing the work on control given knowledge of the distortion pattern.

Results: In [11], a comprehensive modeling tool for inlet distortion was developed. Detailed validation based on system identification is shown in Figure 3 [12], against the 3-stage axial compressor at MIT. This model starts with the inlet distortion total pressure profile, and predicts both the steady-state and unsteady response of the compressor. Through NASA-sponsored grants and SBIR studies which followed these studies [1, 13], this modeling tool has proved useful in industrial scale machines of various types, and has recently been used on a two stage military fan [2]. Controllers designed using these models were shown to be sufficient to stabilize compressors with distortion [11,12], although robust controllers based on system identification were found to be more effective. See more on this subject under task 2.5.

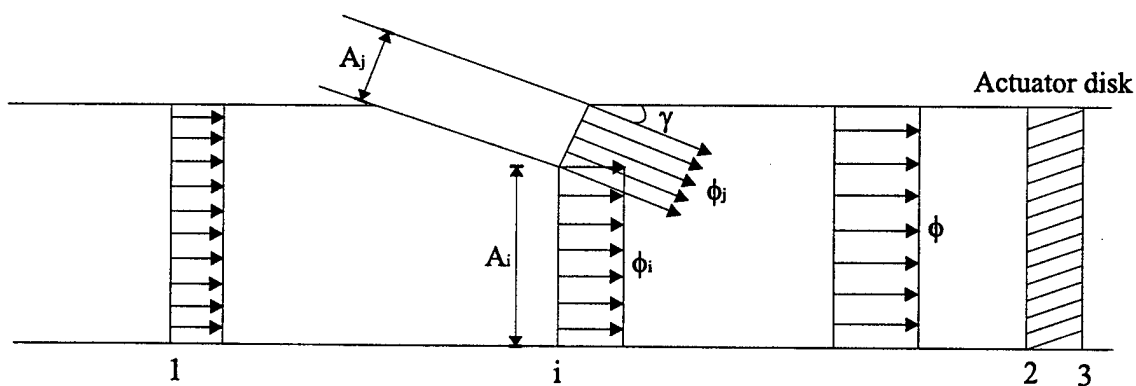


Figure 2: Experimentally validated 2-dimensional model for jet actuation.

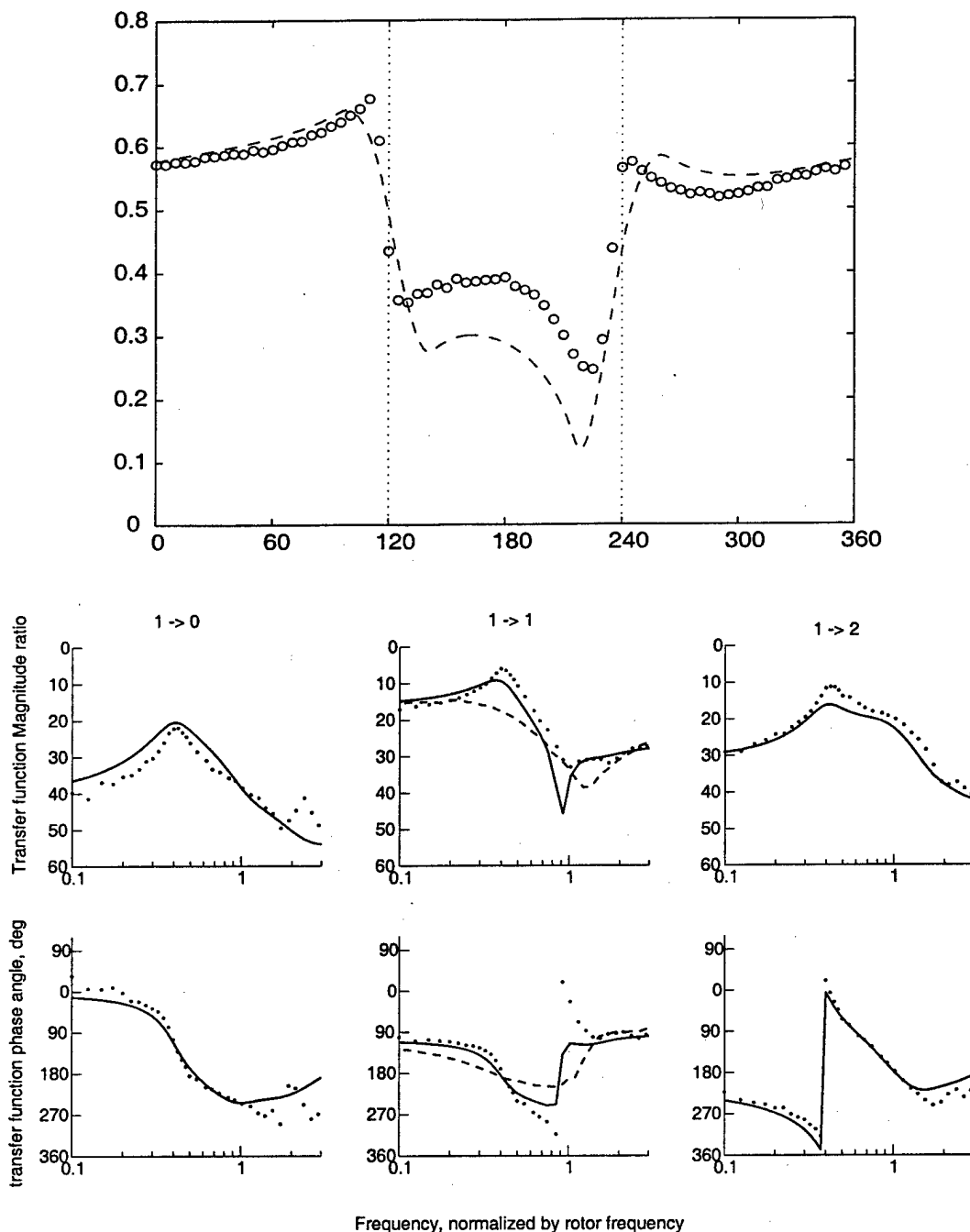


Figure 3: Experimental validation of distortion modeling [10]. Top - Comparison of theoretical (dashed) and measured (circles) velocity profile due to an inlet distortion. Bottom - Transfer function from first Fourier coefficient of inlet guide vane deflection to 0th, 1st and 2nd Fourier coefficient of axial velocity. Data taken with 1.9 dynamic head inlet distortion (circles and compared to theory (solid lines). Dashed line gives undistorted flow prediction.

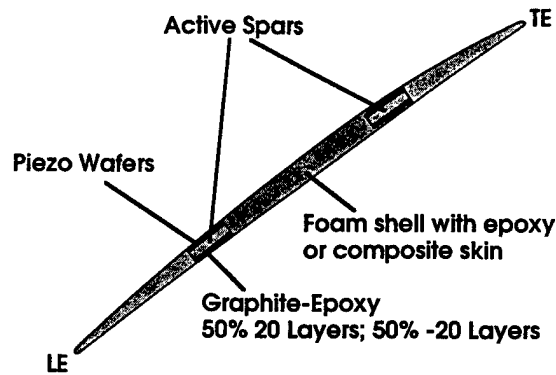


Figure 4 - Spar-and-shell concept for the active rotor blade.

Task 2.1: Conduct a preliminary design study of the active rotor concept including structural dynamics, aerodynamics, control, and fabrication concerns.

Results: Preliminary studies concluded that the structural dynamic and fabrication concerns were the most high-risk aspects of the active rotor design. Solid rotor blades were found to be incapable of reaching the desired bending and twist deflection levels. Therefore a spar-and-shell construction was embarked upon, see Figure 4. Finite element analysis, coupon tests, and procedure development for imbedding piezo-ceramics in the spars were conducted to create the baseline design concept for the active rotor blade. Further development and testing of this blade is described under Task 2.4 and 3.2.

Task 2.2: Quantitatively examine the way in which an active rotor can improve the performance of an advanced military compressor stage.

Results: Two studies were conducted to address the capabilities of the active rotor. First, a transonic Euler-based CFD analysis of the input-output properties of the active rotor was conducted, to determine if the signal-to-noise properties of the diagnostic signals coming out of the device would be sufficient. Figure 5 shows that the active rotor, if it can achieve

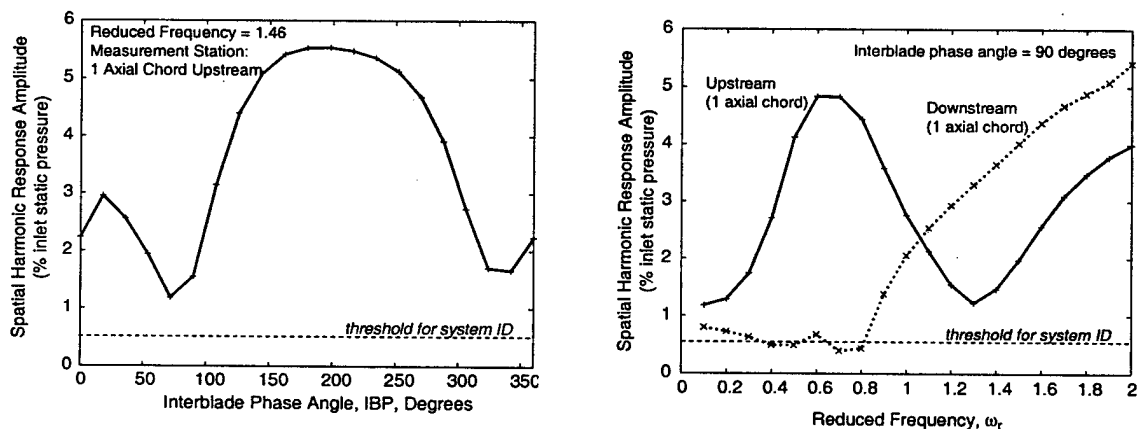


Figure 5: Off-blade pressure amplitudes induced by blade vibration, as a function of interblade phase angle (left) and frequency (right). Threshold levels are based on signal levels used for system identification in a transonic compressor at NASA Glenn [4,5].

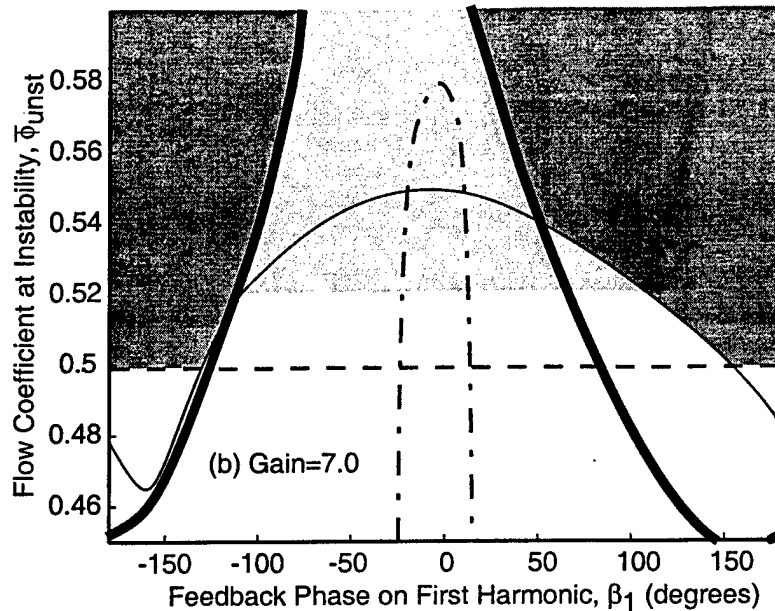


Figure 6 - Simultaneous stabilization of rotating stall and flutter using the active rotor. bold line - bending flutter stability boundary; solid line - rotating stall stability boundary; dashed line - surge stability boundary; dash-dotted line - torsion flutter stability boundary; light gray - open loop stable region; dark gray - closed loop stable region.

0.2 to 0.5 degrees of blade deflection, will deliver a large enough signal to allow detailed system identification of the flow fields associated with flutter over a large range of both spatial and temporal frequency, providing unique insight into the fundamental mechanisms associated with flutter. Figure 6 shows that active simultaneous stabilization of both flutter and rotating stall can be achieved with the active rotor [14]. These studies were conducted using new, control-theoretic models for flutter developed under the AFOSR PRET program with UCSB (Marc Jacobs, technical monitor) and the associated AASERT program. Results shown here were generated specifically for the active rotor project.

Task 2.3: Choose the geometry of the rotor and stage to be constructed as an active rotor.

Results: After contacting several possible sources, we accepted the suggestion of GE personnel to use the "Fan C" geometry that GE tested for NASA Lewis. This industrially-designed high-pressure ratio transonic fan exhibited stall flutter phenomena of the type this program was interested in studying, and the geometry is in the public domain. Figure 7 shows the geometry, as well as the spar design (see next task).

Task 2.4: Design and build a prototype active compressor rotor blade.

Results: This task proved to be the most challenging step in the active rotor development, and is only now coming to full fruition [17]. The first step was choice of materials for the spar, and finite-element validation of the spar path. The next, and most difficult, step was design and validation of a method for attachment of piezos to the graphite epoxy spars, in such a way that the severe stress levels at 16,500 RPM would not break the brittle piezo crystals. Finally, procedures for building the composite blade to meet all of the

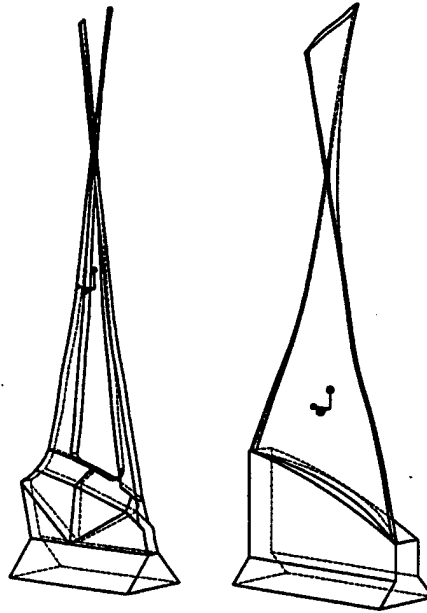


Figure 7 - GE "Fan C" Civil Fan Blade Geometry (right), together with the graphite-epoxy spar design for the active rotor. Rotor interface geometry is for prototype testing purposes only.

aerodynamic, structural strength, actuation and sensing requirements were developed. Many of these procedures are outlined in an attached document [18]. They include:

- 1) Numerical definition and CNC machining of spar plate molds.
- 2) Layup of graduated layers of graphite-epoxy prepreg to achieve spar taper (required for structural integrity). Layers are sequentially 'dropped' internal to the spars to achieve taper. hub interface geometry allows simple connection to hub.
- 3) Specialized vacuum heat-press curing of the prepreg to achieve good plate morphology.
- 4) Transfer of 3-D spar patterns onto spar plate (which is essentially a 'blank' out of which the spars must be cut), and subsequent 'hogging out' of the spars.
- 5) Piezo and strain gauge attachment. Spar twist can cause cracking of the piezos if not carried out properly.
- 6) Numerical definition and CNC machining of shell molds. Pre-twist of the aerodynamic shapes (to account for the flexible active rotor blade untwist at high RPM) can be easily achieved based on the numerical definition procedures (Matlab pre-twistable blade sections).
- 7) Numerical 'untwisting' of the blade planform (described by .stl-type triangular facets) to create a flat pattern for Rohacell blank cutting.
- 8) Rohacell cutting, shaping, and thermoforming into blade profile. Rohacell thermoforming procedures were developed specifically for this project, in cooperation with the manufacturer.

- 9) Machining spar paths into the Rohacell blade shell. Currently this a by-hand procedure; in the future this and other steps will be programmed into CNC machines using numerical definitions that we currently have in place.
- 10) Bonding of blade shell to spars, layup of leading edge and trailing edge skins, and final cure of complete assembly. The details of this step determine the integrity of the overall system, and modifications to this step are still being considered and tested.

Because of the complexity of this procedure, and the assessment that the rotor blade is by far the highest-risk component of the active rotor, a parallel program to develop a spin test facility for the rotor blades was put into place. Although this was not part of the original plan, it was deemed necessary. A DURIP grant was obtained for equipment acquisition, and some of the design work was done under co-sponsorship by the PRET program entitled "Robust Nonlinear Control of Aeroengine Stall and Flutter". The spin test facility (assembly drawing shown in Figure 8) was designed to be general purpose, but some unique features were designed in to make it compatible with the active rotor project:

- 1) The spindle of the facility is designed to have the capability to operate in the blow-down compressor facility, so that shake-down of the active rotor can be done using the same drive, bearing, shaft, seal, and slip ring hardware.
- 2) A power slip ring was designed into the facility, to allow piezo actuation signals to be transferred into the rotating frame.
- 3) The first rotor designed for the facility was designed especially for testing active rotor blades. This design allows rotor designs to be quickly changed and tested (Figure 9).

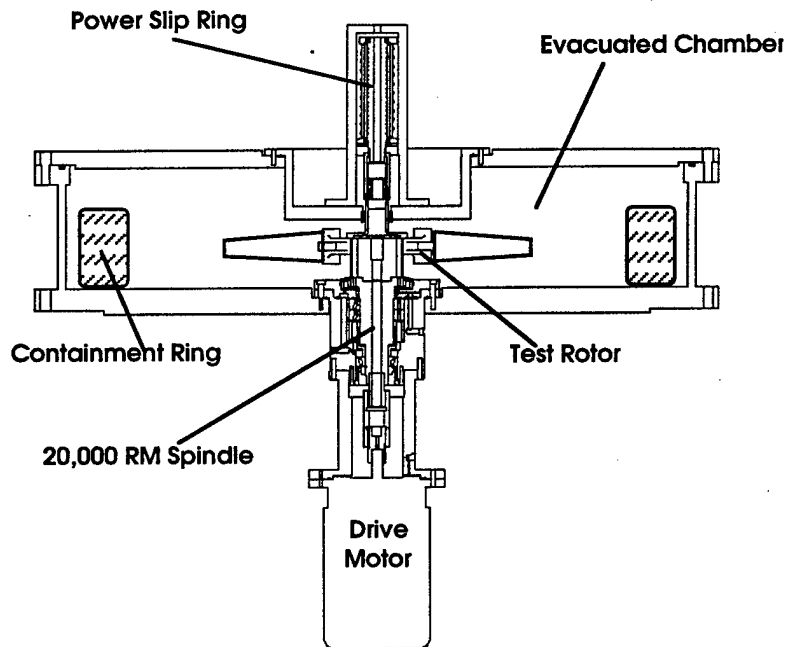


Figure 8 - Assembly Drawing of the 20,000 RPM evacuated spin test facility.

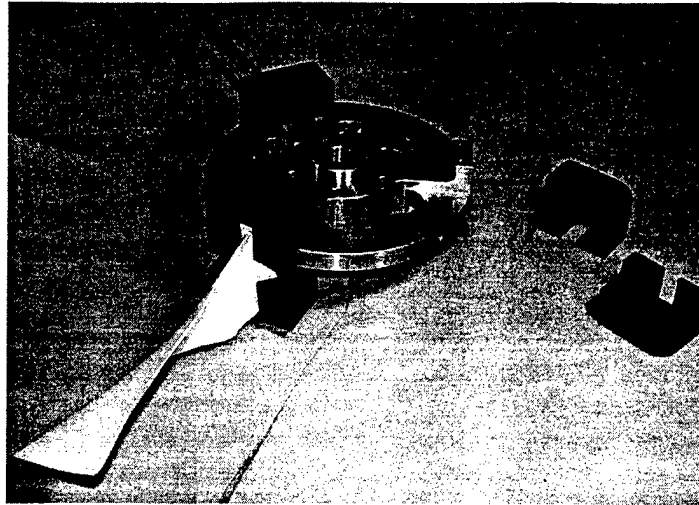


Figure 9 - Rotor for testing active rotor blades, shown with typical test articles.

Task 2.5: Continue the theoretical and experimental research on active compressor stabilization with inlet distortion, specifically, work on control with unknown distortion patterns.

Results: This task was based on the realization that one prefers control laws which are independent of the incoming distortion magnitude and location - we will call this 'insensitivity'. The primary drawback of the original, model-based LQG control laws was their sensitivity - one must know the location and amplitude of the inlet distortion before a control law can be enacted. In order to address this issued, two other control laws were considered, which are independent of distortion location and magnitude. These are described here, and compared in Table I.

The first 'insensitive' control law is simply a SISO controller - each measured SFC is fed back to a corresponding SFC of actuator deflection. This allows one to separately stabilize each of the unstable modes during clean inlet flow. During distorted flow, however, SFC coupling degrades the performance of such a control law. This controller is at one end of the spectrum of trading off performance (range extension) for robustness (insensitivity to distortion location). A simple method to improve performance is to experimentally introduce and tune cross-coupling terms; this however makes the control law sensitive to the location of the distortion pattern.

Type of Control	Range Increase
Linear Quadratic Gaussian	1.5%
Cross-Coupled Harmonic Feedback	3.0%
SISO Harmonic Feedback	2.2%
Distributed Feedback	3.7%

Table I: Stable Operating Range Increase of Various Control Laws, 0.8 Dynamic Head Distortion

The second 'insensitive' control law developed is termed *distributed feedback*. This control law measures the entire measured shape of the disturbance, and feeds back a shifted and amplified version of it to the actuators. This control law has several advantages: It is a fixed rather than dynamic controller, thus very simply implemented. It is insensitive to the location of the distortion. It simultaneously considers all of the Fourier harmonics, and utilizes the measured relative phases of the SFCs to directly determine the phase of the actuation - thus, according to simulation studies, it is also insensitive to the *type* of distortion introduced. Finally, this control law performed as well or better than any other control law tested. Interestingly, the trade-off between range extension and insensitivity is broken by the distributed feedback controller - it is both the best performer and the most insensitive to distortion type and location. This attests to the fact that lack of robustness can mar performance considerably in an experimental setting.

Task 3.1: Complete experimental and analytical studies of active compressor stabilization with inlet distortion.

Results: Described under previous task. As noted earlier, the lessons learned in this program have formed an integral part of various follow-on efforts. Some of these efforts are described in [1, 2, 13].

Task 3.2: Experimentally evaluate the behavior of the active blade by bench testing.

Results: Figure 10 shows preliminary blade deflection results. Predicted tip twist angle is based on actual tip deflection results, converted to angular twist by assuming both spars achieve similar deflections. Clearly the foam shell has a significant impact on the tip deflection of the blade, reducing the effectiveness by one order of magnitude. Although the resulting deflection would still be sufficient for system identification studies (based on the results shown in Figure 5, additional work is underway to reduce the detrimental impact of the shell on control power.

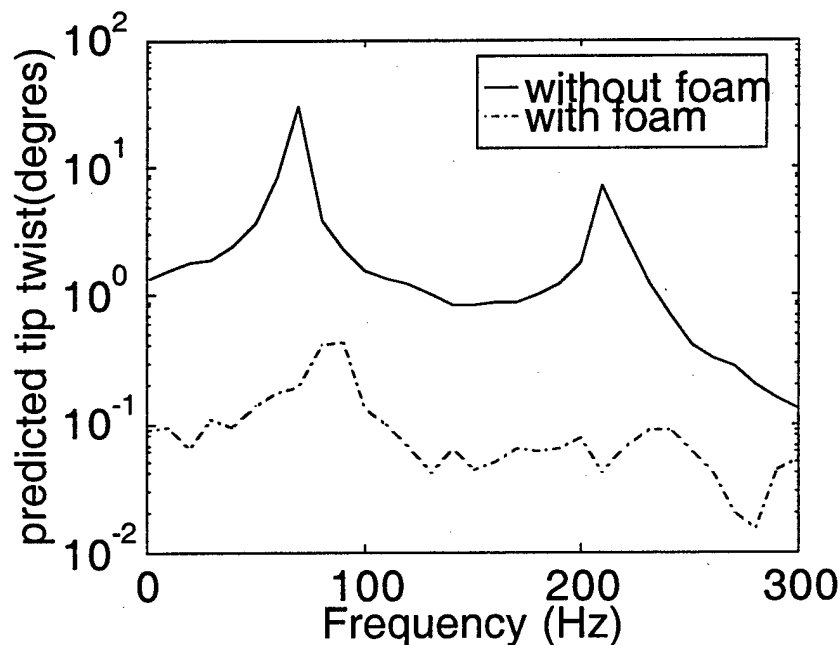


Figure 10 - Measured active rotor spar deflections, plotted on an axis which predicts the tip deflection achievable.

Task 3.3: Continue the studies of the aerodynamics of an active rotor.

Two primary aero-structures tools reached completion during the last year of effort, and are described respectively in [5] and [16]. Although these were developed under joint support with the PRET and AASERT programs, one of the driving applications behind them was the active rotor, and examples (already shown) were derived directly from active rotor considerations. In particular, the "Fan C" aerodynamic and flutter properties, which are the starting point for the active rotor research, were captured in a low order model developed jointly with UTRC [5]. Figure 11 shows an analytical Campbell diagram for Fan C, which compares favorably with experimental results from GE.

Task 3.4: Based on the preliminary design study, the aeroperformance study and the bench testing of the prototype blade, design in detail an active rotor.

This task was only partially completed due to the complexity of the blade design. It remains to design a suitable hub interface for the blade, to design the rotor hub, and finally to design

OPTIONAL Task 3.5: Fabricate an active rotor suitable for installation in the MIT blowdown compressor and the Wright laboratory single-stage compressor facility.

RESULT: This optional task was not funded. Our goal is complete the testing and prototype fabrication results necessary to do the final design and fabrication of the active rotor this Spring.

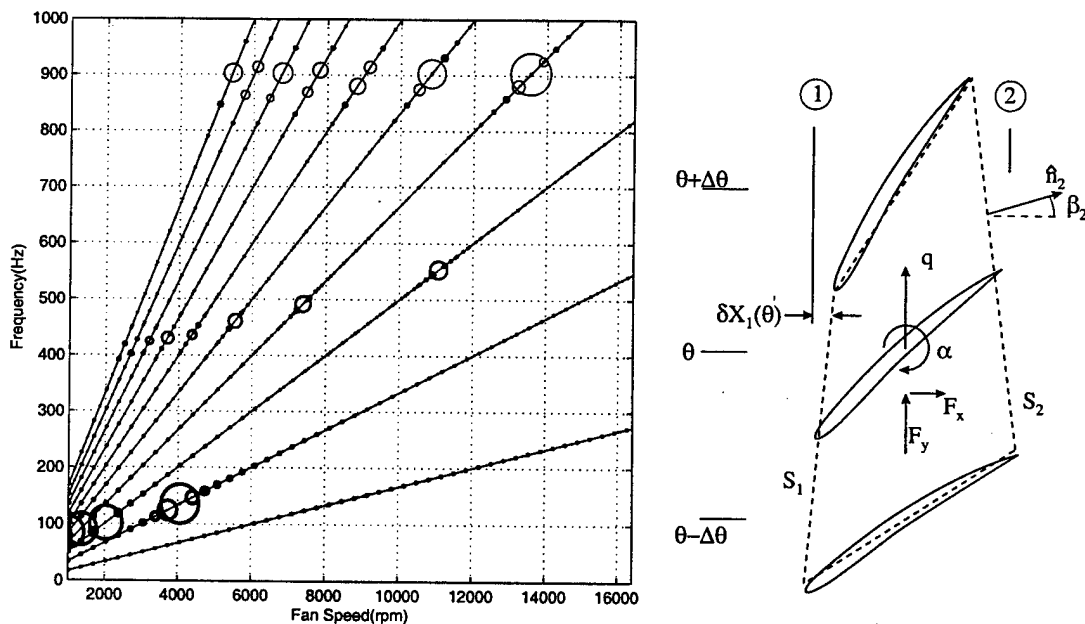


Figure 11 - Analytical Campbell diagram for GE Fan C, based on first-principles low-order model (shown at right). Lines represent 1st through 4th harmonics of rotor frequency excitation. Large circles represent structural frequency crossing circles size indicates forced response amplitude.

Accomplishments/New Findings

Accomplishments and new findings will be briefly summarized here, with references to the attached papers for further details. They are organized into the following four major areas of effort: rotating stall control with inlet distortion, injectors as actuators for rotating stall control, surge stabilization in engines, and the active rotor.

Rotating Stall Control with Inlet Distortion

The AFOSR-funded tools and procedures for analyzing and controlling inlet distortion have been the foundation for a wide variety of follow-on projects, both directly and indirectly related to inlet distortion. The robustness of the procedures, the importance of distortion-related phenomena to engine operability and performance, and the success of the results at MIT, NASA, GE, and Wright-Patterson make this one of the most successful components of the research results presented here. A brief list of the applications that have been impacted follows.

1. NASA Glenn transonic compressor tests of active control with inlet distortion utilized the codes and concepts developed under this project, achieving significant stall margin improvements. Chris van Schalkwyk, whose Ph.D. was supported by AFOSR, was a key researcher on this project.
2. Tip clearance non-uniformities result in distorted inlet flow, which couples with the non-uniform compressor performance in a way that reduces stability and pressure rise. GE performed compressor tests to quantify the impact of asymmetric tip clearance, and to validate a model developed at MIT using the codes developed under AFOSR support. This model now allows GE engineers to quantify the impact of tip clearance asymmetry.
3. GE is currently engaged in a program to quantify the effect of aerodynamics on rotordynamic stability. Rotor whirl induces a rotating asymmetric tip clearance, which in turn induces a rotating distortion, which creates aerodynamic forces on the rotor that can destabilize the rotordynamics. Again, the fundamental tools for modeling unsteady asymmetric distortion is a key technology being used in this study.
4. Recent tests at Wright-Patterson tested the concept of active control of rotating stall with inlet distortion in a full-scale military fan. Chris van Schalkwyk (see item 1) was again a key researcher in these tests.

The key discovery of the distortion control research is that distortion-related phenomena, although complex, are not only amenable to engineering modeling, but also to alteration through open-loop and feedback control. Several examples now exist where large- and full-scale apparatus exhibit behaviors consistent with our models, even to the point of *changing in the way we force them to* through application of control.

Injectors as Actuators for Rotating Stall Control

Injectors is another area where work initiated under AFOSR support has come to fruition in larger scale applications. One of the main findings of the research conducted at MIT was that injection cannot effectively penetrate beyond the casing wall. Fortunately, we have also found that injection into the tip of the compressor has an enormous impact on the

stability and pressure rise of the compressor. This discovery, together with analysis, design, and engineering tools developed under AFOSR support, have been expanded upon and transitioned to industry by NASA Glenn (Michelle Bright, Tony Strazisar, Ken Suder, and Michael Hathaway). The key finding that NASA has developed is that very small amounts of steady blowing in the tip region, if properly designed, can have very large impact on compressor operating range. Because of the controllable nature of injection, this experimentally verified fact can be used to improve the performance of compressors without incurring the design-point penalties normally associated with other stability enhancement methods such as casing treatment.

Follow-on research on the use of injectors for control of unknown distortion patterns was conducted under the PRET program [17]. Experimental results showed that nonlinear controllers could effectively use injectors to increase the 'distortion tolerance' of compressors, opening up new possibilities for performance improvement in the engine-inlet-airframe integration problem.

Surge Stabilization in Engines

The key accomplishment which was achieved under AFOSR was demonstration of stabilization of the dynamics leading to surge in a full scale engine. This demonstration was conducted as a fundamental study of engine surge stability properties, as opposed to an engineering demonstration of active control. Thus we differentiate our results from other recent results by the scientific information that was acquired. Specifically, we showed that although there are many forms of unsteadiness in a typical engine, the input-output behavior of the compression system, when forced by a high-response actuator, yields easily interpretable information about system stability. Thus the often clouded picture of the mechanisms important to system stability is made significantly clearer using control-theoretic methods (signal processing, forced response testing, system identification, and control).

The information obtained from the Allied Signal LTS-101 engine was that two eigenmodes of the compression system dominate the stability behavior -- one at the classical surge or 'Helmholtz' frequency, and one at a frequency related to the acoustic duct modes of the overall engine. We further showed that stabilization of the surge eigenmode stabilizes the system, reducing the mass flow of surge initiation. Although interesting for its practical implication, this result also solidifies the connection between small-amplitude stability and large-amplitude surge phenomena, which is an important fundamental finding.

Active Rotor Research

Active rotor research has concentrated on the technologies and processes that would make an active rotor feasible, and on quantitative determination of the measurements that could be obtained with the device. The primary accomplishment sought in the first arena is fabrication of a composite rotor blade with the strength and actuation properties required for aeroelastic diagnostics, system identification, and control. Continued testing of the graphite-epoxy-Rohacell blades is required to fully achieve this goal, but we expect to reach our conclusions, and incorporate them into an active rotor design, by mid-2000. We expect most if not all of the technologies and processes developed under this grant to prove effective in the active rotor, and therefore these constitute accomplishments awaiting final fruition. Specific results to date include a complete graphite-epoxy base and spar structure which can withstand all centrifugal loads up to 7,000 RPM (designed for 16,500 RPM, but as yet tested only at the lower speed), demonstrated piezo-actuation levels of approximately

0.1 degrees (sufficient for system identification, but lower than the desired level of 0.25-0.5 degrees), and a methodology for pre-stressed piezo bonding which allows the piezos to survive in the stress-strain environment of the rotor at full speed (coupon tests were used to verify the strength properties of the bonded piezos).

In the arena of modeling of aerostructural behavior of the active rotor, significant progress has been made under related grants. Under the PRET program grant "Robust Nonlinear Control of Aeroengine Stall and Flutter," a system-level, first-principles model of the rotor being used as the baseline for the active rotor design (GE Fan C). Using this model we determined that simultaneous stabilization of rotating stall and flutter can be achieved with an active rotor. Furthermore, methods for quantifying sensor and actuator effectiveness for flutter control were devised. Under an AASERT grant, a CFD-based model of transonic compressor flutter was developed, and used to quantify the expected input-output properties of the active rotor. This analysis concluded that the original goal of 1 degree tip deflection would achieve 2 to 5 times the signal levels (on off-blade sensors) necessary for system identification (see Figure 5).

Publications/References (* - Attached)

1. * Spakovsky, Z., Weigl, H. J., Van Schalkwyk, C. M., Paduano, J. D., Bright, M. M., Strazisar, T., and Suder, K., "Rotating Stall Control in a High-Speed Stage with Inlet Distortion Part I: Radial Distortion, and Part II: Circumferential Distortion," *Journal of Turbomachinery*, Vol. 121, July 1999.
2. M. Bright, NASA Glenn Research Center, and C. van Schalkwyk, Scientific Systems Corporation, personal communication.
3. * Nelson, E. B., Paduano, J. D., and Epstein, A. H., "Active Stabilization of Surge in an Axi-Centrifugal Turboshift Engine," presented at the International Gas Turbine and Aeroengine Congress and Exhibition, Indianapolis, June 7-10 1999. To be published in *Journal of Turbomachinery*.
4. Shapiro, B., and Willcox, K., "Analyzing the Mistuning of Bladed Disks by Symmetry and Reduced-Order Aerodynamic Modeling," to be published in *Journal of Engineering for Gas Turbines*.
5. Willcox, K. E., "Reduced-Order Aerodynamic Models for Aeroelastic Control of Turbomachines" Ph.D. Thesis, Massachusetts Institute of Technology, February 2000.
6. Willcox, K. E., Paduano, J. D., Peraire, J., and Hall, K.C., "Low Order Aerodynamic Models for Aeroelastic Control of Turbomachines," AIAA 99-1467, 40th SDM Conference, St. Louis, April 1999.
7. Willcox, K., Peraire, J., and White, J., "An Arnoldi Approach for Generation of Reduced Order Models of Turbomachinery," submitted to the 38th Annual Aerospace Sciences Meeting and Exhibit, Reno, NV, January 2000.
8. Willcox, K., Peraire, J., and Paduano, J., "Application of Model-Order Reduction to Compressor Aeroelastic Models for Turbomachinery", To be presented at the ASME Turbo Expo, Munich Germany, May 2000.

9. * Vo, H. D., Paduano, J. D., and Epstein, A. H., "Experimental Development of a Jet Injection Model for Rotating Stall Control," presented at the ASME Turbo Expo, Stockholm, Sweden, June 1998
10. Weigl, H. J., Paduano, J. D., Frechette, L. G., Epstein, A. H., Greitzer, E. M., Bright, M. M., and Strazisar, A. J., "Active Stabilization of Rotating Stall in a Transonic Single Stage Compressor *Journal of Turbomachinery*, Vol. 120, October 1998, pp. 625-636.
11. van Schalkwyk, Christiaan M., "Active Control of Rotating Stall With Inlet Distortion," Ph.D. Thesis, Massachusetts Institute of Technology, June 1996.
12. * van Schalkwyk, C. M., Paduano, J. D., Greitzer, E. M., and Epstein, A. H., "Active Stabilization of Axial Compressors with Circumferential Inlet Distortion," *Journal of Turbomachinery*, Vol. 120, October 1998, pp. 431-439.
13. * van Schalkwyk, C. M., Mehra, R. K., and Paduano, J. D., "Semi-Active Stabilization of Axial Compressors with Circumferential Inlet Distortion using Low Bandwidth Actuators," presented at the IEEE International Conference on Control Applications, Hartford, October 5-7, 1997.
14. Hong J. Y., Wong, M. T. M., and Paduano J. D., "Modeling For Control of Compressors with Aerodynamic And Aerostructural Instabilities," Invited paper, Proceedings of the US-Japan Seminar on Abnormal Flow Phenomena in Turbomachinery, November 1-6, 1998, Osaka, Japan.
15. Maahs, G. L., "Design of an Active Compressor Blade for Aeroelastic Studies," M. S. Thesis, Massachusetts Institute of Technology, February 1999.
16. Hong, J. Y., "Application of a Low-Order Model to Assess Compressor Aeroelastic Response and its Control," M. S. Thesis, Massachusetts Institute of Technology, February 2000 (completed October 1999).
17. * Protz, J. M., and Paduano, J. D., "Rotating Stall and Surge: Alternate Modeling and Control Concepts," presented at the IEEE International Conference on Control Applications, Hartford, October 5-7, 1997.
18. * Maahs, G. L., and Cesnik, C. E. S., "Development of the Active Compressor Rotor Blade - Focus on Piezoelectric Actuation Issues," Internal MIT Report, November 1999.



The Society shall not be responsible for statements or opinions advanced in papers or discussion at meetings of the Society or of its Divisions or Sections, or printed in its publications. Discussion is printed only if the paper is published in an ASME Journal. Authorization to photocopy for internal or personal use is granted to libraries and other users registered with the Copyright Clearance Center (CCC) provided \$3/article is paid to CCC, 222 Rosewood Dr., Danvers, MA 01923. Requests for special permission or bulk reproduction should be addressed to the ASME Technical Publishing Department.

Copyright © 1999 by ASME

All Rights Reserved

Printed in U.S.A.

ACTIVE STABILIZATION OF SURGE IN AN AXI-CENTRIFUGAL TURBOSHAFT ENGINE

E. B. Nelson, J. D. Paduano, A. H. Epstein
Gas Turbine Laboratory, Department of Aeronautics and Astronautics
Massachusetts Institute of Technology
Cambridge, Massachusetts 02139

ABSTRACT

Active stabilization of surge was implemented on an Allied Signal LTS-101 axi-centrifugal gas producer, reducing the surging mass flow by 1%, for an operating range increase of 11%. Control was achieved using high response sensors in the inlet and diffuser throat, coupled to actuators that injected air near the diffuser throat. System identification and modeling indicate that a classical surge-type eigenmode and an eigenmode associated with engine duct acoustics dominate the engine's input-output properties. The surge eigenmode's stability determines the open-loop surge mass flow. A robust linear controller with three inputs and one output stabilized this eigenmode without destabilizing the acoustic mode. The controller facilitated a 1% reduction in surging mass flow at 95% N1 corrected; this increases the engine's choke to surge stable operating range by 11%. This paper elucidates the measured unsteady pre-surge behavior of the engine, and outlines a systematic procedure for surge control law development.

1 INTRODUCTION

In aircraft engines, the compression system instability known as surge is currently avoided using steady state means. This includes vane scheduling and system matching to insure that the surge line is sufficiently far from the operating line. Recent research considers unsteady means, such as active control, to prevent surge. Performance and/or operability benefits can be realized from an extension of the stable operating range, that is, a reduction of the engine mass flow at which surge occurs.

In the research of Fink (1988), Huang and Ffowcs Williams (1989), Pinsley (1991), Gysling (1991), and Simon et al. (1993), active control of surge was studied on laboratory turbocharger rigs. These studies showed that surge is the result of instability of small perturbations at specific frequencies. Furthermore, this work demonstrated that by stabilizing the small-perturbation dynamics, the large-amplitude surge event can be prevented. These initial studies not only demonstrated active control, but also provided an

analytical framework for applying the concept to more complex compression systems.

This work has motivated surge control experiments in engines and engine components. Notable examples include Ffowcs-Williams and Graham (1990), Freeman et al. (1997), and Eveker et al. (1997). These studies shared the notion of preventing surge using unsteady measurements that feed back to high response actuators. The goal of the work reported herein was to demonstrate techniques that reduce the surging mass flow of an engine through stabilization.

An Allied Signal LTS-101 turboshaft helicopter engine was used for this research. By studying the perturbations prior to surge and characterizing the engine's input-output dynamics, we show that the small perturbation properties observed in laboratory scale rigs are present in this engine. We discuss how these perturbations are modeled by incorporating 1-D acoustic ducts into a system model similar to that suggested by Greitzer (1976). Finally, we describe the control law development and implementation, and the range extension that was achieved. At each stage, fundamental concepts developed in previous work are applied, and modified as needed for the engine environment.

The paper traces the control system development process. The first step is to measure frequency responses from the actuator to all of the available sensors. The second step is to select a set of sensors for feedback. Next, a state-space model is fit to the frequency response data between the input and the selected outputs. This model is then used for control law design. The closed-loop behavior measured by all the available sensors motivates changes to both the feedback sensor configuration and the control law design. Implementation issues and control system strategies also influence compensator design and redesign. We present only the ultimate results of this process, emphasizing the system features that have the greatest impact on the success of the stabilizing controller.

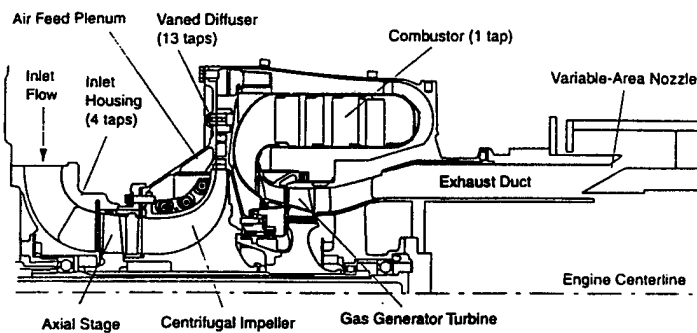


Figure 1: LTS-101 Gas Producer. Note plenum above impeller shroud.

II TEST APPARATUS AND OPEN LOOP TESTS

The tests presented here were conducted on an Allied Signal LTS-101 600A-2 600 horse power class turboshaft helicopter engine¹, modified specifically for active control research. The LTS-101 has a single axial stage and a centrifugal stage with vaned diffuser. Figure 1 shows a side view of the engine. The design pressure ratio is about 8 to 1 and the design corrected weight flow is about 5 lb/s.

The gas producer installed at MIT was modified for these experiments. First, the diffuser throat area was slightly enlarged to ensure that the centrifugal stage limited the stable operating range. Second, the turbine nozzle guide vane area was reduced to move the operating line closer to the surge line and thus reduce the turbine inlet temperature while operating near surge. Third, the power turbine and shaft were removed (Borror, 1994) and replaced with a variable area exit nozzle.

The engine mounting and nozzle arrangement are unusual in that the engine is mounted on linear bearings and translated axially to change the nozzle area (Figure 1). To accomplish this, the nozzle consists of two concentric cones, one mounted to the engine, the other to the stationary exhaust system. This arrangement also facilitates measurement of engine thrust.

Three separate desktop PC computers were used. One recorded steady-state engine performance, controlled engine operation, and monitored diagnostic parameters. The second acquired high speed dynamic data from pressure transducers at five axial stations, which are shown in Figures 1 and 2. The third implemented the feedback control law and sent commands to the actuator.

Actuation Using Air Injection

The centrifugal compressor of this engine employs a vaned diffuser. Actuation is implemented by injecting laboratory air into the throats of the diffuser passages, at about the diffuser discharge pressure. This approach was chosen both because it was expedient and because this form of actuation is 'close-coupled' to the compressor, a desirable feature for effective surge control as discussed by Simon (1993). Close-coupled means that the actuation is located near or in the compressor. Such actuators have a nearly instantaneous effect on the energy source of the surge instability (the compressor), without long delays or intermediate dynamics.

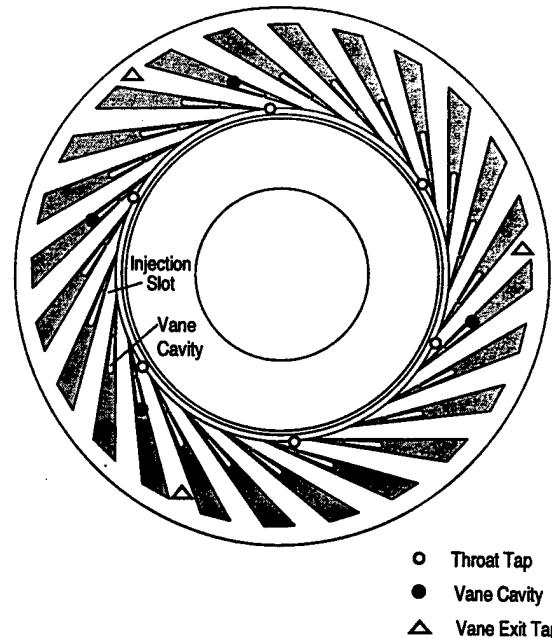


Figure 2: Circumferential Tap Locations Within Diffuser

The standard engine configuration includes slots at the throat of each vaned diffuser passage which communicate through a circumferential plenum above the impeller shroud (the slots can be seen in Figure 2, and the plenum is shown in Figure 1). This approach is used in many high pressure ratio centrifugal compressors to increase their surge margin. For these experiments, the orifices connecting the throat slots and the plenum were enlarged to improve the speed of response, and a control valve was mounted external to the plenum. The valve, adapted from a Moog linear force motor, can modulate the injectant from 2% to 5% of the engine air flow at a full signal bandwidth of 330 Hz.

All tests were conducted at a mean injection level of 3.8%. Thus we "baseline" performance with mean injection, and judge controller performance against this baseline. All compressor characteristics are given in terms of flow downstream of the compressor (inlet flow + injected flow); range extension results based on upstream mass flow are nearly identical, since the mean blowing case is taken as the baseline. All data and analysis presented herein are at 95% corrected speed. Time resolved pre-surge measurements show that a surge mode similar to that seen in laboratory-scale rigs is present, and that when this mode is unstable (or nearly so) the system enters surge. However, unlike the laboratory scale rigs, the engine also exhibits acoustic modes.

Steady Injection Tests

The influence of steady injection on the speed line shape is shown in Figure 3. Without injection, the stable region of the characteristic slopes negatively, and flattens to a peak over a short range of corrected mass flow (Corn, 1998). With steady injection, the characteristic is flatter, with a larger region of shallow slope. Injection also causes surge inception to be more gradual, exhibiting a longer evolution of a dynamic instability. Finally, steady injection stabilizes the compressor to lower corrected mass flows, at the expense of a reduced engine pressure ratio.

¹ Among the many vehicles powered by the LTS-101 are the Kawasaki BK117 "Eurocopter", the Aerospatiale AS350D "Astar" & HH-65 "Dolphin", and the Bell 222.

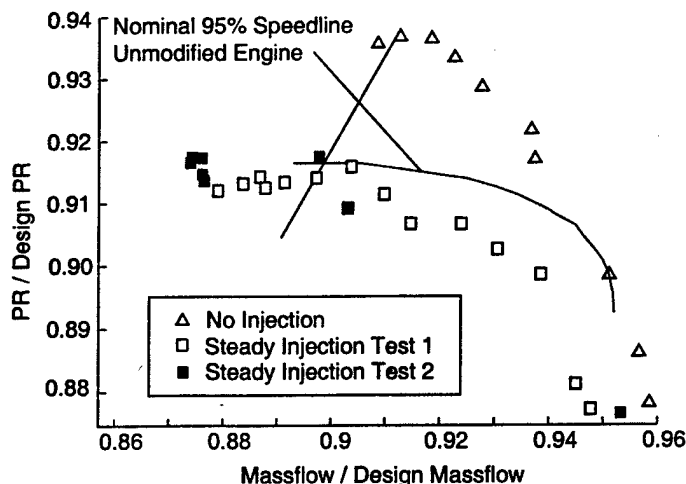


Figure 3: Speed Lines at 95% Corrected Speed

Unsteady data was taken at surge inception with steady injection while closing the exhaust nozzle in small, discrete steps near the surge line. Figure 4 shows static pressure traces, taken at two axial stations, during the last 230 rotor revolutions prior to surge. Note that although the data is quite noisy, a high frequency resonance is visible, as well as a lower frequency resonant transient immediately prior to surge.

Figure 5 shows the power spectrum of static pressure in the small diffuser-vane cavity that feeds into the throat slot (see Figure 2). Spectra were taken at three operating points: one at +4.7% mass flow from surge, one at +0.3% mass flow and one immediately prior to surge. Two peaks are apparent immediately prior to surge, at 28 Hz and 68 Hz. As the compressor is throttled toward the surge line, these two peaks grow dramatically.

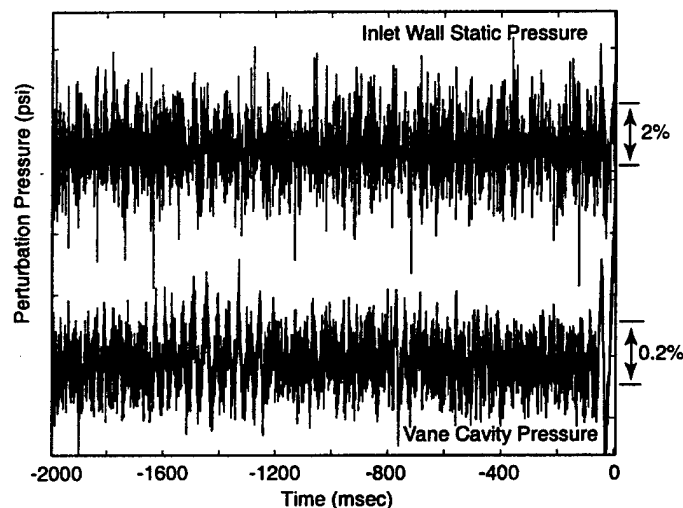


Figure 4: Open loop unsteady pressure traces 2 seconds prior to surge. See Figure 2 for location of vane cavity pressure taps. Perturbation magnitudes are in percent compressor exit pressure.

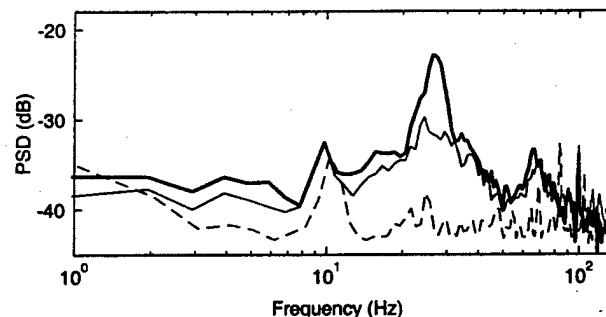


Figure 5: Power Spectral Density of Vane Cavity Pressure. Bold = Immediately prior to surge. Solid = 0.34% in mass flow from surge. Dashed = 4.7% in mass flow from surge.

Based on the above observations, the time resolved pressure data were low-pass and band-pass filtered at 30 and 70 Hz, respectively. The 70 Hz band-pass filtered time history (Figure 6) shows a resonance for hundreds of revolutions prior to surge. Examination of the relative phases measured at the inlet, vane cavity, diffuser exit, and combustor stations suggest that this is an acoustic mode; it has a standing-wave-like, spatially varying pressure. Acoustic modes at other frequencies were also observed. Because they do not appear to play a role in surge inception, they will not be discussed in detail here.

The low-pass filtered time history shows a 28 Hz signal with different characteristics than the 68 Hz signal. First, the phase is similar at all axial locations, indicative of a 'slug flow' type oscillation, like the surge mode described in the model of Greitzer (1976). Second, the 28 Hz signal grows rapidly just prior to surge, suggesting that this mode leads to surge inception. This conjecture is strengthened by system identification results below; thus we identify this eigenmode as the 'surge mode'.

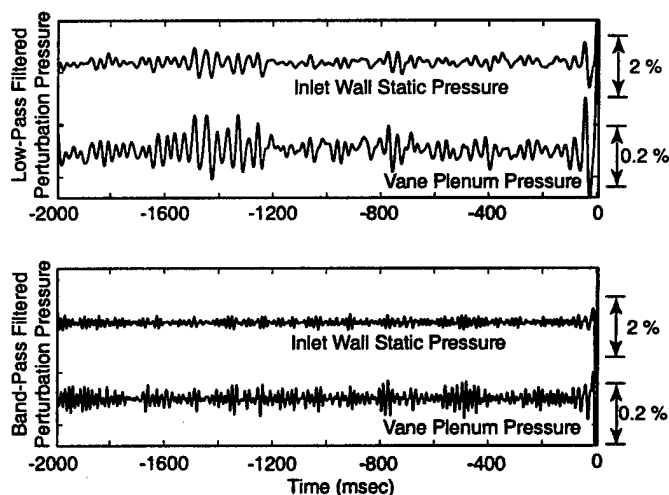


Figure 6 Static pressure data from Figure 4, low-pass filtered at 30Hz to highlight the surge mode (top), and band-pass filtered with a center frequency of 70 Hz to highlight the acoustic mode (bottom).

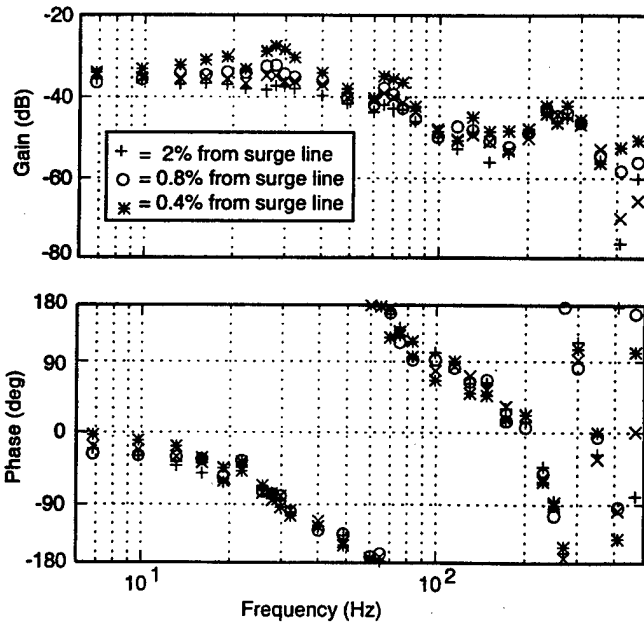


Figure 7: Transfer Functions From Valve Command to Inlet Static Pressure.

Forced Response Tests

Forced response testing was used to obtain transfer functions of the engine dynamics. These transfer functions provide an input-output characterization for control law design, and give a quantitative description of the frequency and stability properties of the system. The input is the command to the injection valve, while the outputs are the pressure signals. These transfer functions include the dynamics of the valve, pressure taps, and anti-aliasing filters in addition to the engine dynamics.

Because the noise levels in the engine are high and frequency sweeps have not proven effective, a series of tests at discrete frequencies were required for system identification. Figure 7 shows transfer functions at three mass flows. Each symbol on this figure represents 45 seconds of data, taken as the valve is modulated at a fixed frequency and $\pm 0.25\%$ mass flow. The peak at 28 Hz becomes sharper as mass flow is reduced, and the phase drop becomes more sudden, indicating that the stability of the 28 Hz 'surge mode' decreases as the mass flow is reduced. Numerical fits to the data in Figure 7 confirm these observations: the fitted eigenvalues become less stable as mass flow is reduced. The 68 Hz 'acoustic' mode does not change as much.

Empirical Model for Control Law Design

To obtain a mathematical model for control law design, the frequency response data in Figure 7 are 'fit' with a state-space model, i.e. a set of ordinary differential equations of the form

$$\dot{x} = Ax + Bu$$

$$y = Cx + Du$$

where x , y , and u are vectors, and A , B , C , and D are matrices. The goal of this fit is to obtain a dynamic model with input-output properties similar to those found experimentally near surge.

Fitting input-output data in this way is more difficult when there are several outputs that must be fit simultaneously (i.e. when the vector y has more than one element). We used the procedure

developed by Jacques (1994). The number of outputs was limited to three by the throughput of the real time control computer. For various choices of three sensors, a state space model was fit to the data and control laws were designed. Figure 8 shows the transfer functions of the state space model which yielded controllers with the largest range extension. The outputs are one diffuser throat and two inlet sensors (the transfer function to only one of the two inlet sensors is shown.) We use this fit to estimate the eigenvalues of the system in the next section.

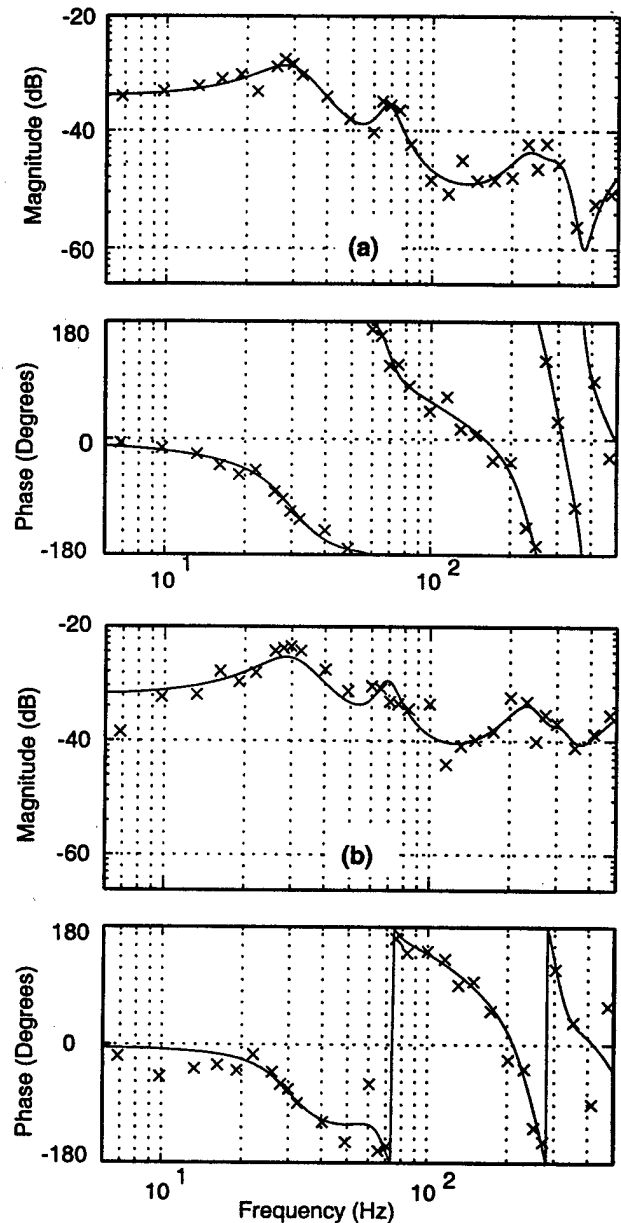


Figure 8: SIMO Transfer Function Fit for Best Compensator Designs: (a) Valve command to compressor inlet static pressure (b) Valve command to valve cavity static pressure

Comparisons with Theoretical Predictions

To validate our physical understanding of the measured behavior, two models were constructed. The first is based on the lumped parameter model of Greitzer (1976). This model has only one eigenmode, which goes unstable when the compressor begins to pump energy into the unsteady oscillations of a Helmholtz-like resonance. The second model uses one-dimensional acoustic duct elements rather than lumped ducts. See Appendix A for details.

Table I shows the measured eigenvalue frequencies (from the fits in Figure 7) and the predicted eigenvalues. The lumped-parameter surge model correctly predicts the existence of a system eigenmode that becomes unstable near the peak of the map. This result reinforces numerous experimental studies showing that this model describes the basic physics involved in surge inception (Fink (1988), Pinsley et al. (1991), Weigl et al. (1997a)). However the frequency of the eigenvalue is not accurately predicted, and the eigenvalue at 68 Hz is not predicted at all by this model.

The acoustic surge model predicts the existence of an infinite number of eigenvalues, at progressively higher frequencies, associated with acoustic modes in the ducts. The lowest of these modes is close to the measured acoustic mode in frequency. An eigenvalue near the surge frequency is also predicted by this model. Note that compressibility in the ducts has a strong effect on the predicted surge frequency, even though its fundamental behavior can be understood by considering incompressible (lumped) ducts. Although further refinement is necessary, the results support our explanation of the physics involved.

Table I: Predicted and Actual Surge Eigenvalues

	Surge Mode	1st Acoustic Mode
Experiment	27 Hz	68 Hz
Lumped Parameter Model	24 Hz	None
Acoustic Duct Model	32 Hz	101 Hz

III CONTROL LAW DESIGN

The goal of the feedback controller is to stabilize the dynamic system at flow rates below the open-loop surge line. Experiments and modeling indicate that there is one unstable eigemode (at 28 Hz) which must be stabilized while operating the engine below the surge line. However, we have shown that another mode participates in the input-output dynamics. Although the acoustic mode need not be explicitly stabilized, it must be accounted for in the controller design. In fact, we found that simple feedback controllers tended to destabilize the 68 Hz acoustic mode and therefore achieved no range extension. Other controllers, designed without the benefit of several sensors and/or without explicit consideration of modeling errors, were also unsuccessful.

Based on this experience we adopted a robust multi-input control design method. This method was successfully used for rotating stall control in a compressor that had resonant acoustic modes (Weigl et al. 1997a&b). The details of the technique and its application to the surge control problem are given in Appendix B. The procedure creates a compensator that stabilizes the surge mode without destabilizing the acoustic mode, and directly accounts for uncertainty in the locations of the system eigenvalues. The following additional features are also important to mention:

- 1) The method is widely available and proven effective for control law design. The design algorithms are easily understood and used by a control engineer.
- 2) It automatically accounts for multiple inputs and multiple outputs.
- 3) Robustness constraints, such as models of uncertainty and noise in the system, are included to improve the resulting design.

For details on the design procedure, see Weigl et al. (1997a) and Weigl and Paduano (1997b). Appendix B discusses some of the properties of the compensator that was used to achieve the results in the next section.

IV EXPERIMENTAL STABILIZATION OF SURGE

The robust multi-input controller was experimentally tested on the LTS-101 using the following procedure: the engine was brought to a point near the surge line while operating open loop. Then, the control loop was closed. The nozzle exit area was then reduced in discrete steps, eventually driving the system below the open loop surge line. The engine operated for at least 45 seconds between steps. The closed loop surge point was then recorded for comparison with open loop results.

Figure 9 shows the power spectra of pressure in the diffuser vane cavity and at the compressor inlet with and without control, near the open loop surge line. Feedback reduces the 28 Hz resonance peak by about 10 dB. The vane cavity sensor shows a small closed loop excitation of the acoustic resonance. This was found to be an acceptable level of relative stability for this mode.

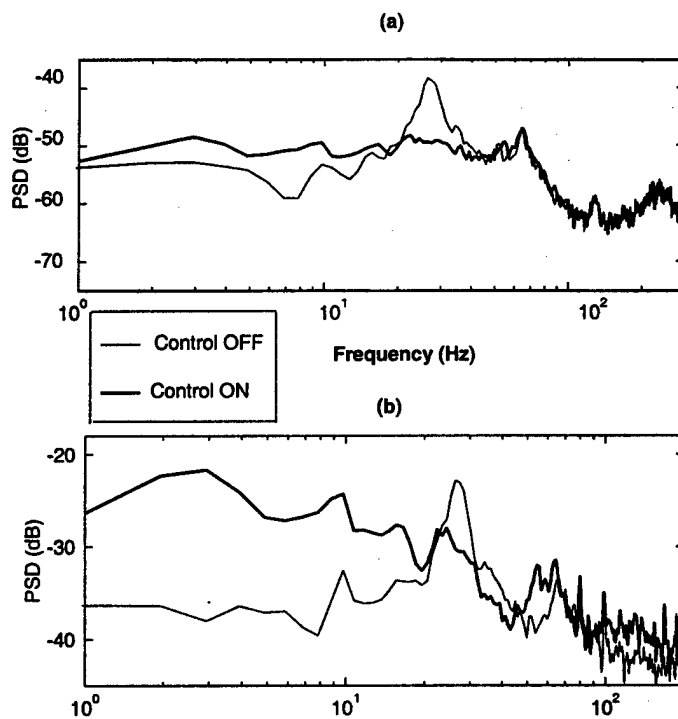


Figure 9: Control effectiveness in suppressing surge mode, at open loop surge mass flow. (a) Inlet static pressure. (b) vane cavity static pressure

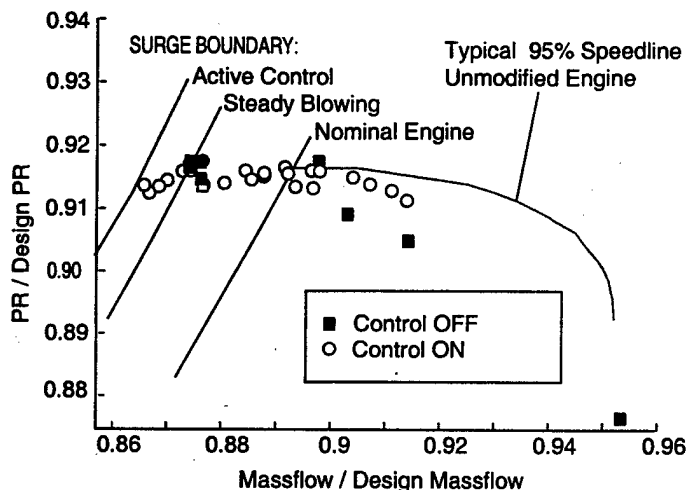


Figure 10: Compressor Range Extension with Active Stabilization of Surge

Figure 10 shows the compressor map with and without control. At the same level of average air injection into the diffuser, the closed loop stabilized machine surges at a mass flow 1.0% less than the engine without control. This is an 11% increase in the operating range of the baseline engine without injection, from choke to surge. The stabilized engine produces about 3.7% more thrust than the baseline, as measured on the test stand. Recall that all quantities are respect to the steady blowing baseline case described in Section II.

V SUMMARY AND CONCLUSIONS

Active surge control experiments have been performed on a turboshaft engine gas producer. By sensing static pressure in the engine inlet and compressor diffuser, and injecting air into the diffuser, systematic identification and control studies were conducted, and the following conclusions were drawn:

- I. Surge without control results from instability of a lumped parameter type oscillation mode.
- II. By feeding back small amplitude perturbations, the mode associated with surge can be stabilized, allowing operation in previously unstable and inaccessible regimes. A useful range extension results.
- III. Acoustic modes also exist in the engine's unsteady behavior. A model incorporating 1D duct acoustics gives good agreement with measured resonance frequencies.
- IV. Acoustic modes in the engine can be excited by feedback. Therefore control laws designed to stabilize surge must account for the existence of these modes. A systematic procedure for such control law design has been demonstrated.

At the 95% N1 corrected speed line, the mass flow range from choke to surge was increased by 11% with active control. Furthermore, the test stand thrust of the gas producer increased by 3.7% with control. The mass flow range and thrust with and without control were compared at the same nominal injection level of 3.8% corrected engine mass flow.

Although these results represent a full-scale validation of the concept of surge stabilization, much work remains. No attempt has

been made to assess the trade-offs that exist associated with the actuation; only range extension with respect to a baseline is given. The actuator configuration was chosen mainly for its ease of implementation; clearly the pressure drop associated with injection into the diffuser must be weighed against the benefits of range extension, to determine the impact on overall engine performance. This calculation is somewhat premature for this experiment; more realistic actuators (which either bleed or recirculate engine mass flow) should be tested before benefits are analyzed. Finally, one must devise stabilization methods that actuate only when necessary (see Freeman et al. 1997 for a discussion). We have successfully tested such methods, but thorough quantification of the behavior of these control laws is still needed. Based on these comments, we reiterate that the main goal here has been to validate our understanding of surge inception, and to illustrate a systematic procedure for applying this understanding. By stabilizing the dynamics presumed to lead to surge, we are able to delay surge onset; thus our dynamic model is corroborated.

ACKNOWLEDGMENTS

This research was funded by AFOSR Grant #F49620-95-1-0409, Marc Jacobs, technical monitor, by AFOSR Grant #F49620-96-1-0407, Mark Glauser, technical monitor, and by the Allied Signal Engine Company. Moog provided the high speed control actuator and Kulite Semiconductor provided high frequency response pressure transducers. Harald Weigl provided the initial Hoo design codes. Jin-Woo Bae, Jim Lentendre, and Bill Ames assisted in running the tests, and Brian Corn aided in the engine set up and operation. Brandon Gordon assisted in engine modeling. Lt. Nelson was partially supported by AFIT, and by the Air Force Research Laboratory (AFRL/VAAD).

REFERENCES

- Bae, J. W., 1998 "An Experimental Study of Surge Control in a Helicopter Gas Turbine Engine," M. S. Thesis, Dept. of Aeronautics and Astronautics, Massachusetts Institute of Technology.
- Berndt, R. G., 1995 "Actuation for Rotating Stall Control of High Speed Axial Compressors," M. S. Thesis, Dept. of Aeronautics and Astronautics, Massachusetts Institute of Technology.
- Borror, S. L., 1994 "Natural and Forced Response Measurements of Hydrodynamic Stability in an Aircraft Gas Turbine Engine," M. S. Thesis, Dept. of Aeronautics and Astronautics, Massachusetts Institute of Technology.
- Corn, B. A., 1998 "Surge Dynamics of a Helicopter Engine Gas Generator," M. S. Thesis, Dept. of Aeronautics and Astronautics, Massachusetts Institute of Technology.
- Corn, B. A., 1998 "LTS-101 Gas Generator Data Archive", Run 80, 6 August, Created by Eric B. Nelson.
- Epstein, A. H., Ffowcs-Williams, J. E., and Greitzer, E. M., 1989, "Active Suppression of Aerodynamic Instabilities in Turbomachines," *Journal of Propulsion*, Vol. 5, No. 2, pp. 204-211.
- Fink, D. A., 1988 "Surge Dynamics and Unsteady Flow Phenomena in Centrifugal Compressors," MIT Gas Turbine Laboratory Report No. 193.
- Ffowcs Williams, J. E. and Graham W. R., 1990 "An Engine Demonstration of Active Surge Control," ASME 90-GT-224.
- Ffowcs Williams, J. E., Harper M. F. L., and Allwright, D. J., 1993 "Active Stabilization of Compressor Instability and Surge in a Working Engine," *ASME Journal of Turbomachinery*, Vol. 115, January, pp. 68-75.

Eveker, K. M., Gysling, D. L., Nett, C. N., and Sharma, O. P., 1997 "Integrated Control of Rotating Stall and Surge in High-Speed Multi-Stage Compression Systems," 97-GT-352, ASME Turbo Expo '97, June 2-5, Orlando.

Freeman, C., Wilson, A. G., Day, I. J., and Swinbanks, M. A., 1997 "Experiments in Active Control of Stall on an Aeroengine Gas Turbine," 97-GT-280, ASME Turbo Expo '97, June 2-5, Orlando.

Greitzer, E. M., 1976 "Surge and Rotating Stall in Axial Flow Compressors, Part I: Theoretical Compression System Model, and Part II: Experimental Results and Comparison with Theory" *ASME Journal of Engineering for Power*, Vol. 98, April, pp. 190-217.

Greitzer, E. M., Epstein, A. H., Guenette, G. R., Gysling, D. L., Haynes, J., Hendricks, G. J., Paduano, J. D., Simon, J. S., and Valavani, L., 1992 "Dynamic Control of Aerodynamic Instabilities in Gas Turbine Engines," AGARD Lecture Series 183, *Steady and Transient Performance Prediction of Gas Turbine Engines*, AGARD-LS-183, May.

Gysling, D. L., Dugundji, J., Greitzer, E. M., and Epstein A. H., 1991 "Dynamic Control of Centrifugal Compressor Surge Using Tailored Structures," *Journal of Turbomachinery*, Vol. 113, October, pp. 710-22.

Huang, X. Y. and Ffowcs Williams J. E., 1989 "Active Stabilization of Compressor Surge," *Journal of Fluid Mechanics*, Vol. 204, pp. 245-62.

Jacques, R., 1994 "FORSE Transfer Function ID," Space Engineering Research Center, Massachusetts Institute of Technology.

Kwakernaak, H., 1993 "Robust Control and H-Infinity Optimization: Tutorial Paper" *Automatica*, Vol. 29, No. 2, pp. 255-73.

McNulty, G. S., 1993 "A Study of Dynamic Compressor Surge Control Strategies for a Gas Turbine Engine," M.S. Thesis, Dept. of Aeronautics and Astronautics, Mass. Institute of Technology.

Moore, F. K. and Greitzer, E. M., 1986 "A Theory of Post-Stall Transients in Axial Compression Systems, Part I - Development of Equations, and Part II - Application," *ASME J. of Engineering for Gas Turbines and Power*, Vol. 108, pp. 68-97.

Nelson, E. B., 1998 "An Experimental Study of Surge Control in the Allied Signal LTS-101 Helicopter Turboshaft Engine," M. S. Thesis, Department of Aeronautics and Astronautics, Massachusetts Institute of Technology.

Pinsley, J. E., Guenette G. R., Greitzer E. M., and A. H. Epstein., 1991 "Dynamic Control of Centrifugal Compressor Surge Using Tailored Structures," *Journal of Turbomachinery*, Vol. 113, October, pp. 723-32.

Simon, J. S., Valavani, L., Epstein, A. H., and Greitzer, E. M., 1993 "Evaluation of Approaches to Active Compressor Surge Stabilization," *ASME Journal of Turbomachinery*, Vol. 115, January, pp. 57-67.

Smith, R. S., Chu, C. C., and Fanson, J. L., 1994 "The Design of H ∞ Controllers for an Experimental Non-collocated Flexible Structure Problem," *IEEE Transactions on Control Systems Technology*, Vol. 2, No. 2.

Takahashi, Y., Rabins, M. J., and Auslander, D. M., 1972, *Control of Dynamic Systems*, Addison-Wesley.

Weigl, H. J., Paduano, J. D., Frechette, L. G., Epstein, A. H., Greitzer, E. M., Bright, M. M., and Strazisar, A. J., 1997a "Active Stabilization of Rotating Stall in a Transonic Single Stage Axial Compressor," 97-GT-411, ASME Turbo Expo '97, June 2-5, Orlando.

Weigl, H. J., and Paduano, J. D., 1997b "Application of H-infinity Control With Eigenvalue Perturbations to Stabilize a Transonic Compressor," presented at the IEEE International Conference on Control Applications, Hartford, October 5-7.

APPENDIX A: SURGE MODEL DEVELOPMENT

In this Appendix a classic lumped-parameter surge model is first reviewed. Although the essence of pre-surge oscillations is captured by this model, neither the existence of acoustic modes is not predicted by this model. Therefore, the model is modified to include duct acoustics. Both models are compared to experimental results in Section II.

Lumped-Parameter Surge Model

To obtain a simple model which captures the physics governing surge, Greitzer (1976) divided the compression system into four lumped components (see Figure 9): 1) a duct to account for all the kinetic energy of the unsteady flow in the system, 2) a plenum to represent the potential energy of expansion and compression of fluid, 3) a throttle which dissipates energy, and 4) the compressor, which can either dissipate energy or add energy to oscillations, depending on the slope of the compressor map. Using mass and momentum conservation, and assuming isentropic compression in the plenum, the following second-order model can be developed:

$$\dot{\phi} = \frac{1}{B} (\Psi_c(\phi) - \psi)$$

$$\dot{\psi} = \frac{1}{B^2} \left(\frac{\alpha_{pi}}{\rho^*} \phi - \alpha_{pe} \Phi_t(\psi) \right)$$

where $\psi = P/\rho U_{ref}^2$ is the nondimensional pressure in the plenum, $\phi = u/U_{ref}$ is the flow velocity in the duct, $\Psi_c(\phi)$ is the compressor total-to-static pressure rise map, and $\Phi_t(\psi)$ is the inverse of the throttle map, i.e. $\Phi_t = \sqrt{2\psi/K_t}$, K_t being the throttle coefficient. The rest of the parameters depend on the systems dimensions. B is Greitzer's non-dimensional parameter governing surge behavior, $B = U_{ref}/a_p \sqrt{V/LA_{ref}}$, where a_p is the speed of sound in the plenum and U_{ref} , A_{ref} , V , and L are a reference velocity, a reference area, the plenum volume, and the duct length respectively. Finally, α_{pi} and α_{pe} are the plenum inlet and exit areas non-dimensionalized by A_{ref} , and ρ^* is the plenum fluid density non-dimensionalized by some reference density. This model differs from Greitzer's formulation only in the details of the non-dimensionalization. For instance, here we have taken L_{ref}/U_{ref} as the reference time, instead of one over the Helmholtz

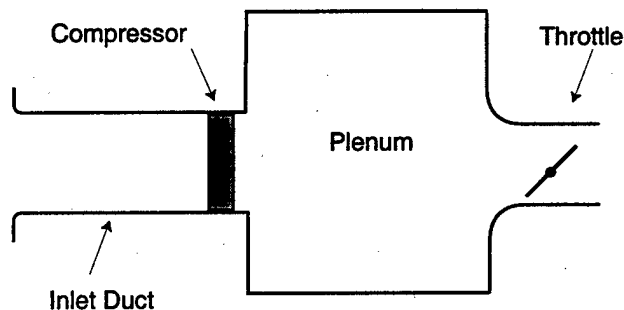


Figure 9: Compression System Geometry for Lumped-Parameter Surge Model

frequency, to simplify the acoustic expressions below.

We can use this model to understand the behavior of compressors as they approach and enter surge, the influence of the compliance-to-inertia ratio B (Greitzer 1976), or (if additional dynamics are added, as in Moore and Greitzer, 1986), to elucidate the interaction between rotating stall and surge. Thus as a basic model, this representation is valuable. In the context of the current research, we are interested in understanding the physics which govern the frequency of the pre-surge oscillations in engines, and in understanding the source of the second peak in the spectra and frequency responses. This second eigenvalue was conjectured to arise due to longitudinal variations in velocity and pressure in the ductwork of the engine. To check this conjecture, an acoustically coupled model is developed in the next section.

Modified Surge Model - Acoustic Ducts

To introduce acoustics into the surge model, we use a transmission matrix approach (Nelson 1998) applied to the system representation shown in Figure 12. Each of the seven segments in this model is represented by a 2x2 transmission matrix. These matrices relate the Laplace transforms of the nondimensional perturbation pressure and axial velocity at the inlet to those at the exit (Takahashi et al., 1972). The general form for the transmission properties of a duct is:

$$\begin{bmatrix} \psi_{out}(s) \\ \phi_{out}(s) \end{bmatrix} = \begin{bmatrix} T_{11}(s) & T_{12}(s) \\ T_{21}(s) & T_{22}(s) \end{bmatrix} \begin{bmatrix} \psi_{in}(s) \\ \phi_{in}(s) \end{bmatrix},$$

where perturbation pressure and velocity are nondimensionalized as in the previous surge model. By stacking transmission matrices from inlet to exit and applying the boundary conditions, an eigenvalue problem can be derived. Alternatively, one can develop an input-output relationship between any two variables. We choose the latter approach, using velocity into the injector as the input, and inlet static pressure at station 2 as the output.

The model in Figure 12 consists of three acoustic ducts, one lumped duct, a compressor, and two lumped segments representing expansion and contraction. One can derive a transmission matrix for each segment using continuity, momentum and, for the acoustic ducts, Euler's equation and perfect gas relations. The results are summarized below.

Acoustic Duct:

$$T_{Ac} = \begin{bmatrix} \cos(l\omega/c^*) & -i \cdot c^* \cdot \rho^* \sin(l\omega/c^*) \\ -\frac{i}{c^* \cdot \rho^*} \sin(l\omega/c^*) & \cos(l\omega/c^*) \end{bmatrix},$$

$$l = (\text{duct length}) / L_{ref},$$

$$c^* = (\text{duct sound speed}) / U_{ref},$$

$$\rho^* = (\text{duct fluid density}) / \rho_{ref}.$$

Lumped Duct:

$$T_{Duct} = \begin{bmatrix} 1 & -\rho^* l \omega \\ 0 & 1 \end{bmatrix}$$

Compressor and Throttle

$$T_C = \begin{bmatrix} 1 & \rho_{in}^* m_c \\ 0 & \rho_{in} / \rho_{out} \end{bmatrix}, T_{Th} = \begin{bmatrix} 1 & \rho_{in}^* m_t \\ 0 & \rho_{in} / \rho_{out} \end{bmatrix},$$

$$\text{where } m_i = \frac{\partial \Psi_i}{\partial \phi}$$

$$\text{Sudden Expansion: } T_{Ex} = \begin{bmatrix} 1 & 2\rho^* \Phi_o (1 - \alpha_r) \\ 0 & \alpha_r \end{bmatrix}$$

$$\text{Smooth Contraction: } T_{Con} = \begin{bmatrix} 1 & 2\rho^* \Phi_o (1 - \alpha_r^2) \\ 0 & \alpha_r \end{bmatrix},$$

where in the last two equations α_r is the ratio of inlet to outlet area, and Φ_o is the mean flow through the component.

To derive a transfer function for the system, we start by writing continuity at station 4 in terms of pressure and velocity:

$$\begin{bmatrix} \psi_4 \\ \phi_4 \end{bmatrix} = \begin{bmatrix} \psi_3 \\ \phi_3 \end{bmatrix} + \begin{bmatrix} 0 \\ \alpha_o \end{bmatrix} \phi_0$$

where ϕ_0 is the velocity at the exit of the injector. Since the injector valve is choked, station 0 is assumed to have infinite impedance; thus, this boundary is assumed to be a pure velocity source independent of the pressure at station 0. Next, we substitute this equation into the transmission matrix relation between station 3 and station 8, writing the conditions at station 3 in terms of those at station 1 using the upstream transmission matrices:

$$\begin{bmatrix} \psi_8 \\ \phi_8 \end{bmatrix} = T_{Duct}^{78} \cdot T_{Con}^{67} \cdot T_{Ac}^{56} \cdot T_{Ex}^{45} \cdot T_{Ac}^{34} \left(T_C^{23} \cdot T_{Ac}^{12} \begin{bmatrix} \psi_1 \\ \phi_1 \end{bmatrix} + \begin{bmatrix} 0 \\ \alpha_o \end{bmatrix} \phi_0 \right)$$

Each matrix in this equation is evaluated as a function of frequency ω , the matrices are multiplied out, and variables are defined for the results as follows:

$$\begin{bmatrix} \psi_8 \\ \phi_8 \end{bmatrix} = \begin{bmatrix} T_1(i\omega) & T_2(i\omega) \\ T_3(i\omega) & T_4(i\omega) \end{bmatrix} \begin{bmatrix} \psi_1 \\ \phi_1 \end{bmatrix} + \begin{bmatrix} U_1(i\omega) \\ U_2(i\omega) \end{bmatrix} \phi_0.$$

The boundary conditions are then applied. The inlet and exit are assumed to be 'pressure release' boundaries to atmosphere (i.e. $\psi_1 = \psi_8 = 0$). Rearranging yields the relation

$$\phi_1(i\omega) = -\frac{U_1(i\omega)}{T_2(i\omega)} \phi_0(i\omega).$$

Finally, we obtain the transfer function from the injector to the static pressure measurement station (2) by applying the appropriate transmission matrix:

$$\begin{bmatrix} \psi_2 \\ \phi_2 \end{bmatrix} = T_{Ac}^{12} \cdot \begin{bmatrix} \psi_1 \\ \phi_1 \end{bmatrix} = \begin{bmatrix} V_1(\omega) & V_2(\omega) \\ V_3(\omega) & V_4(\omega) \end{bmatrix} \begin{bmatrix} 0 \\ \phi_1 \end{bmatrix},$$

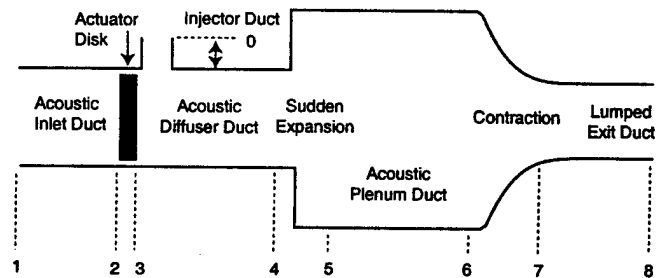


Figure 12: Acoustic Model of LTS-101 With Acoustic Ducts and Plenum

where the boundary condition at station 1 has already been introduced. The desired transfer function is thus obtained as:

$$\frac{\psi_2(i\omega)}{\phi_0} = -V_2(i\omega) \frac{U_1(i\omega)}{T_2(i\omega)}$$

Our modified version of the surge model appears to be much different than the basic surge model; but if the acoustic ducts are replaced by lumped ducts and plenums, the model is essentially the same. Acoustics introduces transcendental relationships in the transfer function, making eigenvalue computation difficult. Rather than solve for eigenvalues directly, fits to the derived transfer function are performed to deduce the eigenvalue locations.

APPENDIX B: CONTROL LAW DESIGN

Modern robust control design procedures use models that take into account modeling and/or system identification errors. Consider a linear system, with multiple inputs and multiple outputs, of the form:

$$\begin{aligned} \dot{x} &= A_{true} x + B_{true} u \\ y &= C_{true} x + D_{true} u \end{aligned}$$

The subscript 'true' indicates that this dynamic system is the actual system to be controlled. We can develop a model for this system using either theoretical or experimental methods, but neither will yield an exact replica of the true system. To represent the inaccuracy of our model, we develop a 'family' of models that is sufficiently general to include the true system as one of its members. We have found that for rotating stall and surge problems, a useful family of models is of the following form (Smith 1994, Weigl and Paduano 1997b):

$$\begin{aligned} \dot{x} &= T^{-1} \Lambda T x + \hat{B} u \\ y &= \hat{C} x + \hat{D} u, \end{aligned}$$

where

$$\Lambda = \text{diag}(\lambda_1, \lambda_2, \dots, \lambda_N),$$

$$\lambda_n = \lambda_{n0} + \Delta\omega_n e^{i\phi}, \quad 0 < \phi < 2\pi$$

and

$$\lambda_{n0} = \text{eigenvalues of } \hat{A}.$$

In this family of models, most of the structure of the input-output system is assumed to be well known (that is, $\hat{B} \equiv B_{true}$, $\hat{C} \equiv C_{true}$, and $\hat{D} \equiv D_{true}$), but each eigenvalue is allowed to exist anywhere inside a disk of radius $\Delta\omega_n$, centered at the nominal location λ_{n0} .

The control law design requirements are completed by imposing the following two requirements:

$$\sigma_{\max} \left(\frac{u}{r}(j\omega) \right) < |W_2^{-1}(j\omega)|$$

$$\sigma_{\max} \left(\frac{y}{r}(j\omega) \right) < |W_3^{-1}(j\omega)|$$

where u , r , and y are defined above and shown in Figure 13, and σ_{\max} denotes the maximum value of the multivariable transfer function. The magnitudes of the diagonal transfer functions $W_2^{-1}(s)$ and $W_3^{-1}(s)$ are plotted in Figure 14. These are standard robust design constraints which are adjusted to limit both the

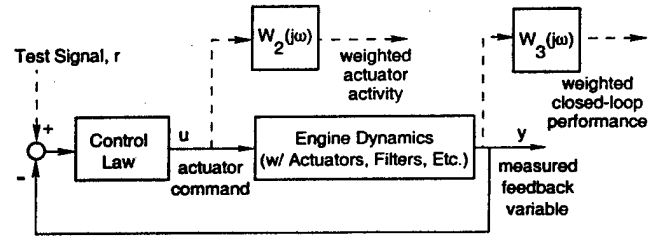


Figure 13 - Block diagram of control system used for specification of design constraints

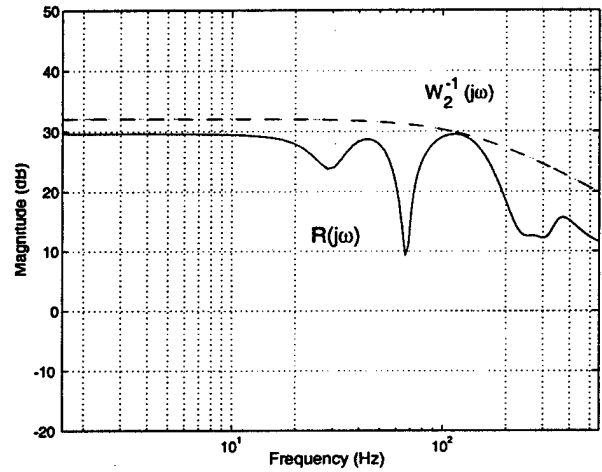


Figure 14 a) Closed Loop Transfer Function from r to u (solid): Shaped by W_2^{-1} (dashed).

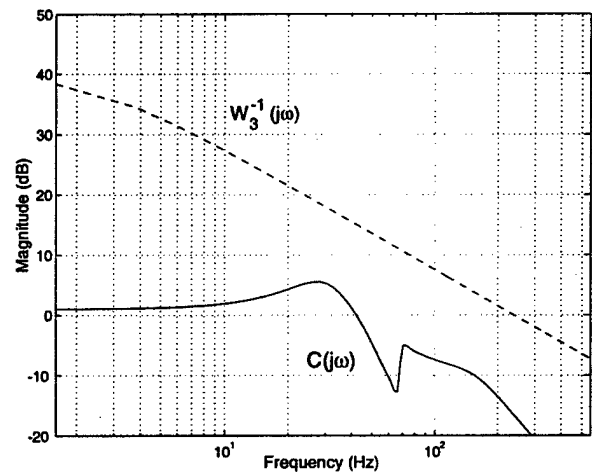


Figure 14 b) Closed Loop Transfer Function from r to y (solid): Shaped by W_3^{-1} (dashed).

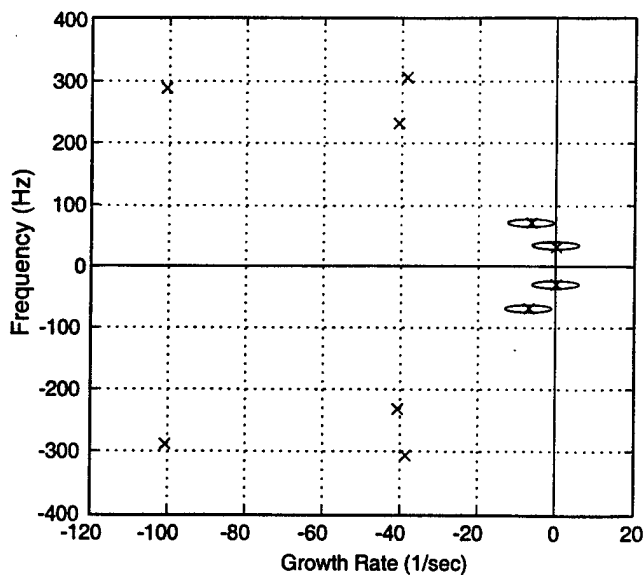


Figure 15. Design plant model, showing eigenvalue perturbation circles. Note that surge eigenvalues are neutrally stable.

controller bandwidth (W_2^{-1}) and the closed loop frequency response magnitude (W_3^{-1}). See Kwaakernaak (1993) for more details. The control law design procedure creates a compensator that is guaranteed to stabilize any linear system which is a member of the family defined above, and to meet the above robustness constraints.

Design Results

The identification results in Section II are used as the nominal model for control law design, with one modification. To create a stabilizing controller, the eigenvalue associated with surge is moved (using the diagonalized formulation in the previous section) to the neutral stability axis. Then the design uncertainty of the eigenvalues is modeled, as shown in Figure 15. Note that the identified eigenvalue location for the surge mode is a member of the family defined by this figure; thus the system is required to remain stable for the identified system as well as the unstable one beyond the surge line. Note also that the uncertainty disks are stable for all modes except the surge mode. In other words, for every model in this family, only the surge mode can be unstable. This reflects our conjecture that acoustic modes remain stable over the operating range of interest.

Recall that the sensors chosen for control are one diffuser throat and two inlet sensors. These choices are the result of an iterative process of control law design, experimental testing, data analysis and redesign. The automated nature of the control law design procedure makes this iteration possible. In all, fifteen compensators were created and available for testing.

The compensator which solves the control design problem defined here consists of three scalar transfer functions -- one from each sensor to the actuator. Two of these three transfer functions are shown in Figure 16 (since two of the sensors chosen are in the same place axially, two of the compensator transfer functions are

almost identical). Note that both transfer functions contain a zero at ~ 70 Hz, to avoid destabilization of the 68 Hz acoustic mode. The design procedure has optimally placed this notch to avoid destabilization even if the acoustic mode should be different in frequency or damping than the identified model states. Note also that the throat tap transfer function has a 20 dB/decade upward slope in the 30 Hz region (surge frequency). Apparently the design procedure has automatically chosen to introduce Proportional-Derivative (PD) type action into the compensation, consistent with a lead-lag compensator design.

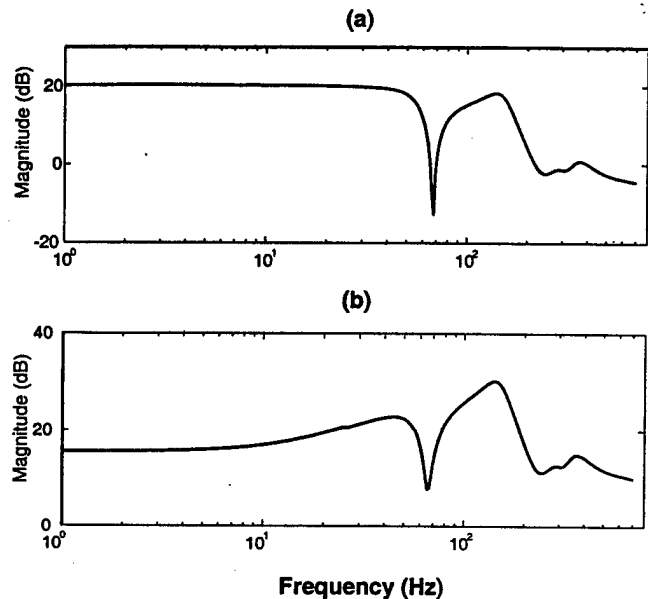


Figure 16: Compensator Transfer Functions. (a) Compressor inlet static pressure to valve command (one of two similar transfer functions). (b) Valve cavity static pressure to valve command.



The Society shall not be responsible for statements or opinions advanced in papers or discussion at meetings of the Society or of its Divisions or Sections, or printed in its publications. Discussion is printed only if the paper is published in an ASME Journal. Authorization to photocopy for internal or personal use is granted to libraries and other users registered with the Copyright Clearance Center (CCC) provided \$3/article or \$4/page is paid to CCC, 222 Rosewood Dr., Danvers, MA 01923. Requests for special permission or bulk reproduction should be addressed to the ASME Technical Publishing Department.

Copyright © 1998 by ASME

All Rights Reserved

Printed in U.S.A.

EXPERIMENTAL DEVELOPMENT OF A JET INJECTION MODEL FOR ROTATING STALL CONTROL

Huu Duc Vo
James D. Paduano
Gas Turbine Laboratory
Massachusetts Institute of Technology
Cambridge, Massachusetts

ABSTRACT

The effectiveness of jet actuation for active modal control of rotating stall is investigated experimentally. The dominant physical effects of injection, such as momentum and mass addition, are elucidated. The results indicate that several of the theoretical assumptions used in past studies of jet injection for rotating stall control must be revised. An updated model of the compression system with jet actuation which allows for the effect of control feedback dynamics to be adequately characterized is developed and verified with forced response measurements. It predicts the right trends of movement of the critical pole. Preliminary active control results are presented, among which is a 5.5% range extension in downstream flow coefficient.

NOMENCLATURE

Symbols

A : area
 $A(s)$: actuator dynamics
 $D(s)$: feedback time delay transfer function
 $F(s)$: Butterworth Filter transfer function
 f : cut off frequency of $F(s)$
 K_n : controller feedback gain
 L_u : pressure loss across the compressor due to viscous losses
 L_{uR} : pressure loss across the rotors due to viscous losses
 L_{uS} : pressure loss across the stators due to viscous losses
 \dot{m} : mass flow
 n : mode (harmonic) number
 P_t : total (stagnation) pressure
 P_s : static pressure
 R : mean compressor radius
 r : compressor reaction
 s : Laplace transform variable

t : time
 u : velocity
 U : mean rotor blade velocity
 $ZOH(s)$: discrete sampling dynamics transfer function
 α : injection angle in the η - θ plane w.r.t. the η direction
 β_n : controller feedback phase
 γ : injection angle in the η -radial plane w.r.t. the η direction
 η : nondimensional axial direction
 λ : rotor fluid inertia
 μ : total fluid inertia in the compressor
 ρ : air density
 ξ : nondimensional time
 Φ : local flow potential
 ϕ : axial flow coefficient
 $\bar{\phi}$: annulus averaged axial flow coefficient
 ξ : non-dimensional time
 τ_a : convection time constant
 τ_R : time lag associated with L_{uR}
 τ_S : time lag associated with L_{uS}
 τ_f : feedback delay ($D(s)$) time constant
 τ_z : sampling ($ZOH(s)$) time constant
 ω : temporal frequency
 θ : circumferential direction
 ϕ_n : n^{th} spatial Fourier coefficient of ϕ -disturbance $\delta\phi$
 ψ : steady-state total-to-static pressure rise coefficient
 ψ_i : isentropic ψ

Operator, Superscripts and Subscripts

$\delta(\cdot)$: small perturbation
 (\cdot) : spatial Fourier coefficient
 $(\cdot)^{\cdot}$: derivative with respect to nondimensional time (ξ)
 $(\cdot)^*$: complex conjugate

- (.)_c : pertaining to the input
- (.)_i : station (i) in fig. 5
- (.)_j : pertaining to the jet
- (.)_n : nth harmonic
- (.)_{hw} : hot-wires
- (.)_u : upstream of jet actuator
- (.)_d : downstream of jet actuator
- (.)_{ss} : steady state

INTRODUCTION

Some of the main limiting factors in efficiency improvement of current gas turbine engines are the aerodynamic instabilities associated with axial compressors, notably surge and stall. Surge is an axisymmetric oscillation of the flow while rotating stall is a circumferentially non-uniform velocity disturbance rotating around the compressor at a fraction of the compressor speed. Both are detrimental to the performance and durability of the compressor, and attempts to avoid them through establishing an operational safety margin often do so at the expense of efficiency.

To alleviate this problem, an approach pursued by researchers over recent years has been to suppress aerodynamic instabilities through active control. The basis of this technique was developed by Moore (1984) and Moore and Greitzer (1986), who state that rotating stall grows from small rotating disturbances. Therefore at stall inception, small disturbance generators can be used to stabilize pre-stall disturbances and thus prevent their growth. In addition, the small disturbance assumption allows linearization of the stall inception equations, where upon the spatially periodic disturbance can be decomposed into independent harmonics, which facilitates the task of control. This concept was successfully implemented by Paduano et al. (1992) on a single-stage axial compressor using a set of 12 independently moving inlet servo guide vanes (SGVs) and constant gain feedback control capable of controlling the first three harmonics. Paduano was able to extend the compressor operating range by 23%. Haynes (1994) applied the same technique on a three-stage axial compressor and improved its range by 7.8%. Van Schalkwyk (1996) added inlet distortion to Haynes' experiment and extended the operating range by 3.7% for an inlet distortion of 0.8 dynamic head covering 180° of the compressor annulus.

The above results encouraged a theoretical comparison by Hendricks and Gysling (1994) of the effectiveness of different sensor-actuator schemes in controlling rotating stall for the MIT Low Speed Three-Stage Compressor. The sensors studied were transducers for measuring static and total pressure and velocity, with the conclusion that velocity measurement (as used in the previous experiments) was the best choice. However, upon comparing different actuators (SGVs, upstream jets, upstream intake port and downstream bleed), upstream jet actuators theoretically gave the largest range extension and the lowest rotational frequency of the pre-stall disturbance for the same feedback gain values. Based on these results, jet actuation was explored on both a single-stage high speed compressor by Weigl (1997) and on the MIT Three-Stage Low Speed Compressor, where a set of twelve jet actuators designed by Diaz (1994) replaced the SGVs on Haynes' apparatus. The objective of this research was to test the jet injection model and predictions of Hendricks and Gysling.

This paper seeks to experimentally validate and correct the injection and system models used by Hendricks and Gysling (1994). First, a brief description of the experimental apparatus is given.

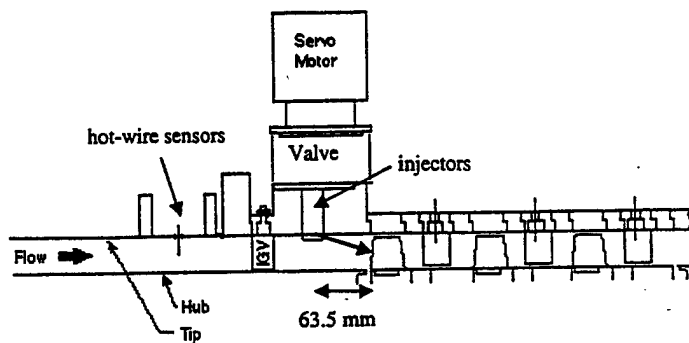


Fig. 1 Side view of the compressor apparatus.

Thereafter, the original jet injection and system models are described followed by a verification with steady state data, from which an empirical model which reveals the dominant effects of injection is obtained. The theoretical active control predictions of the original and updated models are presented. Subsequently, the updated system model is dynamically verified with system identification data and its performance predictions are compared with the results of active control experiments.

EXPERIMENTAL APPARATUS

The MIT Low Speed Three-Stage axial compressor used in this research was designed by Pratt & Whitney as a research compressor. It has a hub-to-tip ratio of 0.88 and operates at 2400 rpm. This compressor was used by Haynes (1994) and Van Schalkwyk (1997). A side cross-section of the compressor is shown in fig. 1. The compressor, driven by an electric motor with a tachometer and a torque sensor, sucks air through a bellmouth inlet and two coarse screens. A set of eight pitot tubes and 16 hot-wires (h.w.) are placed at mid-span of the annulus upstream of the inlet guide vanes (IGVs) for time-averaged and unsteady velocity measurements, respectively. An actuator ring is sandwiched between the IGVs and first rotor as shown in fig. 1. Time-averaged pressure measurements are obtained through a set of static pressure taps at the inlet and exit of the compressor. The air exiting the compressor enters a small annular exhaust plenum and passes through a conical valve used as the throttle. The plenum volume is small enough to preclude surge. The air subsequently traverses a dump plenum and a duct going through several screens and an orifice plate, for mass flow measurement, before exiting outdoors.

For active control with jet actuation, the servo guide vanes used previously were replaced by twelve jet actuators designed by Diaz (1994). Each jet actuator consists of a valve and two "shower head" injectors. Each injector (fig. 2) has three 3/16" diameter holes pointed 30° into the flow and 30° from each other to give as complete and uniform a radial and circumferential coverage as possible as shown by the velocity profile (fig. 3) with injection measured in a wind tunnel. Figure 4 is a schematic view of the overall system with closed-loop control. A model of this system is presented in the next section.

SYSTEM MODELING AND THEORETICAL PREDICTIONS

The following section describes the model of the compression system from the inlet duct to the exit duct starting with the derivation of the jet actuator model followed by its integration into the compres-

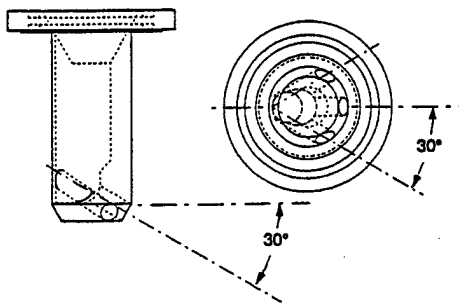


Fig. 2 Injector design.

sion system model. A model of the feedback dynamics associated with the control system is also incorporated. Steady experimental data is then used to verify and correct the injection model. Subsequently, the theoretical stall predictions based on increasing modeling complexity are presented.

The general assumptions associated with the compression system model are the same as that used by Haynes (1994) including small disturbances (linearity), two-dimensionality (no radial variation of flow parameters) and incompressibility of the flow, a semi-actuator disk representation of the compressor, and long enough ducting upstream and downstream for pressure disturbances to die out. However, additional modeling assumptions are required for the derivation of the theoretical injection model. First, the 24 discrete injectors between the IGVs and first blade row are replaced by one circumferentially continuous injector of equivalent total injection area, placed upstream of the IGVs as shown in fig. 5. Instead of injecting at

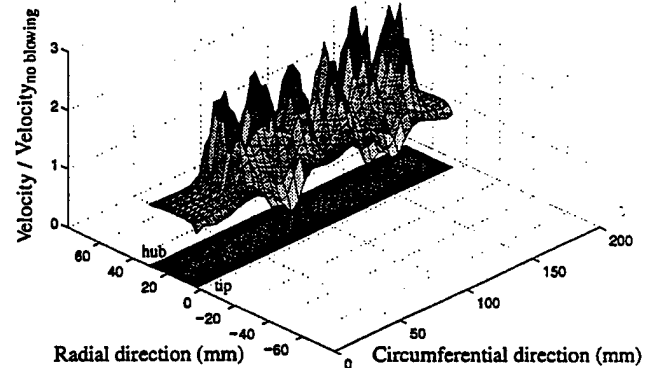


Fig. 3 Measured velocity profile at axial location of first rotor for steady injection with two injectors at 14.8% of the background mass flow at stall through this section representing 1/12 of the unwrapped compressor annulus (Diaz (1994)).

the exit circumferential flow angle (α) of the IGVs and a 30° radial angle, the modeled injector points axially with an effective axial injection velocity proportionately reduced by $\cos\alpha$, and injects at a radial angle (γ) with an axial momentum transfer that is equivalent to the actual injected axial momentum. Second, from fig. 5, it is assumed that no losses occur between stations 1 and i , and that total mixing occurs between stations i and 2. Finally, the distance between stations 1 and 2 is assumed to be short enough for the fluid inertia effects to be neglected.

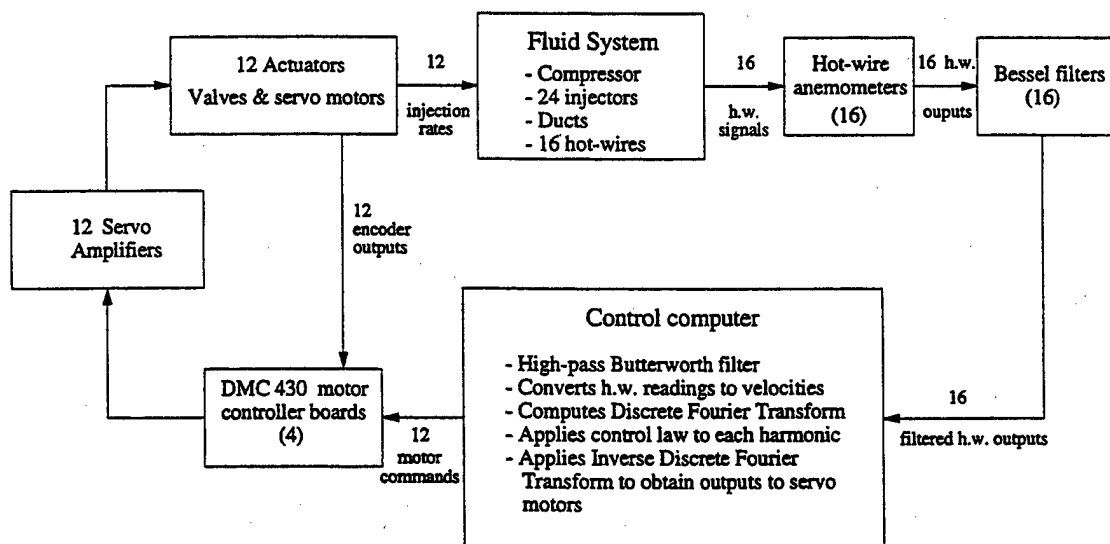


Fig. 4 Closed-loop control feedback configuration.

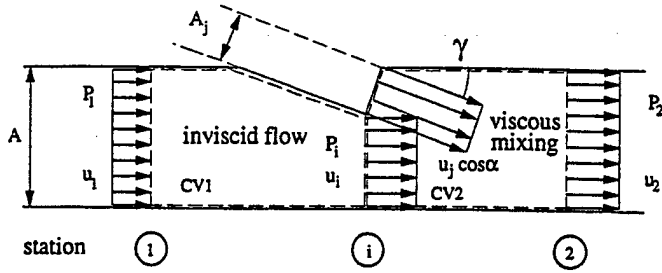


Fig. 5 Control volume analysis of the modeled jet actuator.

Injector Model

Based on fig. 5, a control volume (CV) analysis of the jet actuator yields the following equations:

From station 1 to station i (CV1):

$$\text{Continuity} : \rho u_i A_i = \rho u_1 A \quad (A_i = A - A_j \cos \gamma) \quad (1)$$

$$\text{Bernoulli} : P_i + \frac{1}{2} \rho u_i^2 = P_1 + \frac{1}{2} \rho u_1^2 \quad (2)$$

From station i to station 2 (CV2):

$$\text{Continuity} : \rho u_2 A = \rho u_j \cos \alpha A_j + \rho u_i A_i \quad (3)$$

Axial momentum :

$$(P_i - P_2)A = -\rho u_i^2 A_i - \rho u_j^2 \cos^2 \alpha A_j \cos \gamma + \rho u_2^2 A \quad (4)$$

The second term on the right hand side of equation (4) represents the effect of momentum addition, whereas the other two terms are the effect of mass addition. Combining equations (1) through (4), then simplifying and non-dimensionalizing gives:

$$\phi_2 = \phi_1 + \left(\frac{A_j}{A} \cos \alpha \right) \phi_j \quad (5)$$

$$\frac{P_{i2} - P_{i1}}{\rho U^2} = -\frac{1}{2} M \phi_2^2 - (N \cos \alpha) \phi_2 \phi_j + \frac{1}{2} (R \cos^2 \alpha) \phi_j^2 \quad (6)$$

$$\text{where: } R \equiv \frac{A_j}{A} (2 \cos \gamma + N),$$

$$M \equiv \left(\frac{\frac{A_j}{A} \cos \gamma}{1 - \frac{A_j}{A} \cos \gamma} \right)^2, \quad N \equiv \frac{\frac{A_j}{A} \left(1 - 2 \frac{A_j}{A} \cos \gamma \right)}{\left(1 - \frac{A_j}{A} \cos \gamma \right)^2}$$

which in linearized form are:

$$\delta \phi_2 = \delta \phi_1 + \left(\frac{A_j}{A} \cos \alpha \right) \delta \phi_j \quad (8)$$

$$\frac{\delta P_{i2} - \delta P_{i1}}{\rho U^2} = -X \delta \phi_2 - Y \delta \phi_j \quad (9)$$

$$\text{where: } X \equiv M \bar{\phi}_2 + N \bar{\phi}_j \cos \alpha, \quad Y \equiv (N \bar{\phi}_2 - R \bar{\phi}_j \cos \alpha) \cos \alpha$$

Fluid System Model

The Moore-Greitzer model with unsteady losses is used to describe the three-stage compressor and has been extensively described and derived by Paduano (1992) and Haynes (1994) as well as by Hendricks and Gysling (1994). Appendix A presents the integration of the injection model into the compression system and the Fourier decomposition of the final model's equations. The final equations for the system are:

$$\begin{aligned} k \dot{\phi}_n = & \left(\frac{d\psi_i}{d\phi} - X + in\lambda \right) \tilde{\phi}_n - e^{n\eta_{hw}} \tilde{L}_{uSn} - e^{n\eta_{hw}} \tilde{L}_{uRn} j_n \\ & + e^{n\eta_{hw}} \left[\left(\frac{d\psi_i}{d\phi} - X + in\lambda \right) \frac{A_j}{A} \cos \alpha - Y \right] \tilde{\phi}_{jn} \\ & - e^{n\eta_{hw}} \left[\left(\frac{1}{n} + \mu \right) \frac{A_j}{A} \cos \alpha \right] \dot{\tilde{\phi}}_{jn} \end{aligned} \quad (10)$$

$$\tau_S \dot{\tilde{L}}_{uSn} = \left(\frac{dL_{uS,ss}}{d\phi} e^{-n\eta_{hw}} \right) \tilde{\phi}_n - \tilde{L}_{uRn} + \left(\frac{dL_{uS,ss}}{d\phi} \frac{A_j}{A} \cos \alpha \right) \tilde{\phi}_{jn} \quad (11)$$

$$\tau_R \dot{\tilde{L}}_{uRn} = \left(\frac{dL_{uR,ss}}{d\phi} e^{-n\eta_{hw}} \right) \tilde{\phi}_n - (1 - in\tau_R) \tilde{L}_{uRn} + \left(\frac{dL_{uR,ss}}{d\phi} \frac{A_j}{A} \cos \alpha \right) \tilde{\phi}_{jn} \quad (12)$$

$$\tau_a \dot{\tilde{\phi}}_{jn} = \tilde{\phi}_{jcn} - \tilde{\phi}_{jn} \quad (13)$$

$$\text{where: } k \equiv \frac{2}{n} + \mu \quad (n > 0)$$

Equation (13) represents the delay due to the convection time lag of the jet from the valve slit to the compressor, modeled as a first order lag. Finally, the temporal Laplace transform of equations (10) to (13) is taken and the four equations can be solved to give the desired transfer function from the n^{th} harmonic spatial Fourier coefficient (SFC) of the input disturbance $\delta \phi_j$ to that of the perturbation amplitude $\delta \phi$ at the hot-wire location, as expressed by equation (14).

$$\frac{\tilde{\phi}_n(s)}{\tilde{\phi}_{jcn}(s)} = \frac{G's + B' - \frac{C' L_{uRj}}{1 - in\tau_R + \tau_R s} - \frac{C' L_{uSj}}{1 + \tau_S s}}{\left(s - A' + \frac{C' L_{uR\phi}}{1 - in\tau_R + \tau_R s} + \frac{C' L_{uS\phi}}{1 + \tau_S s} \right) (\tau_a s + 1)} \quad (14)$$

$$\text{where: } L_{uR\phi} \equiv \frac{dL_{uR,ss}}{d\phi} e^{-n\eta_{hw}}, \quad L_{uRj} \equiv \frac{dL_{uR,ss}}{d\phi} \frac{A_j}{A} \cos \alpha,$$

$$L_{uS\phi} \equiv \frac{dL_{uS,ss}}{d\phi} e^{-n\eta_{hw}}, \quad L_{uSj} \equiv \frac{dL_{uS,ss}}{d\phi} \frac{A_j}{A} \cos\alpha,$$

$$A' \equiv \frac{1}{k} \left(\frac{d\psi_i}{d\phi} - X + in\lambda \right), \quad G' \equiv -\frac{e^{n\eta_{hw}}}{k} \left(\frac{1}{n} + \mu \right) \frac{A_j}{A} \cos\alpha,$$

$$B' \equiv \frac{e^{n\eta_{hw}}}{k} \left[\left(\frac{d\psi_i}{d\phi} - X + in\lambda \right) \frac{A_j}{A} \cos\alpha - Y \right], \quad C' \equiv \frac{e^{n\eta_{hw}}}{k}$$

Modeling of Control System Dynamics

The theoretical study by Hendricks and Gysling (1994) employs a direct feedback on the model of the fluid system derived above. However, to better predict the performance of air injection actuation in practice, one must incorporate all the dynamics associated with the feedback loop. In this case, the pertinent control system dynamics are the feedback time delay, the high-pass filter, the sample and hold dynamics of the discrete-time control process and the actuator dynamics. These dynamics, with the exception of the high-pass filter, were modeled in detail by Haynes (1994), although some aspects are modified here to account for changes in the system.

First, the total feedback time delay from the velocity disturbance at the compressor face to the commanded actuation sent to the servo motors can be lumped and modeled by a first order approximation of a pure time delay ($D(s)$). Second, the only filter whose dynamics can significantly affect the system is a first order Butterworth high-pass filter with a cutoff frequency (f) of 0.1Hz. It was used to correct for the drift of the hot-wires during the experiments. The filter was implemented in the computer software and can be modeled by the transfer function $F(s)$ shown below. Third, the sample and hold dynamics of the discrete-time control system was modeled in continuous time by Haynes with the transfer function $ZOH(s)$. Finally, the actuator dynamics incorporates the dynamics from the commanded to actual servo motor position. This is modeled with the measured transfer function $A(s)$.

$$D(s) = \frac{1 - \frac{\tau_t}{2}s}{1 + \frac{\tau_t}{2}s}, \quad F(s) = \frac{s}{s + \frac{2\pi f R}{U}}, \quad ZOH(s) = \frac{1}{1 + \frac{\tau_z}{2}s},$$

$$A(s) = \frac{(s + 1.1934)(s + 0.3869 \pm i0.3443)(s - 3.2229 \pm i1.8607)}{(s + 0.1824 \pm i0.2933)(s + 1.5971 \pm i3.0352)(s + 3.2229 \pm i1.8607)}$$

To complete the model, the values of the parameters need to be obtained. Some, such as fluid inertias, can be calculated from geometry. Others were obtained empirically. Such is the case for the isentropic and actual compressor speedlines. The former is derived from the torque input and compressor velocity, the latter from pressure measurements. The difference between them is the total fluid loss L_u , with $L_{uR,ss} = rL_u$ and $L_{uS,ss} = (1-r)L_u$, where r is the reaction of the compressor. The values of the parameters are:

$$\psi = -9.9222\phi^2 + 9.2018\phi - 1.1310 \quad (0.443 \leq \phi \leq 0.528)$$

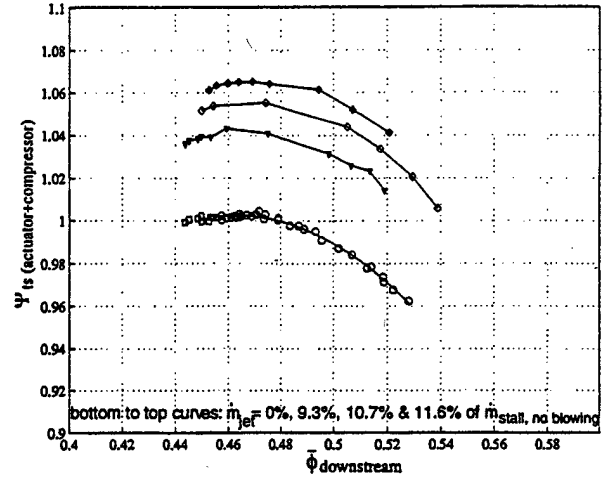


Fig. 6 Actuator/compressor characteristics at several mean injection rates with closed-loop control (lowest solid line is fit of base speedline).

$$\psi_i = -0.5467\phi^2 - 1.6328\phi - 2.0400 + \frac{0.1173}{\phi} \quad (0.458 \leq \phi \leq 0.528)$$

$$r = 0.75, \quad \lambda = 0.6787, \quad \mu = 1.2937, \quad \eta_{hw} = -0.6034, \quad \tau_R = 0.177/\bar{\phi}_d,$$

$$\tau_S = 0.162/\bar{\phi}_d, \quad \alpha = 8.2^\circ, \quad \gamma = 37.9^\circ, \quad \frac{A_j}{A} = 0.0197, \quad \tau_a = 0.6132,$$

$$\tau_t = 0.248, \quad \tau_z = 0.503$$

Experimental Verification of Injection Model

Total-to-static pressure rise speedlines across the actuator/compressor at several injection rates were measured to verify the injection model, as shown in fig. 6. By subtracting the baseline case (zero injection) from the other curves, the effect of injection can be extracted as shown in fig. 7. Figure 7 also shows the corresponding prediction of the injection model described by equation (6) as well as that of the model which solely incorporates the momentum addition term in equation (4).

The main conclusions one can extract from fig. 7 is first that the effect of mass addition significantly reduces the stagnation pressure rise of the injector (approximately 25% in this case). Second, the experimental results, which are obtained with discrete actuators and incomplete mixing, have slightly positive slope with mass flow, while the theory shows negative slope, implying a reduction in actuation effectiveness with closing throttle. This is a relatively small effect. An empirical model of jet injection is obtained by fitting the data points, as shown by the solid lines in fig. 7, which gives the experimental model:

$$\frac{P_{t2} - P_{t1}}{\rho U^2} = a\phi_j^2 + b\phi_j + c\phi_j\phi_2 + d\phi_2 + e\phi_2^2 \quad (15)$$

where: $a=0.0119$, $b=-0.0259$, $c=0.0429$, $d=1E-4$, $e=-2E-4$

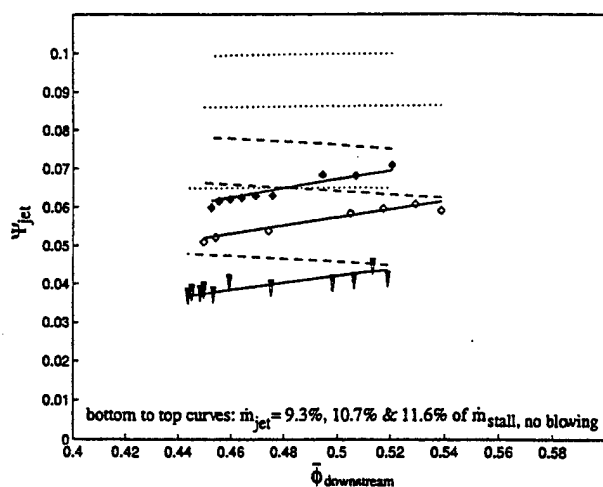


Fig. 7 Jet contribution to ψ_{ts} (actuator+compressor) (symbols) and fit (solid lines) versus full mixing model (dashed lines) and pure momentum addition model (dotted lines).

Theoretical Stall Predictions

The system model set up previously is used here to predict the stall point of the MIT Three Stage compressor with constant gain feedback control. Three different levels of modeling are used to evaluate the potential effect of non-ideal injection and feedback dynamics on the performance of the closed-loop system. The first configuration is similar to that used in Hendricks and Gysling (1994), with idealized injectors described by equation (6) and no control system dynamics, i.e. feedback is done directly on equation (14). The second uses the real injectors represented by equation (15). The last configuration adds feedback dynamics to the control loop, thus incorporating the transfer functions $D(s)$, $F(s)$, $ZOH(s)$ and $A(s)$ in the loop depicted in fig. 4. The controller is a simple proportional control described by a gain K and a phase lag β for each harmonic. Figure 8 shows the lowest attainable flow coefficient for first harmonic control with optimum gain (within a range of 0 to -0.006) and varying phase, using the different models.

The effect of non-ideal injection (dashed line) is a reduction in range extension by about the same proportion as the reduction in pressure rise due to the jet, without modifying the phase (or optimization) curve of the system. At a fixed ideal phase, the stalling coefficient continuously decreases with increasing gain as is the case with the ideal injection. However, the addition of the feedback dynamics not only causes another sharp drop in performance but alters the system. The dash-dotted curve in fig. 8 shows that the optimum phase has shifted from the cases without feedback dynamics. At a fixed ideal phase value, a minimum stall coefficient is reached at finite gain value of approximately -0.0025 , as indicated in the legend of fig. 8.

These observations suggests that the effects of non-ideal injection and feedback dynamics can be severe, especially the latter, in limiting the performance of the control system with jet actuators. Thus, these effects should be included in any predictions of closed-loop system performance and control law design with jet actuation. Furthermore, performance can be improved through faster sensors and better control law design.

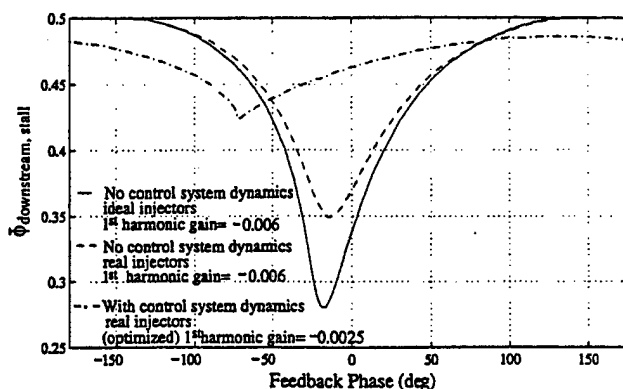


Fig. 8 Theoretical predictions of the downstream flow coefficient at stall for the first harmonic with an optimum feedback gain and varying feedback phase for various level of modeling.

SYSTEM IDENTIFICATION

System identification experiments were performed to verify the accuracy of the model of the compression system with non-ideal injection and control system dynamics. This is done by comparing the theoretical and experimental root locus of the system. Both open-loop and closed-loop comparisons are made for varying throttle and control feedback gain and phase.

Identification Methodology

The system identification runs were performed with an input temporal frequency sweep from 0 to 100 Hz on the amplitude of a stationary spatial cosine injection wave for one harmonic at a time. The temporal variation of the corresponding harmonic, in the form of the coefficients of the spatial cosine and sine waves, is computed from the hot-wire measurements. The output of the system contains both positive and negative frequencies, which represents clockwise and counter clockwise rotational disturbances. The transfer functions from commanded SFC to measured SFC for each harmonic are computed over the frequency domain of interest and fitted using Matlab (Little et al., 1995) with the coherence used as a weighting factor in the fit. The poles and zeros derived from the fitted transfer functions are plotted along with the theoretical poles and zeros calculated for the same operating conditions using the system's model.

Identification Results

The open-loop system identification results for varying throttle for the first harmonic are shown in fig. 9, with the corresponding plot for the closed-loop system in fig. 10. The corresponding root loci for the second and third harmonic show the same trends and thus are not shown. The root loci for the first and second harmonic with varying gain and phase are shown in figs. 11 through 14. Third harmonic control results were similar, but had lower coherence. Some features on these root locus plots need to be explained. First, poles that are associated with the stall precursor are enclosed by a box with solid lines. (Dashed boxes enclose other experimental poles obtained from coherent data and satisfactory fit.) Second, the large arrows close to groups of poles indicate the direction of closing throttle, increasing

gain or decreasing phase, depending on the root locus plot under consideration. Third, the throttle position, feedback gain and phase values are indicated on the figures.

The root locus with throttle variation, illustrated in figs. 9 and 10, show that the model captures the stall precursor pole well in terms of rotational frequency for the first harmonic, but overestimates its damping. Corresponding root loci for the second and third harmonics (not shown) show the same results. As for the closed-loop case with varying gain, fig. 11 shows that the general trajectory of the first harmonic precursor pole is fairly accurately predicted, showing the fact that active control with constant gain feedback moves the first harmonic precursor pole into the undesirable zone of higher frequency for this system. However, it is observed that the model's pole reaches maximum damping at a gain between -0.002 and -0.003, consistent with the optimum predicted gain of -0.0025 indicated in fig. 8, whereas the corresponding identified pole's damping peaks at a gain of about -0.005. As for harmonic 2, fig. 12 shows that the increase in damping of the precursor pole with gain is lower than that predicted by the model. Similarly, the root loci with respect to the controller phase, depicted in figs. 13 and 14, show that the model predicts the general trajectory of the precursor pole with regard to controller phase correctly, although the error in the prediction of the position of the critical pole is larger than that for the case of varying gain.

The above observations suggest that the model is accurate in terms of predicting the dynamic behavior associated with the stall precursor pole, which is the critical pole leading to stall. As such, it is useful in designing compensators to counter undesirable effects such as the migration of the first harmonic precursor pole into the high frequency zone. However, the overestimation of the damping of the critical pole suggests that the compressor will stall at a higher flow coefficient than predicted. In addition, slight inaccuracies in the detailed trajectory of the critical pole would indicate that the predicted optimum controller gain and phase will be slightly off.

ACTIVE CONTROL EXPERIMENTS

Active control experiments with jet actuation and constant gain feedback control were performed to quantitatively compare the model's stall predictions with real values. During experimental tuning of the controller's gain and phase for the first three harmonics, the flow coefficient downstream of the compressor at stall was recorded, so that it can be compared with theoretical predictions.

Experimental Procedure

The tuning experiments were carried out at a mean injection rate of 9.3% of the stalling mass flow. First, fixing the feedback phase at a value close to the predicted optimal phase, the throttle position at which the system stalled was recorded at different values of the feedback gain. Once an optimum gain was chosen and fixed, the procedure was repeated to find the optimum phase. With the compressor under first harmonic feedback control at the optimum gain and phase, the control parameters for the second harmonic were tuned in the same manner, and so on.

Rotating Stall Control Results

Figures 15 and 16 show the experimental stall flow coefficients and the corresponding predicted stall flow coefficients for the first two harmonics. Figure 15 suggests that the model accurately predicts the

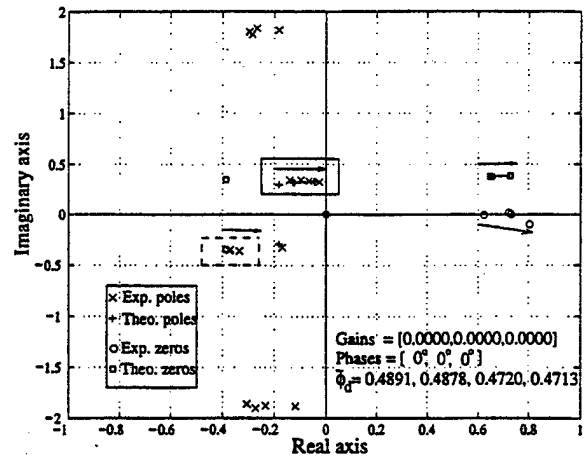


Fig. 9 Open-loop root locus for harmonic 1 with varying throttle.

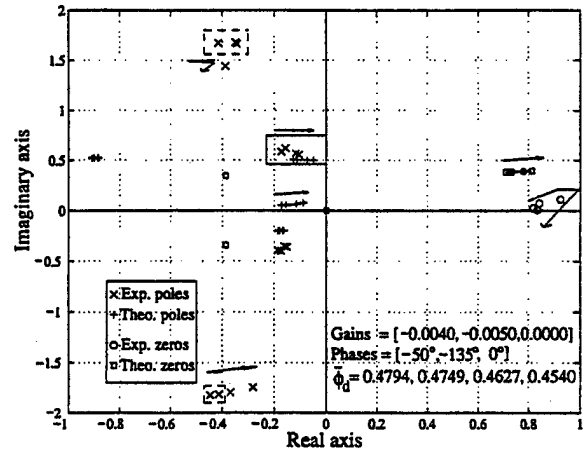


Fig. 10 Closed-loop root locus for harmonic 1 with varying throttle.

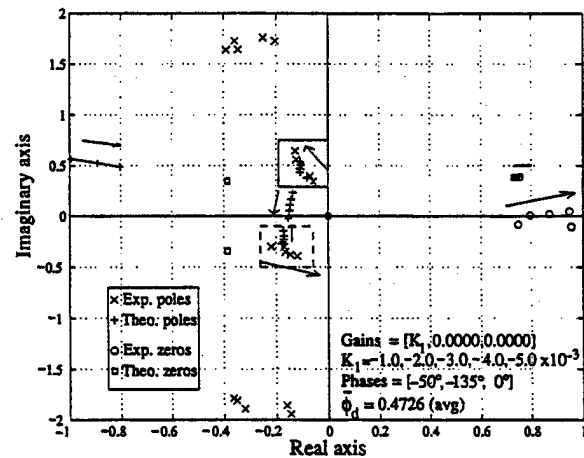


Fig. 11 Closed-loop root locus for harmonic 1 with varying gain.

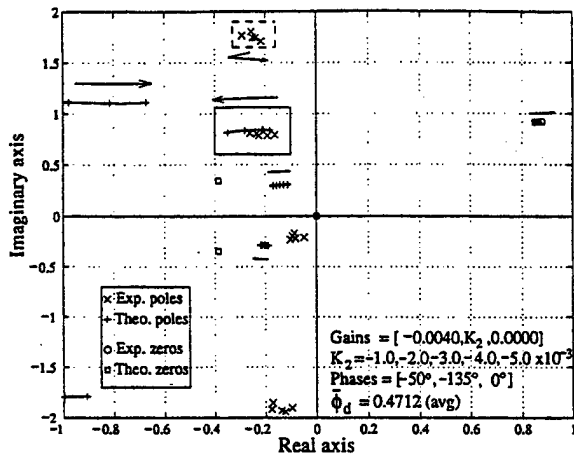


Fig. 12 Closed-loop root locus for harmonic 2 with varying gain.

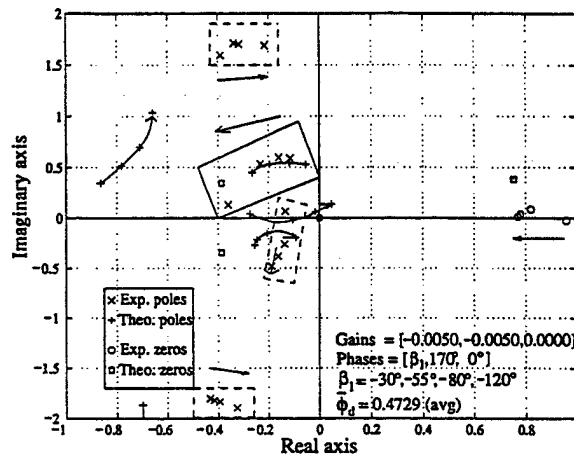


Fig. 13 Closed-loop root locus for harmonic 1 with varying phase.

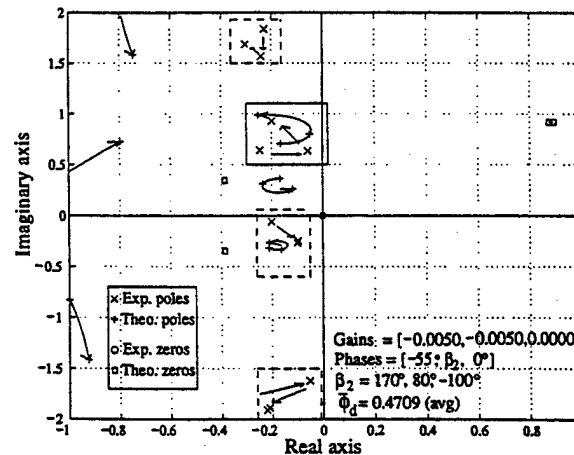


Fig. 14 Closed-loop root locus for harmonic 2 with varying phase.

effect of feedback phase on the system for the first harmonic. However, it is completely off in predicting the optimum gain of about -0.0025 compared to the actual value between -0.004 and -0.005. This difference in the optimum gain value agrees with fig. 11, which shows the theoretical root locus attaining maximum damping of the precursor pole at gain values between -0.002 and -0.003. For the second harmonic (fig. 16), the predicted trends are approximately correct for the feedback gain and phases but the values are off. Similar results for the third harmonic show little effect, as predicted by the model, which indicates that the cause of stall is the second harmonic. In general, the actual stall points are slightly higher than the predicted stall points in the area of optimum controller gain and phase.

Control experiments using the empirically optimized control parameters were subsequently performed with a maximum improvement in downstream stall flow coefficient of 5.5%. Table 1 compares the maximum experimental range extension with optimal theoretical values given by the various level of modeling. Again, one observes that the models with ideal injection and/or no control system dynamics overestimate the performance of the system.

DISCUSSION AND SUMMARY

We have experimentally evaluated the effectiveness of jet actuation in active control of rotating stall in a multi-stage compressor. Detailed modeling of jet actuation indicates that although momentum addition is still the main factor in the stagnation pressure rise due to the jet, mass addition can significantly reduce this pressure rise. Moreover, practical considerations such as discrete actuators and non-ideal mixing reduce the effectiveness (i.e. pressure rise) of jet actuation as the throttle is closed. The above effects must be taken into account in any theoretical predictions. With an updated empirical model for injection integrated into a Moore-Greitzer compressor model with losses, it was shown that the effect of non-ideal injection is to reduce the stall range extension by about the same proportion as the reduction in stagnation pressure rise due to the jet. In addition, the presence of feedback dynamics in the control loop can result in a dramatic drop in range extension and must absolutely be accounted for in any theoretical studies and controller design using jet actuation. Better controller design (see for instance Weigl (1997)) should mitigate the effect of control system dynamics, where upon the limitation in range extension of the compressor under closed-loop control should rest on the effectiveness of the injectors.

System identification experiments indicate that the complete model of the system is qualitatively correct in predicting the movement of the critical pole but overestimates its damping. Although quantitatively inaccurate, the model can be used to design control laws that move the critical pole in the desirable direction. Clearly, the constant gain feedback controller is inadequate for this particular system as it puts stress on the bandwidth of the actuator.

Comparison of preliminary control experiments using constant gain feedback control with theoretical predictions are consistent with system identification; the trends are right but the stall predictions are slightly optimistic. The best result achieved with jet actuation in this system with constant feedback control is a range extension of 5.5% in downstream flow coefficient compared with a theoretical maximum of 6.8%.

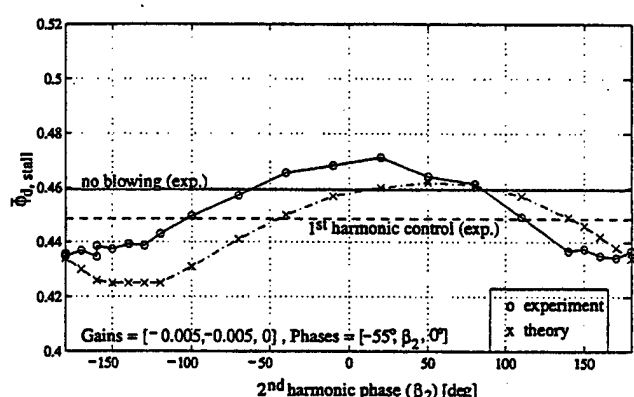
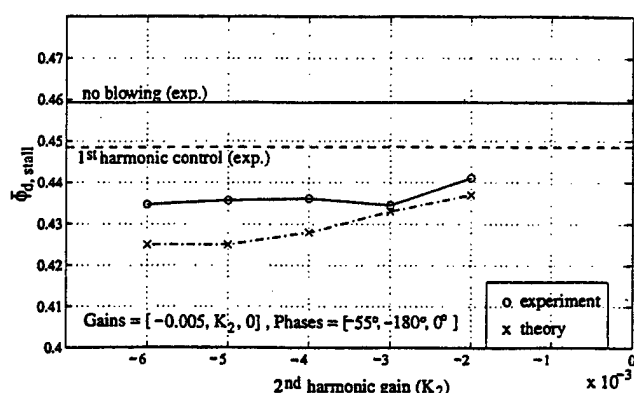
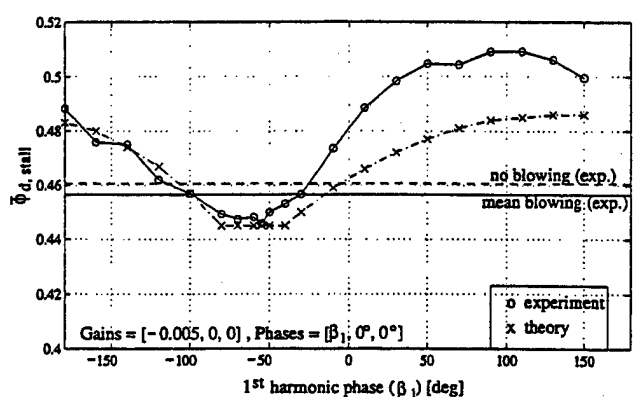
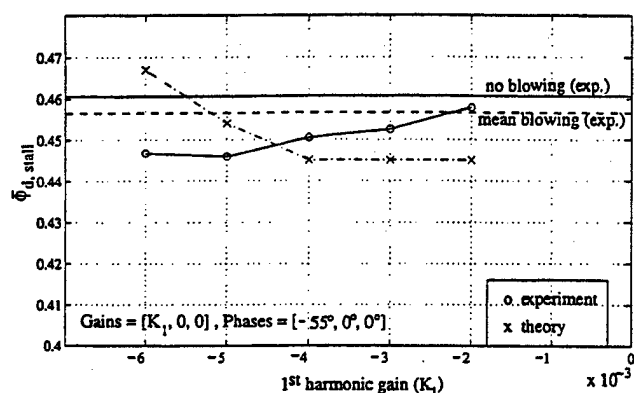


Fig. 15 Experimental gain and phase optimization for harmonic 1 controller. Top: gains = $[K_1, 0, 0]$ and phases = $[-55^\circ, 0^\circ, 0^\circ]$. Bottom: gains = $[-0.005, 0, 0]$ and phases = $[\beta_1, 0^\circ, 0^\circ]$.

Fig. 16 Experimental gain and phase optimization for harmonic 2 controller. Top: gains = $[-0.005, K_2, 0]$ and phases = $[-55^\circ, -180^\circ, 0^\circ]$. Bottom: gains = $[-0.005, -0.005, 0]$ and phases = $[-55^\circ, \beta_2, 0^\circ]$.

Table 1 Summary of experimental and theoretical stall points for optimized controllers with a maximum allowable gain of 0.0050 in magnitude.

Description	Downstream flow coefficient at stall ($\bar{\phi}_{d, stall}$) [% decrease in $\bar{\phi}_{d, stall}$ from baseline]			
	experiment	Model w/o external dynamics & ideal injection	Model w/o external dynamics & real injection	Model With external dynamics & real injection
no blowing (baseline)	0.458	0.456	0.456	0.456
mean blowing, no control	0.455 [0.7%]	0.454 [0.4%]	0.461 [-1.1%]	0.461 [-1.1%]
1 st harmonic control	0.447 [2.4%]	0.436 [4.3%]	0.445 [2.4%]	0.445 [2.4%]
1 st and 2 nd harmonic control	0.436 [4.8%]	0.402 [11.8%]	0.414 [9.2%]	0.425 [6.8%]
1 st , 2 nd and 3 rd harmonic control	0.433 [5.5%]	0.385 [15.6%]	0.409 [10.3%]	0.425 [6.8%]

REFERENCES

- Behnken, R.L., D'Andrea, R. and Murray, R.M., 1995, "Control of Rotating Stall in a Low-Speed Axial Flow Compressor Using Pulsed Air Injection: Modeling, Simulation, and Experimental Validation," *In Proc. IEEE Conference on Decision and Control*.
- Berndt, R.G., Weigl, H.G., Paduano, J.D., and Epstein, A.H., 1995, "Experimental Techniques for Actuation, Sensing and Measurement of Rotating Stall Dynamics in High Speed Compressors," *In Proc. for SPIE*, Vol. 2494, Orlando, April 17-18, pp.166-185.
- Diaz, D.S., 1994, "Design of a Jet Actuator for Active Control of Rotating Stall," M.S. Thesis, Department of Aeronautics and Astronautics, MIT, Cambridge, MA.
- Eastland, A.H.J., 1982, "Investigation of Compressor Performance in Rotating Stall," MIT GTL Report No.164.
- Gamache, R.N., 1985, "Axial Compressor Reversed Flow Performance," Ph.D. Thesis, Department of Aeronautics and Astronautics, MIT, Cambridge, MA.
- Garnier, V.H., Epstein, A.H., and Greitzer, E.M., 1991, "Rotating Waves as a Stall Inception Indication in Axial Compressors," *ASME Journal of Turbomachinery*, Vol. 113, pp.290-301.
- Gysling, D.L. and Greitzer, E.M., 1994, "Dynamic Control of Rotating Stall in Axial Flow Compressors Using Aeromechanical Feedback," *ASME Paper No. 94-GT-292*.
- Haynes, J.M., 1994, "Active Stabilization of Rotating Stall in a Three-Stage Axial Compressor," *ASME Journal of Turbomachinery*, Vol. 116, pp. 226-239, April 1994.
- Hendricks, G.J. and Gysling, D.L., 1994, "A Theoretical Study of Sensor-Actuator Schemes for Rotating Stall Control," *Journal of Propulsion and Power*, Vol. 10, No.1, pp.101-109.
- Little, J. and Moler, C., 1995, "Matlab User's Guide," MathWorks, Natick, MA.
- Moore, F.K., 1984, "A theory of Rotating Stall of Multistage Compressors, Part I-III," *ASME Journal of Engineering for Power*, Vol. 106, pp. 313-336, 1984.
- Moore, F.K. and Greitzer, E.M., 1986, "A Theory of Post-Stall Transients in Axial Compressors: Part I - Development of Equations," *ASME Journal of Engineering for Gas Turbines and Power*, Vol. 108, pp.68-76.
- Paduano, J.D., 1992, "Active Control of Rotating Stall in Axial Compressors," MIT GTL Report No. 208.
- Van Schalkwyk, C.M., Paduano, J.D., Greitzer, E.M., and Epstein, A.H., 1997, "Active Stabilization of Axial Compressors with Circumferential Inlet Distortion," Paper No. 97-GT-316, ASME Turbo Expo'97, June 2-5, Orlando.
- Vo, H.D., 1997, "Active Control of Rotating Stall in a Three-Stage Axial Compressor with Jet Actuators," M.S. Thesis, Department of Aeronautics and Astronautics, MIT, Cambridge, MA.
- Weigl, H.J., Paduano, J.D., Frechette, L.G., Epstein, A.H., Greitzer, E.M., Bright, M.M., and Strazisar, A.J., 1997, "Active Stabilization of Rotating Stall in a Transonic Single-Stage Axial Compressor," Paper No. 97-GT-411, ASME Turbo Expo'97, June 2-5, Orlando.

ACKNOWLEDGEMENTS

The authors wish to thank Professor A.H. Epstein and H. Weigl for their advice, and J. Protz, C. Van Schalkwyk and the technicians of the MIT Gas Turbine Laboratory for their help in setting up the

experimental facilities. This work was supported by the U.S. Air Force Office of Scientific Research, Dr. J. McMicheal, Technical Manager.

APPENDIX A

Model of Fluid System

This section presents the integration of the injector model into that of the compressor and into the model of the upstream and downstream flow fields. The resulting model of the fluid system is then linearized and subjected to Fourier decomposition. For spatial reference in the following derivation, station 0 is located far upstream of the actuator, stations 1 and 2 delimit the actuator as shown in fig. 5, and stations 2 and 3 refer the inlet and exit of the compressor, respectively.

Compressor Model

The Moore-Greitzer model with unsteady losses is used to describe the three-stage compressor. The model consists of a local pressure balance across the compressor taking into account the ideal pressure rise of the compressor and the viscous losses in the rotors and stators as well as the fluid inertia in the blade passages. Two additional equations account for the time lag associated with the viscous losses. The linearized model is represented by equations (A1) through (A3).

$$\frac{\delta P_{s3} - \delta P_{t2}}{\rho U^2} = \frac{d\psi_1}{d\phi} \delta\phi_2 - \delta L_{uR} - \delta L_{uS} - \lambda \frac{\partial(\delta\phi_2)}{\partial\theta} - \mu \frac{\partial(\delta\phi_2)}{\partial\xi} \quad (A1)$$

$$\tau_s \frac{\partial(\delta L_{uS})}{\partial\xi} = \frac{dL_{uS,ss}}{d\phi} \delta\phi_2 - \delta L_{uS} \quad (A2)$$

$$\tau_R \left(\frac{\partial(\delta L_{uR})}{\partial\xi} + \frac{\partial(\delta L_{uR})}{\partial\theta} \right) = \frac{dL_{uR,ss}}{d\phi} \delta\phi_2 - \delta L_{uR} \quad (A3)$$

where L_{uS} and L_{uR} are the instantaneous (unsteady) viscous pressure loss across the stators and rotors, respectively. τ_s and τ_R are the associated time lags, which are equivalent to 1.5 times the nondimensional flow convection time through the average stator and rotor in the compressor, respectively (Haynes (1994)). Lastly, mass conservation across the compressor and the infinitesimal compressor thickness from the semi-actuator disk assumption implies that $\delta\phi_3 = \delta\phi_2$.

Upstream and Downstream Flow Fields

As derived by Moore and Greitzer (1986), the upstream flow field was assumed to be incompressible, inviscid and irrotational such that a nondimensional velocity potential Φ_u exist, obeying $\nabla^2 \Phi_u = 0$ and $\phi_u = \partial\Phi_u / \partial\eta$, or in linearized form:

$$\nabla^2(\delta\Phi_u) = 0 \quad (A4)$$

$$\delta\phi_u = \frac{\partial(\delta\Phi_u)}{\partial\eta} \quad (A5)$$

At station 1, one has $\delta\phi_1 = \delta\phi_u(\eta=0)$. In addition, applying the linearized nondimensional unsteady Bernoulli equation, one gets:

$$\frac{\delta P_{s1}}{\rho U^2} = \frac{\partial(\delta\Phi_u)}{\partial\xi} \bigg|_{\eta=0} \quad (A6)$$

Downstream of the compressor, the incompressible and inviscid (not irrotational) flow field, with the assumption of constant exit flow angle at the last stator, can be described by the linearized Euler equation along the axial location:

$$\frac{\partial(\delta P_{sd}/\rho U^2)}{\partial\eta} = -\frac{\partial(\delta\phi_d)}{\partial\xi} \quad (A7)$$

At station 3, one has $\delta\phi_2 = \delta\phi_3 = \delta\phi_d(\eta=0)$ and $\delta P_{s3} = \delta P_{sd}(\eta=0)$. In addition, since the static pressure disturbances of the higher (i.e. non-surge) modes decay downstream as mentioned by Paduano (1992), δP_{sd} obeys the Laplace equation:

$$\nabla^2(\delta P_{sd}/\rho U^2) = 0 \quad (A8)$$

Injector/Compressor/Flow Fields Integration

The above equations will now be combined, transformed into the Fourier domain and solved to give a transfer function from the input disturbance amplitude $\delta\phi_j$ to the perturbation amplitude $\delta\phi$ at the hot-wire location for each mode.

First, one combines the actuator and compressor by adding equation (9) to equation (A1) and substituting $\delta P_{s1}/\rho U^2$ with equation (A6) to obtain:

$$0 = \frac{\partial(\delta\Phi_u)}{\partial\xi} \bigg|_{\eta=0} + \left(\frac{d\psi_i}{d\phi} - X \right) \delta\phi_2 - Y\delta\phi_j - \delta L_{uR} - \delta L_{uS} - \mu \frac{\partial(\delta\phi_2)}{\partial\xi} - \lambda \frac{\partial(\delta\phi_2)}{\partial\theta} - \frac{\delta P_{s3}}{\rho U^2} \quad (A9)$$

To solve equation (A9), one looks for a solution to the upstream and downstream flow fields. In the upstream zone, the boundary conditions state that the velocity disturbances start at the actuator/compressor ($\eta=0$) and die out at the inlet ($\eta \rightarrow -\infty$). Similarly in the downstream flow, pressure disturbances die out at ($\eta \rightarrow +\infty$). In

addition, the flow quantities are periodic in θ . Therefore, the solutions to equations (A4) and (A8) are, respectively:

$$\begin{aligned} \delta\Phi_u &= \sum_{n>0} \text{Re} \left\{ A_n^*(\xi) e^{n\eta} e^{in\theta} \right\} \\ \delta P_{sd} &= \sum_{n>0} \text{Re} \left\{ \delta \bar{P}_{3dn}^*(\xi) e^{-n\eta} e^{in\theta} \right\} \end{aligned} \quad (A10)$$

where $A_n(\xi)$ and $\delta \bar{P}_{3dn}(\xi)$ are time-dependent spatial Fourier coefficients. Putting equation (A10) in (A5), one gets:

$$\delta\phi_u = \sum_{n>0} \text{Re} \left\{ \tilde{\phi}_n^*(\xi) e^{n(\eta-\eta_{hw})} e^{in\theta} \right\}, \quad \left(A_n = \frac{\tilde{\phi}_n e^{-n\eta_{hw}}}{n} \right)$$

where $\tilde{\phi}_n$ is the velocity coefficient SFC at the hot-wires' axial location. The above Fourier expansions applied to the pertinent flow quantities at the actuator/compressor ($\eta=0$) leads to:

$$\begin{aligned} \delta\phi_j &= \sum_{n>0} \text{Re} \left\{ \tilde{\phi}_{jn}^*(\xi) e^{in\theta} \right\} \\ \delta\phi_d &= \sum_{n>0} \text{Re} \left\{ \left[\tilde{\phi}_n^*(\xi) e^{-n(\eta+\eta_{hw})} + \left(\frac{A_j}{A} \cos\alpha \right) \tilde{\phi}_{jn}^*(\xi) \right] e^{in\theta} \right\} \\ \delta L_{uS} &= \sum_{n>0} \text{Re} \left\{ \tilde{L}_{uSn}^*(\xi) e^{in\theta} \right\} \\ \delta L_{uR} &= \sum_{n>0} \text{Re} \left\{ \tilde{L}_{uRn}^*(\xi) e^{in\theta} \right\} \end{aligned}$$

If one substitutes the above Fourier expansions for δP_{sd} , $\delta\phi_j$, $\delta\phi_d$, δL_{uS} and δL_{uR} into equations (A2), (A3), (A7) and (A9) and consider each mode n separately, as mathematically permitted by the linearity assumption, one gets, after simplification, the three ordinary differential equations (10), (11) and (12) for $\tilde{\phi}_n$, \tilde{L}_{uSn} and \tilde{L}_{uRn} .



The Society shall not be responsible for statements or opinions advanced in papers or discussion at meetings of the Society or of its Divisions or Sections, or printed in its publications. Discussion is printed only if the paper is published in an ASME Journal. Authorization to photocopy material for internal or personal use under circumstance not falling within the fair use provisions of the Copyright Act is granted by ASME to libraries and other users registered with the Copyright Clearance Center (CCC) Transactional Reporting Service provided that the base fee of \$0.30 per page is paid directly to the CCC, 27 Congress Street, Salem MA 01970. Requests for special permission or bulk reproduction should be addressed to the ASME Technical Publishing Department.

Copyright © 1997 by ASME

All Rights Reserved

Printed in U.S.A.

Active Stabilization of Axial Compressors with Circumferential Inlet Distortion

C.M. van Schalkwyk

Scientific Systems Co., Inc.
Woburn MA 01801

J.D. Paduano, E.M. Greitzer, A.H. Epstein

Department of Aeronautics and Astronautics
Massachusetts Institute of Technology
Cambridge MA 02139

Abstract

This paper describes the first experimental validation of transfer function modeling and active stabilization for axial compressors with circumferential inlet distortion. The inlet distortion experiments were carried out in a three stage low-speed compressor. Theory-experiment comparisons of steady performance, unsteady stall precursor, and forced response (transfer function) data were all used to assess a control-theoretic version of the Hynes-Greitzer distorted flow model. The tests showed good agreement between theory and data and demonstrated that *a priori* predictions, based on geometry and steady-state performance data, can be used to design control laws which stabilize rotating stall with inlet distortion.

Based on these results, active feedback control has been used to stabilize the inlet distortion induced instability associated with rotating stall onset. The stabilization allowed stall free operation to be extended below the natural (distorted flow) stall point by up to 3.7% for a 0.8 dynamic head distortion. For a 1.9 dynamic head distortion, 40% of the mass flow range lost due to inlet distortion was regained through active control. The paper elucidates the difficulties associated with active control with distortion, and introduces a new control law that addresses many of these challenges.

1 Introduction and Problem Definition

The detrimental impact of distortion on compressor stability is well documented, both qualitatively and quantitatively [18, 13]. Stall and surge safety margins can be severely degraded by inlet separation and other sources of inlet flow nonuniformity. As such, a substantial percentage of the stall margin built into a compressor design specifically addresses the effects of inlet distortion. Further, especially in military engines, distorted flow is typically the situation under which instability is encountered.

The concept of active stabilization to improve compressor operating range has received wide attention (see for instance [4, 5]), but a key question is whether improvements in operating range can be obtained by active stabilization in the presence of inlet distortion. Prior to this study, active stabilization of rotating stall has been demonstrated exclusively under "clean" inlet flow conditions — that is, steady-state operation of the compressor with circumferentially uniform flow.

Circumferential distortion creates a nonaxisymmetric flow field in the compressor that fundamentally changes the nature of the control problem to be addressed. The nonuniform medium through which prestall waves travel causes more complex wave dynamics than in undistorted flow, because circumferential sinusoids are no longer eigenmodes of the flow in the compressor annulus. The implication for control is that the system can no longer be viewed as a parallel interconnection of single-input

Nomenclature

Abbreviations	Symbols	Symbols (cont.)
DF distributed feedback	b chord	r reaction
HF harmonic feedback	b_G "B" parameter	\bar{r} mean radius
HFC harmonic feedback with cross coupling	β spatial phase shift of DF controller	t time
IGV inlet guide vanes	c_x axial velocity	τ_t time constant
LQG linear quadratic Gaussian	δ perturbation	u velocity
MIMO multi-input multi-output	γ inlet guide vane deflection	μ fluid inertia
PSD power density spectrum	k_t throttle constant	ω_r rotor frequency
RMS root mean squared	l duct length	x_m upstream sensor location
SISO single-input single-output	ϕ flow coefficient	Subscripts
XHG extended Hynes-Greitzer model	ψ_c compressor inlet-total to exit-static pressure rise	a actuator inlet guide vane
	ρ density of air	i inlet guide vane, ideal
	θ angle around annulus	r rotor
		s stator
		w wheel

single-output (SISO) systems (decoupling of sinusoidal eigenmodes) as in past rotating stall research, such as that of Paduano et al. [17] and Haynes et al. [7]. With distortion the system is inherently multiple-input multiple-output (MIMO).

Two related techniques will be brought to bear on control of compressors with inlet distortion in this paper. The first is modeling of the unsteady compression system behavior, which began with the work of Moore [15] and Moore and Greitzer [16]. In these papers, hydrodynamic stability models for rotating stall in compressors without distortion were derived. Based on this work, Longley [11], Hynes and Greitzer [8] and Chue et al. [2] extended the model to the case with inlet distortion, and showed that many of the experimental features of distortion were captured by the method. We have further extended this model to include the effects introduced by Haynes et al. [7], as well as forcing, and developed a state-space model for actuated compression systems with inlet distortion.

The second set of methods we will apply are those of system identification and control theory. By incorporating high-bandwidth, distributed actuation into an experimental compressor, we are able to assess the fluid dynamic model more rigorously than has been possible in the past. We will capitalize on the measurements of Haynes et al. [7] to build a predictive model of the effects of distortion, and verify this model through system identification. We will

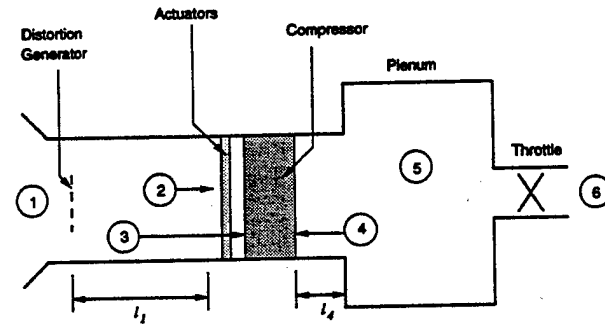


Figure 1: Schematic of compressor flow field.

then investigate the effectiveness of various control schemes to stabilize rotating stall and increase the compressor stable operating range with distortion.

The paper is organized as follows. After briefly reviewing the effects of inlet distortion and describing the experimental setup, we verify our extension of the model of [8] against a detailed set of steady-state, unsteady, and input-output data. Second, we elucidate the main features of the active stabilization problem when distortion is present. Finally, we demonstrate that active stabilization can be achieved with distortion, and quantify the gains attained in the our experiment.

2 Compressor Response to Small Perturbations

The basic tenet of the work described here is that instability and subsequent growth of small perturbation traveling waves leads to fully developed rotating stall. We thus briefly describe compression system response to these small perturbations.

2.1 Uniform Flow

We start with a conceptual description of the compression system without distortion. Figure 1 shows the compressor annulus unwrapped into a 2-D setting, as is valid for compressors with high hub-to-tip radius ratio. The compressor is modeled as a high solidity semi-actuator disk. The flow in the upstream duct is considered irrotational, and the flow in the downstream duct is rotational but linearized (see Lavrich [10] for experimental justification of these assumptions). A plenum exists downstream of the compressor, but the dynamics associated with the plenum do not interact with the (linearized) rotating stall dynamics if there is no inlet distortion. A detailed description of the analysis for uniform flow can be found in Haynes et. al [7].

The flow variables at the compressor face can be expressed as Fourier series. For example, the axial velocity coefficient ϕ at the compressor face is given by

$$\phi(\theta, t) = \sum_{n=-\infty}^{\infty} \tilde{\phi}_n(t) e^{in\theta} \quad (1)$$

where ϕ is the axial velocity divided by the wheel speed c_x/u_w , θ is the angle around the annulus, t is time, and (\cdot) denotes the Fourier coefficients. If the flow far upstream is uniform, there is no coupling of waves of different harmonic number. In this situation Moore [14] has derived a simple relationship which holds *independently* for each of the Fourier coefficients of the unsteady perturbations:

$$\frac{2}{|n|} \frac{\partial \tilde{\phi}_n}{\partial t} = \frac{d\psi_c}{d\phi} \delta \tilde{\phi}_n - in\lambda \delta \tilde{\phi}_n - \mu \frac{\partial \tilde{\phi}_n}{\partial t}, \quad n \neq 0. \quad (2)$$

In Equation (2) $\frac{d\psi_c}{d\phi}$ is the slope of the compressor total-to-static pressure rise characteristic, $\delta \tilde{\phi}_n$ is the

n th harmonic of the perturbation $\delta \phi(\theta) = \phi(\theta) - \phi_{ss}$, with ϕ_{ss} the steady state flow, and λ and μ are parameters which quantify the inertia in the blade row passages. The left-hand side of the equation captures the impedance characteristics of the flow fields upstream and downstream of the compressor face (see Moore [15] or Longley [12] for a full derivation). The important thing to note is that the slope of the pressure rise characteristic, $\frac{d\psi_c}{d\phi}$ in Equation (2), is uniform around the annulus of the compressor, so that $\frac{d\psi_c}{d\phi} \tilde{\phi}_n$ effects only the n th harmonic, and there is no coupling between circumferential harmonics.

2.2 Inlet Distortion

When inlet distortion is present, the picture is quite different. The compressor time mean pressure rise and axial velocity are nonuniform in θ . The nonuniform velocity field, which now needs to be computed, is the background environment in which the small unsteady disturbances that lead to instability propagate.

Hynes and Greitzer [8] derived the following description of distorted flow in a compressor, which must be satisfied by the steady state axial velocity coefficient at the compressor face:

$$\psi_p - \psi_{\text{dist}}(\theta) = \psi_c(\phi_{ss}) - \lambda \frac{\partial \phi_{ss}}{\partial \theta}. \quad (3)$$

This is the nonlinear condition satisfied by the steady-state velocity field $\phi_{ss}(\theta)$ at the compressor face. ψ_p is the plenum pressure, which is set by the throttle constant k_t and mean compressor flow ($\psi_p = \frac{1}{2} k_t \bar{\phi}^2$). ψ_{dist} is the total pressure distortion, determined by the loss through a screen or otherwise specified. Note that the linearized compressor characteristic in Equation (2) is replaced here by the nonlinear compressor characteristic $\psi_c(\phi)$.

Because the steady flow pattern $\phi_{ss}(\theta)$ which satisfies Equation (3) is not circumferentially uniform, $\frac{d\psi_c}{d\phi}$ is also a function of θ . When distortion is present, the equation describing small perturbation

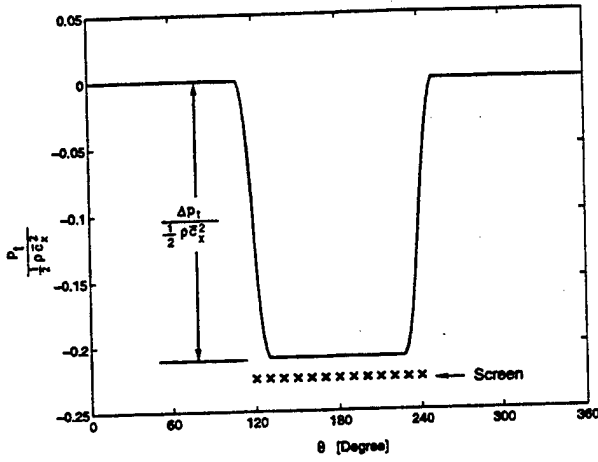


Figure 2: Distortion magnitude and extent.

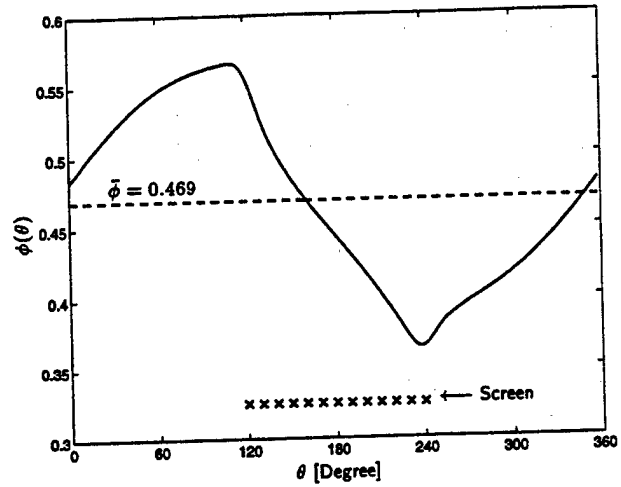


Figure 3: Computed compressor inlet steady-state axial velocity profile for the distortion shown in Figure 2.

dynamics (Equation (2)) is thus modified as follows:

$$\frac{2}{|n|} \frac{\partial \tilde{\phi}_n}{\partial t} = \left\{ \frac{d\psi_c}{d\phi}(\theta) \times \delta\phi(\theta) \right\}_n - in\lambda\delta\tilde{\phi}_n - \mu \frac{\partial \tilde{\phi}_n}{\partial t}, \quad n \neq 0. \quad (4)$$

In Equation (4) $\{\cdot\}_n$ evaluates the n th harmonic of the product in brackets, which is evaluated at each θ in the spatial domain. In [8] this term was given as a convolution sum; it involves *all* of the harmonics of both $\frac{d\psi_c}{d\phi}$ and $\delta\phi$. The central point and the essential difference from the uniform flow situation is that *the Fourier harmonics are coupled through the interaction of $\frac{d\psi_c}{d\phi}$ and $\delta\phi$, which are both functions of θ .* The eigenmodes of the system, i.e., the perturbations which grow into rotating stall, are no longer sinusoidal in θ , and the modal control approach described in Paduano et al. [17] and Haynes et al. [7] for uniform background flow becomes difficult.

We will have more to say about the control problem with distortion in a later section; here it suffices to give a pictorial example and a qualitative description of the behavior. Figure 2 defines the magnitude and extent of a square total pressure inlet distortion introduced far upstream of the compressor. Using Equation (3) and knowing the geometry and uniform flow pressure rise capability of the compressor, we can solve for the steady-state velocity profile at the compressor face, as shown in Figure 3. The

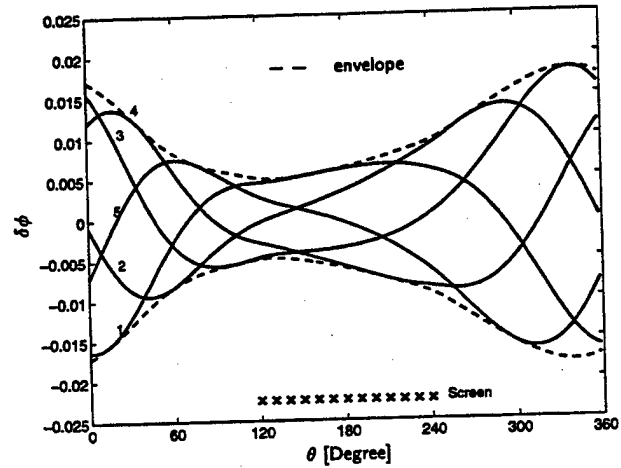


Figure 4: Neutrally stable eigenmode associated with the background distorted flow given in Figure 3. Numbers denote the eigenmode at different points in time. Velocity scale is arbitrary.

least stable eigenmode of the dynamic system described by coupling Equation (4) and the plenum response is pictured in Figure 4. Several realizations of the wave as it travels around the compressor annulus are shown, with the eigenmode pictured for the mass flow at which it is neutrally stable. For uniform inlet flow, this picture would be a first harmonic sinusoid translating around the annulus, but we now see a wave shape which changes as it travels around the

annulus. The modeling, identification, and stabilization through active control of this and other complex eigenmodes are the subject of this paper.

3 Experimental Design and Setup

The MIT three-stage low-speed (tip Mach number = 0.2) active control research compressor was modified to study inlet distortion by adding an inlet duct extension and distortion ring. Figure 5 shows, from left to right the following elements of the rig: 1) the distortion ring, which is designed so that the distortion screen can be slowly rotated to enable high spatial resolution distortion measurements; 2) the inlet duct extension, which was incorporated to decouple the potential flow effects of the distortion screen and the compressor; 3) the inlet guide vanes; 4) the 12 servo-controlled guide vanes, which are driven by independent computer-controlled servo motors – the incidence of these vanes can be commanded at a bandwidth of approximately 100 Hz (2.5 times rotor frequency); and 5) the three stages of the compressor.

Table 1 gives nondimensionalized parameters which describe this system; these parameters were measured by Haynes [6, 7], and were used to develop *a priori* models for the system with inlet distortion. The parameters required for the model are divided into three categories in Table 1: geometric parameters, measured pressure rise characteristics, and two additional parameters determined by Haynes, reaction r and characteristic time constant τ_f associated with loss generation. The theoretical value of τ_f is between 1 and 2. The actual value was determined from system identification results (see Haynes et al. [7] and Van Schalkwyk [20]). Varying the value from $\tau_f = 1$ to $\tau_f = 2$ does not significantly affect our predictions.

The distortion screens were designed to represent “worst case” distortions encountered in practice [18]. A circumferential extent (see Figure 2) of 120 degrees was used for both distortion screens tested. The first screen imposed a distortion magnitude (also defined in Figure 2) of 0.8 dynamic head, that is,

$$\frac{\Delta p_t}{\frac{1}{2}\rho\bar{c}_x^2} = 0.8 \quad (5)$$

Table 1: Three-stage compressor model parameters.

Geometric parameters (see list of symbols for definitions). Hub-to-tip ratio = 0.88.

$$\begin{aligned} \lambda = \mu_r &= 0.679 & \mu_s &= 0.334 \\ \mu_a &= 0.286 & \mu_i &= 0.071 \\ \bar{b}_r &= 0.118 & \bar{b}_s &= 0.108 \\ l_1 &= 2.992 & l_4 &= 1.529 \\ b_G &= 0.163 & x_m &= -0.6 \\ \bar{r} &= 286 \text{ mm} \end{aligned}$$

Pressure rise characteristics (Haynes [6, 7]).

(a) Pressure rise characteristic

$$\psi_c = -10.07\phi^2 + 9.4306\phi - 1.1849$$

(b) Ideal (no loss) pressure rise characteristic

$$\psi_i = -15.5341\phi^3 + 24.1238\phi^2 - 15.0262\phi + 4.6951$$

(c) Pressure rise sensitivity with respect to control vane deflection

$$\frac{d\psi_c}{d\gamma} = 2.8880\phi^2 - 3.6550\phi + 0.8251$$

Other parameters.

$$\text{Reaction } r = 0.75 \quad \tau_f = 1.5$$

where \bar{c}_x is the mean axial velocity, Δp_t is the drop in total pressure across the screen, and ρ is the air density. Because the effect on stalling flow coefficient and peak pressure rise due to this distortion was relatively small, a second screen which imposed a 1.9 dynamic head distortion was also tested.

A parameter often used to assess the severity of inlet distortion is the DC(60) descriptor (see Williams [21]) defined by

$$\text{DC}(60) = \frac{\bar{p}_t|_{360^\circ} - \bar{p}_t|_{\text{worst } 60^\circ}}{\frac{1}{2}\rho\bar{c}_x^2} \quad (6)$$

where the overbar indicates average over the specified range of angles. For an idealized case with uniform inlet static pressure, $\text{DC}(60)=1$ corresponds to zero-velocity flow in a 60 degree sector of the annulus, i.e. very poor inlet aerodynamics (Williams [21]). Experiments by Aulehla and Schmitz [1] on the Tornado showed $0.15 \leq \text{DC}(60) \leq 0.55$ as the angle of attack is varied over the range 3 to 35 degrees. At the re-

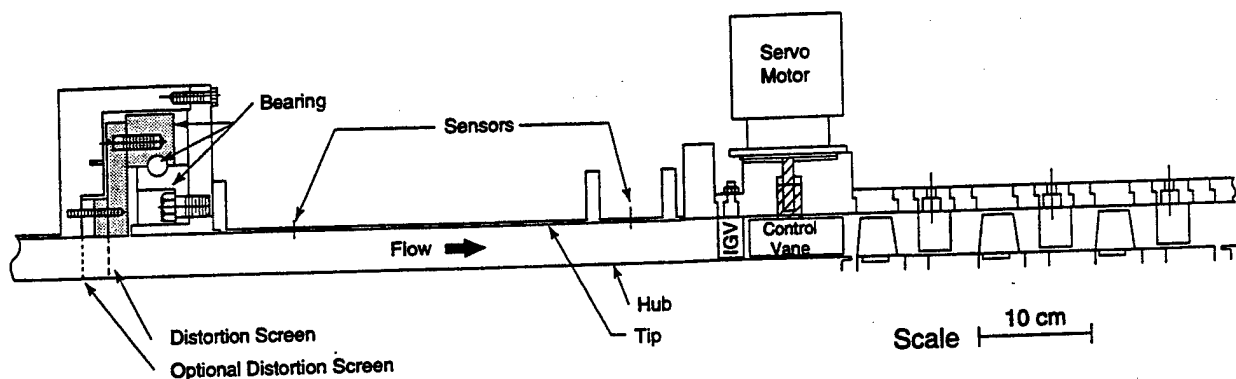


Figure 5: Experimental setup / Distortion Generator.

spective stalling flow coefficients the 0.8 and 1.9 dynamic head distortions correspond to $DC(60)=0.53$ and $DC(60)=1.31$ respectively, so that these are severe in terms of practical situations.

4 Model Assessment

In this section we compare predictions of the extended Hynes-Greitzer model to three types of experimental data. First, steady-state performance is compared to that predicted by the model. Second, the unsteady behavior of prestall waves is studied and compared to predictions. These two comparisons have been done before, most notably by Longley [11]. The third set of comparisons, however, are more informative as regards to dynamic response, and these have not been performed before. These are comparisons of the transfer functions between control guide vane deflection waves and measured waves of axial velocity in the compressor. The comparisons tested the full range of frequencies, spatial harmonics, and input-output characteristics modeled.

4.1 Steady-State Performance with Inlet Distortion

The first comparison is the steady-state predicted velocity profile. The velocity profile at the compressor face for the 1.9 dynamic head distortion has been given in Figure 3. The hot-wire measurements are taken approximately 0.6 rotor radii upstream of the compressor face, and at this location the velocity profile is much different (see Van Schalkwyk [20]). Fig-

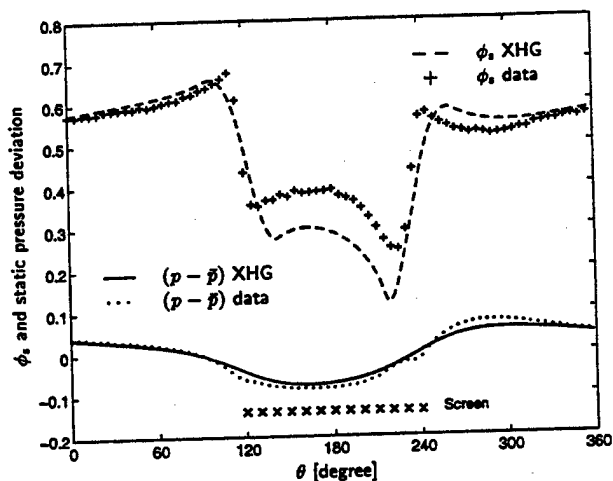


Figure 6: Steady state velocity profiles and static pressure deviations at 0.6 radii upstream of the compressor face, $\phi = 0.5$, 1.9 dynamic head distortion. Pressure is in units of $(p - \bar{p}) / (\frac{1}{2} \rho u_w^2)$.

ure 6 gives the velocity profile and static pressure distribution at the hot-wire measurement station, as well as the experimental data. The features of the measured velocity profile are captured by the model, although they are somewhat more pronounced in the model. The differences are primarily caused by the assumption that the total pressure deficit introduced by the distortion screen convects downstream without changing shape. In reality, some flow redistribution occurs, narrowing the distortion. The static pressure nonuniformity induced by the compressor $(p - \bar{p})$ is well captured.

The velocity profiles can be used to compute the pressure rise delivered by the compressor at any flow coefficient and thus to generate speed lines with distortion. Figure 7 shows the measured and predicted compressor characteristics for 0.8 and 1.9 dynamic head distortions. The 1.9 dynamic head distortion reduces the operating range by 4.3% and the compressor pressure rise by 8%.

Figure 7 also shows the uniform inlet data and the polynomial curve fit given in Table 1 and used as one of the model inputs. Both measured and predicted characteristics are terminated at the “no control” stall point. To determine the stall point using the model, an eigenvalue analysis is performed at each flow coefficient; the minimum flow coefficient for which all eigenvalues are stable is taken as the stall point.

Note how well the Hynes-Greitzer model predicts degradation in stall margin for a 0.8 dynamic head distortion. This prediction capability is by itself a valuable feature of the model. For a 1.9 dynamic head distortion, the model is less accurate. One reason may be that the compressor characteristic is steeper than predicted at flow coefficients below stall. This part of the compressor characteristic cannot be measured, so the potential error tends to increase with larger distortions, which access lower flow coefficients over part of the annulus (as shown for example in Figure 3).

4.2 Unsteady Behavior at Stall Inception (Unforced)

It is instructive to examine the unforced unsteady behavior for two reasons. First, it shows how theory-to-experiment comparisons can be made even for unforced experiments [11]. Second, however, we can see the shortcomings associated with measuring system dynamics in the noisy compressor environment without a known forcing input.

Figure 8 gives the spectrum of the zeroth and first spatial Fourier coefficient immediately prior to stall for the 1.9 dynamic head distortion. Three features can be noted in these spectra. First, the most unstable eigenvalue, represented by the resonant peak at roughly 0.42 of the rotor frequency, res-

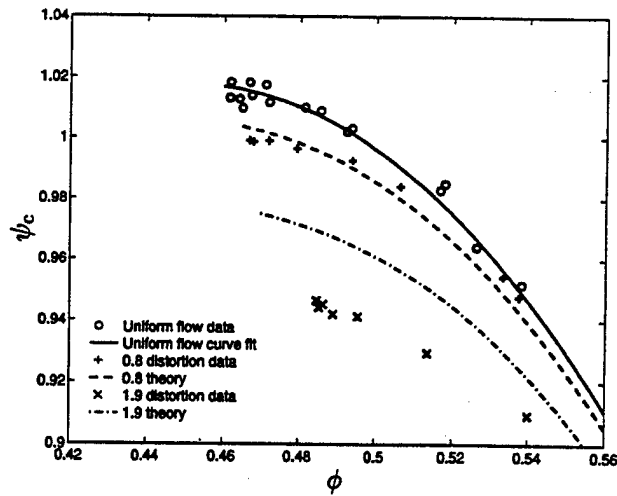


Figure 7: Compressor performance lines with uniform flow, 0.8 and 1.9 mean dynamic head distortions.

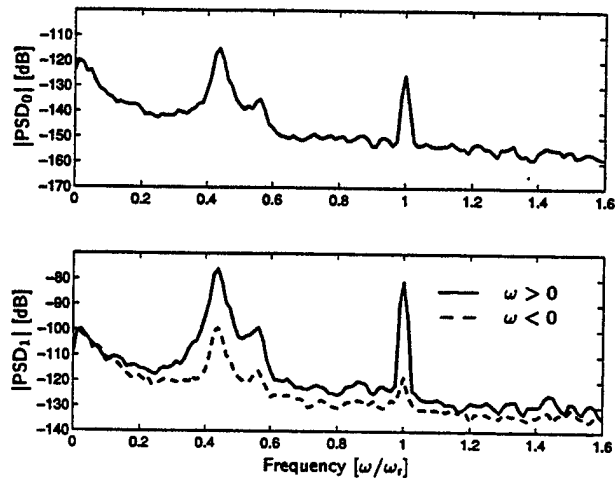


Figure 8: PSDs of $\delta\tilde{\phi}_0$ (top) and $\delta\tilde{\phi}_1$ (bottom). The PSDs at positive and negative frequencies are shown by the solid and dashed lines in the bottom figure respectively; 1.9 dynamic head distortion.

onates in both the zeroth and the first spatial Fourier coefficient. Coupling into the second and third spatial harmonic is also predicted and measured; but the fact that the zeroth spatial harmonic also participates in the mode is particularly important. This coupling of surge-type and rotating stall-type perturbations makes surge-type dynamics important in determining compressor stability. Chue et al. [2] noted

this effect, and showed that when this resonance occurs compressor stability degrades.

The second feature of note in Figure 8 is the peak at negative frequency at the frequency magnitude of the eigenvalue. As described in Tryfonidis et al. [19], this indicates that the spatial wave is oscillating in amplitude as it rotates around the annulus. The graphs in Figure 9 show why this occurs. As the spatial wave encounters the region of high flow and negative compressor slope $\frac{d\psi_c}{d\phi}$ (stabilizing), the amplitude of the wave decreases. In the region where the slope is positive (destabilizing), the wave grows. This occurs once per revolution of the wave and the resulting pulsation shows up as a negative frequency component in the spectrum. The peak of the envelope occurs approximately where the slope changes sign from positive to negative.

Figure 9 also shows the experimental envelope of RMS axial velocity fluctuation, and compares this to the RMS amplitudes given by the model. Qualitative agreement is obtained between experimental and theoretical results, but the data is quite noisy.

The third observation in Figure 8 is the large peak at rotor shaft frequency and the smaller peak at 0.58 of the rotor frequency. The peak at one rotor revolution is not predicted by the model and we associate it with a nonuniformity of the rotor blade geometry. This peak is observed in uniform flow but is more pronounced in the presence of distortion. The peak at 0.58 indicates interaction between the first mode and the rotor shaft frequency disturbance ($0.58 = 1 - 0.42$). There is also a small peak at $1.42 = 1 + 0.42$ in the PSD of the first harmonic (bottom graph of Figure 8). The interaction between the first mode and the rotor frequency is also not predicted by the model; this type of behavior is characteristic of nonlinear systems.

4.3 Input-Output Behavior of the Actuated Compressor (Forced)

A more complete comparison of model and data can be obtained by performing *forced-response experiments*. These allow the linearized dynamics to be examined as functions of both spatial and temporal frequency. Eigenvalues can be identified as the peaks

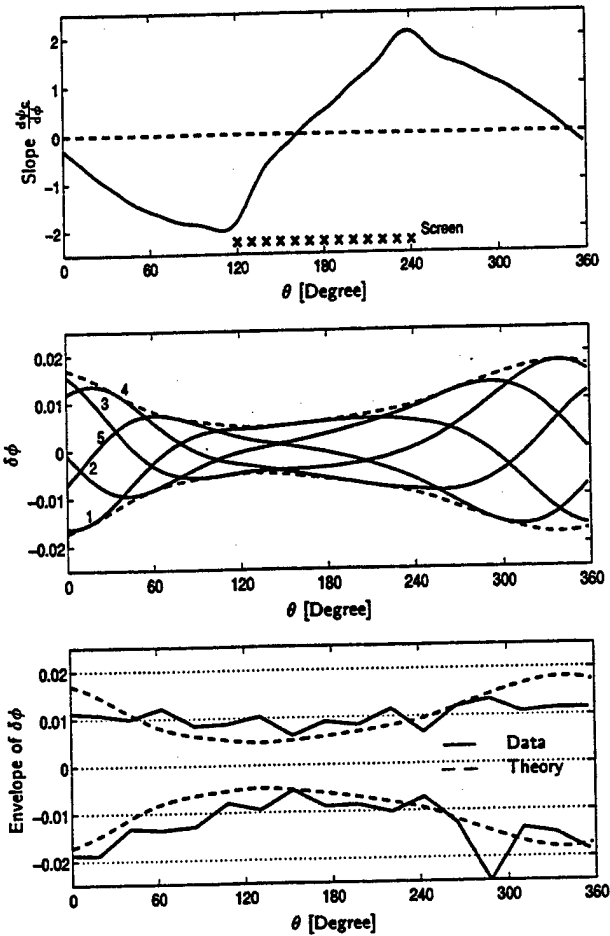


Figure 9: Slope $\frac{d\psi_c}{d\phi}$ (top), axial velocity perturbation at different points in time (middle), and analytical and measured RMS of velocity perturbations around the annulus (bottom). RMS values of the perturbations are shown for $\delta\phi > 0$ and $\delta\phi < 0$. The RMS values obtained from the different hot-wires were connected by straight lines to show the trend. 1.9 dynamic head distortion, at neutral stability point.

in the transfer functions, and cross-coupling between spatial harmonics can be quantified. The transfer function information can also be used for design of control laws.

A brief explanation of the input-output system is in order. The 12 control vane deflections represent a "wave" of actuation which forces the compressor unsteady aerodynamics. This wave can be decomposed into spatial Fourier coefficients, just as the axial ve-

locity was decomposed in Equation (1)

$$\delta\gamma(\theta, t) = \sum_{n=-3}^3 \delta\tilde{\gamma}_n(t) e^{in\theta} \quad (7)$$

where $\delta\gamma$ is the deflection from the mean position, measured in radians. Actuation of the zeroth, first, second, and third Fourier coefficient can be introduced and the responses of $\delta\tilde{\phi}_n$ ($n = 0, 1, 2, 3$) can be measured. Thus there are 16 transfer functions which can be measured and compared to the theory. Transfer functions are identified using sinusoidal excitation at discrete frequencies, to improve the signal-to-noise ratio. A full MIMO transfer function estimate is made at each frequency, regardless of whether distortion is present. See Van Schalkwyk [20] for further details on the system identification procedures.

Figure 10 gives a representative subset of the 16 identified transfer functions for a mass flow coefficient of $\bar{\phi} = 0.5$. This is approximately 17% above the stalling flow coefficient so that we expect the system to exhibit behavior that is well damped. Results for both uniform flow and inlet distortion are shown. Actuating the n th harmonic $\delta\tilde{\gamma}_n$ and measuring the m th harmonic $\delta\tilde{\phi}_m$ is denoted by $\delta\tilde{\gamma}_n \rightarrow \delta\tilde{\phi}_m$. In Figure 10 $|\cdot|$ and $\arg(\cdot)$ indicate the magnitude and phase of a transfer function respectively.

Peaks in the transfer function magnitudes indicate lightly damped modes at which the system will tend to resonate. The magnitude of the measured transfer function from $\delta\tilde{\gamma}_1 \rightarrow \delta\tilde{\phi}_1$ has a small peak at approximately $0.38\omega_r$, while the theory gives the peak at $0.40\omega_r$. The corresponding eigenvalue in the uniform flow transfer function is highly damped (although an eigenvalue is still present as indicated in the phase plot). This shows that at the same flow coefficient, distortion causes a significant decrease in damping. The peak at $0.38\omega_r$ is visible in the magnitude of the distorted flow $\delta\tilde{\gamma}_0 \rightarrow \delta\tilde{\phi}_0$ transfer function, indicating that the zeroth harmonic is also present in the first eigenmode.

Valleys in the transfer functions indicate zeros close to the $i\omega$ -axis. A zero is visible in the transfer function $\delta\tilde{\gamma}_1 \rightarrow \delta\tilde{\phi}_1$. The minimum values of the measured and theoretical transfer function magnitudes occur at $0.93\omega_r$ and $1.03\omega_r$ respectively (with

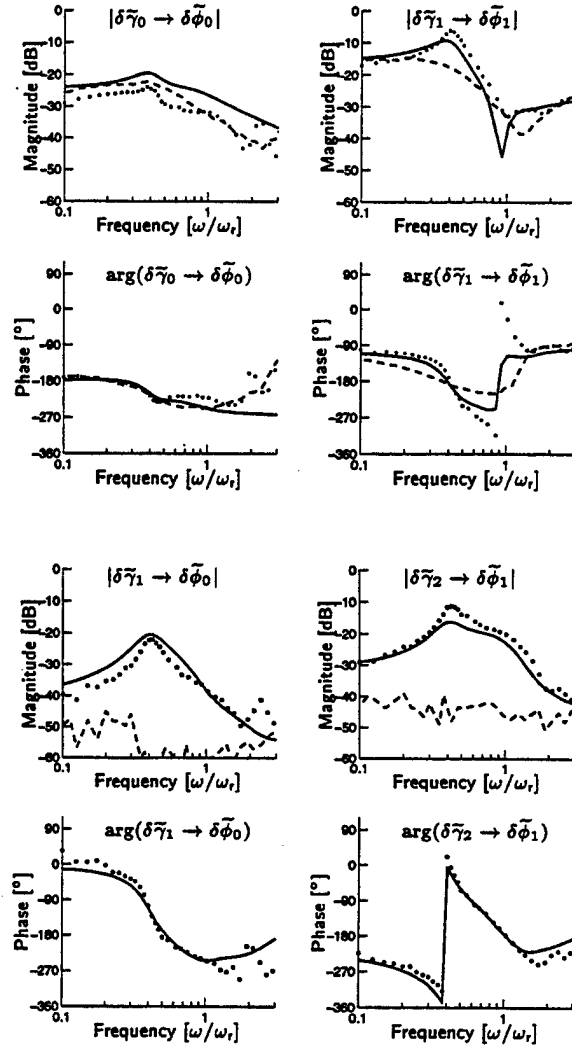


Figure 10: Transfer functions $\bar{\phi} = 0.500$, 1.9 dynamic head distortion. — = theory, distorted flow, ··· = experiment, distorted flow, --- = experiment, uniform flow.

distortion). However, for this transfer function the measured and calculated phases change abruptly¹ to within $0.05\omega_r$ and we conclude that the frequency of the zero is given accurately by the model.

Theoretically, with no distortion all coupling transfer functions (for instance, $\delta\tilde{\gamma}_2 \rightarrow \delta\tilde{\phi}_1$) are zero.

¹ Abrupt phase changes in either the positive or negative direction, as in the $\delta\tilde{\gamma}_1 \rightarrow \delta\tilde{\phi}_1$ transfer function, indicate a zero near the $i\omega$ -axis. Slight errors in the position of such zeros cause reversal in direction of the abrupt phase change.

The experimental results with uniform flow (see Figure 10 for the $\delta\tilde{\gamma}_1 \rightarrow \delta\tilde{\phi}_0$ and $\delta\tilde{\gamma}_2 \rightarrow \delta\tilde{\phi}_1$ results) show that the cross transfer functions remain at very low levels (roughly 20 dB below the distorted flow results) and show no coherent magnitude or phase behavior. This implies that the cross coupling is a feature of a linear fluid system with a non-uniform mean flow rather than an effect of nonlinearity. For the 1.9 dynamic head distortion, the amplitude of $\delta\tilde{\gamma}_2 \rightarrow \delta\tilde{\phi}_1$ is almost as large as the direct transfer function $\delta\tilde{\gamma}_1 \rightarrow \delta\tilde{\phi}_1$. Thus substantial coupling occurs between spatial harmonics, including the zeroth, so the harmonic-by-harmonic feedback control method that has been applied to undistorted cases may not be effective in distorted flow.

Finally, Figure 11 shows the predictive capability of the model across the entire operating range where transfer functions can be measured. Here, the evolution of the $\delta\tilde{\gamma}_1 \rightarrow \delta\tilde{\phi}_1$ transfer function from very stable to slightly unstable is shown. Once again the main features of the response are well captured. The eigenvalue and zero frequencies of the real system increase in frequency with respect to the model as flow coefficient is reduced, and the zero is less stable than the theory says. Nevertheless, the dynamics have been represented well enough for control purposes.

5 Features of the Control Problem with Distortion

The experimental results shown above provide a backdrop for describing active stabilization with distorted flow, particularly the challenges that exist compared to undistorted flow. There are several features of the distorted flow control problem that need to be addressed.

One of these, the coupling between spatial harmonics, has already been mentioned. In uniform flow each spatial harmonic is an eigenmode, and evolves according to a single eigenvalue equation. With distortion, however, each spatial harmonic participates in more than one eigenmode. A corollary is that commanding a given spatial harmonic in guide vane deflection affects many other spatial harmonics; the system is fully coupled and multi-input multi-output.

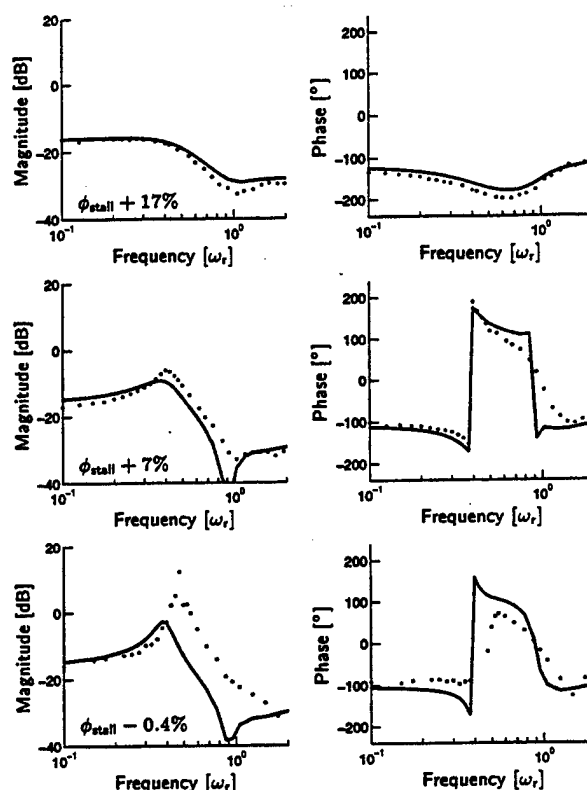


Figure 11: $\delta\tilde{\gamma}_1 \rightarrow \delta\tilde{\phi}_1$ transfer function at three different flow coefficients, 1.9 dynamic head distortion. Magnitude and phase are shown on the left and right respectively. — = theory, ... = experiment.

Feedback laws must therefore account for all spatial harmonics, including the zeroth order (surge type) disturbance, simultaneously rather than one at a time.

Another feature of distorted flow is that the poles and zeros become unstable more abruptly as a function of flow coefficient compared to uniform flow. This is because much of the compressor is experiencing flow values well below the values at which uniform inlet flow would be unstable and the local flow is strongly destabilized in this region. The most unstable pole and zero as a function of distortion extent are shown in Figure 12, based on results of the model described earlier. We see that the pole is unstable (positive real part) over a large range of distortion extents.

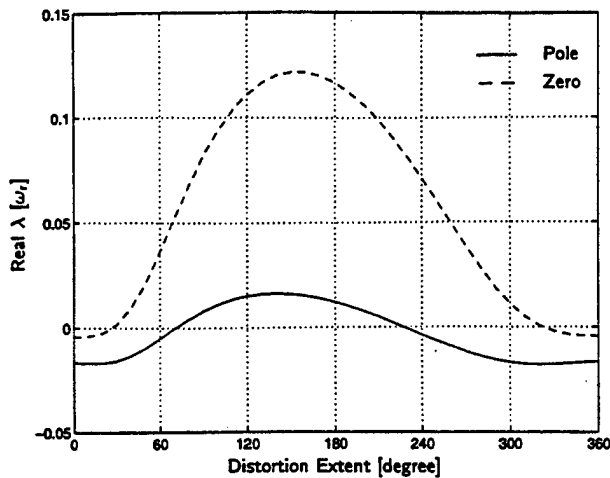


Figure 12: Effect of distortion extent on the most unstable pole and dominant zero, $\bar{\phi} = 0.465$, 1.9 dynamic head distortion. Results from model.

Also shown in Figure 12 is the zero location associated with the multi-input multi-output transfer function. This zero has a positive real part, and is known as a “nonminimum phase zero.” Such zeros severely degrade the ability of feedback control to stabilize the system [3]. Although this zero location depends on the choice and placement of actuators and sensors, the main issue is that for the actuator/sensor configuration used here distortion degrades the control problem.

Distortion also appears to have an impact on the background noise level in the compressor, perhaps due to the part of the annulus operating at positive slope amplifying random fluctuations in the flow. Whatever the cause, the RMS of random axial velocity fluctuations with 1.9 dynamic head distortion are about twice those in uniform flow. Increased noise levels cause the actuators to work harder than they otherwise would, and make determining the location and size of unstable waves more difficult. They also increase the likelihood of nonlinear events which are not accounted for in the control law design procedure.

The final feature of the control problem with inlet distortion is its spatial character. With uniform flow, the circumferential orientation of the compressor is arbitrary and control laws do not depend on orientation with θ . Inlet distortion creates a definite

spatial orientation so that a control policy different from that used in uniform flow may be necessary. Distortion control laws must account for both the orientation of the disturbance wave *and* the orientation of the inlet distortion. Further, a control law which depends on the distortion profile must maintain some “robustness” to its orientation and shape, because these typically are not well known.

6 Control Law Design and Implementation

The results of the model-to-data comparisons imply that a first-cut control law can be designed based on the physical description provided by the model. A control law was thus designed using the Linear Quadratic Gaussian (LQG) design approach [9]. This approach was successful at stabilizing rotating stall, but because of the inherent lack of robustness in such control law designs, performance was poor. The mass flow operating range extension afforded by LQG control was 1.1%, or 26% of the operating range lost due to a 1.9 dynamic head distortion. For a 0.8 dynamic head distortion the LQG controller increased the stable flow range 1.5% below the open loop undistorted flow stall point.

The primary drawback of an LQG control law (or any direct model-based control law) is sensitivity — one must know the circumferential location, magnitude, and extent of the inlet distortion before a control law can be enacted. The LQG controller maintained its performance for an 80 degree range of distortion locations but outside this range, the control law actually destabilized the system.

One therefore expects a trade-off between range extension and insensitivity to distortion location. Table 2 lists the control laws tested in order of sensitivity to distortion location. The poor performance of LQG control reflects its sensitivity to other modeling errors as well.

The next control law shown is the SISO harmonic feedback (HF) controller experimentally optimized by Haynes [7], with additional cross-feed channels introduced to account for coupling between harmonics. This controller will be referred to as harmonic feedback plus coupling (HFC). Figure 13 gives

Table 2: Stable Operating Range Increase of Various Control Laws, 0.8 Dynamic Head Distortion.

Type of Control	Range Increase
Linear Quadratic Gaussian	1.5%
Cross-Coupled Harmonic Feedback	3.0%
SISO Harmonic Feedback	2.2%
Distributed Feedback	3.7%

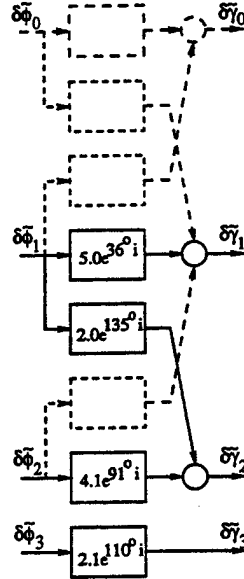


Figure 13: Cross-coupled harmonic feedback control law. Cross coupling between harmonics that did not lower the stalling flow coefficient are shown with dashed lines.

a functional block diagram as well as numerical values for the control scheme used. The cross-feed channels introduce coupling with a spatial orientation. This control law is thus also sensitive to distortion location, although it might be considered less sensitive than LQG control because fewer cross-feeds exist than in the LQG controller.

To arrive at the HFC gains in Figure 13, a procedure similar to that employed by Haynes was used. Gains are initially chosen to be as high as possible without saturating the system. Then the phases are chosen by experimentally testing the range extension afforded by each choice of phase. The feedback paths are added sequentially, and each one is optimized

with the preceding gains fixed. Experience and additional experiments govern the order that feedback paths are added. In this case the direct gains are optimized first, followed by the cross-feed gains. Attempts were made at optimization of several other cross-feed channels, but no additional range extension was provided by these. Final gain adjustments are made after the phase optimization.

This controller's performance can be compared to the original SISO harmonic feedback controller designed by Haynes [7], which would be represented by Figure 13 with all cross-feed channels set to zero. This control law is completely insensitive to distortion location but, because it does not account for coupling, is not as effective as the cross-coupled control law. (See Table 2.)

The final control law, termed distributed feedback (DF), measured the entire shape of the disturbance $\delta\phi(\theta)$, and fed back a rotated and amplified version of it to the actuators (see Figure 14.) The specific formulation was

$$\delta\gamma(\theta) = k\delta\phi(\theta - \beta) \quad (8)$$

where the gain k and rotation angle β are design variables. These variables are optimized in the same fashion as the gains and phases in the HFC control law: gain is fixed by saturation considerations, and stalling mass flow reduction is then tested for a complete sequence of β 's. This is followed by gain adjustment tests at the optimized β .

The gain tuning procedure is less tedious than the HFC procedure because only two parameters need to be optimized. This control law has several other advantages. It is a fixed rather than dynamic controller, thus simply implemented. It is insensitive to the location of the distortion. According to simulation studies, it is also insensitive to the type of distortion introduced. This control law performed as well or better than any other control law tested.

Figure 15 summarizes the range extensions obtained with the different controllers for the 0.8 and the 1.9 dynamic head distortions. The uniform flow stall flow coefficient (without control) is indicated by the dashed line. The lowest flow coefficient at which Haynes [7] stabilized this compressor in uniform flow ($\phi = 0.42$) is also indicated. For the 0.8

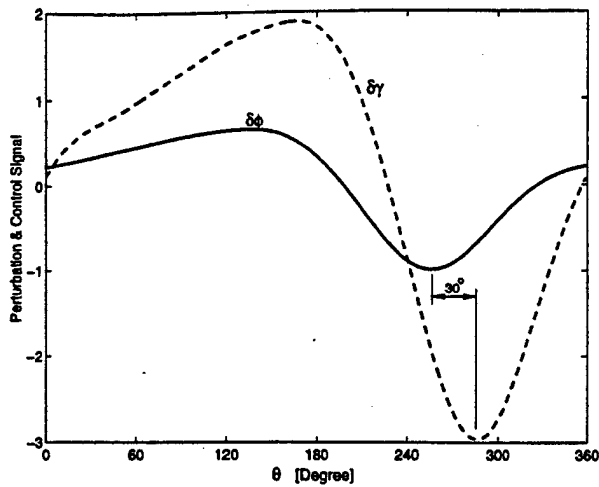


Figure 14: Distributed feedback control signal for a typical velocity perturbation. Gain $k = 3$, spatial phase shift $\beta = 30^\circ$.

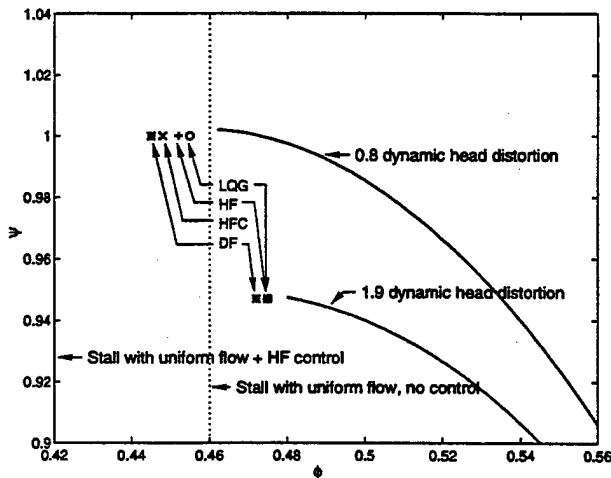


Figure 15: Measured compressor performance for 0.8 and 1.9 dynamic head distortions and various control laws (Note: no HFC results exist for 1.9 dynamic head distortion). Each symbol represents the minimum flow coefficient obtained using the indicated control law.

dynamic head distortion the range extension was approximately 43% of the extension obtained for uniform flow.

The effectiveness of the DF controller is also characterized by comparing the open and closed loop PSDs of the zeroth and first harmonics in Figure 16.

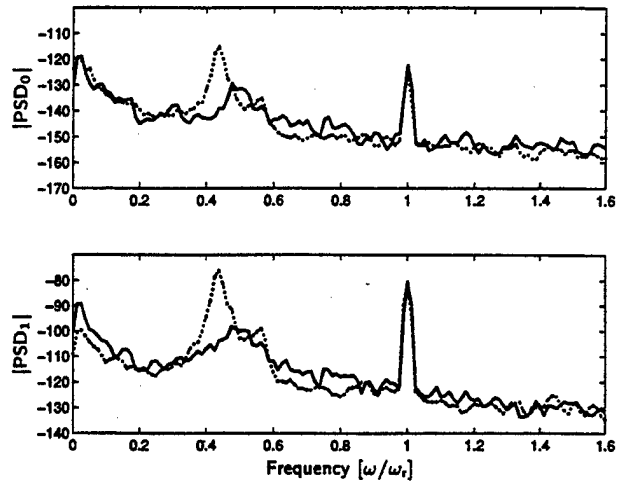


Figure 16: PSDs immediately prior to stall inception, with and without control. \cdots = open loop PSD, $—$ = closed loop PSD for DF controller, 0.8 dynamic head distortion.

Both PSDs were taken immediately prior to stall, to show the pre-stall behavior of the system. Thus the closed-loop PSDs are at a lower flow coefficient. Even at this more unstable condition, the DF controller suppressed the zeroth and first harmonics of the first mode by approximately 15 and 23 dB respectively.

The distributed feedback controller was both the best performer and the most insensitive to distortion type and location. Because the measured shape of the perturbation is used, this control law takes into account cross-feed effects while remaining insensitive to distortion location. The structure is also compatible with nonlinear behavior; as perturbations become larger and more localized, the control law responds accordingly.

7 Summary and Conclusions

The experiments reported in this paper represent the first systematic attempt to apply system identification and control theory to a compressor with circumferential inlet distortion. The behavior of such a dynamic system is qualitatively different than that of compressors in uniform flow and thus requires a different control strategy and approach.

Active control has been demonstrated to stabilize rotating stall with inlet distortion, extending

the stable operating range of the compressor. Using our validated model, we can also show that the distributed feedback (DF) controller is insensitive to both the size and location of the distortion. Of course, our study is limited to 2D distortions, the system is incompressible, and the surge dynamics are relatively stable in this system. Also, the effects of rotating or otherwise unsteady distortions, which may be significant, were not considered.

Based on theory-experiment comparisons of (i) distortion profiles, (ii) compressor characteristics, (iii) unforced transients, (iv) eigenvalues, (v) transfer functions, and (vi) the effect of stabilizing control, the extended Hynes-Greitzer distortion model was found to be adequate to both describe phenomenology and to design control laws. Thus a tool exists for investigating extensions and different implementations. The predictions of the model were found to be accurate enough to allow working LQG control laws to be successfully implemented.

Other control laws, however, were found to have better performance. In particular, a new distributed feedback control law was introduced which achieves the best overall performance, extending the stable operating range by 3.7% for a worst case, practical distortion ($DC(60)=0.53$). Using this control law, approximately 40% of the operating range lost due to a 1.9 dynamic head ($DC(60)=1.31$) total pressure distortion was regained using active control.

Much extension of this technology is required to impact a real system. For instance, additional research is required to understand the physical limitations that determine maximum range extension. In addition, robustness to distortion as a (possibly three-dimensional) unsteady disturbance, the effects of lightly damped surge dynamics, and implementation in a high speed compressor must all be addressed. The results here indicate that the modeling and control concepts used are valuable for addressing these issues.

8 Acknowledgments

This work was conducted under AFOSR Grant F49620-93-1-0032, Dr. James McMichael technical manager, and ONR Grant N00014-91-J-1575,

Dr. Eric Hendricks technical monitor. This support is gratefully acknowledged. We also acknowledge the help of Dr. J. P. Longley and Mr. Y. F. Gong at different stages in this research.

References

- [1] F. Aulehla and D.M. Schmitz. New Trends in Intake/Engine Compatibility Assessment. In *AGARD-CP-400: Engine Response to Distorted Inflow Conditions*, March 1987.
- [2] R. Chue, T.P. Hynes, E.M. Greitzer, C.S. Tan, and J.P. Longley. Calculation of Inlet Distortion Induced Compressor Flow Field Instability. *International Journal of Heat and Fluid Flow*, 10(3):211-233, September 1986.
- [3] J.S. Freudenberg and D.P. Looze. Right Half Plane Poles and Zeros and Design Tradeoffs in Feedback Systems. *IEEE Transactions on Automatic Control*, 30(6), June 1985.
- [4] E.M. Greitzer, A.H. Epstein, G.R. Guenette, D.L. Gysling, J. Haynes, G.J. Hendricks, J.D. Paduano, J.S. Simon, and L. Valavani. Dynamic Control of Aerodynamic Instabilities in Gas Turbine Engines. *Steady and Transient Performance Prediction of Gas Turbine Engines*, AGARD-LS-183, pages 8-1-8-21, May 1992.
- [5] G. Gu, S. Banda, and A. Sparks. An Overview of Rotating Stall and Surge Control for Axial Flow Compressors. Technical report, Wright-Patterson, November 1995. Private communication.
- [6] J.M. Haynes. Active Control of Rotating Stall in a Three-Stage Axial Compressor. Master's thesis, Department of Aeronautics and Astronautics, MIT, 1993.
- [7] J.M. Haynes, G.J. Hendricks, and A.H. Epstein. Active Stabilization of Rotating Stall in a Three-Stage Axial Compressor. *ASME J. of Turbomachinery*, 116:226-239, 1994.
- [8] T.P. Hynes and E.M. Greitzer. A method for assessing Effects of Circumferential Flow Distortion on Compressor Stability. *ASME J. of Turbomachinery*, 109:371-379, July 1987.

- [9] H. Kwakernaak and R. Sivan. *Linear Optimal Control Systems*. Wiley-Interscience, 1972.
- [10] P. L. Lavrich. *Time Resolved Measurements of Rotating Stall in Axial Flow Compressors*. PhD thesis, Department of Aeronautics and Astronautics, MIT, August 1988. Also available as Gas Turbine Lab Report #194.
- [11] J.P. Longley. *Inlet Distortion and Compressor Stability*. PhD thesis, Trinity College, Cambridge University, 1988.
- [12] J.P. Longley. A Review of Nonsteady Flow Models for Compressor Stability. *ASME J. of Turbomachinery*, pages 202-215, April 1994.
- [13] J.P. Longley and E.M. Greitzer. Inlet Distortion Effects in Aircraft Propulsion System Integration. *Steady and Transient Performance Prediction of Gas Turbine Engines, AGARD-LS-183*, pages 6-1 - 6-18, May 1992.
- [14] F.K. Moore. A Theory of Rotating Stall of Multistage Axial Compressors: Part I — Small Disturbances. *ASME J. of Engineering for Gas Turbines and Power*, 106:313-320, April 1984.
- [15] F.K. Moore. A Theory of Rotating Stall of Multistage Axial Compressors: Part II — Finite Disturbances. *ASME J. of Engineering for Gas Turbines and Power*, 106:321-326, April 1984.
- [16] F.K. Moore and E.M. Greitzer. A Theory of Post-Stall Transients in Axial Compressors: Part I — Development of the Equations. *ASME J. of Engineering for Gas Turbines and Power*, 108:68-76, 1986.
- [17] J.D. Paduano, A.H. Epstein, L. Valavani, J.P. Longley, E.M. Greitzer, and G.R. Guenette. Active Control of Rotating Stall in a Low-Speed Axial Compressors. *ASME J. of Turbomachinery*, 115:48-56, January 1993.
- [18] C. Reid. The Response of Axial Flow Compressors to Intake Flow Distortion. *ASME paper 69-GT-29*, 1969.
- [19] M. Tryfonidis, O. Etchevers, J.D. Paduano, A.E. Epstein, and G.J. Hendricks. Pre-Stall Behavior of Several High-Speed Compressors. In *ASME Gas Turbine and Aeroengine Congress and Exposition, The Hague, The Netherlands*, June 1994.
- [20] C.M. van Schalkwyk. *Active Control of Rotating Stall with Inlet Distortion*. PhD thesis, Department of Aeronautics and Astronautics, MIT, June 1996. Also available as Gas Turbine Lab Report #222.
- [21] D.D. Williams. Engine Compatibility. Technical report, Rolls-Royce PLC, May 1991.

Semi-Active Stabilization of Axial Compressors with Circumferential Inlet Distortion using Low Bandwidth Actuators*

C.M. van Schalkwyk, R.K. Mehra

Scientific Systems Co., Inc.

Woburn MA 01801

J.D. Paduano

Department of Aeronautics and Astronautics

Massachusetts Institute of Technology

Cambridge MA 02139

Abstract

This paper discusses a new method to increase the stable operating range of a compressor operating in the presence of large total pressure inlet distortion by using low bandwidth actuators. A stabilization criterion is defined and an algorithm for finding the optimal control law is presented. Practical issues related to the implementation of the ideal distributed actuators are discussed and additional results are presented for currently available actuators.

1 Introduction

The operating range of compression systems are subject to aerodynamic instabilities that limit the range over which safe operation is possible. As the mass flow through the compressor is decreased, the peak pressure rise across the compressor increases until a point is reached where the flow through the compressor becomes unstable. The amplitudes of these unstable oscillations are very large and can cause damage to the engine. In addition, the loss of stability is accompanied by a significant loss in pressure rise.

Two types of aerodynamic instabilities are commonly observed in compression systems. The first, called surge, is a mainly axisymmetric, system-type instability. The second instability, called rotating stall, has the form of a stall cell that rotates around the annulus at a fraction of the rotor speed. Rotating stall often starts out as a small perturbation wave that travels around the annulus, grows in amplitude, and finally develops into a large amplitude limit cycle, called rotating stall. Due to hysteresis

the only way to stop this limit cycle oscillation is to increase the mass flow significantly beyond the point where stall occurred. Whether the compressor surges or stalls depends on the specific system geometry and configuration Greitzer [5]. A review of axial compressor stall phenomena is given by Greitzer [4]. Because of these instabilities operation near the unstable region must be avoided. However, this margin of safety forces operation at mass flows that deliver lower than the maximum peak pressure rise. If the flow through the compressor is circumferentially or radially nonuniform the pressure rise across the compressor decreases. In addition, the compression system goes unstable at higher mass flows. This nonuniform flow is also called distortion.

Epstein et al. [3] suggested that active control could be used to increase the stable operating range of compression systems. We refer to the survey paper by Greitzer et al. [6] for a discussion of various experiments and concentrate here only on the control of rotating stall. Model validation and control of rotating stall in the presence of large total pressure inlet distortion was first performed by Van Schalkwyk et al. [13] on a low speed three-stage compressor at MIT. System identification procedures were used to examine the dynamic behavior of the disturbance modes in the compressor. Their research showed that the dynamics of small velocity perturbations were accurately predicted by the Hynes-Greitzer model [8], extended to include unsteady viscous effects [11]. The frequencies of the controlled modes are typically in the order the rotor frequency and thus high bandwidth actuators are needed for control.

The objective of this research is to show that it is possible to increase the stable operating range of

*This work was supported by ONR Contract nr. N00014-96-C-0127

a compressor operating in the presence of large total pressure inlet distortion by using low bandwidth actuators. The paper is structured as follows. The modeling assumptions are stated in Section 2. The solution to the nonlinear partial differential equations and optimization of the compression system stabilization is discussed in Section 3. Several actuator configurations are discussed in Section 4 which also presents the main results. A summary is given in Section 5.

2 Compression System Modelling

We will study the compression system shown schematically in Figure 1. The system consists of a distortion screen, long upstream duct, injection valves, a compressor, bleed valves, downstream duct, plenum, and throttle. Actuation upstream of the

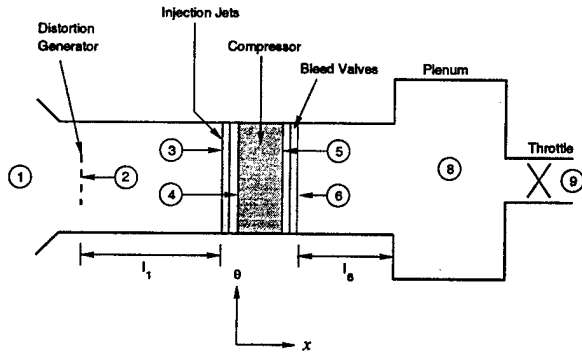


Figure 1: Compression System.

compressor is modeled as a circumferentially distributed valve through which air is injected axially into the annulus. See [7] for further discussion. Actuation downstream of the compressor is modeled as a circumferentially distributed bleed valve through which air is removed from the annulus [7].

The equation describing the steady state is obtained by writing a pressure balance for the compression system

$$d + \left[\left(1 + \frac{1}{2} \gamma_{is} \right) \phi_i - \phi_s^{(4)} \right] \phi_i \gamma_{is} + \psi(\phi_s) - \mu_r \frac{\partial \phi_s}{\partial \theta} + (\phi_s^{(4)} - \phi_b \gamma_{bs}) - \frac{1}{2} k_t \tilde{\phi}_{s0}^2 = 0 \quad (1)$$

where the distortion $d = d(\theta)$, ϕ is the flow coefficient, ψ the pressure rise characteristic, ϕ_i and ϕ_b the injection and bleed velocities, γ_{is} and γ_{bs} are

the steady state control, and k_t the throttle constant. For simplicity we will write Equation (1) as $f_s(\phi, \gamma) = 0$ to indicate that the main variables of interest are the flow ϕ and control γ .

3 Optimal Stabilizing Control

There are several measures that can be used to determine the "best" control law that increases the tolerance of the compressor to inlet distortion. Schulmeyer [10] used a linearized model of the compression system to determine the guide vane re-stagger angle that would minimize the velocity perturbation. Experimental results showed that the nonuniformity of the flow around the annulus was decreased but no improvement in the stalling flow coefficient was obtained.

Distortion introduces strong coupling between the various harmonics of the traveling rotating stall wave and one may design the control law so as to minimize the coupling between the harmonics. It is, however, not clear how to quantify this coupling.

Hynes and Greitzer [8] and Chue et al. [2] found that the mass flow at which the integrated mean slope (IMS) of the compressor characteristic is equal to zero, approximately corresponds to the point where the compression system loses stability. It is also well known that, for uniform flow, the system is stable when the IMS is less than zero. An alternative criterion would thus be to minimize the IMS. However, Longley [9] and Van Schalkwyk [11] showed that the IMS is not an accurate indicator of the stability of the system. In addition, if the compressor pressure rise characteristic is given by a parabola the same value of the IMS is always obtained at a given mass flow irrespective of the circumferential shape of the mass flow [12].

When the distortion changes slowly the real parts of the eigenvalues are good indicators of the stability of the system. Here, slowly means that the rate at which the magnitude and extent of the distortion (and thus the steady flow) changes is at least an order of magnitude smaller than the frequency of the rotating stall wave. Inlet distortion are typically caused by high angle-of-attack maneuvers, and thus changes at a rate of order 1 Hz. This is an order lower than the rotating stall wave which typically travels at 50% of the rotor speed. Therefore, for typical distortions caused by take-off and maneuvers the flow through the compressor can be considered steady and we can use the dynamics of small perturbations to determine the stability of the compression system. Once we have found the optimal stabilizing

control for a specific distortion, we can update the control recursively as the distortion changes. The actuator bandwidth is thus determined by the slow rate of change of the distortion. This is the criterion that will be used and will be described in more detail in the following paragraphs.

The optimization criterion can be described loosely as

$$\gamma^* = \min_{\gamma \in \gamma_f} \sum_k \text{re}(\lambda_k), \quad k = 0, 1, 2 \quad (2)$$

where γ^* is the optimal control, γ_f is the set of feasible controls, λ_k is the eigenvalue corresponding to the k th mode, and $\text{re}(\cdot)$ is the real part.

Analysis of this criterion showed that high frequency modes (second, third, etc.) were stabilized easier and at the cost of the dominant low frequency modes. It was further found that the eigenvalues corresponding to the zeroth and first modes had a tendency to coalesce which is not desirable as it increases the possibility for an engine to surge [2]. We thus modify the cost function by minimizing the distance between the dominant eigenvalues and a set of desired eigenvalues, that is

$$\gamma^* = \min_{\gamma \in \gamma_f} \sum_k w_k^2 |\lambda_k - \lambda_{dk}|^2 \quad (3)$$

where w_k and λ_{dk} is the k th relative weight and desired eigenvalue respectively. The desired locations are chosen so that the eigenvalues of the zeroth and first modes do not coalesce.

The optimization posed in the last equation is a constrained minimization problem. Standard algorithms exist to solve such problems but it was found that they are extremely slow to converge or did not converge at all. The criterion was thus modified by including the bounds on the control signal into the cost function by means of a barrier function. A barrier function $b(\gamma)$ penalizes the control γ whenever it is outside its minimum and maximum values and (ideally) is zero when the control is inside the allowable range. The barrier function used for the study is shown in Figure 2. The criterion now becomes

$$\gamma^* = \min_{\gamma} \sum_k w_k^2 |\lambda_k - \lambda_{dk}|^2 + [b(\gamma)]^2. \quad (4)$$

The optimization algorithm is summarized below.

Optimization Algorithm

1. Initialization

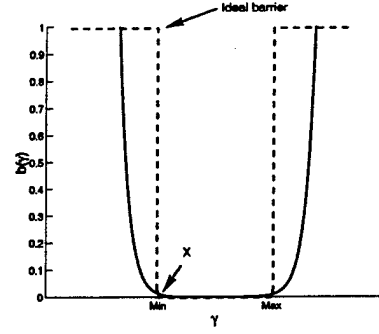


Figure 2: Approximate and ideal barrier function.

- (a) Select distortion magnitude and extent
- (b) Select throttle constant k_t
- (c) Select modes numbers to stabilize
- (d) Select desired eigenvalues λ_{dk} & weights w_k
- (e) Select initial guess γ_0
- (f) Select initial guess ϕ_0 (does not have to satisfy $f_s(\phi_0, \gamma_0) = 0$)

2. Compute admissible ϕ_{0a} so that $f_s(\phi_{0a}, \gamma_0) = 0$

3. Repeat the following steps until optimization converged

- (a) Compute new estimate for γ
- (b) Compute admissible steady flow such that $f_s(\phi, \gamma) = 0$ using ϕ_{0a} as initial guess
- (c) Linearize system about (ϕ, γ)
- (d) Compute eigenvalues λ_k
- (e) Compute barrier function $b(\gamma)$
- (f) Compute cost = $\sum_k w_k^2 |\lambda_k - \lambda_{dk}|^2 + [b(\gamma)]^2$

4 Results

Unless stated otherwise, all the results are for distributed actuators, and the mass flow used for actuation is limited to 5% of the mean mass flow through the compressor. In all the cases a 0.8 dynamic head distortion with an extent of 120° is used. This magnitude of the distortion was chosen to be representative of large distortions encountered in practical situations, and the extent was chosen to be close to the worst case extent for the particular compressor being studied [11]. We present only a subset of the results here and refer the reader to [12] for a detailed presentation.

4.1 Upstream Injection

In this configuration we assume a distributed valve is injecting air directly upstream of the compressor as shown in Figure 1. The results of the optimization is shown in Figures 3 to 4, which we discuss next.

Figure 3 shows the eigenvalues for the zeroth, first, second, and third modes. The eigenvalues for

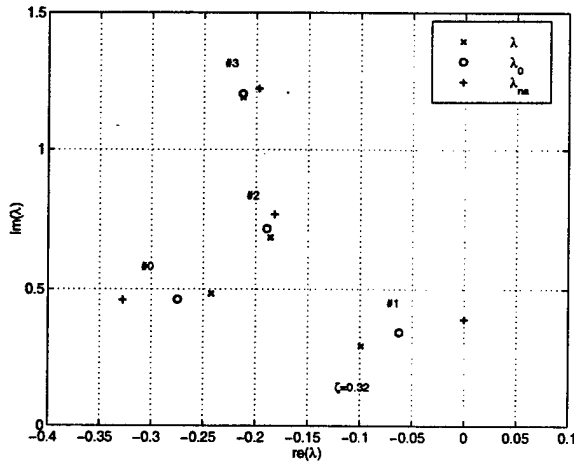


Figure 3: Eigenvalues for upstream injection.

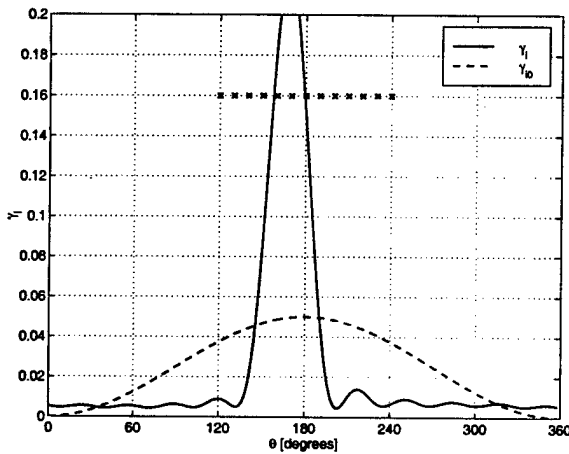


Figure 4: Upstream injection profile.

no actuation λ_{na} is indicated by +. The eigenvalues λ_0 associated with initial guess γ_{i0} is indicated by o, and the optimal values of λ are indicated by x. The corresponding mode numbers are also shown in the vicinity of the eigenvalues. The eigenvalue associated with the first mode that used to be marginally stable has been moved well into the left half plane. Thus,

the system has been stabilized by steady injection upstream of the compressor. The equivalent damping of the optimally stabilized mode is $\zeta = 0.32$. This figure clearly indicates that the stability of the three cases are different even though the IMSs are exactly the same. Stabilization of the first mode came at the expense of the stability of zeroth mode. The eigenvalue associated with the zeroth mode has moved towards the right by almost the same distance that the first mode eigenvalue has moved towards the left. This "stabilizing the first mode/destabilizing the zeroth mode" was found to be a general rule. If the weighting on the second mode is set to zero in the cost function, stabilization of the first mode would have a destabilizing effect on the second mode as well. This was considered undesirable as the second mode is already lightly damped and an additional decrease in its damping would result in large velocity perturbations around the annulus which may result in non-linear behavior that can trigger stall. The optimum injection profile and initial guess γ_{i0} are shown in Figure 4. The injection is concentrated close to the center of the distortion and is much narrower than the distortion. The action of the control can be explained as follows. If a partially blocked passage in the rotor moves through the region of concentrated injected air, the passages will be cleared by the high velocity air. Therefore, a stall cell will never be able to complete a full path around the annulus so that rotating stall is prevented. The narrow width of the control signal suggests that a single discrete valve may be suitable to stabilize the compressor in the presence of a known distortion. This possibility will be investigated in Section 4.4.

4.2 Downstream Bleeding

In this configuration we assume a distributed valve through which mass is removed directly downstream of the compressor as shown in Figure 1. The eigenvalue associated with the first mode has again been stabilized [12]. The amount that the eigenvalue moved into the left half plane is about half of that obtained with upstream injection. With bleeding, the damping of the first mode is $\zeta = 0.18$ whereas the corresponding number for injection is $\zeta = 0.32$. This clearly shows the superior performance of upstream injection to downstream bleeding.

4.3 Combined Upstream Injection/ Downstream Bleeding

In combined injection/bleeding the upstream injection valves and downstream bleed valves are used at the same time. Both the profiles are free for opti-

mization, that is, the upstream injection profile is allowed to be different from the downstream bleed profile. This is the maximum freedom allowed by the configuration. The eigenvalues associated with the first three modes are shown in Figure 5. The damping of the first mode is $\zeta = 0.39$. The combination of upstream injection and downstream bleeding gives the best stabilization of the configurations considered so far.

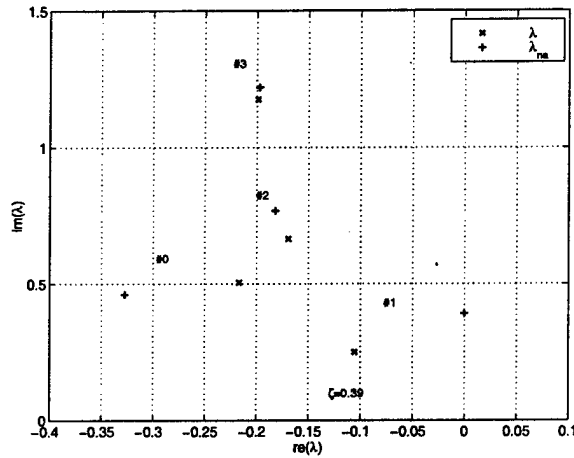


Figure 5: Eigenvalues for upstream injection/downstream bleeding.

4.4 Discrete Actuators with Recirculation

We have seen in Section 4.1 that the optimal profile for upstream injection was a narrow jet. For downstream bleeding the optimum profile was also narrower than the distortion extent, although it was not as narrow as that of the upstream jet. This suggests that it may be possible to use a small number (one or two) of discrete actuators rather than a large number of discrete actuators that approximates an ideal distributed actuator. Even though the optimal profile for downstream bleeding is not as narrow as the upstream profile, we will also use a small number of discrete bleed valves. This approach is very important from a practical view as it is cost effective and adds little weight. Further more, because we are again considering low bandwidth actuators, reliable, existing, off-the-shelf components can be used. The formulation of the discrete actuator problem is completely different from the previous optimal stabilization formulations. Now we simply choose a set of upstream and downstream jets and determine the stabilization that can be obtained with the configura-

tion. The only optimization that is done is that of determining the optimal location of the jets. Only recirculation is considered as it is the most practical configuration. The width of the jets has been chosen to be representative of the valve designed by Berndt [1]. The recirculated mass flow is still restricted to be 5% of the mass flow through the compressor. Analysis showed that the best location for the discrete actuator is at the center of the distortion. The eigenvalues associated with the first three modes are shown in Figure 6. The eigenvalue associated with the first

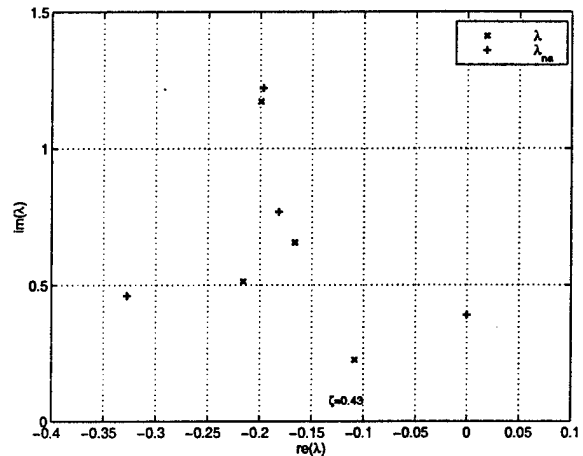


Figure 6: Eigenvalues for discrete actuator recirculation.

mode has been stabilized very well. The damping of the first mode is $\zeta = 0.43$, whereas the damping for optimal injection/bleeding is 0.39. This is surprising as more damping has been achieved through recirculation from a discrete actuator compared to optimal upstream injection/downstream bleeding with ideal distributed actuators. This apparent paradox is explained in [12].

The results of the various actuation configurations are summarized in Figure 7. In this figure we display the stalling flow coefficients and associated pressure rises at stall for a 0.8 dynamic head distortion with an extent of 120° . For all the configurations the stable operating range has been increased. The discrete recirculation actuator gives the highest pressure rise at the lowest stalling flow coefficient of all the configurations. This is followed by combined upstream injection/downstream bleeding (both profiles free), and then upstream injection. Also shown in the figure are stall lines with and without control. The area between the two lines are the increase in stable operating range that can be achieved with discrete

actuator recirculation. This figure clearly shows the effectiveness of steady actuation to increase the stable operating range of a compressor operating in the presence of distortion.

5 Summary

The results presented showed that it is possible to increase the stable operating range of a compressor operating in the presence of large total pressure inlet distortion by using low bandwidth actuators. The analysis showed that the optimal placement of a discrete actuator is at the center of the distortion and that the same degree of stability can be obtained as in distributed injection/bleeding.

References

- [1] Roland G. Berndt, Harald J. Weigl, James D. Paduano, and Alan H. Epstein. Experimental Techniques for Actuation, Sensing, and Measurement of Rotating Stall Dynamics in High Speed Engines. In James D. Paduano, editor, *Sensing, Actuation, and Control in Aeropropulsion*, volume 2492. SPIE, April 1995.
- [2] R. Chue, T.P. Hynes, E.M. Greitzer, C.S. Tan, and J.P. Longley. Calculation of Inlet Distortion Induced Compressor Flow Field Instability. *International Journal of Heat and Fluid Flow*, 10(3):211–233, September 1986.
- [3] A.H. Epstein, J.E. Williams, and E.M. Greitzer. Active Suppression of Aerodynamics Instabilities in Turbomachines. *J. of Propulsion*, 5(2):204–211, March-April 1989.
- [4] E.M. Greitzer. Review — Axial Compressor Stall Phenomena. *ASME J. of Fluids Engineering*, 102:134–151, June 1980.
- [5] E.M. Greitzer. The Stability of Pumping Systems — the 1980 Freeman Scholar Lecture. *ASME J. of Fluids Engineering*, 103:193–243, 1981.
- [6] E.M. Greitzer, A.H. Epstein, G.R. Guenette, D.L. Gysling, J. Haynes, G.J. Hendricks, J.D. Paduano, J.S. Simon, and L. Valavani. Dynamic Control of Aerodynamic Instabilities in Gas Turbine Engines. *Steady and Transient Performance Prediction of Gas Turbine Engines*, AGARD-LS-183, pages 8-1–8-21, May 1992.
- [7] D.L. Gysling. *Dynamic Control of Rotating Stall in Axial Flow Compressors Using Aeromechanical Feedback*. PhD thesis, Department of Aeronautics and Astronautics, MIT, 1993.
- [8] T.P. Hynes and E.M. Greitzer. A method for assessing Effects of Circumferential Flow Distortion on Compressor Stability. *ASME J. of Turbomachinery*, 109:371–379, July 1987.
- [9] J.P. Longley. *Inlet Distortion and Compressor Stability*. PhD thesis, Trinity College, Cambridge University, 1988.
- [10] A. Schulmeyer. Enhanced Compressor Distortion Tolerance using Asymmetric Inlet Guide Vane Stagger. Master's thesis, Department of Aeronautics and Astronautics, MIT, 1989.
- [11] C.M. van Schalkwyk. *Active Control of Rotating Stall with Inlet Distortion*. PhD thesis, Department of Aeronautics and Astronautics, MIT, June 1996. Also available as Gas Turbine Lab Report #222.
- [12] C.M. Van Schalkwyk, R.K. Mehra, and J.D. Paduano, J. Active Feedback Control of Rotating Stall and Surge in Axial Flow Compressors with Inlet Distortion. Technical report, Scientific Systems Co., Inc., March 1997.
- [13] C.M. Van Schalkwyk, J.D. Paduano, E.M. Greitzer, and A.H. Epstein. Active Stabilization of Axial Compressors with Circumferential Inlet Distortion. In *ASME Gas Turbine and Aeroengine Congress and Exposition, (Turbo Expo '97)*, Orlando, FL, June 1997.

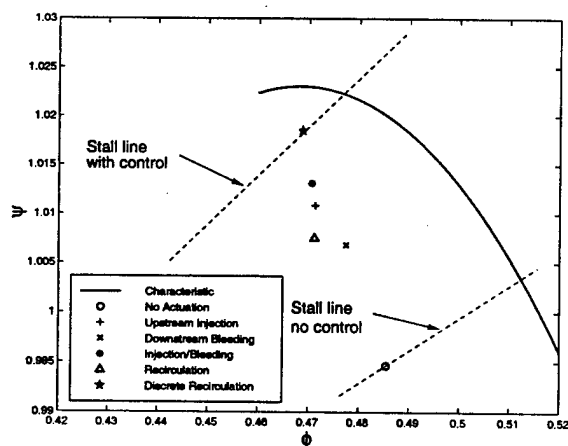


Figure 7: Stalling flow coefficients and associated pressure rises for different configurations. 0.8 dynamic head distortion.

Rotating Stall Control in a High-Speed Stage with Inlet Distortion, *Part I - Radial Distortion*

Z. S. Spakovszky, J. D. Paduano

Gas Turbine Laboratory, Department of Aeronautics and Astronautics
Massachusetts Institute of Technology
Cambridge, MA 02139

C. M. van Schalkwyk

Scientific Systems Co., Inc.
Woburn, MA 01801

K. L. Suder, M. M. Bright, A. J. Strazisar

NASA Lewis Research Center
Cleveland, OH 44135

Abstract

This paper presents the first attempt to stabilize rotating stall in a single-stage transonic axial flow compressor with inlet distortion using active feedback control. The experiments were conducted in the Stage 35 compressor rig at the NASA Lewis Research Center.

Two different types of inlet distortion were introduced to the compressor. First, the effects of radial distortion on the compressor performance and the dynamic behavior were investigated. Radial distortion still implies *decoupled* compressor dynamics which allows the application of single-input-single-output (SISO) control strategies for each harmonic. Based on empirical transfer function estimates control laws were designed and tested using an annular array of air injectors. Steady state blowing achieved a reduction in stalling mass flow of $x\%$. The application of a robust dynamic control law allowed a further range extension of 8.3% above steady blowing resulting in a total reduction in stalling mass flow of $x+8.3\%$. As expected simple constant gain feedback control laws did not work due to the compressible stall inception dynamics. *Part I* describes and discusses the results with radial distortion.

In a second set of experiments the effects of a more realistic circumferential distortion as it can occur in aero engine intakes were investigated. The distortion profile and the compressor stall inception dynamics have been measured again. The circumferential inlet distortion *ouples* the harmonics and the stall inception dynamics turn into a multi-input-multi-output (MIMO) system. The strategies for MIMO system identification and control design with coupled dynamics for the case of circumferential inlet distortion are discussed in *Part II* [8] and the experimental results and range extensions using simple constant gain feedback control and a more sophisticated robust H_∞ controller are presented.

1. Introduction

The classic Moore-Greitzer model [5] describes the modal stall inception dynamics for an incompressible flow field and deals with the circumferential decomposition of the flow field quantities into harmonics. The solution to this model are spatial waves of sinusoidal shape (harmonics) which are traveling around the annulus at rotation rate ω and which can grow or decay in time with growth rate σ . For example the two-dimensional pressure perturbation field solution can be written as

$$\delta p(x, \theta, t) = \sum_{n=-\infty}^{\infty} \tilde{p}_n(x, t) e^{jn\theta}.$$

with

$$\tilde{p}_n(x, t) = a_n e^{(\sigma - jn\omega)t},$$

where x is the axial and θ the circumferential direction. Hence the overall compressor stability is defined by the growth rate of the least stable perturbation mode. Furthermore the axial velocity perturbations at a given θ are uniform through the whole compressor. For this incompressible flow field each spatial harmonic n is one *decoupled* (independent of the other harmonics) traveling perturbation mode characterized by ω and σ .

Generally for distorted inlet flow the major change in the compressor pre-stall behavior is, that the distortion introduces non-linearities which couple the compressor dynamics. The mode-shapes are no longer purely sinusoidal but have contributions of other harmonics. In other terms there is a strong *coupling* between the harmonics due to inlet distortion. *Part II* [8] discusses this in more detail. However when the distortion is circumferentially uniform (e.g. radial distortion) the harmonics can still be decoupled, which is going to be shown in this paper.

If the compressor flow field is compressible as it is the case for NASA Stage 35, new 'acoustic' modes with an

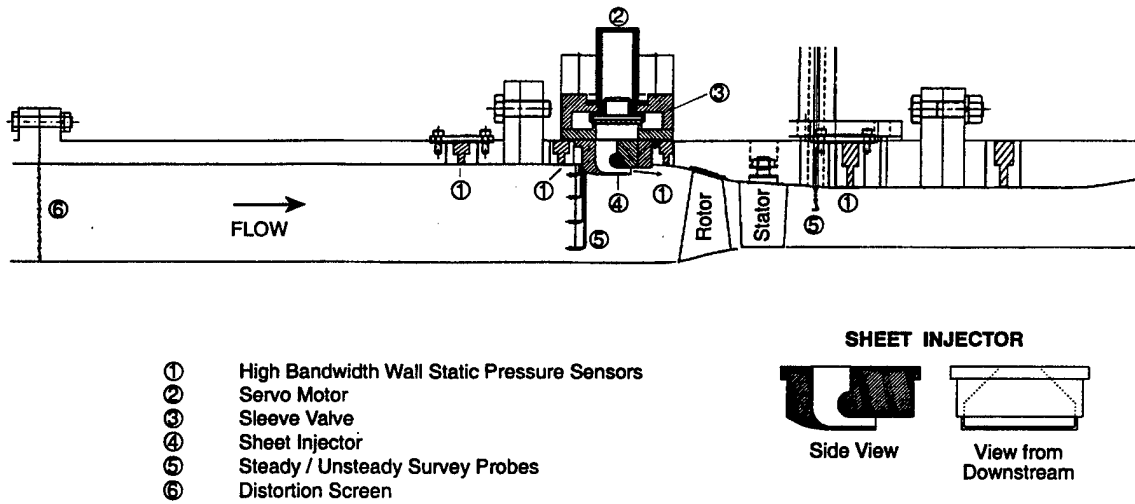


Figure 1: NASA Stage 35 actuation and instrumentation schematic with inlet distortion

axial structure are introduced. In other terms each spatial harmonic of sinusoidal shape in θ has multiple modes (eigenvalues of the compression system) of different axial structures. A first modeling effort has been made by Bonnaure (1991) and was extended by Hendricks *et al.* (1993) and Feulner *et al.* (1994) who included actuation and converted the model to input-output form compatible with control theory. Since there is no low order compressible compressor model with inlet distortion in existence the understanding and the effect of inlet distortion in terms of compressible system dynamics and constraints to control laws is one of the major issues of this paper.

1.1 General input-output compressor dynamics with inlet distortion

From now on all input and output quantities to the compressor system are going to be defined in terms of spatial Fourier coefficients (SFC) denoted by superscript tilde (e.g. \tilde{y}_n is the n -th spatial Fourier coefficient of signal y). If the output vector is defined as the SFC's of the pressure perturbations and the input vector contains the corresponding SFC's of the injection, the transfer function matrix of the compressor can be written for example for the first three harmonics as follows:

$$\begin{bmatrix} \tilde{y}_0(s) \\ \tilde{y}_1(s) \\ \tilde{y}_2(s) \end{bmatrix} = \begin{bmatrix} G_{00}(s) & G_{01}(s) & G_{02}(s) \\ G_{10}(s) & G_{11}(s) & G_{12}(s) \\ G_{20}(s) & G_{21}(s) & G_{22}(s) \end{bmatrix} \begin{bmatrix} \tilde{u}_0(s) \\ \tilde{u}_1(s) \\ \tilde{u}_2(s) \end{bmatrix},$$

or in short form

$$\tilde{\mathbf{y}}(s) = \mathbf{G}(s) \tilde{\mathbf{u}}(s). \quad (1)$$

Note that $\tilde{y}_i(s)$ and $\tilde{u}_j(s)$ are *complex* spatial Fourier coefficients (phasors) and therefore the transfer functions $G_{ij}(s)$ are *complex valued* transfer functions (for $\tilde{y}_i(s), \tilde{u}_j(s) \in \mathbb{R}$, $G_{ij}(s)$ would still be complex but a *real*

valued transfer function going from a real input to a real output).

In the case of clean and circumferentially uniform inlet flow the off-diagonal elements of $\mathbf{G}(s)$ are zero ($G_{ij}(s) = 0 \ \forall i \neq j$) because the harmonics are decoupled as discussed in the previous section. Therefore the compressor dynamics for uniform inlet flow can be treated separately by harmonics and single-input-single-output (SISO) control laws can be designed independently for each harmonic. This was done by Weigl [10] for this compressor. We are going to show in this paper that the decoupled dynamics still hold for radial inlet distortion.

However if circumferential inlet distortion is present the harmonics are no more decoupled and the off-diagonal elements of $\mathbf{G}(s)$ are non-zero ($G_{ij}(s) \neq 0 \ \forall i \neq j$). Therefore the strength of the coupling between the harmonics can be determined by the magnitude and the coherence of these transfer functions. The consequence of this coupling is, that the harmonics can no more be treated independently as SISO systems. The control problem turns in to a multi-input-multi-output (MIMO) problem which makes life much more difficult and increases the complexity of system identification and control law design. *Part II* [8] discusses these issues in detail.

2. Experimental setup

All experiments described in this paper were conducted at the NASA Lewis Research Center in the Single-Stage Axial Compressor Test Facility. The NASA Stage 35 test compressor, originally designed as an inlet stage of an eight-stage 20:1 pressure ratio core compressor (Reid and Moore 1978a), has a total pressure ratio of 1.82, a mass flow of 20.2 kg/s, a rotor tip speed of 455 m/s and a rotation frequency of 286 Hz at design conditions. Rotor 35 consists of 36 blades with an aspect ratio of 1.19, a hub-to-tip radius ratio of 0.7 and a blade tip diameter of

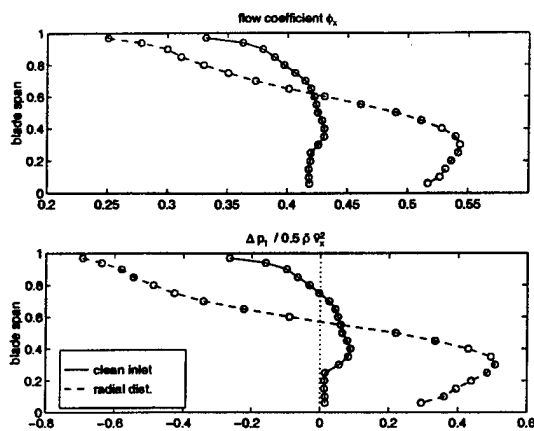


Figure 2: Measured radial distortion profile: flow coefficient (top) and total pressure drop (bottom)

approximately 50 cm. The mean-line rotor chord length is 56 mm. Stator 35 has 46 blades with an aspect ratio of 1.26 and a chord length of 40 mm. Detailed performance descriptions are given by Reid and Moore (1978b).

The control computer used for the experiments is a 90 MHz Pentium PC with 64 input and 16 output channels. The sample rate used for all experiments is 3 kHz while data is acquired in a circular buffer of up to 45 seconds in length (limited only by RAM). The inputs to the control computer are high-response pressure transducer measurements (Kulites), position sense signals from the actuator motors and steady state compressor performance measurements (static pressures at various hub and casing locations, mass flow, pressure rise and throttle position). The unsteady high-response sensors are circumferentially distributed (8-12 wall static pressure probes) at several axial locations. The cleanest traveling wave measurements were obtained from a location immediately upstream of the rotor and were therefore used for system identification and control law testing. The outputs of the control computer are 12 independently commanded mass flow injection rates.

The 12 circumferentially equally spaced jet actuators are placed 63 mm (1.1 rotor chord lengths) upstream of the rotor face. They were designed by Berndt (1995) and developed by Moog Inc. and MIT. The actuators are capable to deliver 5.8% of the design compressor mass flow when supplied with 100 PSI air and have a bandwidth of 400 Hz. Since rotor 35 is tip critical and an extensive study of two different types of injectors (the 3-hole injector and the sheet injector) conducted by Weigl [10] showed that the maximal range extension was obtained by the sheet injector, all experiments were done with this kind of injector. The sheet injectors protrude into the flow by 7% of the rotor inlet span. A detailed description and the actuator design requirements are described in [1].

3. Radial Inlet Distortion

The first set of experiments was conducted using a radial distortion screen which consisted of a fine mesh covering about 38% of the blade span in the tip region and which was located at about ten chord lengths upstream of the rotor. The inlet flow with radial distortion is still circumferentially uniform but has a total pressure loss in the tip region as it is shown in figure 2. Plotted are the radial distributions (measured downstream of the distortion screen) of the flow coefficient $\phi_x = \frac{u}{U}$ and the total pressure drop $\Delta p_t = p_t - \bar{p}_t$ normalized by the mean dynamic head \bar{q} for the case with clean inlet flow and the case with radial distortion. Due to this total pressure loss the axial velocity is reduced in the tip region resulting in a higher incidence and therefore a higher loading of the blades at the tip. The effect of this is on the stall inception pattern is going to be discussed later on.

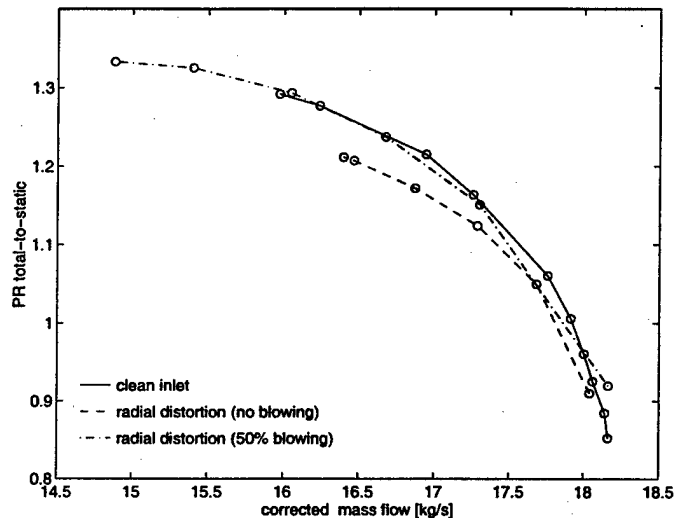


Figure 3: Speed-lines: clean inlet and radial distortion

3.1 Steady state experiments

The twelve sheet injectors were mounted at a yaw angle of -15° (negative incidence angle with respect to the rotor) which was found by Weigl [10] to achieve the best range extension and the highest pressure rise with 50% steady state blowing. Throughout this paper the reference of "50% blowing" will imply a 100 PSI supply pressure with a 50% valve opening. All experiments were conducted at 85% corrected design speed. It was impossible to run the compressor at design speed due to mechanical problems with one of the journal bearings causing a whirling shaft. 85% speed was determined as the highest possible speed setting with acceptable shaft orbits. All of the presented compressor speed-lines are constructed from the measured total inlet pressure upstream of the actuators, the exit static pressure (average of hub and casing wall static pressures downstream of the stage) and the

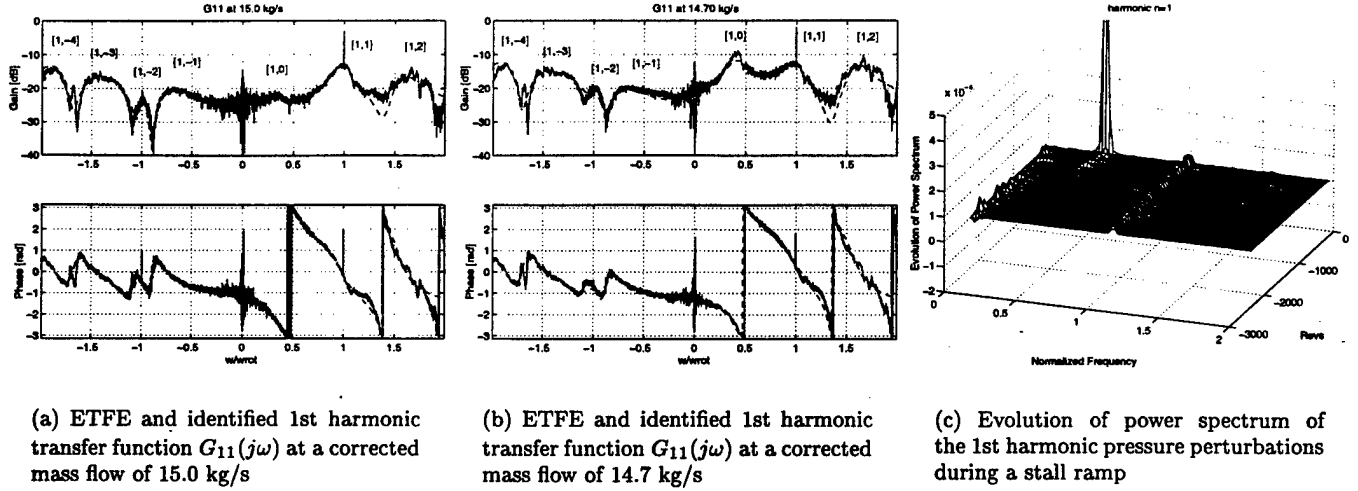


Figure 4: Open loop compressor dynamics with radial distortion

total corrected mass flow through the compressor. The total corrected mass flow is the sum of the inlet flow rate (measured by an orifice far upstream of the compressor and corrected by the total pressure and temperature at the same location) and the injector flow rate (determined by a separate venturi meter and corrected by the total pressure and temperature in the injector).

First the nominal speed-line at 85% corrected design speed (no distortion and no blowing) was measured. The radial distortion screen was then mounted and the speed-lines were measured without and with 50% steady state blowing. Figure 3 depicts the total-to-static speed-lines for the mentioned cases. The slopes of the total-to-static speed-lines are analogous to the slopes of the total-to-static pressure rise coefficients which are crucial for the determination of compressor stability. One can see that the peak pressure rise drops and the compressor stalls at higher mass flows when radial distortion is introduced to the compressor. However steady state injection can recover this pressure drop and even results in a range extension of x% in stalling mass flow.

3.2 Open loop compressor dynamics

The most important issue and the basis for an empirical control law design is the full understanding of the compression system dynamics. Forced response experiments have been conducted to deduce and to construct the transfer functions of the compressor dynamics. The idea of a non-parametric frequency domain measurement called Empirical Transfer Function Estimate (ETFE) is to sweep a sinusoidal injection pattern over a certain frequency range through the compressor and to measure its response.

The compressor transfer functions $G_{ij}(j\omega)$ as stated in equation (1) can be deduced from the measured signals

$u(t)$ and $y(t)$ as follows (for details see [4]):

$$G_{ij}(j\omega) = \frac{\Phi_{\tilde{y}_i \tilde{u}_j}(j\omega)}{\Phi_{\tilde{u}_j \tilde{u}_j}(j\omega)}, \quad (2)$$

where $\Phi_{xx}(j\omega)$ is the power spectrum of signal $x(t)$ and $\Phi_{xz}(j\omega)$ the cross spectrum between $x(t)$ and $z(t)$. Note that the spectra are computed for the SFC's of the measured signals. The whole j -th column of $G(j\omega)$ can be constructed from the j -th harmonic excitation $u_j(t)$ since the compressor response $y_j(t)$ can be decomposed into all the harmonics of interest i giving the spatial Fourier coefficients $\tilde{y}_{ij}(t)$.

To determine the accuracy of the transfer function estimate, the coherence between the actuator command input $c(t)$ and plant output $y(t)$ can be computed at each frequency where $u(t)$ and $c(t)$ are coupled through additional actuator dynamics (for details see [10]). The coherence $\gamma_{\tilde{y}_i \tilde{c}_j}^2(j\omega)$ is then defined by

$$\gamma_{\tilde{y}_i \tilde{c}_j}^2(j\omega) = \frac{|\Phi_{\tilde{y}_i \tilde{c}_j}(j\omega)|^2}{\Phi_{\tilde{c}_j \tilde{c}_j}(j\omega) \Phi_{\tilde{y}_i \tilde{y}_i}(j\omega)}. \quad (3)$$

The value of $\gamma_{\tilde{y}_i \tilde{c}_j}^2(j\omega)$ can vary from zero to one and indicates the correlation between the command input and the response of the compressor to this forcing. Low values of coherence reflect that noise or other external forcing sources (e.g. a whirling shaft, rotor noise) are present, and that the input and output signals are not really correlated. This allows also to determine the strength of the coupling between the different harmonics. For example if the coherence between a first harmonic excitation input and a zeroth harmonic compressor response is very low, one can tell that the coupling between these harmonics is poor.

Measurements of the zeroth, first and second harmonic transfer functions revealed that the off-diagonal elements

$G_{ij}(j\omega) \forall i \neq j$ of the transfer function system (1) had low and noisy magnitudes, distorted phases and very poor coherence. As expected the compressor dynamics with a circumferentially uniform radial distortion screen in the inlet are *decoupled*. Multiple compressible modes are visible in the zeroth, first and second harmonic transfer functions. Figures 4(a) and 4(b) depict the measured transfer function (ETF) of the first harmonic $G_{11}(j\omega)$ for two different mass flows. The compressible modes are labeled as $[1, m]$, '1' denoting the corresponding first harmonic and m the mode number. In addition to the transfer function measurements open loop stall ramps have been accomplished. The jet-injectors were operated at a 50% steady blowing level while the throttle was closed slowly until the compressor was driven into stall. The pre- and post-stall pressure measurements were taken from eight Kulites located between the jet-injectors and the rotor face. The Kulite pressure signals were decomposed into the first three harmonics by a Discrete Spatial Fourier Transform. For each harmonic the evolution of the power spectrum was then computed. Figure 4(c) depicts the evolution of the power spectrum for the first spatial Fourier harmonic during a throttle ramp into stall. The time axis is in rotor revolutions and the frequency axis is normalized by rotor frequency.

The measurements show that the first harmonic perturbations are very dominant in the pre-stall compressor dynamics. There are mainly two modes visible in the power spectrum: mode $[1, 0]$ is traveling around the annulus at about 40% of rotor speed and can be referred to the classical incompressible Moore-Greitzer mode and there is mode $[1, 1]$, the first compressible mode, which lines up with rotor frequency when the compressor is operated at 85% corrected design speed. One can clearly see in figures 4(a) and 4(b) that the growth rate of mode $[1, 0]$ is significantly increasing and the phase is rolling off faster when the mass flow is reduced. In fact it is mode $[1, 0]$ which goes unstable first when the compressor is driven into stall as it is depicted in figure 4(c). Therefore it has been considered to concentrate on the design of first harmonic controllers in order to stabilize the compressor.

The empirical design of control laws requires an identified model of the compression system dynamics. FORSE (Frequency Observable Range Subspace Estimation), a program developed at the Space Engineering Research Center at MIT, was used in order to fit and to identify the measured compressor transfer functions. FORSE [9] allows state-space representations $[A, B, C, D]$ of measured real valued MIMO transfer function systems. For the case with radial inlet distortion only the SISO transfer function $G_{11}(j\omega)$ has been fitted. Since FORSE was used the complex valued SISO system had to be transformed to a real valued MIMO system (for details see [7]). The fitted transfer functions are plotted as dashed lines in figures 4(a) and 4(b). Note that the eigenvalues of A are the

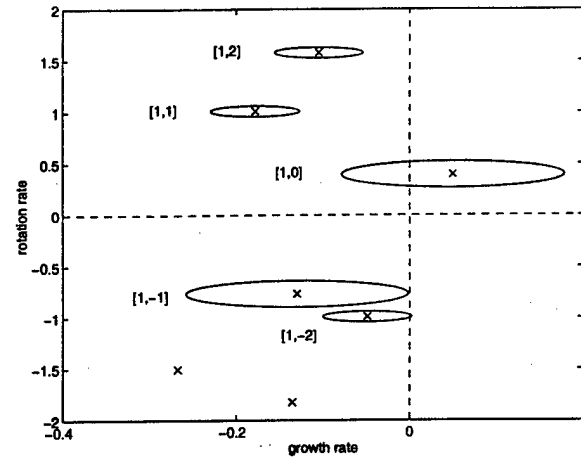


Figure 5: Eigenvalue perturbations for first harmonic robust control design

poles of the compression system and that 14 states have been used to represent 7 oscillatory poles of $G_{11}(j\omega)$ which are plotted as x's in figure 5. It has to be mentioned that it was very difficult to obtain useful fits since FORSE is optimizing a cost function using *one* set of poles for *multiple* transfer functions (MIMO system). It is an intrinsic constraint to keep the system order low in order to limit the complexity of the compressor system with regards to control law design.

4. Control law design and closed loop experiments

There are mainly two strategies to design control laws that can be used for active stall control. Throughout the course of this research simple constant gain feedback control laws and more sophisticated model-based dynamic controllers like H_∞ robust control laws have been designed to stabilize the compressor and to extend the operating range.

4.1 Constant gain control law experiments

The first control experiments were conducted with constant gain controllers. The function of a constant gain feedback control law is to measure the pressure perturbations upstream of the rotor, to multiply it by a constant complex gain and to feed it back to the actuator. The gain and phase of these control laws have to be found through on-line tuning experiments.

However as expected from previous results of constant gain experiments conducted by Weigl [10], none of the constant gain controllers worked and no further range extension could be achieved. The main reason for this is that the compressor dynamics at 85% corrected rotor speed are compressible. As shown in figures 4(a) and 4(b) there are several lightly damped modes. Suppose we apply a first

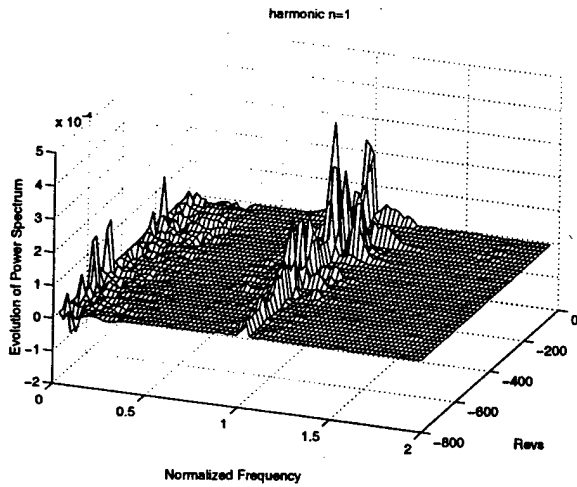


Figure 6: Evolution of power spectrum of the 1st harmonic during a stall ramp with H_∞ control

harmonic constant gain controller and tune a particular phase and gain that damps the $[1, 0]$ mode the other lightly damped modes (like mode $[1, 1]$ and $[1, 2]$) are destabilized. Constant gain can not be applied for compressible dynamics with multiple lightly damped modes and a distinction in frequency or a frequency dependent control law has to be implemented.

4.2 H_∞ robust control law design with eigenvalue perturbations

Using the identified dynamics shown in figure 4 a robust, linear, dynamic H_∞ controller was designed to stabilize the first harmonic modes. The basic concept of the control design strategy is a mixed sensitivity H_∞ problem modified with eigenvalue perturbations, since our task here is not to solve a tracking problem but to stabilize the compressor (for details see [3], [6] and [10]). Such a control law can only be designed using a model of the unstable compressor dynamics. Since on one hand a theoretical model is not yet accurate enough [10] and on the other it is difficult to measure the unstable dynamics of the compressor an estimated unstable identified model had to be used. The unstable identified model was obtained by simply extrapolating the identified stable mode $[1, 0]$ to a lower unstable mass flow. Hereby it was assumed that the other modes do not significantly change in growth rate during a throttle ramp which can also be seen in figure 4. Based on these estimated unstable dynamics a dynamic H_∞ controller was designed with five eigenvalue perturbations as shown in figure 5. Note that mode $[1, 0]$ is assumed to be unstable for the control law design. The circles (the scales in figure 5 make them appear to be ellipses) represent uncertainty in the eigenvalue location. The designed robust control law will stabilize the compressor as long as those first harmonic modes stay within the boundaries of the

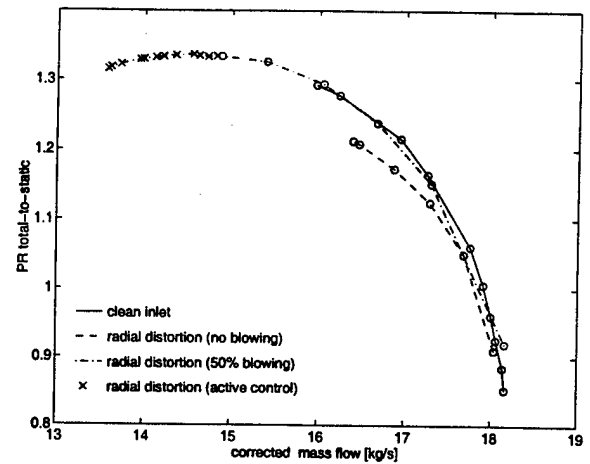


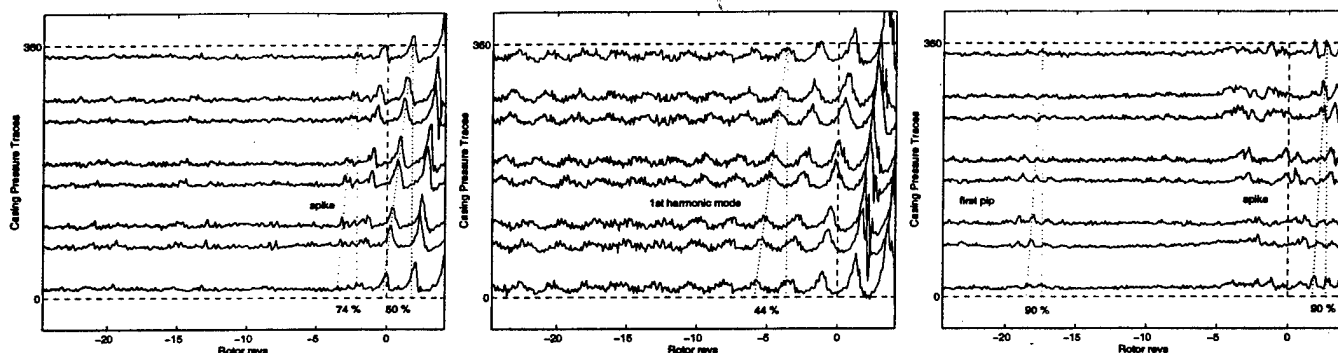
Figure 7: Speed-lines with radial distortion: 50% steady blowing and first harmonic active control

uncertainty circles. Also note that the big circle around mode $[1, 0]$ covers positive (unstable) as well as negative (stable) eigenvalue locations to make sure that the controller does not destabilize the compressor at higher mass flows where mode $[1, 0]$ is in the left hand side plane. All of the presented results of the control experiments with radial inlet distortion were conducted with this H_∞ robust controller.

4.3 Closed loop experiments with H_∞ control law

The designed control law was then implemented on the control computer and tested during stall ramps. Active control of the first harmonic achieved a reduction of stalling mass flow or an extension in operating range of 8.3% above steady blowing. Figure 6 shows the evolution of the power spectrum of the first harmonic during the event with active control. A closer look at the first harmonic modes reveals that mode $[1, 0]$, which was driving the compressor into stall without control (see figure 4(c)) is completely damped out (the magnitude of the power spectrum is flat around $\omega/\omega_{rot} = 0.4$). In fact it is now mode $[1, 1]$ which is growing and going unstable when mass flow is decreased. It has to be mentioned also that the power spectra of the zeroth and second harmonic perturbations (not plotted here) showed poor modal activity when the compressor was driven into stall and that these modes were all highly damped during the event.

These results justify the choice of only implementing and concentrating on a first harmonic controller. As a matter of fact additional zeroth and second harmonic controllers do not allow further reduction of mass flow or extension of operating range as it was experimentally confirmed with an additional zeroth harmonic H_∞ controller since the first harmonic mode $[1, 1]$ determines now the compressor stability. The only way to operate be-



(a) No blowing: spike speed is 74%, initial stall cell speed about 50% of rotor speed

(b) 50% steady blowing: dominant first harmonic modal prestall behavior

(c) First harmonic H_∞ control law: spike speed is about 90% of rotor speed

Figure 8: Spike and modal stall patterns with radial inlet distortion

yond these mass flows is to increase the uncertainty circle around mode [1,1] in the control law design. However the eigenvalue perturbations shown in figure 5 represent the case with the biggest possible uncertainty circles and a further increase in any of those circles would lead to divergence in the H_∞ design when the controller and observer Algebraic Riccati Equations (ARE) are solved.

The closed loop active control results are summarized in figure 7. Only with 50% steady blowing the stalling mass flow could be reduced by x%. Applying the first harmonic robust H_∞ controller allowed a further reduction in stalling mass flow of 8.3% above steady blowing and resulted in a total range extension of x+8.3%. Earlier experiments conducted by Weigl [10] at 100% corrected speed without inlet distortion achieved a reduction in stalling mass flow of 4.3% with 50% steady blowing and about 3.5% upon steady blowing with zeroth, first and second harmonic active robust control. Comparing these results to the ones discussed above with radial inlet distortion and only first harmonic control reveals an improvement in range extension by a factor of almost 3.

5. 'Spike' and 'modal' stall patterns in Stage 35 with radial inlet distortion

Previous stall inception studies and experimental work by Day (1993) have lead to the identification of two common flow breakdown processes in low speed axial flow compressors. According to Day [2] there can be a first type of stall inception sequence with short length scale disturbances prior to stall known as 'spikes' or 'pips' or a second type of longer length scale disturbances known as 'modal oscillations' before the compressor goes into stall.

A spike may be described as an embryonic stall cell which is created by the local stalling of a particular blade row. Spikes usually start in low velocity troughs and travel quickly around the annulus between 60% to 80% of rotor

speed. The fewer blade passages a stall cell occupies the faster the spike will rotate (Day 1996). Once a spike is formed it quickly increases in size, loses rotational speed and turns into a rotating stall cell. Modal stall is the stall inception pattern we have been discussing in the preceding sections. Day (1997) describes the nature and the appearance of these two prestall flow phenomena in several low speed compressor configurations and explains the mechanism for each case with a simple model. According to Day [2] spike stall inception occurs when the critical incidence at the rotor tip is reached before the total-to-static pressure rise characteristic turns over ($\frac{\partial \Psi^{t*}}{\partial \phi} \leq 0$) and modal stall inception is observed when the peak of the total-to-static pressure rise characteristic (neutral stability, $\frac{\partial \Psi^{t*}}{\partial \phi} = 0$) is reached before critical incidence is exceeded. This has been shown experimentally in a multi-stage low speed axial compressor where the effects of stage matching and blade row incidence angles were investigated using variable geometry features of the test compressor. The same stall inception behavior has been observed in a low speed single-stage axial compressor where the tip incidence was changed by artificially skewing the flow towards the casing or the hub [2]. We are going to show the existence of spikes and modes in NASA Stage 35 with radial inlet distortion.

The first experiment shown in figure 8(a) is an open loop stall ramp without blowing. All actuators were turned off and the compressor was driven into stall. Plotted are the eight circumferentially distributed Kulite static pressure traces upstream of the rotor face during the event. The pressure perturbations have been scaled by their mean standard deviations. One can see that there is a spike emerging from the pressure traces a couple of rotor revolutions before stall and traveling very fast (about 74% of rotor speed) around the annulus. Its size is quickly growing while its speed is slowing down and within a few

revolutions the spike forms a stall cell with an initial rotation rate of about 50% of rotor speed. Fully developed rotating stall is then traveling at a rotation rate of about 40% of rotor speed. The stall inception mechanism in Stage 35 with radial inlet distortion and no blowing is clearly determined by spikes.

In a second experiment the jet-injectors were turned on to a level of 50% steady blowing and the compressor was again throttled into stall. Figure 8(b) depicts the pre-stall pressure traces during this event. In this case the pre-stall flow field was modal. The pressure traces reveal a very dominant first harmonic pressure perturbation wave traveling around the annulus at about 44% of rotor speed long before the compressor is going in to stall. The amplitude is growing as neutral stability is reached and the modal oscillations turn into a stall cell. Note that the wave speed does not change significantly during the stall ramp and that the stall cell speed is about equal to the mode speed. This corresponds to the previous observations and is consistent with the growing of mode [1, 0] as it has been shown and discussed in figure 4.

The reason for these two different stall inception sequences depending on the level of blowing can be explained as follows. The radial distortion screen upstream of the rotor leads to a total pressure loss in the tip region and skews the flow towards the hub as it was shown in figure 2. The axial velocities drop, the incidence and the turning increases and the blades have a higher loading in the tip region. Critical incidence is therefore exceeded before neutral stability is reached during the throttle ramp and spikes appear in the pre-stall flow field and form the stall cell. When the injectors are turned on a high momentum jet is blown into the rotor face in the tip region. The increased tip incidence caused by the distortion screen is decreased due to the higher axial velocities with blowing. The total-to-static characteristic changes in such a way that neutral stability is reached before the critical incidence occurs and modal oscillations develop into rotating stall. This verifies the above described simple model formulated by Day [2] also for a single-stage transonic axial compressor.

Another interesting result with radial inlet distortion is the pre-stall flow field for a closed loop stall ramp. One would expect pips or spikes in the flow field when active control is applied. Indeed using the first harmonic H_{∞} robust controller all the modes are damped out. A closed loop throttle ramp using the mentioned robust control law is shown figure 8(c). There is a first spike or pip emerging about 20 rotor revolutions before stall traveling at about 90% of rotor speed. However this pip dies out and the spike activity restarts a few revolutions later. The spike does not show a continuous growth. Note that at this time the pressure traces are no longer uniform on the circumference. One can see that a first large sized spike starts to rotate out of a pressure trough but dies again when it hits

a region of higher pressures and thus higher velocities.

6. Summary and Conclusions

The experiments discussed in this paper represent the first attempt of active rotating stall control in a transonic compressor with radial inlet distortion using an annular array of jet-injectors. The measurements of the distortion profile showed that the flow is still circumferentially uniform but skewed towards the hub resulting in a total pressure drop and thus in higher incidence and loading of the blades in the tip region. The peak pressure rise drops and the compressor stalls at higher mass flows. However steady state injection can recover the original flow profile and even results in a range extension of x% in stalling mass flow. In addition the stall inception pattern with radial inlet distortion turned out to be 'spike-like' or 'modal' depending on if the actuators were turned off or operated at steady blowing. The experiments verify the simple model developed by Day [2] also for a single-stage transonic compressor.

The construction of the compressor transfer functions using forced response experiments revealed that the compressible stall inception dynamics with radial distortion are still *decoupled*. This allowed the design of SISO control laws to stabilize the harmonics independently. Simple constant gain control strategies could not be used due to the compressible pre-stall dynamics, which also verifies the work conducted by Weigl [10]. The pre-stall dynamics showed very strong and dominant first harmonic modes and a more sophisticated first harmonic H_{∞} robust controller allowed a further range extension of 8.3% above steady blowing. This result reflects an improvement in stalling mass flow reduction by a factor of almost 3 compared to experiments with clean inlet flow [10].

7. Acknowledgments

This research was conducted under collaboration between the NASA Lewis Research Center and MIT. We would like to thank H. Weigl for his help and the very useful discussions as well as D. Williams, R. Bruckner and B. Piendl at NASA Lewis for their support during compressor testing. This project was conducted under NASA grant xxxxxx.

References

- [1] BERNDT, R. G., "Actuation for Rotating Stall Control of High Speed Axial Compressors". *M.S. Thesis, Department of Aeronautics and Astronautics, MIT*, (1995).
- [2] DAY, I. J., CAMP, T. R., "A Study of Spike and Modal Stall Phenomena in a Low-Speed Axial Compressor". *Presented at the ASME Turbo Expo, Orlando FL*, (June 1997).

- [3] KWAKERNAAK, H., "Robust Control and H_{∞} -Optimization: Tutorial Paper". *Automatica*, Vol. 29, No. 2, (1993) . pp. 255-273.
- [4] LJUNG, L., "System Identification: Theory for the User". *PTR Prentice-Hall, Inc.*, (1987).
- [5] MOORE, F. K., GREITZER, E. M., "A Theory of Post-Stall Transients in Axial Compression Systems: Part I - Development of Equations, and Part II - Application". *Journal of Engineering for Gas Turbines and Power*, Vol. 108 (1986), pp. 68-76 and 231-239.
- [6] SMITH, R. S., "Technical Notes and Correspondance: Eigenvalue Perturbation Models for Robust Control". *IEEE Transactions on Automatic Control*, Vol. 40, No. 6, (June 1995) . pp. 1063-1066.
- [7] SPAKOVSKY, Z. S., "Active Control of Rotating Stall in NASA Compressor Stage 35 with Inlet Distortion". *GTL Report* (August 1997).
- [8] SPAKOVSKY, Z. S., PADUANO, J. D., VAN SCHALKWYK, C. M., SUDER, K. L., BRIGHT, M. M., STRAZISAR, A. J., "Rotating Stall Control in a High-Speed Stage with Inlet Distortion, Part II - Circumferential Distortion". *To be presented at the 1998 ASME Turbo Expo, Stockholm, Sweden* (June 1998).
- [9] SPACE ENGINEERING RESEARCH CENTER MIT, "Frequency Observable Range Subspace Estimation (FORSE)". , () .
- [10] WEIGL, H. J., "Active Stabilization of Rotating Stall and Surge in a Transonic Single Stage Axial Compressor". *Ph.D. Thesis, Department of Aeronautics and Astronautics, MIT*, (June 1997).

Rotating Stall Control in a High-Speed Stage with Inlet Distortion, *Part II - Circumferential Distortion*

Z. S. Spakovszky, J. D. Paduano

Gas Turbine Laboratory, Department of Aeronautics and Astronautics
Massachusetts Institute of Technology
Cambridge, MA 02139

C. M. van Schalkwyk

Scientific Systems Co., Inc.
Woburn, MA 01801

K. L. Suder, M. M. Bright, A. J. Strazisar

NASA Lewis Research Center
Cleveland, OH 44135

Abstract

This paper reports the first experiments and investigations of active rotating stall control in a single-stage transonic axial compressor with circumferential inlet distortion using an annular array of air injectors. This research was conducted in the Stage 35 high-speed compressor test facility at the NASA Lewis Research Center.

The circumferential distortion had a distortion magnitude of about one dynamic head, which corresponds to a DC(60) descriptor of 0.61 covering 120° of the circumference. Forced response experiments allowed the measurement of the compressor transfer functions, which showed a very strong *coupling* between the harmonics. In order to obtain an identified model of the coupled compressible stall inception dynamics multi-input-multi-output (MIMO) system identification strategies had to be used. It is the very first time that the coupled dynamics of a compressible pre-stall flow field is measured and investigated. Stall-ramp experiments and a further analysis of the compressible stall inception dynamics yielded a very strong first harmonic content in the pressure perturbations which were dominated by the well known incompressible Moore-Greitzer mode.

In distinction to radial inlet distortion discussed in *Part I* [7] the characteristics of the coupled compressible stall inception dynamics allowed simple constant gain feedback control laws to stabilize the compressor. Steady state blowing experiments resulted in a reduction of the stalling mass flow of $y\%$. Constant gain control experiments yielded a further range extension of $y012\%$ upon steady blowing. In addition a more sophisticated robust H_∞ controller has been tested and allowed an operating range extension of $yh\%$ above steady blowing yielding a total reduction in stalling mass flow of $y+yh\%$.

1. Introduction

For a better understanding of the coupled compressor dynamics a short introduction and an overview of basic compressor modeling is given. The classic Moore-Greitzer formulation [4] considers an incompressible 2-dimensional flow field with an axisymmetric and uniform (non-distorted) inlet flow and uses a linearized approach for the perturbations. The rotating stall inception dynamics are described by

$$\left(\frac{2}{|n|} + \mu\right) \frac{\partial \delta\phi}{\partial \tau} = \left(\frac{\partial \Psi^{ts}}{\partial \phi} - jn\lambda\right) \delta\phi, \quad (1)$$

where Ψ^{ts} is the total-to-static pressure rise coefficient over the entire compressor and ϕ and $\delta\phi$ are the flow coefficient and its perturbation respectively. The inertia parameters are the fluidic inertias in the rotors λ , in the rotors and stators μ and in the inlet and exit ducts $\frac{2}{|n|}$, where

$$\lambda = \sum_{\text{rotors}} \frac{c_x/r_0}{\cos^2 \xi}, \quad \mu = \sum_{\text{rotors+stators}} \frac{c_x/r_0}{\cos^2 \xi}.$$

Note that the inertia parameters include only geometry terms (axial chord, mean radius and stagger angle). Solving equation (1) with the following modal formulation separately for each harmonic number n

$$\delta\phi(x, \theta, t) = \sum_{n=-\infty}^{\infty} \tilde{\phi}_n(x, t) e^{jn\theta}$$

yields

$$\delta\phi(x, \theta, t) = \sum_{n=-\infty}^{\infty} a_n e^{(\sigma - jn\omega)\tau} e^{jn\theta},$$

with growth rate σ and rotation rate ω

$$\sigma = \frac{\frac{\partial \Psi^{ts}}{\partial \phi}}{\left(\frac{2}{|n|} + \mu\right)}, \quad \omega = \frac{\lambda}{\left(\frac{2}{|n|} + \mu\right)}.$$

This solution describes spatial waves of sinusoidal shape (harmonics) which are traveling around the annulus at rotation rate ω and can grow or decay in time with growth rate σ . Hence the overall compressor stability is defined by the growth rate of the perturbation modes. Furthermore the axial velocity perturbations at a given θ are uniform through the whole compressor. For this incompressible flow field each spatial harmonic n is one *decoupled* (independent of the other harmonics) traveling perturbation mode characterized by ω and σ .

For distorted inlet flow the major modification is, that $\frac{\partial \psi^{*+}}{\partial \phi}$ is no longer a constant but is a strong function of θ due to the shape and strength of the inlet distortion. This is also reflected in the solution of the flow field perturbations. The mode-shapes are no longer purely sinusoidal but have contributions of other harmonics. In other terms there is a strong *coupling* between the harmonics due to inlet distortion. Hynes and Greitzer [2] have extended the Moore-Greitzer model to the Hynes-Greitzer model which describes the mentioned incompressible compressor dynamics with inlet distortion.

If the compressor flow field is compressible, new 'acoustic' modes with an axial structure are introduced. In other terms each spatial harmonic of sinusoidal shape in θ has multiple modes (eigenvalues of the compression system) of different axial structures. A first modeling effort has been made by Bonnaure (1991) and was extended by Hendricks *et al.* (1993) and Feulner *et al.* (1994) who included actuation and converted the model to input-output form compatible with control theory. Since a low order compressible compressor model with coupled dynamics does not exist yet it is one of the major issues of this paper to investigate on the effects of inlet distortion on the compressor pre-stall behavior.

As already stated in *Part I* [7] the transfer function matrix of the compressor can be written for example for the first three harmonics as follows:

$$\begin{bmatrix} \tilde{y}_0(s) \\ \tilde{y}_1(s) \\ \tilde{y}_2(s) \end{bmatrix} = \begin{bmatrix} G_{00}(s) & G_{01}(s) & G_{02}(s) \\ G_{10}(s) & G_{11}(s) & G_{12}(s) \\ G_{20}(s) & G_{21}(s) & G_{22}(s) \end{bmatrix} \begin{bmatrix} \tilde{u}_0(s) \\ \tilde{u}_1(s) \\ \tilde{u}_2(s) \end{bmatrix},$$

or in short form

$$\tilde{\mathbf{y}}(s) = \mathbf{G}(s) \tilde{\mathbf{u}}(s), \quad (2)$$

where the output vector is defined as the spatial Fourier coefficients (SFC's) of the pressure perturbations and the input vector contains the corresponding SFC's of the injection.

In general if inlet distortion is present the harmonics are no more decoupled and the off-diagonal elements of $\mathbf{G}(s)$ are non-zero ($G_{ij}(s) \neq 0 \quad \forall i \neq j$). Therefore the strength of the coupling between the harmonics can be determined by the magnitude and the coherence of these transfer functions. The consequence of this coupling is, that the harmonics can no more be treated independently as SISO systems. The control problem turns

in to a multi-input-multi-output (MIMO) problem which makes life much more difficult and increases the complexity of system identification and control law design.

2. Experimental setup

The experiments described in this paper were all conducted at the NASA Lewis Research Center in the Single-Stage Axial Compressor Test Facility. The NASA Stage 35 test compressor, originally designed as an inlet stage of an eight-stage 20:1 pressure ratio core compressor (Reid and Moore 1978a), has a total pressure ratio of 1.82, a mass flow of 20.2 kg/s, a rotor tip speed of 455 m/s and a rotation frequency of 286 Hz at design conditions. Rotor 35 consists of 36 blades with an aspect ratio of 1.19, a hub-to-tip radius ratio of 0.7 and a blade tip diameter of approximately 50 cm. The mean-line rotor chord length is 56 mm. Stator 35 has 46 blades with an aspect ratio of 1.26 and a chord length of 40 mm. Detailed performance descriptions are given by Reid and Moore (1978b).

The control computer used for the experiments is a 90 MHz Pentium PC with 64 input and 16 output channels. The sample rate used for all experiments is 3 kHz while data is acquired in a circular buffer of up to 45 seconds in length (limited only by RAM). The inputs to the control computer are high-response pressure transducer measurements (Kulites), position sense signals from the actuator motors and steady state compressor performance measurements (static pressures at various hub and casing locations, mass flow, pressure rise and throttle position). The unsteady high-response sensors are circumferentially distributed (8-12 wall static pressure probes) at several axial locations. The cleanest traveling wave measurements were obtained from a location immediately upstream of the rotor and were therefore used for system identification and control law testing. The outputs of the control computer are 12 independently commanded mass flow injection rates.

The 12 circumferentially equally spaced jet actuators are placed 63 mm (1.1 rotor chord lengths) upstream of the rotor face. They were designed by Berndt (1995) and developed by Moog Inc. and MIT. The actuators are capable to deliver 5.8% of the design compressor mass flow when supplied with 100 PSI air and have a bandwidth of 400 Hz. Since rotor 35 is tip critical and an extensive study of two different types of injectors (the 3-hole injector and the sheet injector) conducted by Weigl [9] showed that the maximal range extension was obtained by the sheet injector, all experiments were done with this kind of injector. The sheet injectors protrude into the flow by 7% of the rotor inlet span. A detailed description and the actuator design requirements are described in [1]. The NASA Stage 35 actuation and instrumentation schematic with inlet distortion is shown in *Part I* [7]. All experiments presented here were conducted at 85% corrected design speed due to mechanical problems with one of the journal bearings causing a whirling shaft.

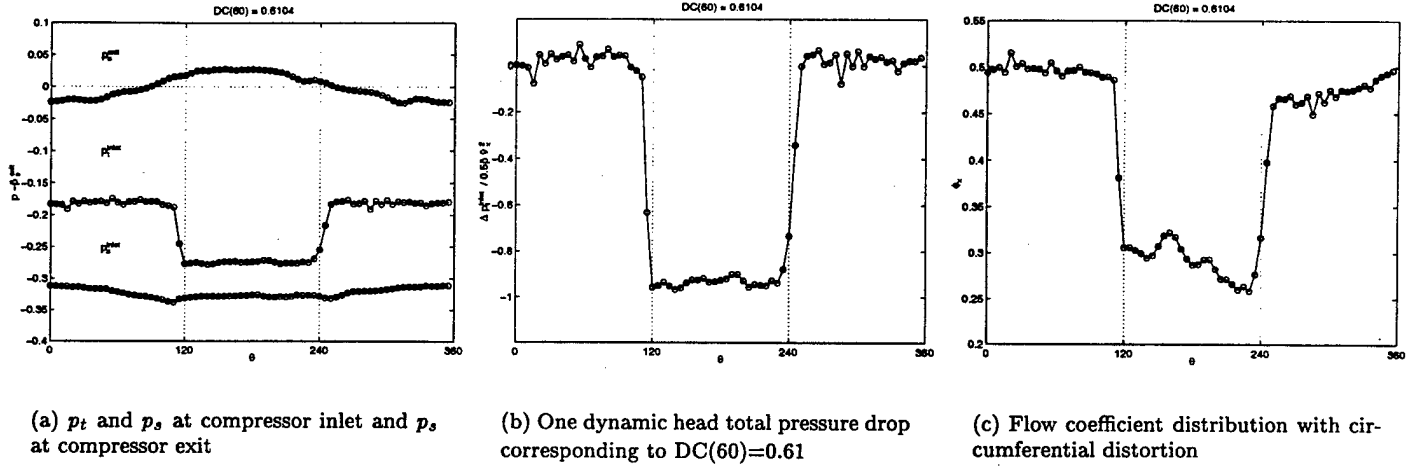


Figure 1: Measured circumferential distortion profile at $\dot{m}_{corr} = 15.3$ kg/s without blowing

3. Circumferential Inlet Distortion

The case of a more realistic distortion as it can occur in aero engine intakes due to flow separation or non-axisymmetric intake duct geometry has been studied and investigated using a circumferential distortion screen. The screen consisting of a fine mesh was mounted on a carrier at the same axial location as the radial distortion screen described in *Part I* [7] allowing a screen rotation of 350 degrees around the annulus. The distortion extent was 120 degrees of the circumference covering the full blade span.

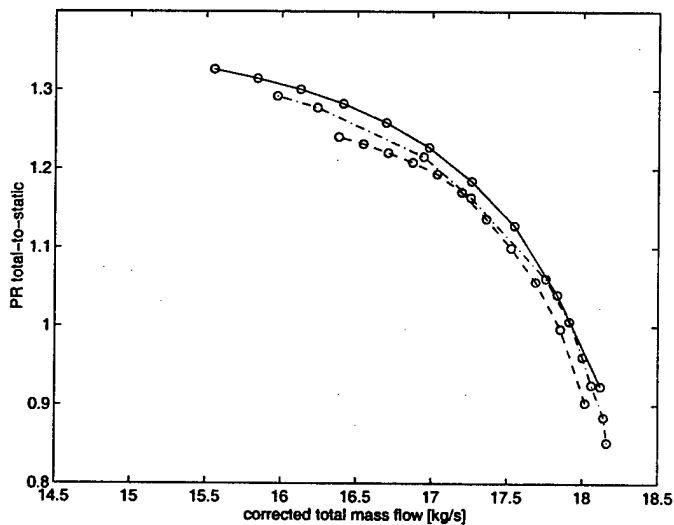


Figure 2: Speedlines: clean inlet (dashed-dotted), circumferential distortion no blowing (dashed) and with 50% steady blowing (solid)

3.1 Circumferential distortion profile

In order to obtain the circumferential distortion profile total and static pressure as well as total and static temperature measurements were conducted with a rake positioned at midspan upstream of the rotor and downstream of the distortion screen. Four circumferentially distributed static wall pressure probes at the hub and the casing and a total pressure and total temperature rake at midspan provided data of the flow field downstream of the compressor. The steady pressure and temperature probes were geometrically fixed and the screen was rotated in five degree steps to obtain the distortion profile. Figure 1(a) depicts the total and static pressure profile at the compressor inlet (thus downstream of the distortion screen) and the static pressure profile at the compressor exit. The mean value of the static pressure at the compressor exit has been subtracted to show the variation around the annulus. The distortion screen blocked the flow in the range of $120^\circ \leq \theta \leq 240^\circ$ which is marked with the dotted lines. The total pressure drop due to the distortion screen was about one dynamic head

$$\frac{\Delta p_t}{\frac{1}{2} \rho \bar{v}_x^2} \approx 1$$

which is shown in figure 1(b). The circumferential variation of the flow coefficient ϕ_x is plotted in figure 1(c). The distortion magnitude can either be expressed in inlet dynamic head or described by a parameter commonly used in engine intake aerodynamics called the DC(60) descriptor [10]. The DC(60) descriptor is defined by

$$DC(60) = \frac{\bar{p}_t|_{360^\circ} - \bar{p}_t|_{worst\ 60^\circ}}{\frac{1}{2} \rho \bar{v}_x^2}$$

taking in account the worst total pressure loss within a sector of 60° . In the ideal case where the static pressure

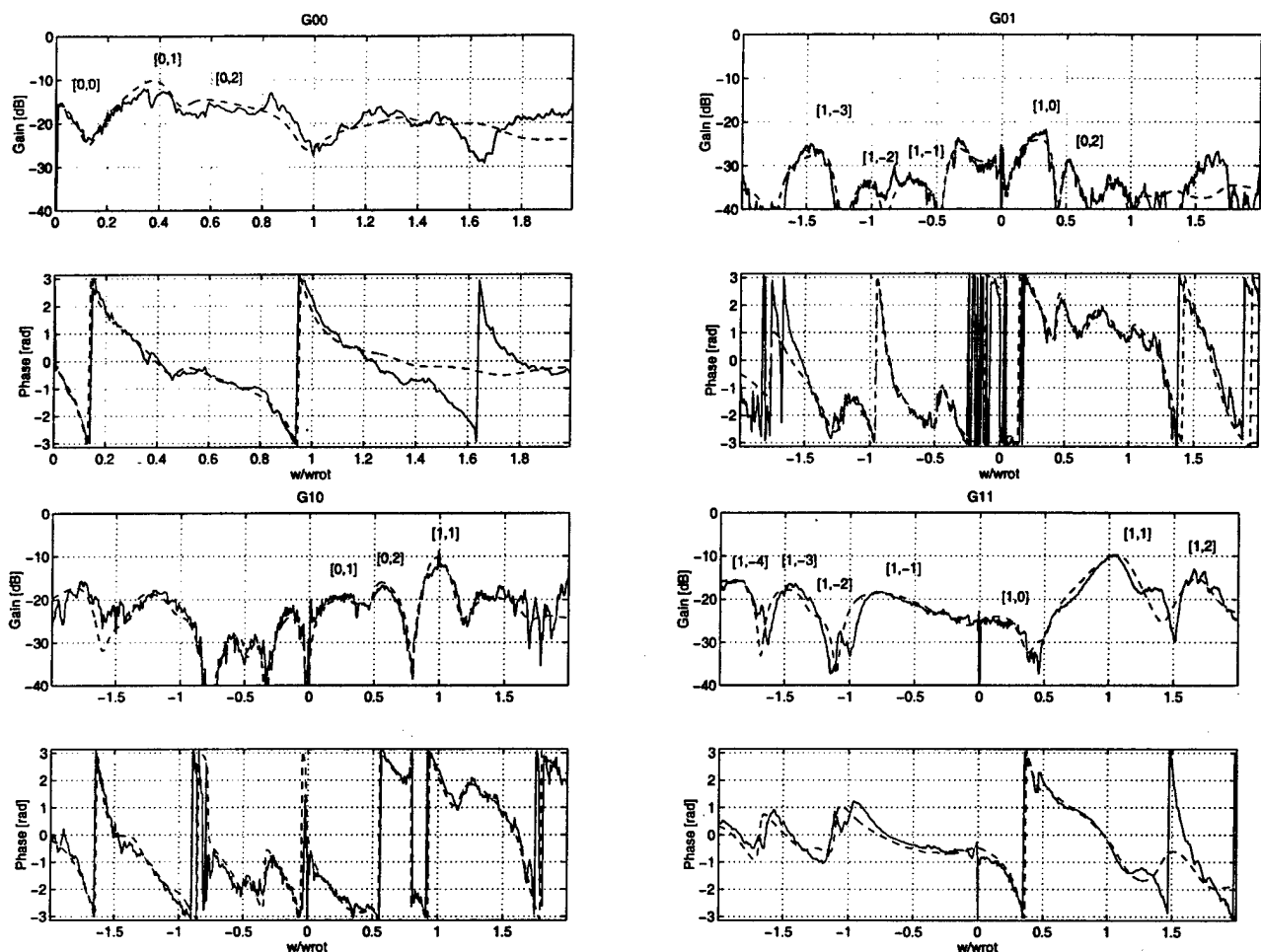


Figure 3: ETFE and FORSE identified MIMO transfer function system $G_{00}(j\omega)$, $G_{01}(j\omega)$, $G_{10}(j\omega)$, and $G_{11}(j\omega)$, with circumferential inlet distortion at $\dot{m}_{corr} = 14.71$ kg/s and 85% corrected design speed.

is uniform, $DC(60)=1$ corresponds to zero-velocity flow within the 60° sector, giving very poor inlet aerodynamics. It has also been found [10] that the loss of surge margin is approximately proportional to the distortion index and a compressor sensitivity S may be defined as

$$S = \frac{\text{loss of surge margin}}{DC(60)}.$$

The distortion screen designed for Stage 35 with 1 dynamic head distortion magnitude corresponds to $DC(60)=0.61$ representing typical and poor inlet conditions.

Note that the static inlet pressure distribution in figure 1(a) is almost uniform and that a strong static pressure rise can be felt within the distorted sector at the compressor exit. The flow angle from the stator vanes can be approximated as uniform around the annulus. If the exit duct is short and of constant area and if we consider the flow field to be two-dimensional, then the uniform exit flow angle implies a uniform static pressure distribution at the compressor exit and a non-uniform static pressure in

front of the compressor. This is not the case for Stage 35. The non-uniform static pressure at the compressor exit is due to the coupling between the circumferential distortion screen and the engine components, which are the compressor and the diffuser of finite length downstream of the compressor (see figure 1 in *Part I* [7]). The static pressure is uniform at the diffuser exit and the compression system can be treated as *two compressors in parallel* [3] pumping from two streams with different inlet total pressure to the same static diffuser exit pressure. In the diffuser the stream with low total inlet pressure and thus low velocity produces a lower pressure rise than the high total pressure and high velocity stream. Since the static pressure at the diffuser exit is uniform the static pressure at the compressor exit has to be higher in the region of low total inlet pressure than in the region of high total inlet pressure.

4. Steady state experiments

In order to capture the change in compressor characteristics and performance speed-lines have been measured

for clean inlet flow and circumferential inlet distortion. The speed-lines are constructed the same way as already described in *Part I* [7] for radial distortion. Also the effect of steady blowing which refers to a steady valve opening of 50% and a supply pressure of 100 PSI was measured. As one can see in figure 2 the one dynamic head circumferential distortion implies a peak pressure rise drop and a higher stalling mass flow. However with steady blowing the peak pressure rise can be recovered and even a considerable range extension of $y\%$ in stalling mass flow can be obtained.

4.1 Open loop compressor dynamics

It is the very first time that the modal stall inception dynamics of a high-speed compressor with circumferential inlet distortion have been measured and investigated. Forced response experiments with frequency sweeps have been conducted the same way as described for radial distortion in *Part I* [7] in order to obtain the transfer function matrix (2) of the zeroth, first and second harmonic pressure perturbation. The analysis revealed that the magnitude and coherence of the off-diagonal elements $G_{ij}(j\omega) \forall i \neq j$ had high values and that there is a strong *coupling* between the different harmonic transfer functions which is depicted in figure 3. In order to identify and to understand the coupled compressible pre-stall dynamics open loop stall ramps have been conducted and the measured ETFE's have been again fitted with FORSE [8]. 24 states have been used to represent 12 oscillatory poles of the 3 by 3 transfer function system (2). The identified transfer functions are plotted as dashed lines in figure 3 for $G_{00}(j\omega)$, $G_{01}(j\omega)$, $G_{10}(j\omega)$ and $G_{11}(j\omega)$. As one can see there are multiple lightly damped modes in the different harmonics of the pressure perturbations.

The major problem is the labeling of these modes in the coupled transfer function system $\mathbf{G}(j\omega)$. The question may rise if there are newly introduced important modes in the compressor dynamics due to the coupling. This question is difficult to answer since there is no low order coupled compressible model for stall inception with distorted flow in existence and the compressible pre-stall dynamics are not trivial as it has been discussed earlier. In order to identify and to label the modes of the coupled compressor system the modeshapes of the different fitted poles can be constructed from the fitted state-space system $[\mathbf{A}, \mathbf{B}, \mathbf{C}, \mathbf{D}]$. Remember that each complex conjugate pair of eigenvalues λ_j and λ_{j+1} of \mathbf{A} and their corresponding eigenvectors \mathbf{v}_j and \mathbf{v}_{j+1} represent the i -th mode and modeshape of the compressor system. The solution to the homogeneous system

$$\dot{\mathbf{x}}(t) = \mathbf{A} \mathbf{x}(t) \quad \text{yields} \quad \mathbf{z}(t) = e^{\Lambda t} \mathbf{z}_0$$

in the transformed coordinates $\mathbf{z}(t) = \mathbf{V}^{-1} \mathbf{x}(t)$. If we choose the initial state \mathbf{z}_0 so that only the i -th mode is

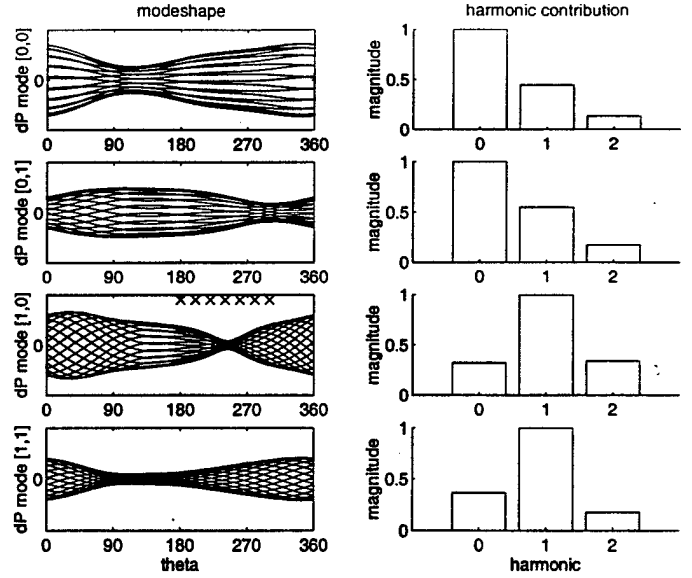


Figure 4: Modeshapes and harmonic contributions of zeroth and first harmonic modes at different points of time

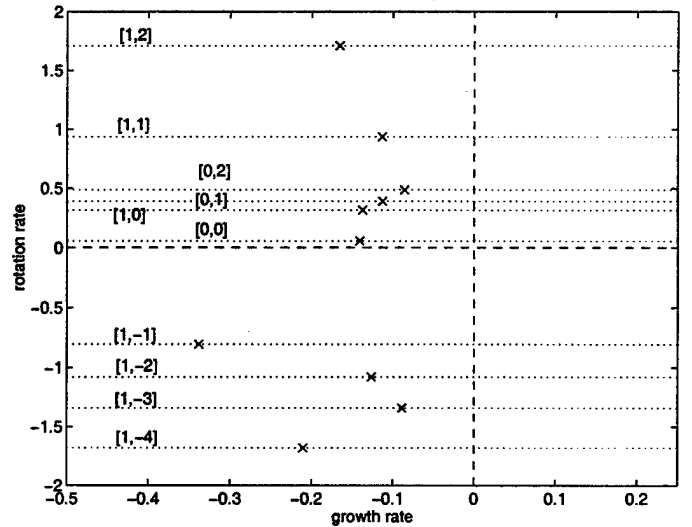


Figure 5: Identified coupled dynamics of the 3 by 3 MIMO transfer function system at $m_{corr} = 14.71 \text{ kg/s}$

excited the contribution of this i -th eigenmode to the system output can be written as

$$\mathbf{y}_i(t) = \mathbf{C} (\mathbf{v}_j e^{\lambda_j t} + \mathbf{v}_{j+1} e^{\lambda_{j+1} t}) .$$

Since the state-space system is in real form $\mathbf{y}_i(t)$ needs to be transformed to complex form in order to obtain the n spatial Fourier coefficients $\nu_n^{(i)}(t)$ (for details see [6]). The modeshape of the i -th mode can then be constructed using

$$\delta p(\theta, t)_i = \text{Re} \left\{ \sum_{n=0}^{\infty} \nu_n^{(i)}(t) e^{jn\theta} \right\} . \quad (3)$$

The contribution of the different harmonics to the mode-shape can directly be determined by the magnitude of the spatial Fourier coefficients $\nu_n^{(i)}(t)$. Figure 4 depicts the modeshapes and harmonic contributions of the modes $[0,0]$, $[0,1]$, $[1,0]$ and $[1,1]$ of the identified 3 by 3 transfer function system (2) at different points of time. The growth rates have been set to zero in order to obtain a picture of the envelope when the perturbations are traveling around the annulus. Note that the distortion screen ranged from 180° to 300° which is marked with the crosses and that the pressure trough in the modeshape of mode $[1,0]$ lines up with the distortion extent. This reminds of *incompressible* pre-stall dynamics with axially uniform perturbation structures. One can clearly see that there is a strong coupling between the zeroth, first and second harmonics. For example the first mode is dominant in the zeroth harmonic but has also first and second harmonic content. Since this mode has the lowest rotational rate and a dominant zeroth harmonic contribution it is labeled as $[0,0]$. Generally the modes are labeled as $[n,m]$ n denoting the harmonic and m the mode number increasing with the rotational rate. This analysis has been applied to each of the fitted poles in order to obtain the labeling and harmonic identification of the different modes which can also be seen in figure 3. These identified modes are plotted in figure 9 and the corresponding labels are linked with dotted lines.

Throttle ramps into stall revealed a very dominant first harmonic mode, the $[1,0]$ mode (often related to the incompressible Moore-Greitzer mode), which was already observed with radial distortion in *Part I* [7]. The evolution of the power spectrum of the first harmonic pressure perturbations during this event is plotted in figure 6. The spectral analysis of this open loop stall ramp showed poor modal activity in the zeroth and second harmonics of the pressure perturbations. To underline the dominance of mode $[1,0]$ the measured transfer function $G_{11}(j\omega)$ is plotted for different mass flows in figure 7. These measurements were obtained by using a different kind of forced response experiment. A frequency distributed method was applied instead of frequency sweeps (for details see [5]) which allowed a better quality of the measurements at lower mass flows. The measurement at 12.8 kg/s shows the *unstable* compressor dynamics (the phase is increasing when the pole is crossed), which can only be measured when the closed loop system is stable, or in other words a control law had to be applied during the measurement in order to stabilize the compressor. This control law is going to be discussed later on. One can clearly see that mode $[1,0]$ increases rapidly in magnitude whereas the other compressible modes $[1,1]$ and $[1,2]$ do not significantly change in stability. This can also be observed in the power spectrum plot of figure 6 at one and at roughly 1.6 times the rotor frequency.

In summary the compressor stall inception dynam-

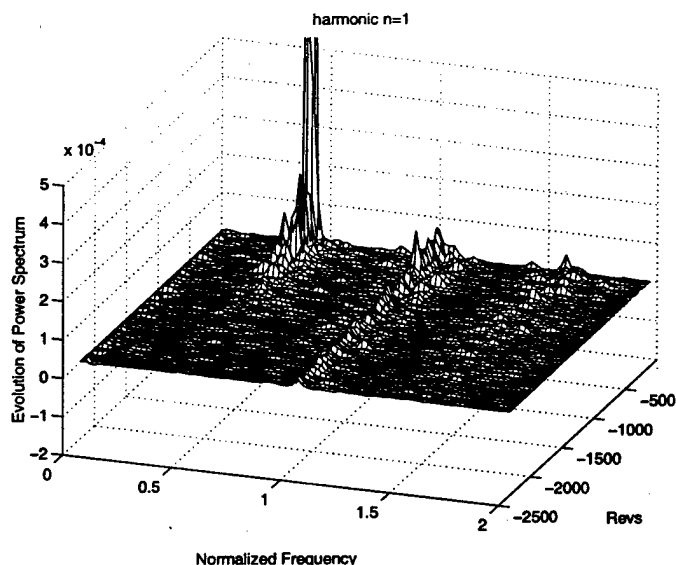


Figure 6: Evolution of power spectrum of the 1st harmonic perturbations during an open loop stall ramp

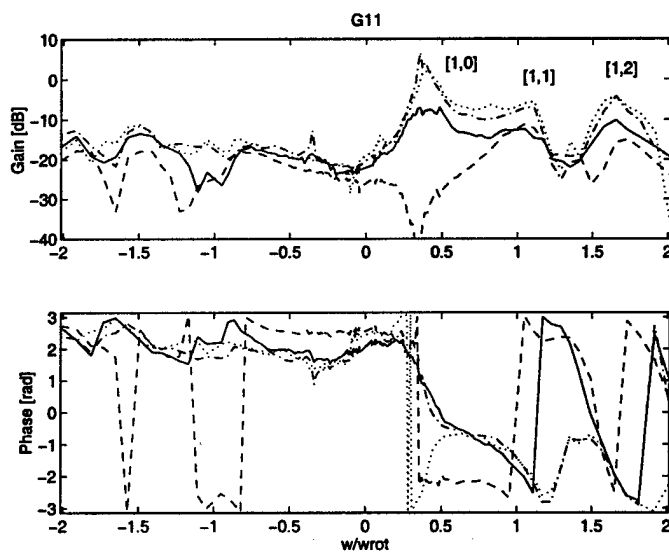


Figure 7: ETFE of $G_{11}(j\omega)$ at 14.71 kg/s (dashed), 13.8 kg/s (solid), 13.35 kg/s (dash-dotted) and 12.8 kg/s (dotted) total corrected mass flow

ics with circumferential distortion consist of mainly the same modes as already encountered with radial distortion in *Part I* [7]. However the analysis shows a strong *coupling* between the harmonics, or in other words a single mode has several harmonic content. The stability of the compressor is determined by a very strong mainly first harmonic mode $[1,0]$ with incompressible features.

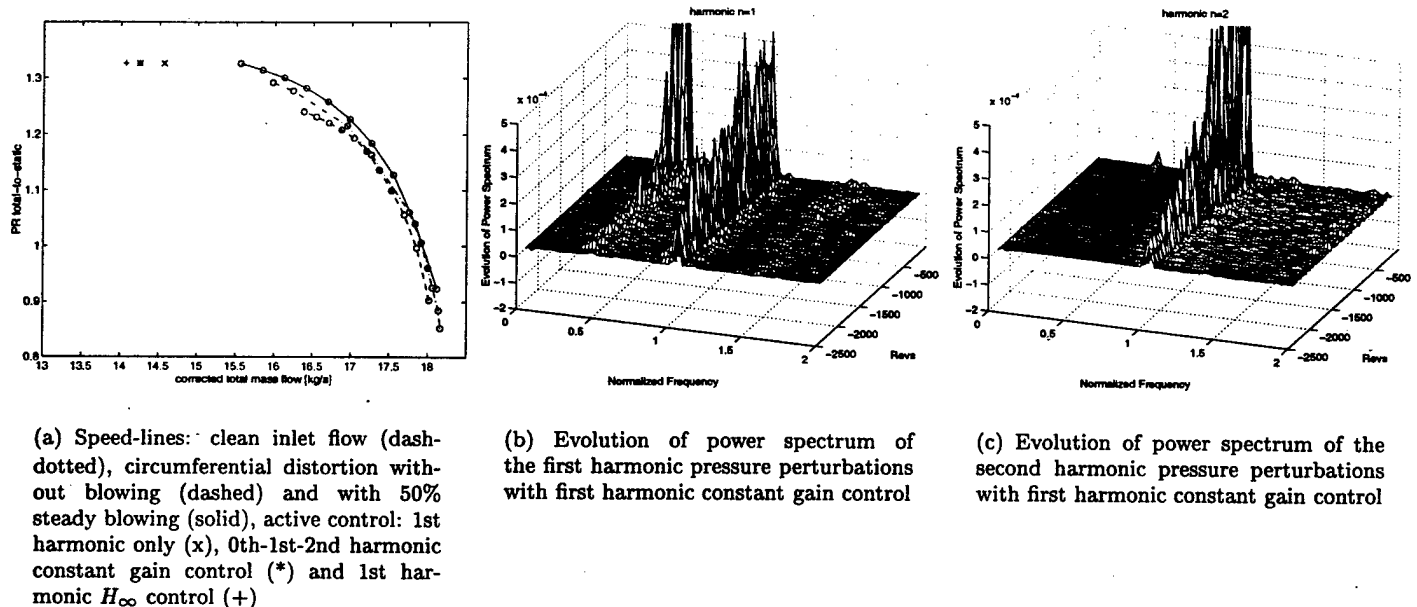


Figure 8: Speedlines with control and power spectra for the case with first harmonic constant gain control

5. Control law implementation and closed loop experiments

Two control strategies have been used to stabilize the compressor. A simple constant gain feedback control law was implemented and tested first. Unlike the case with clean inlet [9] or radial inlet distortion (*Part I* [7]) constant gain control achieved a huge range extension. In addition a dynamic model-based robust H_∞ controller was tested and a further decrease in stalling mass flow was obtained.

5.1 Constant gain control

The function of a constant gain feedback control law is to measure the pressure perturbations upstream of the rotor, to multiply it by a constant complex gain and to feed it back to the actuator. For example for a sensed first harmonic perturbation $\hat{y}_1 = \bar{p}_1$ the feedback law is of the following form

$$\hat{u}_1 = -Z \cdot \bar{p}_1 \quad \wedge \quad Z = z_1 \cdot e^{j\theta_1},$$

where \hat{u}_1 is the corresponding first harmonic SFC of the injection wave. The frequency independent constant amplitude z_1 determines the gain of the control law - that is why it is called constant gain control - and the phase θ_1 defines the spatial phase shift between the sensed and actuated wave. The gain and phase of these control laws have to be found experimentally by on-line tuning.

In a first set of experiments a first harmonic constant gain control law was found to be extremely effective when the gain and phase were set to $z_1 = 1$ and $\theta_1 = \pi$ respectively. The stalling mass flow was decreased by 1% above

steady blowing. The total-to-static speed-lines are plotted in figure 8(a) for clean inlet flow (dash-dotted), circumferential distortion without blowing (dashed) and with 50% steady blowing (solid). The stall point with the first harmonic constant gain control law is marked with a cross. The evolution of the power spectrum during a stall ramp with this control law is depicted for the first and second harmonics of the pressure perturbations in figures 8(b) and 8(c). One can see that mode $[1, 0]$ is initially damped out by the constant gain control. However at these lower mass flows mode $[1, 1]$ starts to grow and in fact a second harmonic mode, mode $[2, 0]$ goes unstable as well. The tuning of additional zeroth and second harmonic control laws with optimal gains $z_0 = 1$, $z_2 = 1$ and $\theta_2 = \pi$ allowed to damp out this second harmonic mode and achieved a further range extension of 0.12-1% in stalling mass flow upon the first harmonic constant gain control case, which is marked with a star in figure 8(a).

As already discussed and experimentally shown in *Part I* [7] and by recent work of Weigl [9] constant gain control could not be applied for decoupled compressible stall inception dynamics. However when circumferential distortion is present and the harmonics are strongly coupled this control strategy works in a very effective way, as one can see from the above results. Since a low order model is not in existence to describe the coupled compressible pre-stall behavior and only the model for incompressible coupled compressor dynamics [5] can be used it is difficult to explain these phenomena physically.

On one hand one can clearly see from the system identification experiments that up to a certain mass flow one

single first harmonic mode with incompressible features dominates the stability picture and seems to allow the application of constant gain control strategies. This was also qualitatively and quantitatively verified with the mentioned incompressible compressor model. But if we recall why constant gain does *not* work in presence of compressible dynamics (see *Part I* [7]) one would expect that since multiple lightly damped modes (see figure 5) - in fact these modes are even more lightly damped with circumferential than with radial distortion - characterize the pre-stall behavior, constant gain control will destabilize other modes when tuned for a particular one. A possible explanation for the success of constant gain control with coupled dynamics can be given as follows: from an energy point of view the blade rows of the compressor represent energy sources or energy sinks in terms of stability. In the case of *decoupled* compressible stall inception dynamics (clean inlet or radial inlet distortion) for example a first harmonic constant gain control tuned for one particular mode can stabilize this mode (the injection turns this mode of the system by changing inlet flow angle, pressure, density etc. into an *energy sink* and energy is dissipated resulting in a damping effect) whereas other modes are destabilized (for the same injection the other first harmonic modes are *energy sources* of the compressor and are energized by the control). However other harmonic modes are not affected by this first harmonic energy excitation due to the decoupling. Now if we consider circumferential inlet distortion yielding *coupled* pre-stall dynamics the injection of first harmonic energy seems to change the compressor dynamics in such a way, that more modes act like energy sinks and the system is more susceptible for the incoming injection pattern. Further more since each mode has several harmonic content energy can be dissipated in other harmonic shapes as well. These ideas and the stall inception mechanism with coupling are still under investigation.

5.2 Robust H_∞ control

As already discussed in *Part I* [7] an identified model needs to be used in order to design a frequency dependent dynamic robust H_∞ control law. Thus for coupled dynamics the general control design strategy turns into a MIMO problem since *one common* set of poles describes the overall coupled compressor dynamics. This increases the complexity and the order of the control problem and makes the design and implementation difficult. MIMO H_∞ have been successfully designed using the presented identified coupled compressor model (see figure 5) but the testing showed that they needed to be tuned further to achieve a considerable range extension [6]. Instead by taking advantage of the dominance of the first harmonic mode [1, 0] and using the knowledge of the pole locations the first harmonic H_∞ controller designed for radial distortion (*Part I* [7]) was tested. The measured *unstable* MIMO transfer function system with circumferential dis-

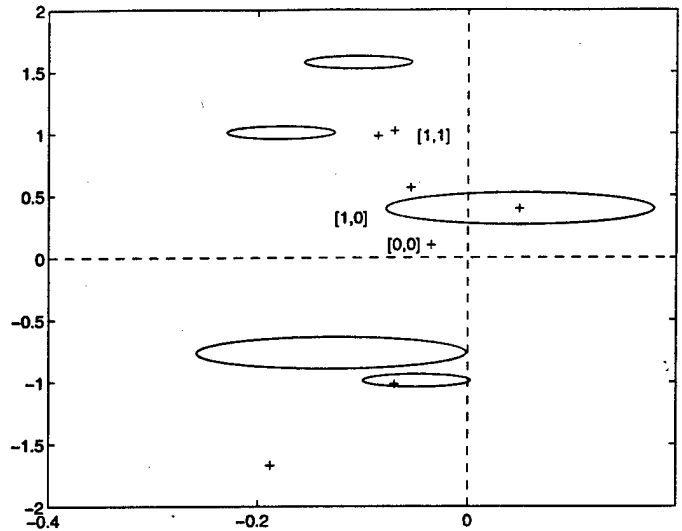


Figure 9: Identified coupled unstable dynamics at $\dot{m}_{corr} = 12.8$ kg/s and perturbation circles of H_∞ control law designed for radial distortion

tortion was also fitted with FORSE and the resulting poles are plotted in figure 9 together with the perturbation circles of the first harmonic H_∞ control law earlier designed for radial distortion. One can clearly see that the notches of the control law or in other words the perturbation circles are at the right frequency. Mode [1, 1] is more lightly damped with circumferential distortion and the circle is at lower growth rates. But the most important mode, mode [1, 0] which dominates the stability picture, is almost centered with the corresponding perturbation circle at this unstable mass flow. One can tell that there is still a big robustness (the control law will stabilize the compressor as long this mode stays within the bounds of the uncertainty circle) and indeed the experiment showed a large range extension. The stalling mass flow could be reduced by y% upon steady blowing resulting in a total range extension of yh+y% which is marked in figure 8(a) by a plus. This first harmonic robust control law achieved the largest range extension which is even bigger than the reduction in stalling mass flow with radial inlet distortion shown in *Part I* [7].

6. Concluding remarks and summary

The results presented in this paper present the very first experimental and empirical investigations on *coupled* compressible stall inception dynamics and it is the first time that a transonic single-stage compressor with circumferential inlet distortion was actively controlled with an annular array of jet-injectors. The distortion magnitude was about one dynamic head corresponding to a DC(60) descriptor of 0.61.

The forced response experiments revealed a very strong coupling between the harmonics but basically the

same modes as with radial distortion were encountered. A further analysis showed that a single eigenvalue of the compressor system dominates the stability picture. Unlike the case with radial distortion constant gain control achieved a large range extension. It is believed that the dominance of an incompressible mode and the coupling between the harmonics changes the stall inception dynamics in such a way, that the tuning of a particular gain and phase for this dominant mode does not destabilize other lightly damped modes. This issue is currently under further investigation. The maximal range extension with a zeroth, first and second harmonic constant gain control law yielded $y_{012} + y\%$ above steady blowing giving a total range extension of $y_{tot}\%$ in stalling mass flow.

In addition to constant gain control strategies the complexity of MIMO robust dynamic control laws could be reduced to the implementation of a first harmonic SISO H_∞ controller by taking advantage of the above described coupled stall inception dynamics. The tested controller was designed for radial distortion and showed a large robustness with respect to the change in the compressible dynamics. This control law allowed an even further total range extension of $y_{tot}\%$ in stalling mass flow including.

The overall comparison of these results and the results of Part I [7] with radial distortion to the case with clean inlet flow shows a great improvement in the extension of compressor operability even in the presence of inlet distortion and is very promising for future work and applications.

7. Acknowledgments

This project was conducted under collaboration between the NASA Lewis Research Center and MIT. The authors would like to thank D. Williams, R. Bruckner and B. Piendl for their help during compressor testing. This work was conducted under NASA grant xxxxxx.

References

- [1] BERNDT, R. G., "Actuation for Rotating Stall Control of High Speed Axial Compressors". *M.S. Thesis, Department of Aeronautics and Astronautics, MIT*, (1995).
- [2] HYNES, T. P., GREITZER, E. M., "A Method for Assessing Effects of Circumferential Flow Distortion on Compressor Stability". *Journal of Turbomachinery, Vol. 109* (July 1987), pp. 371-379.
- [3] LONGLEY, J. P., GREITZER, E. M., "Inlet Distortion Effects in Aircraft Propulsion System Integration". *Steady and Transient Performance Prediction of Gas Turbine Engines, AGARD-LS-183*, (May 1992) . pp. 7-1-7-18.
- [4] MOORE, F. K., GREITZER, E. M., "A Theory of Post-Stall Transients in Axial Compression Systems:

Part I - Development of Equations, and Part II - Application". *Journal of Engineering for Gas Turbines and Power, Vol. 108* (1986), pp. 68-76 and 231-239.

- [5] VAN SCHALKWYK, C. M., "Active Control of Rotating Stall with Inlet Distortion". *GTL Report No. 222* (June 1996)
- [6] SPAKOVSKY, Z. S., "Active Control of Rotating Stall in NASA Compressor Stage 35 with Inlet Distortion". *GTL Report* (August 1997).
- [7] SPAKOVSKY, Z. S., PADUANO, J. D., VAN SCHALKWYK, C. M., SUDER, K. L., BRIGHT, M. M., STRAZISAR, A. J., "Rotating Stall Control in a High-Speed Stage with Inlet Distortion, Part II - Radial Distortion". *To be presented at the 1998 ASME Turbo Expo, Stockholm, Sweden* (June 1998).
- [8] SPACE ENGINEERING RESEARCH CENTER MIT, "Frequency Observable Range Subspace Estimation (FORSE)". , () .
- [9] WEIGL, H. J., "Active Stabilization of Rotating Stall and Surge in a Transonic Single Stage Axial Compressor". *Ph.D. Thesis, Department of Aeronautics and Astronautics, MIT*, (June 1997).
- [10] WILLIAMS, D. D., "Engine Compatibility". *Technical report, Rolls-Royce PLC*, (May 1991) .

Rotating Stall and Surge: Alternate Modeling and Control Concepts

J. M. Protz and J. D. Paduano
Massachusetts Institute of Technology
Cambridge, MA 02139

Abstract.

This paper describes alternative formulations of the rotating stall control problem. Jet injection instead of bleed valve actuation is introduced, and asymmetric instead of one-dimensional (plenum bleed) control of rotating stall waves is cast into the Galerkin framework, resulting in a four-state nonlinear model. Shortcomings of very low-order modeling are discussed, and it is suggested that a more general high-order Galerkin model is more suitable for control law design. Two asymmetric (two-dimensional) nonlinear control examples are then given. The first demonstrates the utility of asymmetric feedback by showing how it can, unlike 1D control, alter the equilibrium properties of the low-order model. The second shows how a Lyapunov analysis motivates a family of nonlinear controllers which account for the multi-dimensional nature of the rotating stall stabilization problem.

1. Introduction

During the past several years, there have been a number of theoretical and experimental studies on the application of active control to the stabilization [1, 2] or bifurcation modification [3, 4, 5, 6] of rotating stall and surge in axial compressors. To simplify the analytical problem, these studies have primarily focused on either linearized models [7] or on a three-state nonlinear version of the Moore-Greitzer compressor model [8]. Furthermore, theoretical nonlinear studies concentrate almost exclusively on the use of axisymmetric actuation through a plenum bleed valve, even though such actuation does not achieve controllability of the primary modes of interest.

Two problems with this state of affairs are addressed in this paper. First, the low-order nonlinear model, although convenient to work with analytically, is fundamentally limited in its ability to accurately describe the experimentally observed dynamics, and in its ability to capture all of the features of compressor behavior that are relevant to control. This paper describes and gives experimental evidence for some of these limitations, and suggests a more accurate formulation of the Moore-Greitzer model.

The second issue addressed is that of 1D vs. 2D actuation. By introducing a 2D actuator in the popular

low-order Galerkin framework, we hope to motivate control studies with this form of actuation. 2D actuation approaches have been or are being tested at the Whittle Lab [9], the MIT Gas Turbine Lab [7, 1, 10], Caltech [11], NASA Lewis [2], Rolls Royce [12], Allied Signal, and others. Thus it is an important alternative to 1D bleed. Furthermore one can easily show, using the models introduced here, that controllability of all the relevant rotating stall and surge modes can be obtained with a single actuator, if this actuator has a sufficiently rich asymmetric influence. Thus complexity arguments do not preclude 2D control; they only suggest that trade studies are required.

Jet injection is by far the most prevalent form of actuation, so it is the focus of the modeling in this paper. Typically a set of servo-controlled high-pressure air injectors is distributed around the annulus of a compressor and independently actuated (see for instance the experimental work in [11, 10, 2]). Other schemes, such as asymmetric compressor exit or interstage bleed, may eventually prove to be more practical for implementation; most of the modeling and control concepts introduced here are applicable to these and other 2D actuation schemes.

Table 1: Notation

The following quantities are used for nondimensionalization:

R	=	mean rotor radius, nondimensionalizes lengths
A_c	=	compressor annulus area
U	=	rotor speed
ρU^2	=	rotor dynamic head
$\rho U A_c$	=	rotor mass flow

The following nondimensional geometric parameters are used in the derivation:

l_u	=	L_u/R , nondimensional upstream duct length
l_d	=	L_d/R , downstream duct length, includes μ
l_c	=	$(l_u + l_d)$, total compressor length
μ	=	cumulative bladerow length
λ	=	cumulative rotor length
B	=	Greitzer B parameter [8]

The following nondimensional flow variables are defined at each station k :

ϕ_k	=	$C_{\phi k}(\theta)/U$, the local mass flow
Φ_k	=	$\frac{1}{2\pi} \int_0^{2\pi} \phi_k d\theta$, annulus average mass flow
ϕ_k	=	$\phi_k - \Phi_k$, the flowfield nonuniformity
P_k	=	$P_k(\theta)/\rho U^2$, the local pressure

The plenum gauge pressure is $\Psi = (p_{s5} - p_{t1})/\rho U^2$.

2. Modeling

The nonlinear Moore-Greitzer model is appended with two-dimensional jet injection actuation in this section. Section 2.1 discusses the infinite dimensional model, Section 2.2 describes the four-state Galerkin form of this model, and Section 2.3 gives a high-order Galerkin form.

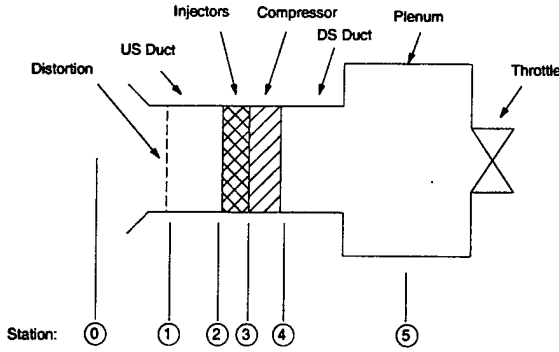


Figure 1: Components of the Moore-Greitzer compression system model.

2.1. Full-Order Model with Jet Injection

The original Moore-Greitzer model was developed by dividing the compressor into several discrete components, each of which is separately modeled [8]. Figure 1 shows the compression system components and labels the axial stations for this approach, where additional stations for inlet distortion and jet injection have been added. The individual component models are coupled, using continuity and momentum relationships, to develop the compression system model.

For instance, conservation of mass allows the mean non-dimensional mass flow ('flow coefficient') at all upstream and downstream stations to be equated, $\Phi_1 = \Phi_2 \triangleq \Phi_u$ and $\Phi_3 = \Phi_4 = \Phi_5 \triangleq \Phi_d$. The jet injectors add mass to the system, so $\Phi_u \neq \Phi_d$. The jet injection process is considered quasi-steady and is modeled using a steady control volume analysis. The analysis assumes uniform mixing and uses conservation of mass and momentum to determine the change in local mass flow and pressure rise across the injection plane. The jet injector model is described in detail in [13] and [10]. The model in [10] accounts for the effects of both mass and momentum addition on the axial momentum (pressure rise) equation for the injector control volume:

$$p_{t3} - p_{t2} = k_{us}\phi_2^2 + k_{ds}\phi_3^2 + k_{jet}\phi_{jet}^2, \quad (1)$$

where the left hand side is the local nondimensional total pressure rise across the injector control volume, and ϕ denotes the local value of the circumferentially non-uniform flow coefficient. The coefficients k_{jet} , k_{us} , and k_{ds} are based on the compressor and injector geometry [10]. To simplify the model for control law design, only the dominant term, injector momentum addition, is considered

here. Together with the mass conservation equation, one finds the matching equations across the injection plane.

$$p_{t3} - p_{t2} = k_{jet}\phi_{jet}^2 \quad (2)$$

$$\phi_3 = \phi_2 + \phi_{jet} \quad (3)$$

The other components in Figure 1 are modeled in [8, 14, 1, 15, 16] and are not re-derived here. Combining the various component models and applying mass conservation one arrives at the following differential equations:

$$4B^2 l_c \dot{\Psi} = \Phi_d - \Phi_t, \quad (4)$$

$$\begin{aligned} [l_u \dot{\Phi}_u + l_d \dot{\Phi}_d] + \left[\frac{1}{n} \dot{\tilde{\phi}}_2 + \left(\frac{1}{n} + \mu \right) \dot{\tilde{\phi}}_3 \right] \\ = \lambda \frac{\partial \tilde{\phi}_3}{\partial \theta} + \psi_c + k_{jet}\phi_{jet}^2 - \Psi, \end{aligned} \quad (5)$$

where $\tilde{\phi}$ denotes the 'asymmetric' component of ϕ , i.e. $\tilde{\phi} = \phi - \Phi$ at any given station. Other variables are defined in Table 1. $1/n$ is an operator, described by the equation

$$\frac{1}{n} \tilde{\phi}_2 = \sum_{n=1}^{\infty} \frac{1}{n} [a_{2n} \cos(n\theta) + b_{2n} \sin(n\theta)], \quad (6)$$

where a_{2n} and b_{2n} are the Fourier coefficients of $\tilde{\phi}_2$. The term $(1/n + \mu)$ is a similar operator, in which $1/n$ in equation (6) is replaced by $(1/n + \mu)$.

Notice that in addition to the pressure rise term, $k_{jet}\phi_{jet}^2$, injection enters through equation (3). Eliminating the jet injection terms from equations (4) and (5) results in the original Moore-Greitzer equations [15, 8].

The influence of jet injection on the Moore-Greitzer model is subtle, because injection has an instantaneous effect on both the upstream and downstream mass flows. Because of this, upstream massflow can no longer be used as a state as in, for instance, [15]. Instead, we introduce two new "effective" mass flow states:

$$l_c \Phi_x = l_u \Phi_u + l_d \Phi_d \quad (7)$$

$$\left(\frac{2}{n} + \mu \right) \tilde{\phi}_x = \frac{1}{n} \tilde{\phi}_2 + \left(\frac{1}{n} + \mu \right) \tilde{\phi}_3. \quad (8)$$

Introducing these relationships into equations (4) and (5), the system of equations required for state space representation is obtained:

$$4B^2 l_c \dot{\Psi} = \Phi_x + \frac{l_d}{l_c} \Phi_{jet} - \Phi_t \quad (9)$$

$$l_c \dot{\Phi}_x + \left(\frac{2}{n} + \mu \right) \dot{\tilde{\phi}}_x = \lambda \frac{\partial \tilde{\phi}_3}{\partial \theta} + \psi_c(\phi_3) + k_{jet}\phi_{jet}^2 - \Psi, \quad (10)$$

where ϕ_3 can be written as a function of ϕ_x by applying the continuity and the state definitions (3), (7), and (8). In fact all of the duct mass flows can be written as linear combinations of the system states and the actuator

input, ϕ_{jet} , in this way. For instance, $\Phi_u = \Phi_x - \frac{l_d}{l_c} \Phi_{jet}$, and similar "direct feedthrough" terms exist for ϕ_2 and ϕ_3 . In the linearized model, direct feedthrough introduces transmission zeros, whose locations depend on the sensing location; for instance upstream sensing results in non-minimum phase zeros. This effect is not limited to jet injection actuators. Any actuator that adds mass to or removes mass from the compression system (e.g. compressor exit bleed) will have a similar influence.

The influence of mass addition is readily illustrated by experimental surge transfer functions. Figure 2 shows measured and fitted surge transfer functions from the MIT low-speed three-stage compressor at a throttle setting near the open-loop stall point of the compressor [16]. The zero locations depend on the mass-addition effect of injection, as well as sensor location. If the mass addition effect is ignored, the model does not exhibit the high-frequency zero seen in the experimental data. At the same time, the measured transfer functions show that there are no unmodeled dynamics (extra poles). Therefore, the assumption of quasisteady mixing is reasonable.

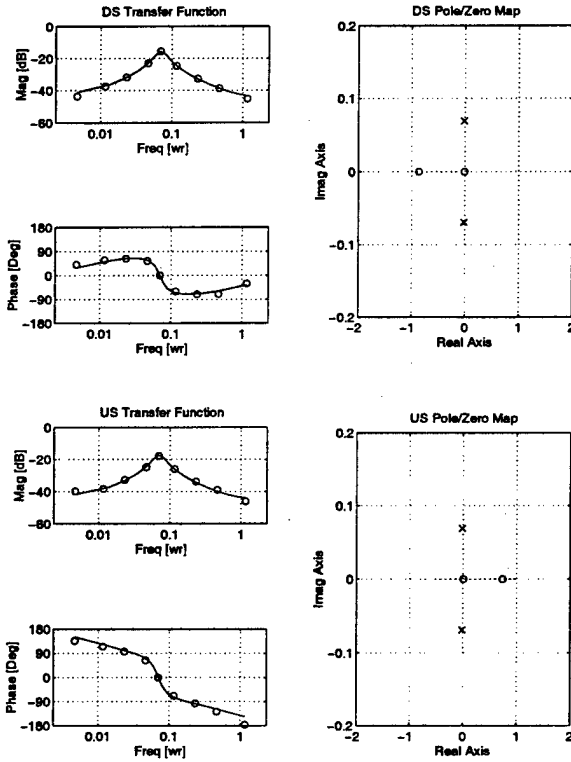


Figure 2: Experimental surge transfer function in MIT 3-stage compressor. DS (top plots) denotes sensors downstream of the actuators, US denotes sensors upstream.

2.2. Four-State Galerkin Projection

The full-order model given above can be approximated by a set of ordinary differential equations using

Galerkin's method. The solution is first written as the linear combination of one or more assumed basis functions and substituted into the partial differential equation. The resulting residual error is minimized by making it orthogonal to each of the assumed basis functions. See [17] for a detailed description of Galerkin's method.

For the rotating stall problem, the flow field's spatial Fourier coefficients are convenient basis functions for the projection. As an example of the orthogonalization procedure, consider the first spatial harmonic. Expanding the series in equation (10) and truncating it at N modes gives the following residual:

$$\begin{aligned} \epsilon = & \sum_{n=1}^N (2/n + \mu) [\dot{a}_{xn} \cos(n\theta) + \dot{b}_{xn} \sin(n\theta)] \\ & - \lambda \sum_{n=1}^N [b_{xn} \cos(n\theta) - a_{xn} \sin(n\theta)] \\ & + \psi_c(\phi_3) + k_{jet} \phi_{jet}^2. \end{aligned} \quad (11)$$

The square of the residual is minimized by making it orthogonal to each basis function. For the basis function $\cos(\theta)$ the orthogonality condition is $\int_0^{2\pi} \epsilon \cos(\theta) d\theta = 0$. Applying this condition, the corresponding condition for $\sin(\theta)$, and a similar condition for the circumferential mean (0th harmonic) gives the four-state Galerkin model:

$$4B^2 l_c \dot{\Psi} = \Phi_x + \frac{l_d}{l_c} \Phi_{jet} - \Phi_t \quad (12)$$

$$l_c \dot{\Phi}_x = \overline{\psi_c(\phi_3)} + \overline{k_{jet} \phi_{jet}^2} - \Psi \quad (13)$$

$$(2 + \mu) \dot{a}_{x1} = \lambda b_{x1} + \int_0^{2\pi} [\psi_c(\phi_3) + k_{jet} \phi_{jet}^2] \cos(\theta) d\theta \quad (14)$$

$$(2 + \mu) \dot{b}_{x1} = -\lambda a_{x1} + \int_0^{2\pi} [\psi_c(\phi_3) + k_{jet} \phi_{jet}^2] \sin(\theta) d\theta \quad (15)$$

where

$$\phi_3 = \Phi_x + \frac{l_u}{l_c} \Phi_{jet} + a_{x1} \cos(\theta) + b_{x1} \sin(\theta) + \frac{1}{(2 + \mu)} \bar{\phi}_{jet}, \quad (16)$$

and an overbar denotes circumferential average, i.e. integration with the basis function 1.

2.3. High-Order Galerkin Model

Relations similar to (14) and (15) hold for all $2N$ basis functions $\cos(n\theta)$ and $\sin(n\theta)$. If the orthogonalization procedure is applied to equations (9) and (10), the following $(2N + 2)$ dimensional system results:

$$\mathbf{H} \dot{\mathbf{x}} = \mathbf{L} \mathbf{y} + \mathbf{g}(\mathbf{y}) + \mathbf{h}(\mathbf{u}) \quad (17)$$

$$\mathbf{y} = \mathbf{x} + \mathbf{D} \mathbf{u}, \quad (18)$$

where the state consists of the plenum pressure and the Fourier harmonics of effective mass flow:

$$\mathbf{x} \triangleq [\Psi, \Phi_x, a_{x1}, b_{x1}, \dots, a_{xN}, b_{xN}]^T = [\Psi, \mathbf{F}\phi_x]^T, \quad (19)$$

the output consists of the plenum pressure and the Fourier harmonics of the downstream mass flow:

$$\mathbf{y} \triangleq [\Psi, \Phi_3, a_{31}, b_{31}, \dots, a_{3N}, b_{3N}]^T = [\Psi, \mathbf{F}\phi_3]^T, \quad (20)$$

and the input vector \mathbf{u} is the spatial Fourier series of the jet injection mass flow:

$$\begin{aligned} \mathbf{u} &\triangleq [0, \Phi_{jet}, a_{jet1}, b_{jet1}, \dots, a_{jetN}, b_{jetN}]^T \\ &= [0, \mathbf{F}\phi_{jet}]^T. \end{aligned} \quad (21)$$

The element u_1 corresponds to plenum bleed; for jet injection this term is set to zero. The vector $\mathbf{g}(\mathbf{y})$ contains the compressor and throttle characteristics and in general can include other natural forcing terms:

$$\mathbf{g}(\mathbf{y}) \triangleq [\Phi_t(\Psi), \mathbf{F}(\psi_c)]^T. \quad (22)$$

The vector $\mathbf{h}(\mathbf{u})$ gives the pressure rise due to jet injection:

$$\mathbf{h}(\mathbf{u}) \triangleq [0, \mathbf{F}(k_{jet}\phi_{jet}^2)]^T. \quad (23)$$

The cumulative inertia matrix is a positive diagonal matrix:

$$\mathbf{H} = \text{diag}[4B^2l_c, lc, (2+\mu), (2+\mu), \dots, (2/N+\mu), (2/N+\mu)]. \quad (24)$$

The rotor inertia matrix is a skew-symmetric block-diagonal matrix:

$$\mathbf{L} = \text{diag} \left[\begin{bmatrix} 0 & 1 \\ -1 & 0 \end{bmatrix}, \begin{bmatrix} 0 & \lambda \\ -\lambda & 0 \end{bmatrix}, \dots, \begin{bmatrix} 0 & N\lambda \\ -N\lambda & 0 \end{bmatrix} \right] \quad (25)$$

Finally, the \mathbf{D} matrix is diagonal with all entries less than unity:

$$\mathbf{D} = \text{diag}[l_u/l_c, 1/(2+\mu), 1/(2+\mu), \dots, 1/(2+N\mu), 1/(2+N\mu)]. \quad (26)$$

In its infinite-dimensional limit, this model is mathematically equivalent to equations (9) and (10) except that it is written in the spatial Fourier domain rather than the θ domain. This Galerkin model is the same as the collocated version of the model presented in [18], except that the \mathbf{F} operator performs Fourier transform integrals on the nonlinear compressor characteristic, while in the collocated version of the model, \mathbf{F} is a discrete Fourier transform (DFT) matrix. As the number of Fourier harmonics goes to infinity the two models become identical, but for low order models the present model approximates the Fourier transform more accurately.

At this point an approximation suggested by Banaszuk [19] is introduced to simplify the stability proofs in Section 4. Consider the limiting case of many compressor stages. The entries of \mathbf{D} (equation (26)) represent the

upstream flow inertia as a fraction of the total inertia. As the number of stages becomes large, the bladerow inertia, μ and the axisymmetric downstream inertia, l_d become large compared to the upstream inertia: in the limit the \mathbf{D} matrix vanishes, and the downstream mass flow becomes the state (see equation (18)). The system therefore reduces to the equation:

$$\mathbf{H}\dot{\mathbf{x}} = \mathbf{L}\mathbf{x} + \mathbf{g}(\mathbf{x}) + \mathbf{h}(\mathbf{u}). \quad (27)$$

This is the equation that is used in the following sections to derive stability proofs and control laws.

The accuracy of the many-stage approximation varies with compressor type. For the approximation to be physically reasonable, one would like the elements of \mathbf{D} to be much less than 1. For the MIT low-speed 3-stage compressor, the \mathbf{D} matrix is:

$$\mathbf{D} = \text{diag}[0, 0.44, 0.30, 0.21, 0.16, \dots]. \quad (28)$$

The approximation is inaccurate for the surge dynamics; $\mathbf{D}_{(2,2)}$, which corresponds to surge, is close to one half. The approximation is somewhat better for rotating stall, but clearly control laws implemented in the MIT rig should consider the fact that output feedback is being used rather than state feedback.

3. Discussion

The high-order Galerkin model described in the previous section illustrates how asymmetric injection enters into the rotating stall control problem, and describes a more accurate implementation of the Fourier analysis needed for a truncated model. In this description we have neglected lags which model the unsteady development of loss, we have ignored important actuators dynamics, and we have simplified the model to motivate nonlinear controllers. These simplifications should in general be avoided, at least during simulations, as they are important influences in practice.

The model in the form used here allows us to make several points. First, by comparing equations (21) and (19) and by recognizing the block diagonal structure of (17) and (24 - 26), it is obvious that linear controllability is determined by the Fourier content of the actuation. High Fourier content can be achieved by a single actuator simply by making it relatively narrow in θ .

The control power of such an actuator may, however, be low, and the control effectiveness must be determined using a realistically sized actuator. Plenum bleed, although it does not achieve linear controllability of any but the zeroth Fourier harmonics, nevertheless can have a strong nonlinear influence on all of the states, because it can change the equilibrium point of the machine.

The strong nonlinear effect of plenum bleed, which extends across all Fourier harmonics, together with the relatively small "B parameter" in many of the rigs in which it has been tested, have allowed concepts developed with the 3-state model to be verified experimentally [5]. However, if the plenum chamber is large or the

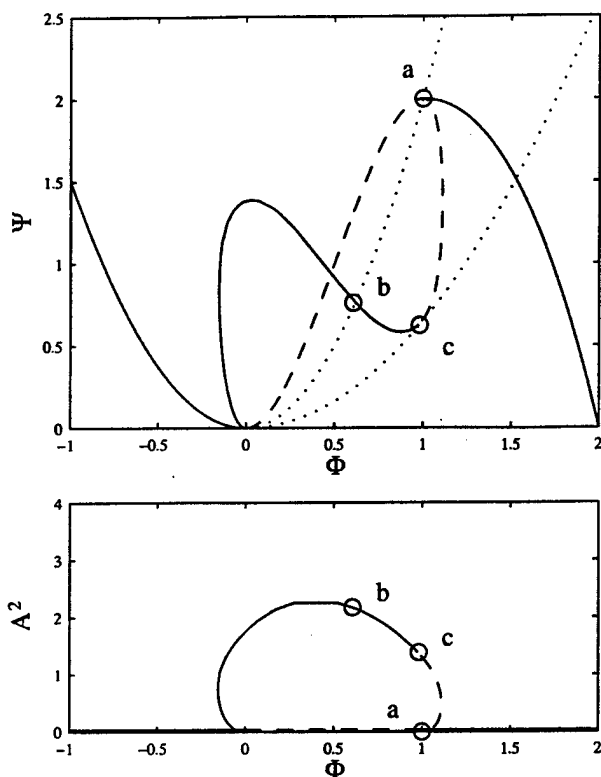


Figure 3: Equilibrium characteristics of a non-cubic, right-skew compressor. Dashed lines are unstable equilibria, solid lines are stable.

compressor pressure ratio is high (as is always the case in real applications), bleeding downstream of the compressor or between stages is much preferable to bleeding from the plenum, because it eliminates the delays and non-minimum phase zeroes associated with plenum bleed [20, 21].

Krstic and Wang [22] have done a thorough study of the difficulties associated with large plenums. They also discuss in detail the control requirements for compressors with what they call 'deep hysteresis' characteristics. Figure 3 illustrates such a compressor: stall equilibria migrate from the peak of the compressor map to higher flow values. At values of Φ below the peak- Ψ value, the only possible equilibria are the axisymmetric branch and the fully developed rotating stall branch; the former being unstabilizable without asymmetric actuation and the latter being unusable. Although the peak of the compressor map can be stabilized for such compressors, doing so imposes severe sensing and bandwidth requirements if 1D control is used [22].

Two alternatives are immediately apparent; both require asymmetric control. The first alternative is simply to stabilize the no-stall branch of equilibria. This is the subject of ongoing work presented in, for instance [23, 1, 2]. A second alternative is to use actuation which is sparse enough (perhaps one to three actuators) to have

short-term practical interest, but placed in such a way as to regain controllability of the spatial Fourier harmonics in the rotating stall model. The control authority of such actuation might not be large or diverse enough to allow stabilization of the no-stall equilibria. It might, however, take a relatively small amount of control power to *shift the locus of the stall equilibria*, and thus render viable controllers that stabilize these equilibria (for instance, using bleed valve control).

Consider the four-state Moore-Greitzer model presented in Section 2.2. Assume for mathematical simplicity that we have a controller which has some effect on the first Fourier coefficient of the distributed injector pressure rise – that is, the injector pressure rise can be expressed as $Fk_{jet}\phi_{jet}^2 = K_z A[a, b]^T$, where $A = \sqrt{a^2 + b^2}$ is the amplitude of the stall cell. Next, fold this control law into the Galerkin model in equations (14) and (15). This system is now the new 'open loop' dynamic system for the bleed valve control presented in, for example, [24, 4, 5]. Figure 4 shows the results of the aug-

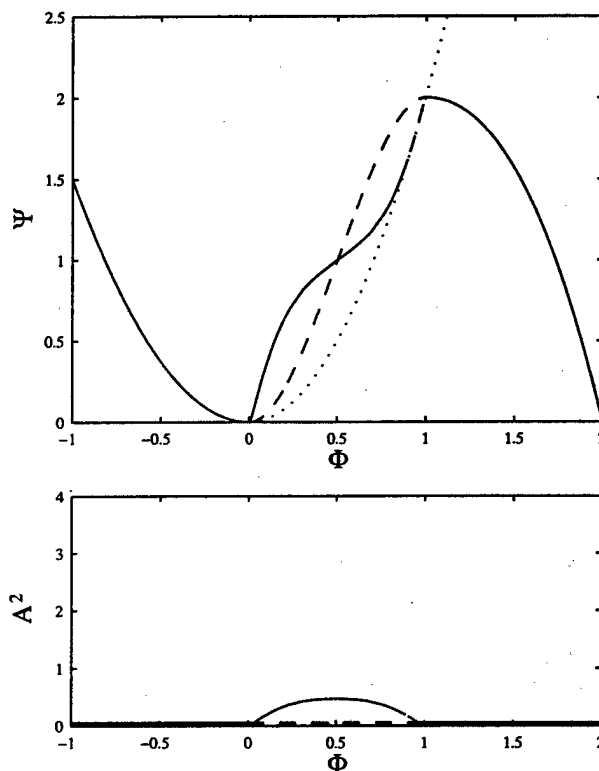


Figure 4: Equilibrium characteristics of non-cubic compressor in Figure 3, with feedback augmentation.

mentation for $K_z = -2.5$. The properties of the stalled branch have improved significantly from the perspective of bleed valve control.

Although this is an interesting demonstration of the utility of 2D control, it should be emphasized that the single-harmonic Galerkin representation has limitations which make it unsuitable for validating many control

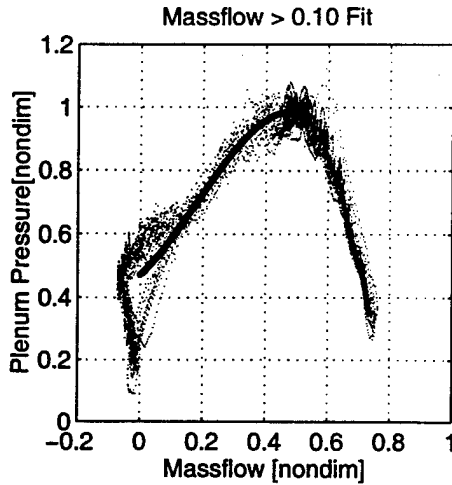


Figure 5: Experimentally identified compressor characteristic for the MIT 3-stage compressor.

concepts. The relationship between 'skewness' and 'deep hysteresis' is one example. In [25, 22], Krstic et. al showed that the 'skew' of the compressor characteristic plays an important role in determining whether a compressor will exhibit deep hysteresis properties when viewed from the 1st harmonic Galerkin approximation. Left-skew characteristics (steeper to the right of the peak) have small amplitude rotating stall equilibria that lie to the left of the peak of the compressor characteristic. Thus they only exhibit hysteresis with respect to throttle position, and not mass flow (i.e. they behave more like Figure 4). On the other hand, right skew characteristics (steeper to the left of the peak) exhibit 'deep hysteresis' as in Figure 4. Mass flow hysteresis and thus 'deepness' is easily tested experimentally by checking the mass flow when stall occurs against when it clears.

Based on the arguments above, the extremely deep mass flow hysteresis observed in MIT's low-speed compressor suggests that it has a right-skew compressor characteristic. However, this is not the case. The compressor characteristic was identified using the technique developed by Behnken [26]. This technique accounts for the impact of both the first and the second spatial Fourier harmonics on the compressor dynamics. As Figure 5 shows, the identified characteristic is left-skew.

For this type of characteristic, the single-harmonic model predicts no mass flow hysteresis. The experimental system, however, exhibits extremely deep hysteresis. This means the higher harmonics must play an important role. Humbert and Krener [27] showed that left-skew characteristics can exhibit deep hysteresis if the higher spatial Fourier harmonics are included in the model. To verify that the higher harmonics are important for the MIT compressor stall solution, the modal content of the fully developed stall cell was measured at several points along the rotating stall characteristic. This data is presented in Figure 6. The figure shows that, at mass flows

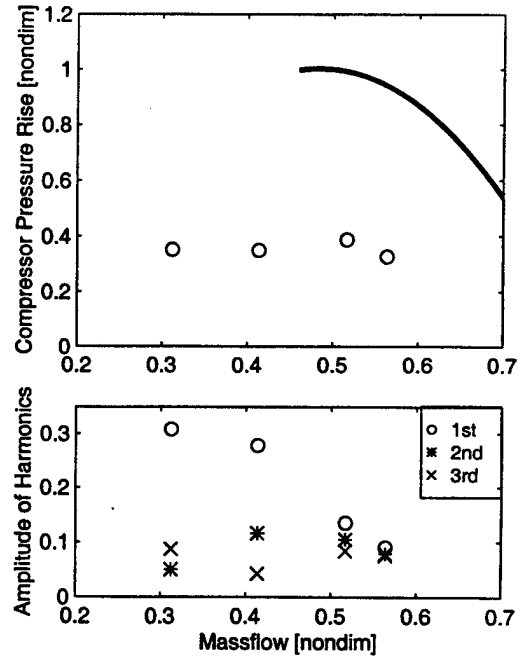


Figure 6: MIT Low-speed compressor harmonic content in stall. Top plot shows four in-stall operating points, bottom plot shows amplitude of each harmonic at each operating point.

above the stall mass flow, the second and third spatial Fourier harmonics are as large as the first and therefore cannot be neglected in the model.

The single harmonic Galerkin model is also limited in its ability to capture the effects of inlet distortion. In [14], Hynes showed that at least three spatial Fourier harmonics are required to accurately capture the compressor instability point with inlet distortion.

4. Theoretical Control Law Design

A new control law is developed in this section using the model of stall with jet injection developed above. Lyapunov analysis is used to motivate a feedback linearizing control law.

4.1. Lyapunov Stability Analysis

Although one might expect the higher order Galerkin approximations to the Moore-Greitzer PDE to be difficult to work with analytically, their special structure makes them relatively easy to deal with using Lyapunov theory. This section illustrates the Lyapunov stability proof for the arbitrary order Moore-Greitzer model and shows how controllers can be derived using this theory.

Consider the state error vector $\mathbf{e} = \mathbf{x} - \mathbf{x}_{eq}$ where \mathbf{x}_{eq} is the desired equilibrium point. A simple candidate Lyapunov function is:

$$V = \frac{1}{2} \mathbf{e}^T \mathbf{H} \mathbf{e}. \quad (29)$$

In the absence of jet injection, this function measures the total perturbation kinetic and potential energy stored in the compression system. It is identical to the Lyapunov function proposed by Mansoux in [15] except that it is written in the spatial Fourier domain rather than the θ domain. When the jets are included, this Lyapunov function measures the perturbation energy in an "equivalent compressor" that accounts for the effects of jet injection on the compressor state.

The perturbation energy is guaranteed to go to zero if the perturbation power, \dot{V} , is negative definite. \dot{V} is found using the chain rule and equation (27):

$$\dot{V} = \mathbf{e}^T [\mathbf{L}\mathbf{e} + \mathbf{L}\mathbf{x}_{eq} + \mathbf{g}(\mathbf{x}) + \mathbf{h}(\mathbf{u})]. \quad (30)$$

Using the symbol $\tilde{\cdot}$ to denote the error value of a variable referenced to its equilibrium value (e.g. $\tilde{\mathbf{g}}(\mathbf{x}) = \mathbf{g}(\mathbf{x}) - \mathbf{g}(\mathbf{x}_{eq})$), the vector $\tilde{\mathbf{g}}(\mathbf{x})$ gives the perturbations in the throttle characteristic and the effective compressor characteristic. Since $\dot{\mathbf{x}}_{eq} = \mathbf{u}_{eq} = 0$, one can also use (27) to write $\tilde{\mathbf{g}}(\mathbf{x}) = \mathbf{g}(\mathbf{x}) + \mathbf{L}\mathbf{x}_{eq}$. Since \mathbf{L} is skew-symmetric, $\mathbf{e}^T \mathbf{L}\mathbf{e}$ is zero. Therefore, one can rewrite (30) as follows:

$$\dot{V} = \mathbf{e}^T [\tilde{\mathbf{g}}(\mathbf{x}) + \mathbf{h}(\mathbf{u})]. \quad (31)$$

Thus, the requirement for stability is:

$$\mathbf{e}^T [\tilde{\mathbf{g}}(\mathbf{x}) + \mathbf{h}(\mathbf{u})] < 0. \quad (32)$$

At this point it is helpful to write $\mathbf{e}^T [\tilde{\mathbf{g}}(\mathbf{x}) + \mathbf{h}(\mathbf{u})]$ as a function of the local mass flow and the throttle and compressor characteristics. Since $\mathbf{e}^T = [\tilde{\Psi}, \mathbf{F}\tilde{\phi}]$ and $\tilde{\mathbf{g}} = [\tilde{\Phi}_t, \mathbf{F}\tilde{\psi}_c]^T$ and $\langle \mathbf{F}\tilde{\phi}, \mathbf{F}\tilde{\psi}_c \rangle = \langle \tilde{\phi}, \tilde{\psi}_c \rangle$ ², we can write:

$$\mathbf{e}^T \tilde{\mathbf{g}}(\mathbf{x}) = \tilde{\Psi}\tilde{\Phi}_t + \langle \mathbf{F}\tilde{\phi}, \mathbf{F}\tilde{\psi}_c \rangle + \mathbf{e}^T \mathbf{h}(\mathbf{u}) \quad (33)$$

$$\mathbf{e}^T \tilde{\mathbf{g}}(\mathbf{x}) = \tilde{\Psi}\tilde{\Phi}_t + \langle \tilde{\phi}, \tilde{\psi}_c \rangle + \mathbf{e}^T \mathbf{h}(\mathbf{u}) \quad (34)$$

where $\langle \cdot, \cdot \rangle$ denotes the inner product. The throttle is always dissipative, so $\tilde{\Psi}\tilde{\Phi}_t$ will always be negative definite. Thus, ignoring actuation, the key requirement for stability is a negative definite $\langle \tilde{\phi}, \tilde{\psi}_c \rangle$.

4.2. Feedback Linearization

There are many ways to design control laws to achieve $\dot{V} < 0$ in the vicinity of the equilibrium point, to enlarge the domain of attraction, and to make \dot{V} more negative to increase robustness to modeling errors. One way to impose a negative definite \dot{V} is to cancel the dynamics introduced by the compressor characteristic and replace them with some desired linear dynamics. This feedback linearizing approach is developed in detail in [16]. It is briefly outlined here.

The feedback linearizing control law is two-sided and, therefore, requires a nominal injection level. The nominal injection level complicates the derivation of the control law. To simplify the derivation, the pressure rise effect of jet injection will be linearized. This linearization is not necessary, but it does make the derivation

more transparent. If the jet injectors have a nominal injection level, $\Phi_{jet}^{(nom)}$, the injector pressure rise can be written:

$$p_{t3} - p_{t2} = k_{jet}(\Phi_{jet}^{(nom)} + \tilde{\phi}_{jet})^2 \quad (35)$$

$$p_{t3} - p_{t2} \approx k_{jet}(\Phi_{jet}^{(nom)})^2 + 2k_{jet}\Phi_{jet}^{(nom)}\tilde{\phi}_{jet}. \quad (36)$$

Substituting this relation into equation (10) gives:

$$\mathbf{H}\dot{\mathbf{x}} = \mathbf{L}\mathbf{x} + \mathbf{g}(\mathbf{x}) + \mathbf{B}\mathbf{u}, \quad (37)$$

where $\mathbf{B} = 2k_{jet}\Phi_{jet}^{(nom)}\mathbf{I}$ is the linear gain on the perturbation injection level. The steady pressure rise from nominal injection, $k_{jet}(\Phi_{jet}^{(nom)})^2$, is a constant that has been made part of $\mathbf{g}(\mathbf{x})$.

The goal of feedback linearization is to cancel the nonlinear dynamics and replace them with desirable linear dynamics. This is done with the control law:

$$\mathbf{B}\mathbf{u} = -\tilde{\mathbf{g}}(\mathbf{x}) - \mathbf{K}\mathbf{e}. \quad (38)$$

Here, \mathbf{K} is a diagonal, positive definite matrix. The term $-\tilde{\mathbf{g}}(\mathbf{x})$ cancels the perturbation compressor pressure rise. The term $-\mathbf{K}\mathbf{e}$ imposes the desired linear dynamics. The mechanism behind the feedback linearizing control law is most easily seen graphically. Consider the example $\mathbf{K} = k_0\mathbf{I}$. Figure 7 shows the initial compressor characteristic, the feedback linearizing control law, and the effective compressor characteristic with control.

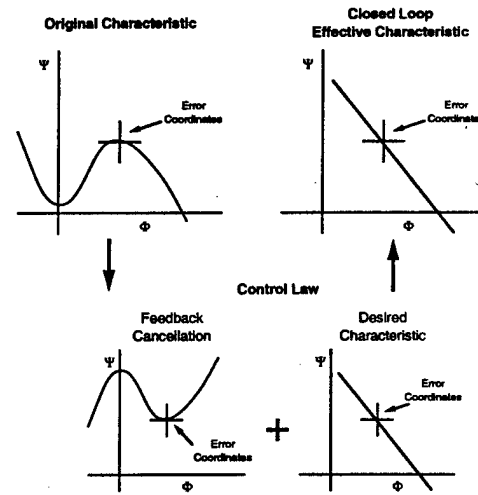


Figure 7: Feedback linearizing control law.

Since the \mathbf{L} matrix is ignored, this control law only changes the damping of the system. The natural frequencies, $\mathbf{H}^{-1}\mathbf{L}$ are unaffected. The natural frequencies can be changed by forming \mathbf{K} from a skew-symmetric matrix and a positive diagonal matrix. The skew-symmetric matrix will not change the positive definite nature of \mathbf{K} .

Substituting the feedback linearizing control law into equation (37) and evaluating \dot{V} gives $\dot{V} = -\mathbf{K}\mathbf{e}$. Thus the unsteady perturbation power is negative definite and the system is therefore asymptotically stable.

¹ \mathbf{F} is a linear operator.

² The inner product is invariant under the Fourier transform.

5. Acknowledgements

The authors have benefitted a great deal from their collaboration with M. Krstic, R. Murray, A. Krener, and P. Kokotovic. We would like to thank S. Liao for contributing some of the figures presented in this paper. We would also like to thank R. Behnken, S. Yeung, S. Humbert, A. Banaszuk and D. Vo for their suggestions and ideas. This work was supported in part by AFOSR grant #F49620-95-0409, Marc Jacobs, technical monitor, and by a U. S. Army NDSEG Fellowship.

References

- [1] J. M. Haynes, G. J. Hendricks, and A. H. Epstein, "Active stabilization of rotating stall in a three-stage axial compressor," *Journal of Turbomachinery*, vol. 116, pp. 226-239, 1994.
- [2] H. J. Weigl, J. D. Paduano, L. G. Frechette, A. H. E. E. M. Greitzer, M. M. Bright, and A. J. Strazisar, "Active stabilization of rotating stall in a transonic single stage axial compressor," in *97-GT-411, ASME Turbo Expo '97, Orlando*, June 1997.
- [3] R. A. Adomaitis and E. H. Abed, "Local nonlinear control of stall, aiaa-932230," in *29th Joint Propulsion Conference and Expo*, June 1993.
- [4] O. O. Badmus, S. Chowdhury, K. M. Eveker, C. N. Nett, and C. J. Rivera, "A simplified approach for control of rotating stall parts i and ii, aiaa 93-2229 and 93-2234," in *29th Joint Propulsion Conference*, June 1993.
- [5] K. M. Eveker, D. L. Gysling, C. N. Nett, and O. P. Sharma, "Integrated control of rotating stall and surge in aeroengines," in *1995 SPIE Conf. on Sensing, Actuation, and Control in Aeropropulsion*, 1995.
- [6] R. L. Behnken, R. D'Andrea, and R. M. Murray, "Control of rotating stall in a low-speed axial flow compressor using pulsed air injection: Modeling, simulations, and experimental validation," in *Proc. 34th IEEE Conf. on Decision and Control*, Dec. 1995.
- [7] J. D. Paduano, L. Valavani, A. H. Epstein, E. M. Greitzer, and G. R. Guenette, "Modeling for control of rotating stall," *Automatica*, vol. 30, no. 9, 1994.
- [8] F. K. Moore and E. M. Greitzer, "A theory of post-stall transients in axial compression systems: Parts 1 and 2," *Trans. of the ASME*, vol. 108, pp. 68+, Jan. 1986.
- [9] I. J. Day, "Active suppression of rotating stall and surge in axial compressors," *Journal of Turbomachinery*, vol. 115, pp. 40-47, Jan. 1993.
- [10] H. D. Vo, "Active control of rotating stall in a three-stage axial compressor with jet actuators," Master's thesis, MIT, Department of Aeronautics and Astronautics, 1997.
- [11] R. D'Andrea, R. L. Behnken, and R. M. Murray, "Active control of rotating stall via pulsed air injection: A parametric study on a low speed, axial flow compressor," in *Proc. of the SPIE*, vol. 2494, pp. 152-165, Apr. 1995.
- [12] C. Freeman, A. G. Wilson, I. J. Day, and M. A. Swinbanks, "Experiments in active control of stall on an aeroengine gas turbine," in *97-GT-280, ASME Turbo Expo '97, Orlando*, June 1997.
- [13] J. S. Simon, *Feedback Stabilization of Compression Systems*. PhD thesis, MIT, Department of Aeronautics and Astronautics, 1993.
- [14] T. P. Hynes and E. M. Greitzer, "A method for assessing effects of circumferential distortion on compressor stability," *Journal of Turbomachinery*, vol. 109, pp. 371+, July 1987.
- [15] C. A. Mansoux, D. L. Gysling, J. D. Setiawan, and J. D. Paduano, "Distributed nonlinear modeling and stability analysis of axial compressor stall and surge," in *American Control Conference*, July 1994.
- [16] J. M. Protz, "Nonlinear active control of rotating stall and surge," Master's thesis, MIT, Department of Aeronautics and Astronautics, 1997.
- [17] T. L. Saaty and J. Bram, *Nonlinear Mathematics*. New York: Dover, 1964.
- [18] C. Mansoux, "Distributed nonlinear stability analysis of rotating stall," Master's thesis, MIT, Department of Aeronautics and Astronautics, 1994.
- [19] A. Banaszuk. Personal communication.
- [20] J. S. Simon, L. Valavani, A. H. Epstein, and E. M. Greitzer, "Evaluation of approaches to active compressor surge stabilization," *Journal of Turbomachinery*, vol. 115, pp. 57-67, Jan. 1993.
- [21] Y. Wang and R. M. Murray, "Effects of noise, magnitude saturation, and rate limits on rotating stall control," in *36th IEEE Conf. on Decision and Control*, 1997.
- [22] M. Krstic and H. H. Wang, "Control of deep-hysteresis aeroengine compressors - part i and ii," in *36th IEEE Conf. on Decision and Control*, 1997.
- [23] J. D. Paduano, A. H. Epstein, L. Valavani, J. P. Longley, E. M. Greitzer, and G. R. Guenette, "Active control of rotating stall in a low speed axial compressor," *Journal of Turbomachinery*, vol. 115, pp. 48-56, Jan. 1993.
- [24] D. C. Liaw and E. H. Abed, "Stability analysis and control of rotating stall," in *Proc. 2nd IFAC Nonlinear Control Systems Design Symposium*, June 1992.
- [25] M. Krstic, J. M. Protz, J. D. Paduano, and P. V. Kokotovic, "Backstepping designs for jet engine stall and surge control," in *Proc. 34th IEEE Conference on Decision and Control*, 1995.
- [26] R. L. Behnken, *Nonlinear Control and Modeling of Rotating Stall in an Axial Flow Compressor*. PhD thesis, California Institute of Technology, Sept. 1996.
- [27] S. Humbert and A. Krener. Personal communication, 1996.

Development of the Active Compressor Rotor Blade – Focus on the Piezoelectric Actuation Issues

Gordon L. Maahs and Carlos E. S. Cesnik

22 November 1999

1 Introduction

1.1 Motivation

The progression of jet engines towards longer lives, higher thrusts, and lower aspect ratio blades increases the importance of damaging blade vibration. Of particular concern is flutter, a dynamic instability caused by complex interactions between the air flow and rotating blades. Currently, the method of flutter prediction relies heavily on experimentation. However, testing the parameter space (including pressure, temperature, corrected speed, and weight flow) is impractical and the resulting compressor maps (today's standard for flutter prediction) do not fully represent all relevant parameters, leading to distrust of such measures [3].

A tool is sought that is capable of identifying the fluid-structure interactions that define flutter. Such a device is not a new idea. In 1972, Dr. Sisto [2] proposed: "I would like to make a very strong plea for... a rotor, that is specifically designed for flutter research with due attention given to the necessity for instrumentation and the need to change geometry easily and quickly." Unfortunately, as critical as experimental measurement is to gaining understanding of flutter, time has not seen this task complete. Today, just as twenty seven years ago, there is scarcely any available flutter data. In 1997, Dr. Srinivasan commented on the flutter literature as having "a conspicuous lack of experimental data" [6].

The absence of experimental data is not because there are more interesting problems to be studied. On the contrary, turbomachinery flutter has received a lot of attention over the past years. The difficulty lies in the hostile environment. Measuring an instability has inherent problems. How does one stop or control the blades once they start fluttering? Measuring the fluid and structural dynamic behavior around a 30 bladed rotor spinning upwards of 16,000 RPM, doing it unobtrusively, controlling the perturbation, and keeping the fluttering blades from destroying themselves and the test rig has confounded experimentalists for more than two and a half decades.

The Active Rotor is a proposed tool to directly measure the unsteady aerodynamic response of a transonic compressor. By controlling the shape and motion of a compressor blade, many engine parameters thought to be relevant to flutter can be systematically investigated. Two requirements necessary for experimentally investigating flutter were defined: each of 30 blades of a compressor stage must be individually controlled, and each blade must be capable of 1° of tip rotation over a large range of frequencies (300 to 1000 Hz). These requirements can be satisfied by piezoelectric actuators attached to each blade.

Piezoelectric actuators, however, lack the power to deform a typical titanium compressor blade, and thus a spar and shell concept is adopted, as shown in Figure 1. The Active Rotor consists of three parts. The outer foam shell keeps an aerodynamic surface with a low torsional stiffness. To keep the stiffness low, there is no outer shell. The composite spars support the blade under the large centrifugal loads and are actuated in bending by the piezoelectric actuators. If the spars are actuated in bending in the same direction, the blade will bend. If the spars are actuated in bending in opposite directions, the blade will twist, as shown in Figure 2. It is important to note that the Active Rotor Blade is not intended to be a prototype industrial blade, but it is an invaluable demonstration, diagnostic, and system identification tool.

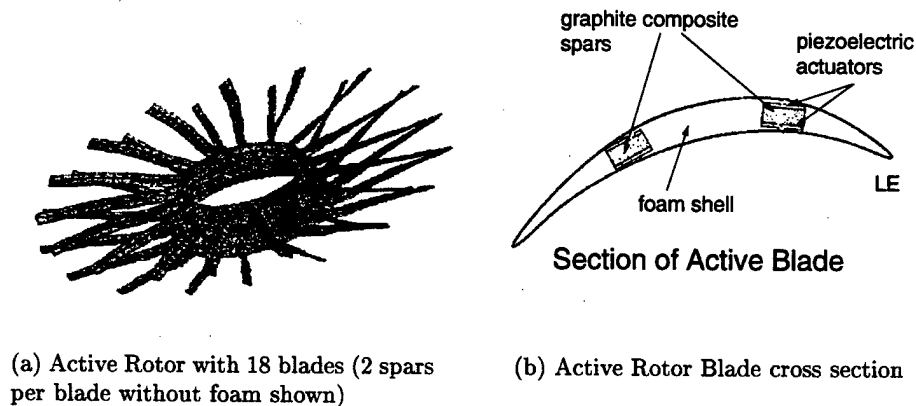


Figure 1: Active Rotor and Blade

1.2 Present Work

The development of the Active Rotor presents many manufacturing challenges: the piezoelectric actuators must be safely incorporated into the structure, the composite spars must be tapered and supported by a root attachment, and the foam shell must be manufactured with the

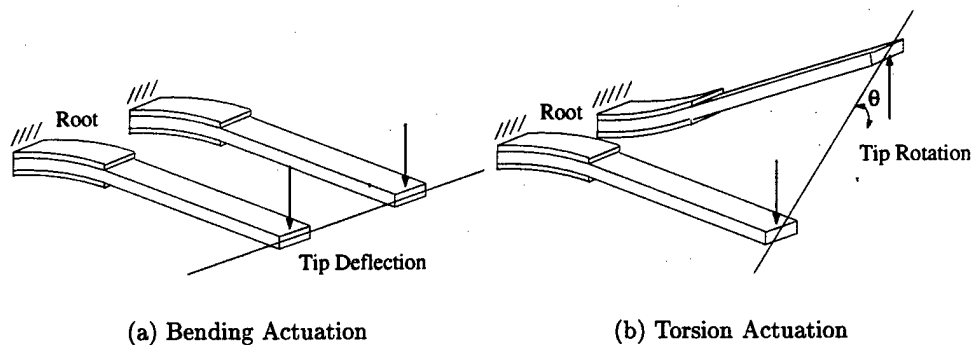


Figure 2: Active rotor blade actuation. Outer foam shell not shown.

appropriate strength and stiffness.

This paper addresses the technical issues associated with the piezoelectric actuators. Three main challenges exist. First, electrical connections must be brought to the on-blade piezoelectric actuators. The electrical leads must be thin and flexible to fit within the Active Rotor geometry constraints, lightweight to keep centrifugal loads small, and insulate the piezoelectric actuators from the composite spars. Encapsulating the piezoceramics in copper-coated Kapton satisfies all of these goals, and is presented in Section 2.1.

Secondly, the piezoceramics must be protected from the tensile strains under the high centrifugal loads¹. A NASTRAN/PATRAN finite element model of the Active Rotor was developed and predicted the strains on the piezoceramics to be above $2500 \mu\epsilon$, which is beyond the nominal failure strain of $2000 \mu\epsilon$. Precompression is adopted to protect the piezoceramic from the large applied strains. To precompress the piezoelectric actuators, an embedding option and a surface bonding option were investigated [5]. Thermal effects during cure of graphite-epoxy composite with an embedded piezoelectric actuator create a permanent stress at room temperature. By rotating the fiber angles of the composite, which alters the difference in Poisson's Ratios between the composite and piezoceramic, a variety of precompressions can be applied to the piezoceramic. However, to satisfy the precompression requirement of $1000 \mu\epsilon$, the fiber angles must be rotated beyond 55° , and the strength requirement is no longer satisfied. Precompression by embedding the piezoceramic in the graphite-epoxy is not a viable option. A surface bonding approach is adopted. An elastic perfectly-plastic shear lag analysis predicts the surface bond will survive the centrifugal loads.

Thirdly, the piezoelectric actuation properties must be understood under a variety of operating stress states. Predicting how piezoelectric actuation properties degrade with compression, recover from release of compression, and operate under tension is necessary to determine the

¹The maximum operating condition of 16,000 RPM results in 35,000 g's at the blade root.

Active Rotor Blade response. Although not all specific loading conditions faced by the Active Rotor Blade were found within the literature, it was found that compressive stress degrades actuation in the direction of stress, release of the compression results in a 80% property recovery [7, 4], and tensile loads are expected to improve actuation [1]. An experiment is conducted to better quantify the tensile strength and actuation property effects for the specific conditions of the Active Rotor.

1.3 Approach

To address the technical challenges of the piezoelectric actuator attachment, protection, and modeling, the following areas are addressed.

1. Characterization of Adhesive Bond Layer
 - (a) Creep between precompressed piezoceramics and composite spars
 - (b) Failure strain
2. Characterization of Piezoelectric Actuators
 - (a) Failure strain comparison for compressed and uncompressed piezoceramics
 - (b) Benchtop actuation
 - (c) Actuation under simulated loading conditions
3. Experimental verification of finite element NASTRAN/PATRAN actuation predictions

The four tests used to investigate the above goals are:

1. **Creep Test**-measure the loss of precompression in the bond layer over time
2. **Benchtop Actuation Test**- actuate the piezoceramics on a cantilevered spar and measure the tip deflection.
3. **Tensile Test**- use the MTS machine to pull the specimens in extension to measure failure strains
4. **Actuation Under Loading Test**-pull the specimen in the MTS machine to a series of static loads, actuate the piezoceramics, and measure the actuation as a function of applied load.

To accomplish the above tests, three coupon types were manufactured. The graphite-epoxy composite beams were manufactured straight and uniform and piezoceramics were bonded to the center of the top and bottom surfaces. The six coupon type layups are given names of A for $[\pm 20]_6s$, B for $[\pm 20]_s$, and C for $[0/90]_s$. The four tests, the goals they address, and the coupons used in the tests are tabulated and shown in Table 1.

Table 1: Experiments and coupon types

Test Name	Address Goal	Coupon Type
Creep	1(a)	A,B
Tensile Test	1(b),2(a)	A
Benchtop Actuation	2(b),3	A,B,C
Actuation Under Loading	1(b),2(a),2(c)	B,C

2 Experimental Testing and Results

The experimental tests introduced in Section 1.3 are presented and discussed after the manufacturing procedures of the test specimens are described.

2.1 Test Specimen Preparation

Piezoelectric actuators were bonded to graphite-epoxy spars either with or without compression. Six types of specimens were manufactured for testing: precompressed $[0/90]_s$, uncompressed $[0/90]_s$, precompressed $[\pm 20]_s$, and uncompressed $[\pm 20]_s$, precompressed $[\pm 20]_{6s}$, and uncompressed $[\pm 20]_{6s}$, where precompressed and uncompressed refer to the state of the bonded piezoceramic. The spar dimensions are 150 mm x 9 mm x .125 mm per ply layer. The PiezoSystems and Morgan Matroc PZT-5A piezoelectric actuator dimensions used are 36.4 mm x 9 mm x .254 mm.

Single-sided copper-coated Kapton, 0.127 mm ($\frac{1}{2}$ mil) thick, is used for the electrical leads to the piezoceramics. Most of the copper is etched away with PCB etchant, leaving only a strip of copper for the electrical connection to the surface of the piezoceramic. Since most commercially available piezoceramics have a conductive surface coating (Morgan Matroc uses nickel), a point connection to the top and bottom surfaces is adequate to provide a uniform electric field through the piezoceramic thickness. To assist in the detection of cracks, two independent connections at the edges of each surface were made, as shown in Figure 3. It was thought that having access to multiple capacitive measurements may help to locate a through thickness crack or indicate damage. However, the multiple leads were not able to identify damage and will be eliminated in future experiments.

The Kapton leads with copper strips are bonded to the top and the bottom surfaces of the piezoceramic with Epotec 301 from Epoxy Technology, Inc. A jig with a vertical slider is used to apply pressure to the bond, as shown in Figure 4. Because of the low viscosity of the epoxy, the applied pressure determines the bond thickness. The bond thickness for an applied pressure of 20 psi results in a bond thickness less than 6.35 microns ($\frac{1}{4}$ mil). The cure cycle is

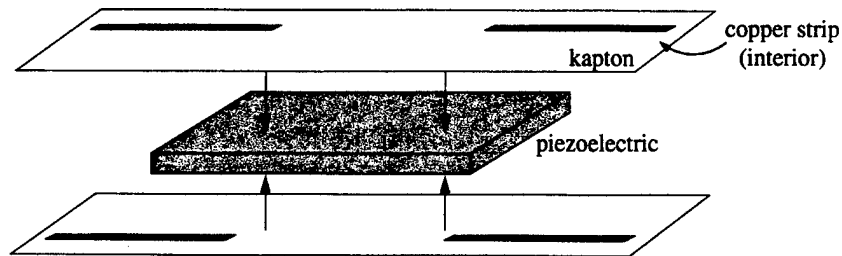


Figure 3: Bonding electrical leads

2 hours at 150°C.

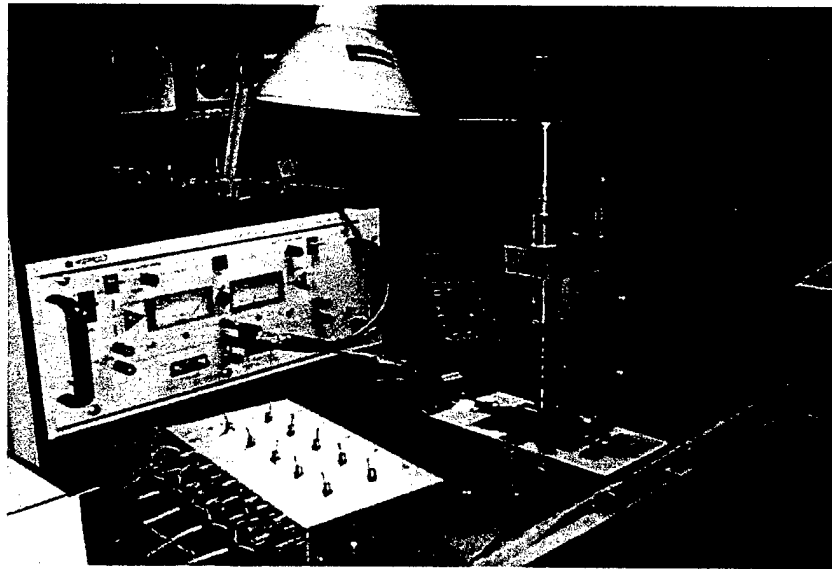


Figure 4: Experimental setup for bond cures

The piezoceramics, packaged in the Kapton leads, are then bonded to the composite beam in a manner similar to the Kapton lead bond. The same epoxy, Epotec 301, and the same jig is used. However, a room temperature bond is performed to eliminate temperature effects associated with the thermal expansion differences between the piezoelectric actuators and graphite-epoxy spars. The room temperature cure time for Epotec 301 is rated as overnight, but is cured for 48 hours under weight to ensure a completely cured bond (12 hours was tried without success).

The piezoceramics are then bonded to the graphite-epoxy beams in one of two ways; com-

pressed or uncompressed. The compressed bond is manufactured by electrically holding compression on the piezoceramics with a large applied voltage during the bond cure. Once the bond is cured the voltage is removed and the bond layer holds the compression on the piezoceramics. For the uncompressed bond, no voltage, and therefore no prestrain is applied.

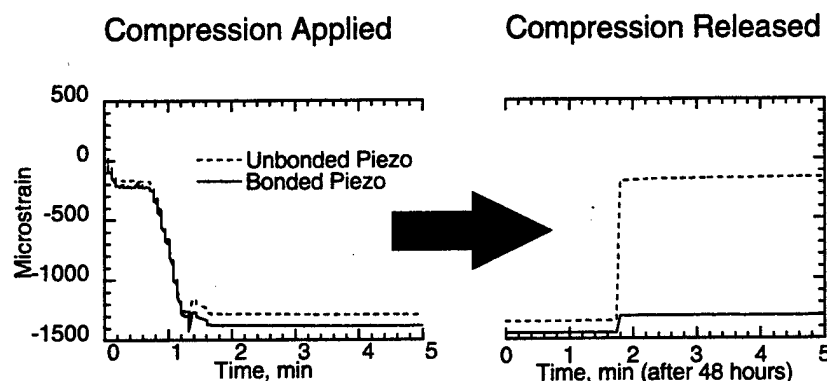


Figure 5: Precompressed bond cure

The ability of the cured Epotec 301 bond to hold the piezoelectric actuator precompression is assessed by comparing the strains of a precompressed piezoelectric actuator to the strains of an actuator that experiences identical voltage but is unbonded and remains free. Strain gages on the surface of the piezoelectric actuators (already packaged in Kapton) show the expected similar responses to the applied voltage, as shown in Figure 5. The voltage is increased² until the strain on the surface of the piezoceramics reaches $-1400 \mu\epsilon$. Upon removal of the voltage (at 1.8 minutes after 48 hrs), the piezoceramic bonded on the $[\pm 20]_s$ composite holds $-1310 \mu\epsilon$. As expected, the free piezoelectric actuator returns to its original strain level, with a small amount of residual strain from the large extended applied voltages. The adhesive successfully held the initial precompression on the piezoelectric actuators.

Not all of the compressed specimens are manufactured with the large strain levels shown in Figure 5, because the thinner spars, $[\pm 20]_s$ and $[0/90]_s$, are more elastic than the stiff spars, $[\pm 20]_{6s}$ and a lower applied voltage during bonding results in fewer electrical breakdowns of the material. The level of piezoelectric actuator precompression attained on the spars, generally around $700 \mu\epsilon$, is acceptable for performing the actuation tests.

²The voltage rampup was done manually which explains the jagged strain increase of the piezoceramic.

³The precompression of $1400 \mu\epsilon$ was arbitrarily chosen as a value above the $1000 \mu\epsilon$ design requirement.

2.2 Creep Test

This test investigates Goal 1(a), the loss of precompression of the piezoceramics through bond relaxation and uses coupon type A, $[\pm 20]_{6s}$, for static tests and coupon type B, $[\pm 20]_s$, for dynamic tests. The Epotec 301 bond layer held the initial precompression on the piezoelectric material bonded to a graphite-epoxy spar, as discussed in Section 2.1. To assess the amount the bond layer relaxes with time, static and dynamic creep tests were performed.

2.2.1 Static Creep Test

Two $[\pm 20]_{6s}$ spars with precompressed piezoceramics (two piezoceramics per beam with one on top and one on bottom, as illustrated in Figure 2) were left sitting free and periodic measurements were taken from surface strain gages. To account for amplifier drift, gain or other amplifier problems, a breakout box was designed with a switch to 120Ω precision resistors. Switching between test gages and the precision resistors allows for assessment of the amplifiers independent of the strain gages. The strain gage wires were not removed from the amplifiers during the months of testing.

The level of creep is illustrated with strain gage readings on the piezoceramic surfaces of coupon type A, $[\pm 20]_{6s}$. See Figure 6. The testing environment was far from ideal. Given the small number of specimens available, the creep specimens were also used in other tests and handled during preparation. They were actuated in benchtop tests, were jostled, had bonding tabs attached, and were without power for the few minutes between equipment changes. Even with the rough handling that occurred during the many months of testing the precompression loses a small $71165 \mu\epsilon$ in 10 months. It is concluded that the static creep of the precompressed bond is small.

2.2.2 Dynamic Creep Test

The precompression held by the bond layer is also tested under cyclic loads. By cantilevering the coupon type B specimen, $[\pm 20]_s$, (see setup for Benchtop Actuation Test, Figure 2.3) the piezoceramics on opposite sides of the spar were actuated with a sinusoidal voltage 180° out of phase to induce bending. The surface strains of the piezoceramic and the tip deflection are measured. Two frequencies of actuation were chosen to maximize the possible damage. A 60 Hz frequency was chosen to be near the 70 Hz resonance for large strain and response actuation, and a 500 Hz actuation was chosen as a high frequency loading. The input voltage is 150 V (590 V/mm). Because the continuous actuation of the Active Rotor is expected to be short in duration, 24 hours at 60 Hz and 8 hours at 500 Hz were deemed adequate testing times. Ten cycles of data were collected and averaged every 15 minutes.

Figures 7(a), 7(b) show the precompression strains during actuation. The 60 Hz test, Figure 7(a), indicates no noticeable change in the level of the $680 \mu\epsilon$ precompression. The 500 Hz test,

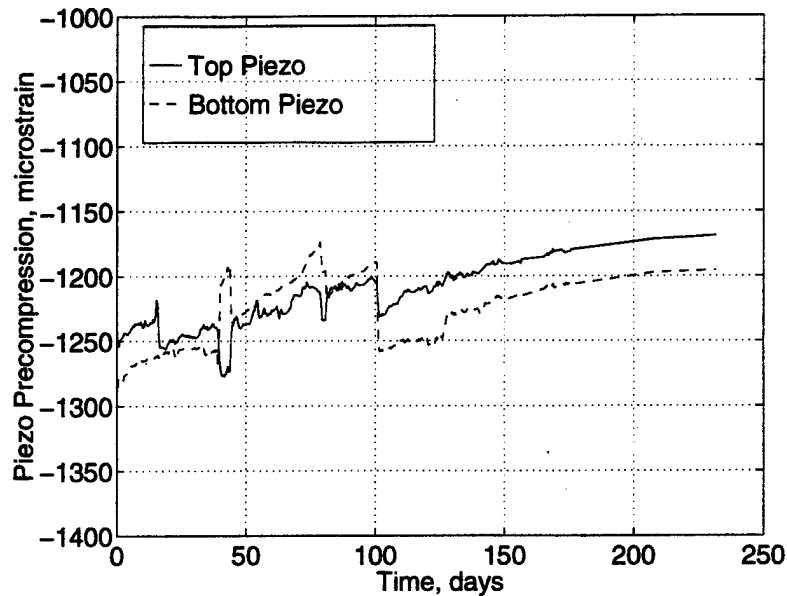


Figure 6: Creep of precompressed bond layer

Figure 7(b), shows a slight loss of about 1.5% of the precompression on the piezoceramic. The loss of precompression due to dynamic creep is too small to be of concern.

2.3 Benchtop Actuation Test

This test investigates Goal 2(b), the frequency response of cantilevered coupons and collects data for Goal 3, the finite element development. All of the coupon types are used, A $[\pm 20]_{6s}$, B $[\pm 20]_s$, and C $[0/90]_s$. Measuring the tip displacement of the coupons for different frequencies of input voltage has two uses. It provides a set of data to be used for finite element model development, and acts as a damage comparison for pulled coupons in Section 2.4.

2.3.1 Benchtop Actuation Test Setup

The experimental setup for the benchtop actuation experiment is shown in Figure 8 and 9. Eight coupons (two compressed and two uncompressed of coupon type A, one compressed and one uncompressed of coupon type B, and one compressed and one uncompressed of coupon type C) were tested. One end of the coupon is clamped to steel blocks such that the piezoceramics have close to a clamped boundary condition. There is approximately a 5mm distance between the end of the piezoceramics and the clamped edge to avoid crushing the kapton electrical leads. The opposite end of the beam is left free and its tip deflection is measured by the laser sensor.

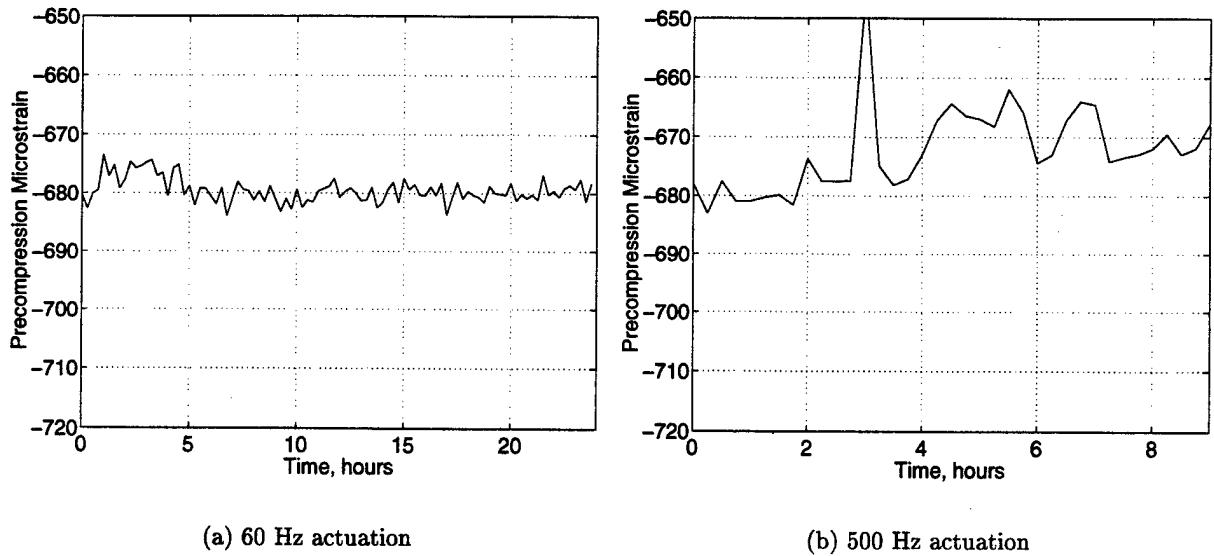


Figure 7: Mean compressive strain during actuation

A LabView program was written to simultaneously actuate the piezoceramics and measure the response with strain gages on the surface of the piezoceramics, and a tip displacement laser sensor. The magnitude of the sinusoidal input voltage must be below the 250 V coercive field to avoid repoling and is arbitrarily set to 150 V.

The frequency of the applied voltage was stepped through 25 Hz increments up to 400 Hz for the 4 ply coupons (to obtain the first two modes) and to 850 Hz for the 24 ply coupons (the theoretical limit of the power amplifiers), with additional frequencies tested near resonances. At each frequency, ten cycles were saved and averaged. Transient effects were eliminated by allowing the beam to vibrate for at least 1 second before saving the measurements.

2.3.2 Benchtop Actuation Test Results

The ten cycles of the output were filtered with a Butterworth low pass filter at three times the driving frequency to eliminate noise. The ten filtered wave peaks and valleys at each frequency were identified with a LabView function and averaged to obtain a single number for each tested frequency, the tip displacement magnitude.

The transfer function between the frequency of applied voltage and the longitudinal strain, transverse strain, and tip displacement magnitude are shown for the 4-ply specimen, coupon type B [± 20]_s, in Figure 10. The data points are shown for the tip displacement plot but are ignored for the strain plots to better see the trend. The first mode was found experimentally

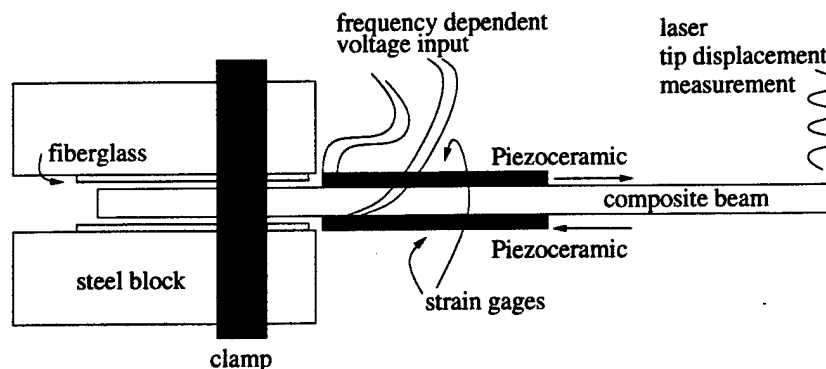


Figure 8: Frequency response test setup schematic. Top view.

to be at 73 Hz and the second was found to be at 245 Hz. The transfer function for a 24-ply specimen is shown in Figure 11. Only the first resonance is investigated before the power of the amplifier is reached just beyond the driving frequency of 600 Hz.

2.4 Tensile Test

This test investigates Goal 1(b), the failure strain of the adhesive bond layer, and Goal 2(a), the failure strain for compressed and uncompressed piezoceramics. It uses the coupon type A, $[\pm 20]_{6s}$.

2.4.1 Tensile Test Setup

Four coupon specimens are statically loaded in an MTS tensile machine to three different load levels and tested dynamically after each test to assess the level of strains the coupons can experience without failure. Failure is defined as the loss of actuation of the piezoceramics, which can be due to a number of possible effects, such as piezoelectric debonding, piezoelectric cracking or composite failure. The first strain level was set near but below the piezoceramic nominal failure strain at $2000 \mu\epsilon$. The second strain level was set at $3500 \mu\epsilon$, well above the predicted piezoceramic failure strain level, and the last strain level continued until composite failure. After each test a transfer function between frequency of applied voltage and the tip displacement response was found and compared to the baseline transfer functions (in Section 2.3) to identify damage.

One inch fiberglass bonding tabs were attached to the ends of the spars before inserting into the MTS grips. The grip pressure was lowered to between 200 and 300 psi to keep from crushing the bonding tabs. During the .001-inch-per-minute ramp, longitudinal and transverse strains on the surface of the piezoceramic pack and on the surface of the composites were measured.

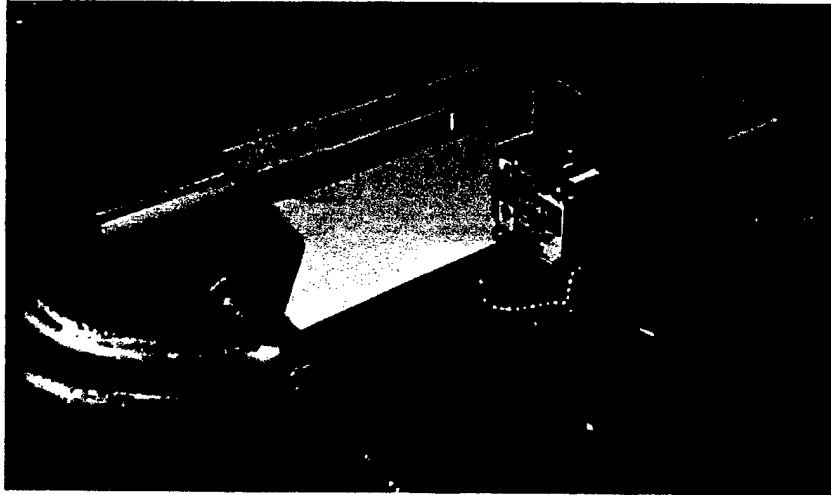


Figure 9: Frequency response test setup.

Each strain level was held for 5 minutes. After the tensile test, the bonding tabs were removed and the excess epoxy cleaned off with a razor blade to keep the extra mass from affecting the frequency response.

2.4.2 Tensile Test Results

The level that the piezoceramics could withstand load without visible damage was higher than expected. The transfer functions of a specimen with no applied strain compared to the transfer functions after being pulled to $3500 \mu\epsilon$ are shown in Figure 12. The static actuation remains unchanged. The resonant frequency is shifted up by 10 Hz, but may be due to the imprecise recreation of the boundary conditions. Other specimens had a resonance shift on the order of 10 Hz between tests, which is also attributed to clamping conditions that were not exactly matched.

The tensile failure of the brittle piezoceramics is rated near $2000 \mu\epsilon$ and yet the piezoceramics withstood above $4000 \mu\epsilon$ before the glue layer debonded. Surprisingly, no cracks were observed in the piezoceramics. It is difficult to assess the actuation properties for a broken coupon, since the frequency analysis can no longer be performed. However, since in all but one case the composite failed away from the piezoceramics and the piezoceramics were not visibly damaged, capacitive measurements can be used as a metric of actuation. There were no measurable changes in the capacitance before and after the tensile tests and it is concluded that the actuation was not effected by the strains. The high strength observed of the piezoceramics may be due to the bonding of the kapton leads, which covers the surface with a flexible adhesive

and polyimide covering. It is speculated that this protective covering extends the piezoceramic failure to more than twice what is expected for a piezoceramic without kapton leads.

The purpose of precompression is to protect the piezoceramics operating under high strains. However, the high strains were not observed to damage the piezoceramics even for those significantly beyond the nominal failure strain of the piezoceramics, and the need for precompression is questioned. However, further investigations on this issue are needed before a firm conclusion can be reached.

2.5 Actuation Under Loading Test

This test investigates Goals 1(b), 2(a), and focused on 2(c), Actuation under simulated loading conditions and uses coupon type B $[\pm 20]_s$ and C $[0/90]_s$ to address the perceived limitations in the literature on stress dependence of piezoceramics properties. By measuring the actuation levels of these two spars under a series of static tensile loads, the response to different biaxial tensile states can be obtained. Because of their different Poisson's ratios of the composite spars, 1.23 for $[\pm 20]_s$ and .04 for $[0/90]_s$, the transverse stress state of the piezoceramics will differ for identical longitudinal stress. As the piezoceramics are pulled to the operating strain levels of the Active Rotor, the influences of the biaxial loading conditions and precompression on actuation are investigated.

2.5.1 Actuation Under Loading Test Setup

The experimental setup is shown in Figures 13, 14. One end of the specimen is held by the lower MTS grips with between 200 and 300 psi. The upper end of the specimen was held in a connector to the PCB dynamic load cell. To accommodate a connector to the dynamic load cell, the upper bonding tabs were sanded from $\frac{1}{2}$ inch thick fiberglass to a 30° angle and bonded with 5 minute epoxy. The steel connector was designed and manufactured using a milling machine located in the Gas Turbine Laboratory at MIT. The angle of the connector holder was designed to a 30° interior angle and a screw hole was tapped to accommodate the PCB load cell screw. Outer dimensions of the connector are 63.5 mm (2.5 inch) width, 101.6 mm (4 inch) high, and 25.4 mm (1 inch) thick. The PCB dynamic load cell screwed flush to both the steel specimen connector and the connector to the 2000 lb load cell.

The MTS machine, in position control, was used to pull the specimens in tension. The piezoceramics were actuated at 150 V, at 1 Hz, and the resulting dynamic force was measured by the PCB dynamic load cell. The actuation frequency, 1 Hz, was chosen to be quasi-static to the piezoceramic but still within the dynamic requirements of the PCB dynamic load cell.

The piezoceramics were actuated together in extension at a series of static loads. Each load was tested twice and unloaded to 5 lbs between each test⁴. Incrementing the load by a corresponding strain level of $500 \mu\epsilon$, the load levels tested were near the following, 5, 50, 5, 50,

⁴The load on the specimens could not be brought to zero load because the load cells would be ineffective.

5, 100, 5, 100, 5, 150, ... 450 lb (limit of PCB load cell) or failure. The MTS machine used a stroke increase rate of .001 inches per minute when ramping up to the desired load levels.

2.5.2 Actuation Under Loading Test Results

In presenting the Actuation Under Loading test data, the external or mechanical loading is separated from the actuated or piezoelectrically-induced loading. Figure 15 shows an example of the type of data gathered during the test. The variables chosen to plot from the data are the Actuated or Piezoelectrically-induced load and External or Mechanical applied strain. This plot shows piezoceramic performance under the operating conditions of the Active Rotor.

Ten cycles of the Actuated or Piezoelectrically-induced load was filtered with a Butterworth low pass filter at three times the driving frequency to eliminate noise. The filtered wave peaks and valleys were identified with a LabView function and averaged to obtain a single number for each tested frequency, the actuated load magnitude.

The actuation for the sinusoidal voltage input versus the tensile strains measured on the surface of the piezoceramic is shown for precompressed and uncompressed specimens in Figure 16 for the $[0/90]_s$ spars and in Figure 17 for the $[\pm 20]_s$ spars. The precompressive strains on the piezoceramics is ignored to allow for a direct comparison between the precompressed and uncompressed specimens. Thus the mechanical strain on the piezoceramics represents only applied strain from the MTS machine. The precompression on $[0/90]_s$ is $650 \mu\epsilon$ and on $[\pm 20]_s$ is $750 \mu\epsilon$. The error bars indicate the standard deviation of the four trials; two were taken at a given load, the specimen was unloaded, and then two more were taken at the repeated load.

As the specimens are pulled in tension, there is a general trend (Figures 16, 17) that is consistent among all of the specimens. The actuation authority first increases, peaks, and then decreases for higher tensile strains. Although tensile properties are inferred from the literature to improve actuation, the cause of the decrease of actuation is currently speculative and more testing needs to be completed to fully characterize the effect. Surprisingly, none of the piezoceramics failed near their nominal failure strain of $2000 \mu\epsilon$. In fact, none of the piezoceramics failed before the composite spars failed, which at times reached $3500 \mu\epsilon$.

Both the reduced actuation and the increased strength is assumed to be due to the Kapton electrical leads that are bonded to the surface. Coating the piezoceramic with a flexible adhesive and polyimide covering may protect the piezoceramic under high strains. Further, the packaging may allow microcracks to grow in the piezoceramics, extending the failure strain but reducing the level of actuation. Release of the load brings the cracks together, and the unloaded actuation properties are unchanged.

The difference in actuation between the compressed and uncompressed specimens at zero applied mechanical strain agree with the uniaxial predictions found in the literature. However, the precompression of the piezoceramics did not have the intended effect of shifting the curves in Figures 16, 17 by the amount of the precompression. The $[0/90]_s$ specimens in Figure 16 were precompressed by $650 \mu\epsilon$, but the curves are shifted by much less, near $200 \mu\epsilon$. A consequence

of the low shift is that a specimen that is compressed and then released of compression will have a higher actuation authority than an untouched specimen, and not the 80% loss seen in the literature.

Biaxial loads are speculated to cause the unusually large property recoveries. The Poisson's Ratio of 0.04 for the $[0/90]_s$ composite in relation to the Poisson's Ratio of 0.3 for the piezoceramic essentially eliminates transverse loading from the tensile test, but attempts to constrain the natural transverse contraction of the piezoelectric material when it is pulled. The response of the $[\pm 20]_s$ specimens appears to be independent of the compressed or precompressed state. Again, the effect is attributed to the biaxial loading and boundary conditions. The Poisson's Ratio for the composite is much larger than the Poisson's Ratio for the piezoelectric material, 1.23 versus 0.3. Thus the tensile test introduces large transverse loads, which may dominate over the effects of longitudinal loads.

The strength extension from the Kapton leads and the dominance of the biaxial stress state over precompression indicates that the precompression may not be required to protect the piezoceramics. However, the level of precompression may be used to tailor the maximum piezoelectric performance to occur at a desired operating tensile load. More testing is needed to complete the piezoelectric actuation characterization under the loading conditions of the Active Rotor. Specifically, composite layups with a variety of Poisson's Ratios need to be tested to complete the biaxial stress state actuation properties of the piezoelectric actuators.

3 Conclusions

A new flutter diagnostic tool, the Active Rotor, is evaluated in this paper. The large centrifugal loads on the Active Rotor Blade require a low density and high strength spar material. Since aluminum and titanium spars are predicted to fail, graphite-epoxy AS4/3506-1 is chosen as the spar material. Results from the finite element model of the Active Rotor Blade predict the available actuation to be within acceptable ranges, but the piezoceramic strains to be near the ultimate. Precompression is chosen to protect the piezoceramics at high strain levels and two methods are investigated. The residual thermal strains produced during the cure of a piezoceramic embedded within a graphite-epoxy laminate is not predicted to produce the desired level of precompression while maintaining the necessary strength. Thus, a surface bonding precompression approach is adopted.

The piezoceramics are packaged between two copper-coated Kapton films for thin, flexible, electrical connections that satisfy the Active Rotor geometrical constraints. The piezoceramics are bonded with a compressive strain (applied electrically) to the composite spars such that the cured bond layer holds the precompression. Creep experiments show the bond layer capable of holding the precompression on the piezoceramics. Applied tensile strains below the failure strain increase piezoelectric actuation, which indicates an improvement of actuation can be obtained at operating conditions. The piezoceramics sustained strains at twice the failure

strain without visible structural failure, which is attributed to the Kapton packaging. Although the actuation decreases when the piezoceramics are strained beyond their failure strains, the decrease is within acceptable levels. Further, results indicate that biaxial loads have more influence on piezoelectric actuation than precompression. The current experiments indicate that the precompression may not be required to protect the piezoceramics. However, the level of precompression may be used to tailor the maximum piezoelectric performance to occur at the operating tensile load. More testing is needed to complete the piezoelectric actuation characterization under the loading conditions of the Active Rotor. The finite element dynamic response predictions of the coupons correlate well with the level of actuation and capture the basic trend of the transfer functions, although the analysis is consistently 10-15% larger than measured results.

Preliminary testing and analysis give encouraging results for the proposed Active Rotor Blade concept and the use of piezoelectric actuators under its high g-field environment.

References

- [1] C. Elissalde, L. E. Cross, and C. A. Randall. Structural-Property Relations in a Reduced and Internally Biased Oxide Wafer (RAINBOW) Actuator Material. *Journal of American Ceramic Society*, 79(8):2041-2048, 1993.
- [2] S. Fleeter. *Aeroelasticity in Turbomachines*. panel session, ONR, 1972.
- [3] J. L. Kerrebrock. *Aircraft Engines and Gas Turbines, Second Edition*. MIT Press, 1992.
- [4] H. A. Krueger. Stress Sensitivity of Piezoelectric Ceramics: Part 3. Sensitivity to Compressive Stress Perpendicular to the Polar Axis. *The Journal of the Acoustical Society of America*, 43(3):583-591, March 1968.
- [5] G. L. Maahs. *Design of an Active Compressor Blade for Aeroelastic Studies*. Master's thesis, Massachusetts Institute of Technology, 1999.
- [6] A. V. Srinivasan. Flutter and Resonant Vibration Characteristics of Engine Blades. *Journal of Engineering for Gas Turbines and Power*, 119:742-775, 1997.
- [7] Q. M. Zhang, J. Zhao, K. Uchino, and J. Zheng. Change of the Weak-Field Properties of $\text{Pb}(\text{ZrTi})\text{O}_3$ Piezoceramics with Compressive Uniaxial Stresses and its Links to the Effect of Dopants on the Stability of the Polarizations in the Materials. *J. Mater. Res.*, 12(1):226-234, 1997.

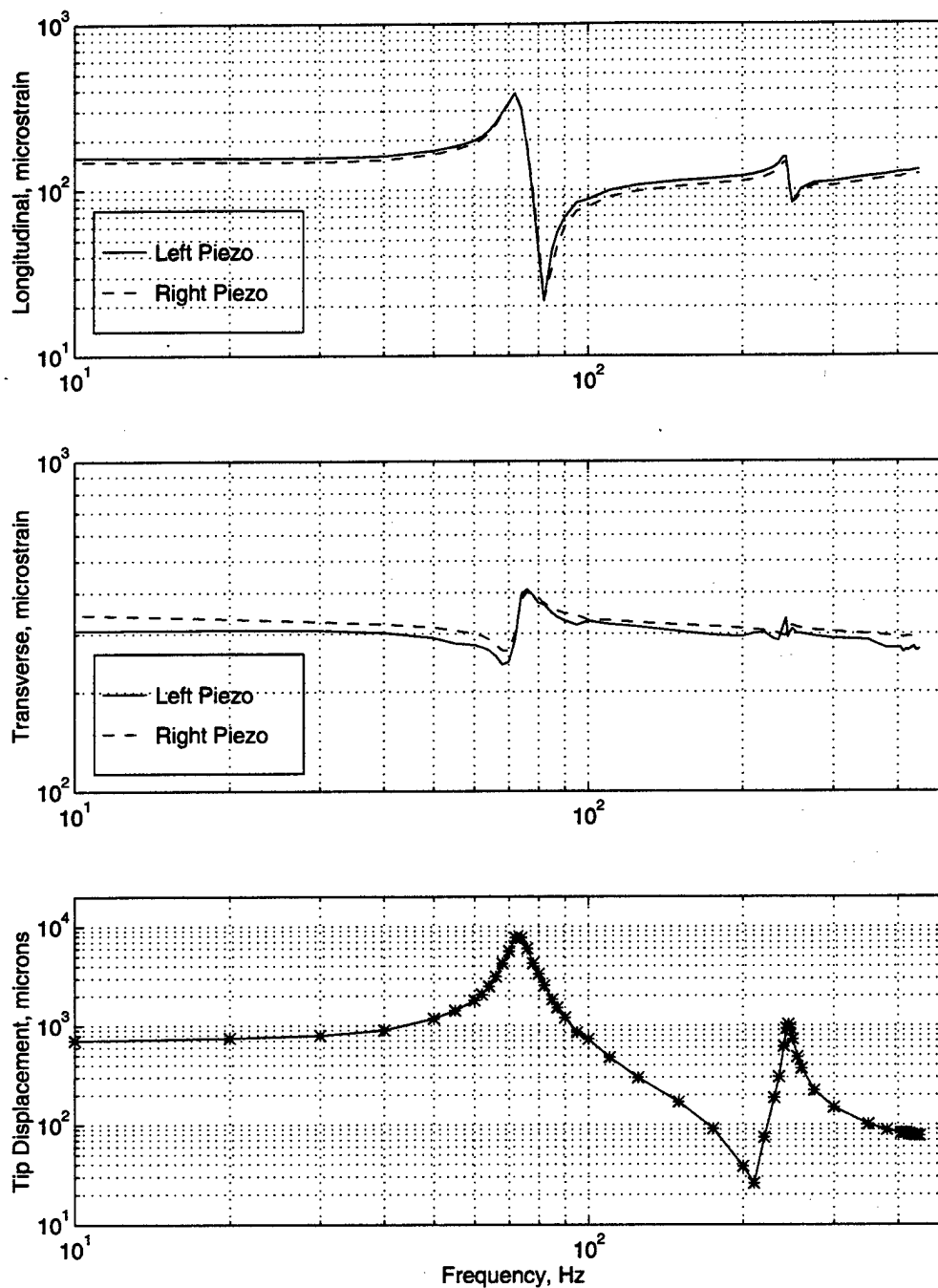


Figure 10: Transfer functions for coupon B, $[\pm 20]_s$. The piezoceramics on opposite sides of the beam, Left Piezo and Right Piezo, have opposite signs, but only magnitude is shown.

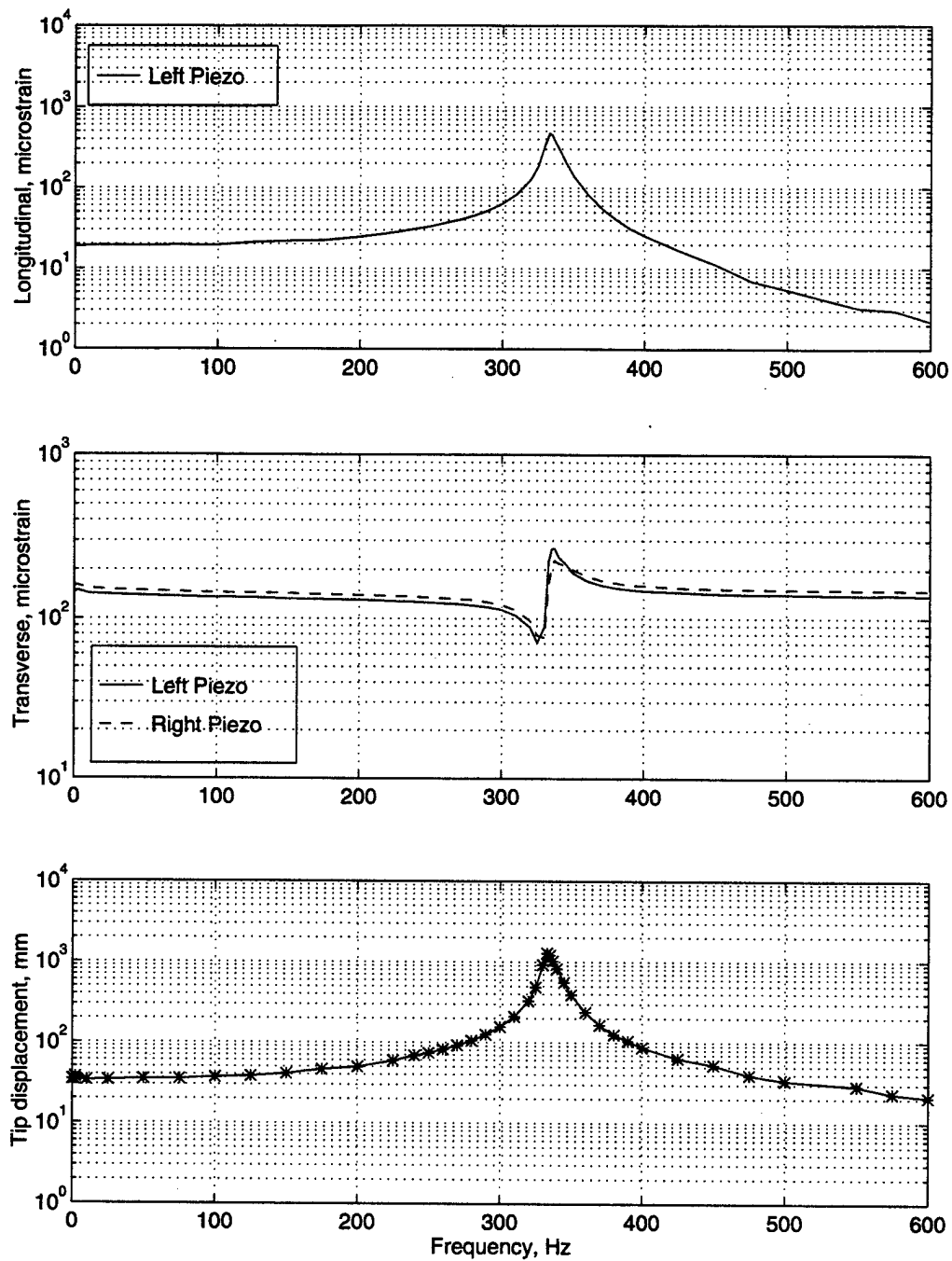


Figure 11: Transfer functions for coupon A, $[\pm 20]_{6s}$. The piezoceramics on opposite sides of the beam, Left Piezo and Right Piezo, have opposite signs, but only magnitude is shown.

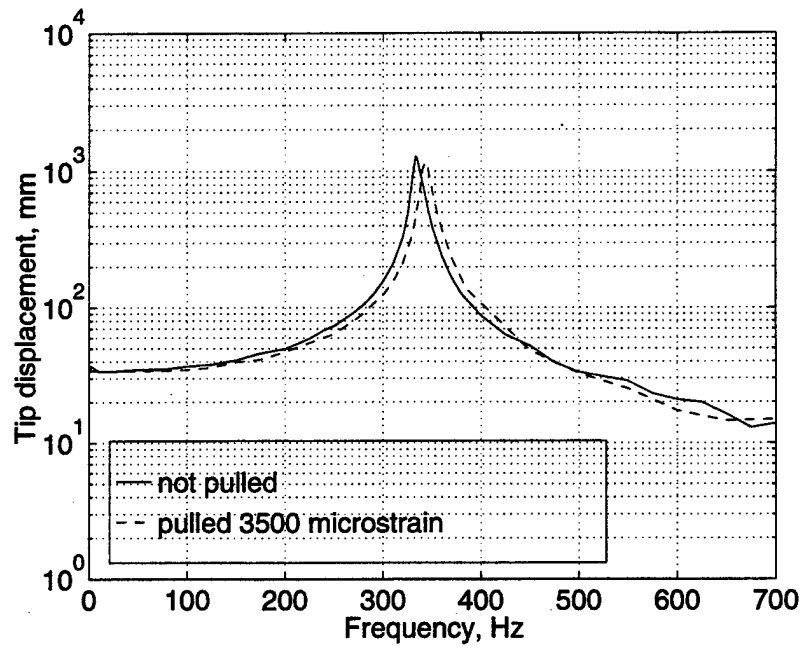


Figure 12: Transfer functions for coupon A, $[\pm 20]_{6s}$. Each test was performed after the specimen had been held at the indicated strain level.

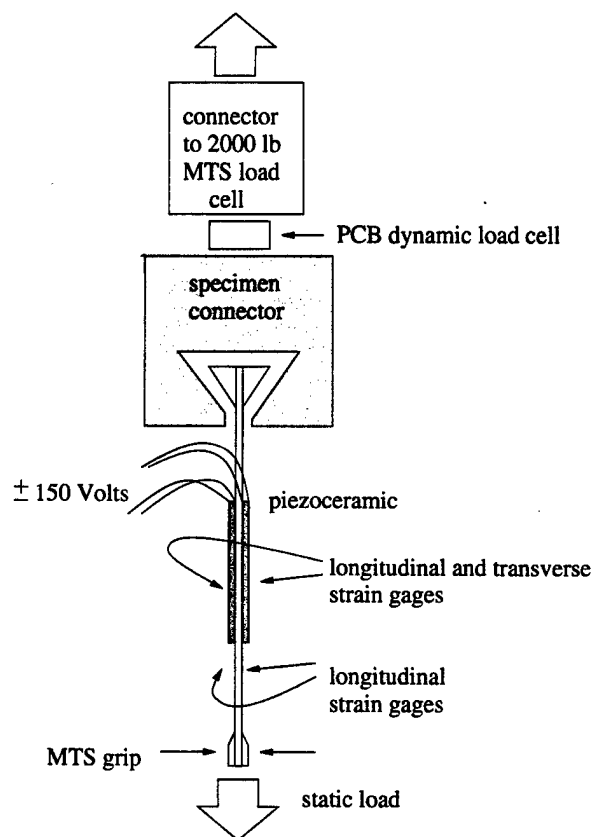


Figure 13: Schematic of Actuation Under Loading Test

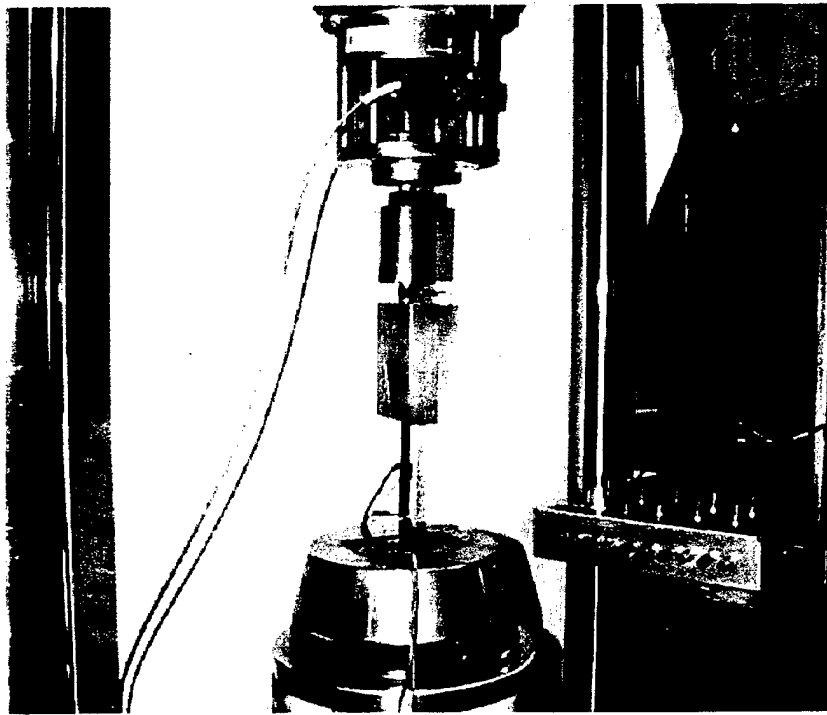


Figure 14: Experimental Setup of Actuation Under Loading Test

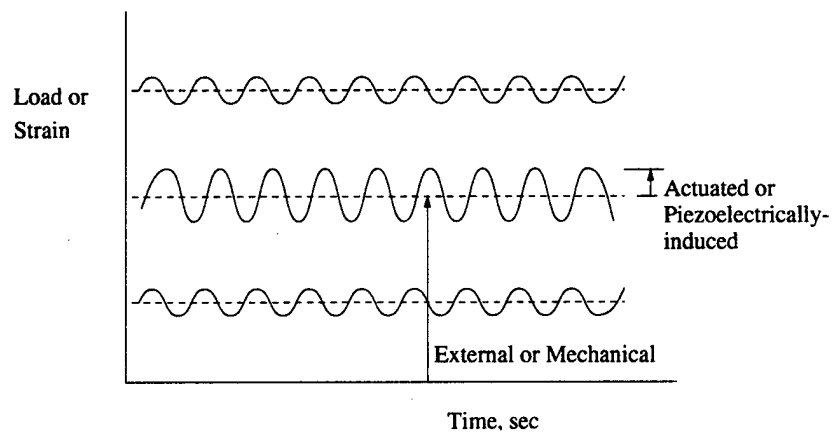


Figure 15: Explanation of Actuation Under Loading variables.

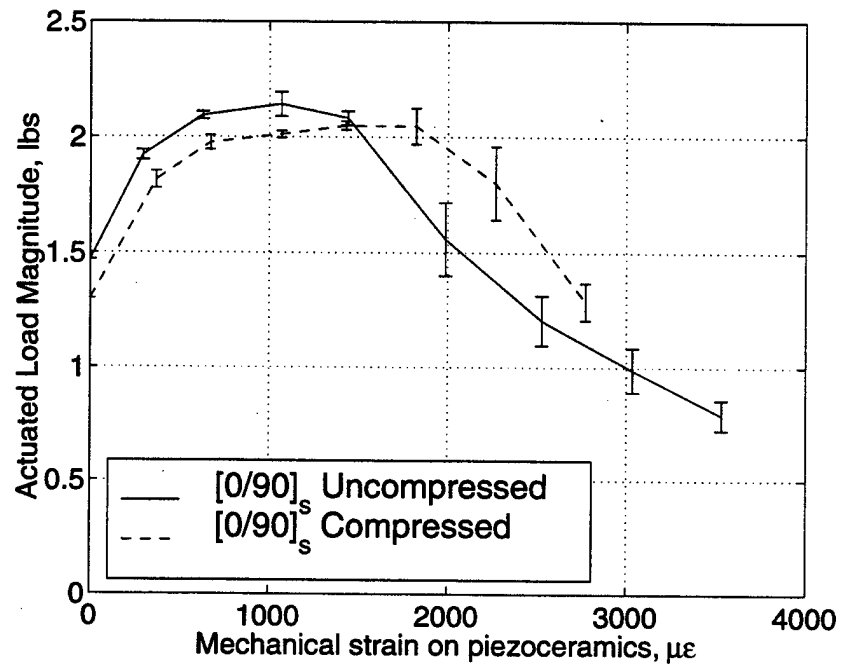


Figure 16: Actuation under static tensile load for $[0/90]_s$ specimens.

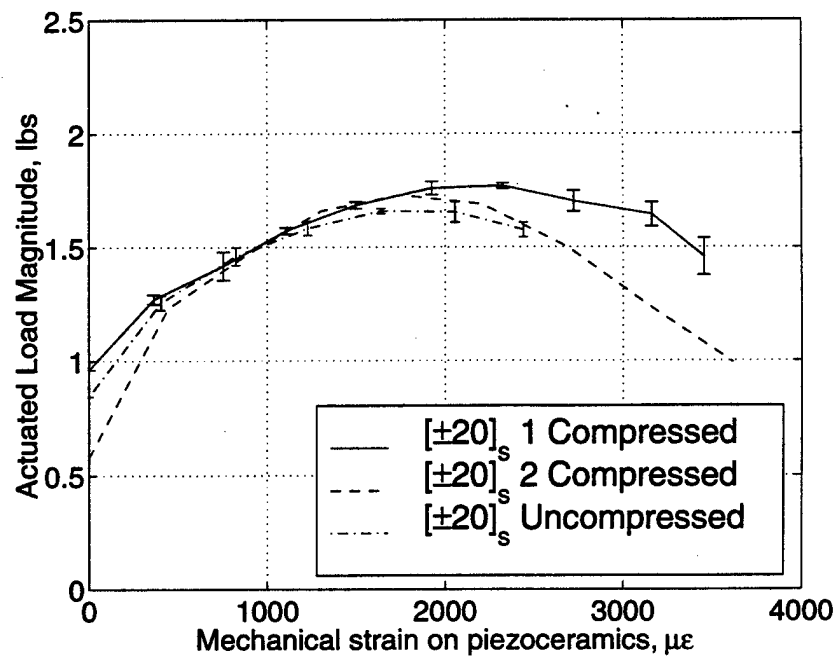


Figure 17: Actuation under static tensile load for $[\pm 20]_s$ specimens.